Low Reynolds number flow control through small-amplitude high-frequency motion

Cleaver, David

Award date:
2011

Awarding institution:
University of Bath

LOW REYNOLDS NUMBER FLOW CONTROL THROUGH SMALL-AMPLITUDE HIGH-FREQUENCY MOTION

David James Cleaver

A thesis submitted for the degree of Doctor of Philosophy

Department of Mechanical Engineering

University of Bath

September 2011

ABSTRACT

There is currently growing interest in the field of Micro Air Vehicles (MAVs). A MAV is characterized by its low Reynolds numbers flight regime which makes lift and thrust creation a significant challenge. One possible solution inspired by nature is flapping flight, but instead of the large-amplitude low-frequency motion suited to the muscular actuators of nature, small-amplitude high-frequency motion may be more suitable for electrical actuators. In this thesis the effect of small-amplitude high-frequency motion is experimentally investigated focusing on three aspects: general performance improvement, deflected jets, and the effect of geometry.

Results presented herein demonstrate that using small-amplitude high-frequency plunging motion on a NACA 0012 airfoil at a post-stall angle of attack of 15° can lead to significant thrust production accompanying a 305% increase in lift coefficient. At low Strouhal numbers vortices form at the leading-edge during the downward motion and then convect into the wake. This 'mode 1' flow field is associated with high lift but low thrust. The maximum lift enhancement was due to resonance with the natural shedding frequency, its harmonics and subharmonics. At higher Strouhal numbers the vortex remains over the leading-edge area for a larger portion of the cycle and therefore loses its coherency through impingement with the upward moving airfoil. This 'mode 2' flowfield is associated with low lift and high thrust.

At angles of attack below 12.5° very large force bifurcations are observed. These are associated with the formation of upwards or downwards deflected jets with the direction determined by initial conditions. The upwards deflected jet is associated with the counter-clockwise Trailing Edge Vortex (TEV) loitering over the airfoil and thereby pairing with the clockwise TEV to form a dipole that convects upwards. It therefore draws fluid from the upper surface enhancing the upper surface vortex leading to high lift. The downwards deflected jet is associated with the inverse. Deflected jets were not observed at larger angles of attack as the asymmetry in the strength of the TEVs was too great; nor at smaller amplitudes as the TEV strength was insufficient.

To understand the effect of geometry comparable experiments were performed for a flat plate geometry. At zero degrees angle of attack deflected jets would form, as for the NACA 0012 airfoil, however their direction would switch sinusoidally with a period on the order of 100 cycles. The lift coefficient therefore also switched. At 15° angle of attack for Strouhal numbers up to unity the performance of the flat plate was comparable to the NACA 0012 airfoil. Above unity, the upper surface and lower surface leading-edge vortices form a dipole which convects away from the upper surface resulting in increased time-averaged separation and reduced lift.

ACKNOWLEDGEMENTS

This work was supported by an EPSRC (Engineering and Physical Sciences Research Council) studentship.

I am grateful for the support, enthusiasm and advice of my supervisors, Prof. I. Gursul and Dr. Z. Wang, for the help of technicians Guy Brace, Paul Griffiths, Les Duddridge, and instrumentation specialists Vijay Rajput, and Stephen Coombes. I am also appreciative of the humour of everyone in the office throughout my time in the department.

Lastly and most importantly, I would like to thank Emily for her unending support and distraction. Although the PhD might have been quicker without her, it would certainly not have been as enjoyable.

CONTENTS

LIST OF FIGURES

LIST OF TABLES

NOMENCLATURE

a	=	amplitude of plunging motion
c	=	chord length
C_d	=	time-averaged drag coefficient
C_{d0}	=	time-averaged drag coefficient at $\alpha = 0°$
C_f	=	force coefficient
C_l	=	time-averaged lift coefficient
$C_{l,max}$	=	maximum time-averaged lift coefficient
C_p	=	time-averaged power coefficient
C_μ	=	blowing momentum coefficient
d_p	=	particle diameter
f	=	frequency
M_∞	=	Mach number
N	=	sample size
R	=	cross-correlation coefficient
Re	=	Reynolds number, $\rho U_\infty c / \mu$
R_{xy}	=	cross-correlation
Sr_A	=	Strouhal number based on double-amplitude, $2fa/U_\infty$
Sr_c	=	Strouhal number based on chord, fc/U_∞
Sr_d	=	Strouhal number based on vertical distance between leading and trailing edge, $fc\sin\alpha/U_\infty$
t	=	time, t = 0 is top of motion
Δt	=	time interval
T	=	plunge period
u_s	=	particle settling velocity
U_∞	=	free stream velocity
U_{pl}	=	peak plunge velocity, $2\pi fa$
V	=	velocity magnitude
x	=	direction parallel to freestream
y	=	direction perpendicular to freestream
α	=	angle of attack
$\alpha_{eff,max}$	=	maximum effective angle of attack during a cycle
$\alpha_{eff,mean}$	=	mean effective angle of attack during a cycle
Γ	=	circulation
$\hat{\Gamma}$	=	normalized circulation, $\Gamma / U_\infty c$
μ	=	viscosity
η	=	propulsive efficiency, C_t/C_p
φ	=	angle of time-averaged jet
ρ	=	fluid density
ρ_p	=	seeding particle density
ω	=	vorticity

OUTLINE OF THESIS

This thesis describes an experimental study of small-amplitude high-frequency motion as a method of improving the performance of a two-dimensional airfoil.

Chapter 1 is a description of both the state of the art as well as justification for the current research. It therefore begins with the application, Micro Air Vehicles (MAVs), from which the fixed-wing type is identified as the most promising. The next subsection describes possible flow control methodologies for improving the performance of a fixed-wing MAV including small-amplitude high-frequency wing motion. The final subsection describes the current understanding of flapping flight due to the relevance of large-amplitude low-frequency motion to small-amplitude high-frequency motion.

Chapter 2 describes the experimental apparatus and methods used. This covers the general setup, force measurements, Particle Image Velocimetry, and hot film.

Chapter 3 is the first results chapter, its purpose is to establish the possible performance improvement for a NACA 0012 airfoil at a post-stall angle of attack of $\alpha = 15°$ and range of amplitudes and frequencies. Significant lift increase, and drag reduction are demonstrated and the causes discussed.

Chapter 4 presents multiple angles of attack in the range $\alpha \leq 20°$. An interesting bifurcation phenomenon is observed where entirely different flow fields and forces are achievable at identical experimental conditions depending upon the initial conditions. The cause of this bifurcation is investigated and criteria devised for predicting its onset.

Chapter 5 explores the effect of geometry, through comparison of the forces and flow fields for a flat plate with a NACA 0012 airfoil. It is demonstrated that geometry has a very significant effect at higher frequencies.

Chapter 6 summarizes the conclusions drawn from chapters 3, 4 and 5. A list of publications, references and appendices follow.

CHAPTER 1. INTRODUCTION

1.0 SUMMARY

This section acts as both outline of the state of the art as well as justification for the current research. It therefore begins with the application, Micro Air Vehicles (MAVs), describing the principal types and identifies the fixed-wing MAV type as the most promising but still in need of further improvement. The following subsection, flow control, therefore goes on to describe possible performance improvement methods and identifies small-amplitude airfoil oscillations as a primary contender. In the final subsection, flapping flight, the flowfields and forces associated with large-amplitude airfoil oscillations are shown, and it is demonstrated that one can reasonably expect similar flowfields and forces from small-amplitude motion.

1.1 MICRO AIR VEHICLES

Currently there is great interest in MAVs due to their potential for a wide variety of applications, both military and civil. MAVs are defined as small (< 15 cm) autonomous or remotely controlled aircraft. This 15 cm limit also coincides with the boundary between quasi-steady and unsteady flight [1]. As a result viscous effects dominate, making flight challenging and inefficient. Consequently there are currently no operational MAVs.

1.1.1 History

Interest in MAVs began in the 1990s with MIT Lincoln Lab's conception of a MAV that could carry a miniature camera system. Although it was only a notional platform it served as a catalyst for further research. In 1996 the US Defence Advanced Research Projects Agency (DARPA) created a $35m research programme to develop MAV technologies. It is from this programme that the definition of a MAV as 'being less than 15 cm' originates. According to Michelson [2] the reasoning is that "this is the juncture at which low Reynolds number effects begin to dominate and beyond which the integration of energy, propulsion, aerodynamic structures and intelligence is a necessity."

In 1997 DARPA selected six proposals to be developed. The most successful of these was undoubtedly the AeroVironment Black Widow, a fixed wing electric-powered vehicle. This design set endurance, altitude and range records. Despite the success of the Black Widow the results of DARPA's study were somewhat negative. The conclusion was drawn that although the concept seemed valid, 15 cm was simply too small to be of practical use with the current technology and understanding. In recent years technological progress has meant that the potential of MAVs is finally being realised, principally as a result of technological gains in the mobile-phone market such as lighter / more efficient batteries, motors and DC-DC converters [3].

1.1.2 Uses

Galinski & Zabowski [4] outline the potential uses of MAVs as being:

- Outdoor nuclear, biological and chemical emergency reconnaissance
- Crowd control
- Observation of suspect facilities
- Snap inspection of pollution
- Road accident documentation
- Urban traffic management
- Search for survivors
- Pipeline inspection
- High risk indoor inspection

The performance requirements for each use vary greatly. In general the first three would require long-endurance; the second three short-endurance with hover; and the last three manoeuvrability and hover. This gives three possible performance scenarios: endurance, endurance with hover, and manoeuvrability with hover. General performance requirements applicable to all three scenarios are shown in Table 1.

Table 1 MAV performance requirements, from Pines & Bohorquez [5]

SPECIFICATION	REQUIREMENTS	DETAILS
SIZE	< 15 cm	Maximum Dimension
WEIGHT	≈ 100 g	Maximum GTOW
RANGE	1 to 10 km	Operational Range
ENDURANCE	60 min	Loiter Time
ALTITUDE	< 150 m	Operational Ceiling
SPEED	15 m/s	Maximum Flight Speed
PAYLOAD	20 g	Mission Dependent
COST	$1500	Maximum Cost

In addition to the performance requirements detailed in Table 1, the MAV must also act as an effective sensor platform. In some cases this sensor will be chemical, however in the majority it will be visual, i.e., a camera. The MAV must therefore be stable and insensitive to changes in wind velocity or direction (gusts).

Gusts are variations in wind speed across the three orthogonal axes induced through the frictional drag of terrestrial surfaces. With flight speeds less than 17m/s these low-frequency velocity fluctuations can constitute a considerable percentage of the mean freestream velocity [6], and are particularly detrimental to a MAV's stability in the rotational modes of freedom, i.e, pitch, roll and yaw. Watkins [7] found that for a MAV flying at 10m/s in an open area, a stable wind speed of 7.8m/s would induce pitch oscillations of 2 to 2.5 degrees. Furthermore field experiments by Liu [8] found that although performance of a static wing is improved in the atmospheric boundary layer (higher lift, lower drag) due to the beneficial effects of turbulence, at lower Reynolds numbers (80,000 to 200,000) the lift coefficient became more variable. One would therefore anticipate serious control instability. The simplest method of developing gust stability is to increase the flight speed, although using a rotary or flapping aircraft [7], or membrane wings [9] could also be effective.

Shown in Fig. 1.1 are some of the current MAV designs. Fig. 1.1 demonstrates the gulf between the desired endurance and that achieved. The two designs closest to meeting both size and endurance requirements are the MicroSTAR and Black Widow designs. These are both standard fixed-wing designs reliant on conventional airfoils for lift, and propellers for thrust. The more novel flapping wing designs

cannot achieve greater than five minutes endurance and rotary designs require significantly larger scales to produce the thrust required.

The principal factor limiting endurance is the propulsive-system weight. MAVs typically have propulsive-system weights of ≈ 60% compared to 39% for a Boeing 767 and ≈ 20% for birds (includes 'propulsion / fuel', see Pines & Bohorquez [5]). To reduce weight whilst maintaining the same lift and thrust performance will necessitate improved efficiency in thrust and / or lift production.

1.1.3 Types

MAVs can be divided into three standard types; fixed-wing, flapping-wing, and rotary-wing. Each of these is described below in terms of their benefits and limitations. When assessing each type it is important to bear in mind that their relative merits are highly dependent on the performance scenario [3], for example fixed-wing vehicles are inherently incapable of hover but more suited to endurance.

a) Fixed-Wing

Fixed-wing MAVs are the most developed type of MAV, with several prototypes built and proposed to customers. A typical example is the NPS design, see Fig. 1.2. This MAV combines a large low-aspect ratio fixed wing with a pair of smaller high-aspect ratio flapping wings acting in counterphase. The fixed wing supplies lift whilst the flapping wings supply thrust. The symmetric flapping motion supplies a mechanically and aerodynamically balanced platform exploiting the ground effect and suppressing stall over the main wing through flow entrainment. Although larger than the 15 cm limit, it is capable of twenty minutes endurance with relatively stable flight at speeds between 2 m/s and 5 m/s. It is this form of novel approach that will be required to overcome the limitations of low Reynolds number fixed wing aerodynamics.

Fixed wing designs tend to rely on standard steady-state aerodynamics, which has several deficiencies:

- *Low Reynolds Numbers* - the low Reynolds numbers encountered mean the boundary layer is laminar and therefore far more prone to separation. According to Woods et al. [10] a NACA 4412 at Re = $3x10^6$ exhibits C_{d0} =

0.005 and C_{lmax} = 1.50; at Re = $2x10^4$, C_{d0} has increased by a factor of ten and C_{lmax} reduced by 63%. Stall is therefore a serious problem and given the low flight speeds typical of MAV flight any gust or disturbance can induce it [11].

- *Forward Velocity* - for steady-state mechanisms to function they require a forward velocity, hover is therefore not an option and in all likelihood the vehicle will have to constantly fly near its maximum velocity due to the low C_{lmax}.
- *Propulsion* - at such low Reynolds numbers propeller-based propulsion becomes difficult due to the propeller's trailing vortex system[12]. An alternative method of propulsion or drag reduction methods may therefore be necessary.

Despite these limitations fixed-wing MAVs are considered advantageous due to their simplicity and efficiency. Simplicity is particularly important because even though it is possible to produce a mechanism with multiple degrees of freedom, it is inevitably heavy and cumbersome. Realistically, designs are therefore limited to a single degree of freedom [3].

A very basic estimation of the comparative efficiency of fixed wing, flapping wing and rotary wing vehicles was demonstrated by Woods et al. [10]. It was shown that fixed wing flight is the most efficient method for wind speeds in the range 0 to 16 m/s; in the low wind speed range (<8 m/s) flapping flight was second, and in the high wind speed range(>8 m/s) rotary flight was second. Hence, with the current technology fixed-wing is preferable unless hover is required. It should be noted that the optimisation routine used by Woods et al. had an upper span criterion of 0.15 m which the fixed-wing design usually approached or equalled. The situation may therefore change if smaller scale is required.

b) Flapping-wing

Flapping-wing flyers are essentially biomimetic or biomorphic designs of birds (ornithopters) and insects (entomopters). Current man-made designs use simplified wing kinematics, and as a result cannot utilize all of the unsteady aerodynamic mechanisms available to nature. To achieve similar performance would require both lighter actuation systems and advanced active control with feedback [1].

Flapping wing flyers can take a variety of forms including: single, tandem, X-wing, bi-plane etc. A typical example is the Microbat shown in Fig. 1.3. So as to maximise endurance every effort was made to minimise weight resulting in a published weight of ≈10 g. The wings are a particularly good example of this effort, they are produced from titanium alloy of variable thickness so as to provide optimal rigidity. Despite these efforts it has a published [13] endurance of only eighteen seconds.

The principal benefit of flapping flight is the simplification endowed in combining the lift and thrust functions into one surface. Whether this simplification offsets the extra mass due to the flapping mechanism will be design specific. In terms of thrust, the greater propulsion surface area entails a lower loading and therefore improved efficiency when compared to a propeller [3]. In terms of lift, properly controlled flapping flight should produce greater maximum lift than fixed-wing designs through the action of unsteady aerodynamics (described in section 1.3). Conversely the large oscillatory aerodynamic and inertia forces of flapping flight will impact negatively on the stability of flapping-wing flyers as a platform for visual sensors. However if these problems are overcome, and a suitable control system devised, then the ultimate benefit can be seen in nature.

c) Rotary

Rotary MAVs are essentially small-scale helicopters. Several designs have reached the flight test phase [4] however they have proven to be inefficient resulting in a maximum endurance of 3 minutes. This inefficiency is a result of the low chord Reynolds number causing increased blade boundary layer thickness, and a more turbulent wake [14].

Typical formats of rotary MAVs are: single-rotor, twin-rotor, quad-rotor or a hybrid of the above. A good example is that of Bohorquez et al. [15] shown in Fig. 1.4. It is a micro-coaxial rotorcraft of 15 cm major dimension which proved to be stable and capable of hover, roll, yaw and lateral trim. It was however inefficient, achieving a maximum endurance of three minutes under its own power. Due to this inefficiency rotorcraft are only preferable where stable hover is a necessity and will only be useful once the efficiency is substantially improved.

1.1.4 MAV Summary

There is current interest in MAVs for their potential in a wide range of applications; however current designs are incapable of the endurance required for them to be practical. Of the current designs, the fixed-wing design type is by far the closest to meeting the desired criteria but falls short due to the limitations of low Reynolds number aerodynamics. A pragmatic approach is therefore to apply appropriate flow control methods to fixed-wing designs as a method of improving aerodynamic efficiency, thereby extending endurance.

1.2 FLOW CONTROL

Flow control refers to any method / process used to alter the characteristics or disposition of a flowfield favourably**.** As such it is a vast topic covering many different avenues of research including transition delay / advancement, separation prevention / provocation, and turbulence suppression / enhancement [16]. It is particularly appropriate at the low Reynolds numbers typical of MAVs as the location and structure of separated regions are very sensitive to changes in flow conditions [6]. The challenge for MAVs is thus separation / stall control.

According to Greenblatt & Wygnanski [17] the underlying stall control problem is the design philosophy of steady flow, i.e., the assumption that there is no time invariance to stall despite the experimental data that acknowledges time-dependent coherence. Hence most forms of separation control move beyond steady-state aerodynamics in an attempt to exploit unsteady characteristics through either active or passive methods. For conciseness only flow separation control applicable to MAVs will be considered here, for more comprehensive reviews see Gad-el-Hak [16], Greenblatt & Wygnanski [17], Colliss et al. [18], and Gad-el-Hak [19].

1.2.1 Active

Active flow control refers to any flow control technique which can be actively controlled, so at least switched on / off. These can be unsteady methods where it is tailored to local conditions, or steady where it is constant. The main advantage of active flow control over passive is that variable actuation allows it to be innocuous when inactive [11].

a) Blowing / Suction

i) Steady

Suction involves the removal of the near-surface, decelerated fluid so as to delay separation. It has shown considerable performance improvements in both wind tunnel experiments and flight tests on both a MiG-21 and F104. However the weight, complexity and inefficiency of the system mean that it has not been applied to production aircraft [17]. Conversely steady blowing aims to impart additional momentum to the near-surface retarded fluid so as to delay separation. In general, steady blowing / suction methods have been found to cause significant improvements but at significant cost and have therefore generally been discarded in favour of their more efficient unsteady counterparts.

ii) Unsteady

It has been reported [11, 17, 20, 21] that unsteady periodic addition of momentum can achieve the same results as traditional steady blowing for far less momentum addition. A typical example [17] showed that steady blowing in the range $C_\mu \sim 2\text{-}3\%$ is ineffective and even detrimental to lift, whereas unsteady blowing at $C_\mu \sim 0.01\text{-}0.1\%$ resulted in lift increases of five to twenty-five per cent.

The underlying flow mechanisms of unsteady blowing / suction are best described by Seifert & Pack [22]: "Experiments performed at low Reynolds and Mach numbers have shown that cyclic vortical oscillations introduced into a separating boundary layer slightly upstream of the average separation location can effectively delay boundary-layer separation. The improved ability of the boundary layer to overcome the adverse pressure gradient is attributed to enhanced mixing between the low momentum fluid near the wall and the high momentum flow. It becomes extremely efficient if the excitation frequency corresponds to the most unstable frequencies of the separating shear layer, generating arrays of spanwise vortices that are convected downstream and continue to mix across the shear layer downstream of the excitation device."

Due to unsteady blowing / suction relying on manipulation of the separating shear layer the position and type of actuation is paramount. It ideally has to be placed near the point of separation [17] with the frequency and amplitude tailored to the type of separation. A leading-edge stall airfoil will require high frequency, short-wavelength

perturbations so as to be amplified at the leading edge; whereas a trailing-edge stall airfoil will require low frequency, long-wavelength excitation that will be amplified further downstream [17].

The majority of studies into unsteady blowing are at high Reynolds numbers where experience has shown that control authority is not degraded by higher Reynolds numbers [11, 23]. Conversely for the lower Reynolds numbers typical of MAVs (Re $< 10^5$) unsteady blowing becomes strongly Reynolds number dependent. Greenblatt & Wygnanski [24] showed that a thick airfoil could achieve C_{lmax} of 1.64 at Re = 150,000, but failed to generate useful lift at Re = 50,000, i.e., $C_l < 0.5$. Furthermore at the low Reynolds numbers the lift was unpredictable and very nonlinear with variation in angle of attack. Nonetheless, at this lower Reynolds number with zero net mass flux blowing activated stable lift performance very similar to the higher Reynolds case could be achieved resulting in $C_{lmax} = 1.48$. However experiments showed that to maintain the same performance at Re = 30,000 would require four times more momentum injection. The performance improvements are therefore potentially unstable and unpredictable at a MAV scale where the Reynolds number and local flow conditions would be in constant flux. Despite this limitation, Ho et al. [1] applied MEMS electrostatic actuators to flapping flight at MAV scale Reynolds numbers and demonstrated a 31% increase in mean lift, and 17% in mean thrust. These improvements were achieved without feedback control and using digital (on-off) type actuators.

b) Geometric Excitation

Geometric excitation refers to the use of any physical surface to directly influence the flow, this includes vibrating ribbons / flaps and vibrating surfaces. An example of this is the study of Park et al. [25] for a vibrating / buzzing bar on the surface of a NACA 0012 at a Reynolds number of 20,000. Only a single amplitude and limited range of frequencies were considered but it was found to be most effective at $Sr_c = 2.20$ (the highest frequency studied) generating a 24% lift improvement and 60% drag reduction. Oil surface flow visualizations showed the improvement to be due to boundary layer reattachment resulting from greater turbulence activity.

A second novel concept is to recess a piezoelectric actuator into the surface of the airfoil to create an oscillating camber. On a NACA 4415 this method produced an oscillation on the order of 0.002c [26] which at Re = 250,000 and 500,000 acted to reduce the separated region by 30-60% (as measured at 0.7c). A similar technique was used by Chandresekhara et al. [27] who dynamically changed the leading-edge shape of an airfoil so as to control dynamic stall. For some cases the dynamic stall vortex was completely eliminated.

More relevant to the current research is the experimental study of Vardaki et al. [28] for low-aspect ratio delta wings undergoing small-amplitude pitch and roll oscillations in the post-stall region. It was shown that these motions promote both early reattachment and vortex reformation, with greatest effect for frequencies nearest to the natural shear layer frequency with an optimum Strouhal number range of $Sr_c = 1$ to 2. A range of sweep angles were studied and a lower limit of 20° sweep angle, below which the motion is ineffectual, identified. So whether a similar small-amplitude motion, either actively or passively created, would be effective for the extreme case of a two-dimensional airfoil (0° sweep angle) is unknown.

c) Plasma Actuators

A more recent development is the use of plasma actuators. Plasma actuators in their simplest form consist of two wires flush-mounted on the profile's wall between which a high DC voltage is applied, resulting in a cold plasma sheet. A corona forms around the smallest diameter electrode, and an electric wind is created acting tangentially to the wall [29]. Hence the airflow in the vicinity of the wall can be accelerated and controlled in a similar manner to MEMS or blowing. Greenblatt et al. [30] employed plasma actuators at the leading edge of both a flat-plate and an Eppler E338 airfoil at very low Reynolds numbers. The effects were significant but required pulsing at frequencies in the kHz range with actuator voltages greater than 6kV, so whether it is practical for MAVs is unclear.

1.2.2 Passive

Passive flow control refers to any technique where the user has no control over its operation, meaning it cannot be switched on / off. This means that although passive

techniques tend to require no direct work they incorporate no control and thus a penalty is usually incurred when flow control is not required.

a) Aircraft Design

By far the simplest example of passive flow control is optimal aircraft design. For example Jones et al. [3] used the flapping propulsion system of their MAV to entrain flow and consequently observed a marked difference in flight performance (see Section 1.1.3). In a similar manner Galinski [31] positioned the propeller in the mid-wing resulting in reduced separation without any extra work input.

An aside to this is the use of turbulators. Turbulators can take the form of serrations, strips, bumps or ridges. They work by creating a turbulent boundary layer which is more resistant to separation and therefore preferable in certain situations, the penalty being that a turbulent boundary layer can create more drag when separation is not present. Turbulators are well established for high Reynolds numbers but untested for low Reynolds numbers and would be completely ineffective at very low Reynolds numbers.

b) Membrane Wings

Multiple studies have found that membrane wings improve aerodynamic performance [32]. One example by Shyy et al. [6] used a membrane wing based on the CLARK-Y profile and showed that the membrane reacted to velocity fluctuations so as to 'damp' gust effects and stabilise lift. A second example is the use of a rigid and membrane wing on a realistic small aircraft in wind tunnel tests [33]. The membrane wing consistently demonstrated higher lift-drag ratios than its rigid counterpart. The underlying cause was however not examined and only one flexible wing was tested. Far greater performance gains are therefore feasibly possible through optimisation of the flexibility.

c) Small-Amplitude Wing Oscillation

As previously described it has been demonstrated [28] experimentally that actively created small-amplitude pitch and roll oscillations of low-aspect ratio delta wings can promote both early reattachment and vortex reformation. Moreover Taylor et al. [34] and Gursul et al. [35] showed that these small-amplitude motions can be created passively through wing flexibility resulting in significant lift performance improvement ($\approx$ 44% in C_{lmax}). The oscillation motion creates leading edge

circulation that would normally promote premature vortex breakdown but in fact delays breakdown, suggesting that a favourable pressure gradient is also created [36].

1.2.3 Flow Control Summary

In summary there are five possible flow control options for MAVs:

- *Aircraft Design* – optimal design can create small performance gains at negligible cost.
- *Small-Amplitude Wing Oscillation* – could be actively or passively created and is proven for delta wings but untested for two-dimensional airfoils.
- *Membrane Wings* – flexible wings delay stall and are inherently lighter.
- *Plasma Actuators* – the practicality of creating the required voltages and frequencies at MAV scales is unclear but the potential gains are significant.
- *Unsteady Blowing / Suction* – well established for high Reynolds numbers but becomes unstable at low Reynolds numbers and the system is probably impractical at MAV scales.

This study falls within the second field, 'small-amplitude wing oscillation'. It attempts to take the work already performed for nonslender delta wings and extrapolate it to two dimensional airfoils. This is a significant step since for delta wings both the motion and flowfield are highly three-dimensional. Nevertheless a similar type of flow control can be found in its larger-amplitude counterpart, flapping flight.

1.3 FLAPPING FLIGHT

Research within the field of flapping flight is historically derived from the study of natural flight, and as such has focussed on the understanding of the large-amplitude low-frequency motion suited to the muscular actuators of nature. Within these studies the most influential parameter is generally accepted as the nondimensional plunge velocity. This can take many forms but all are related to $Sr_A = fA/U_\infty$. The understanding and theory for large-amplitude low-frequency motion is therefore also relevant to small-amplitude high-frequency motion.

This section initially considers natural flight both because it is integral to flapping flight research, and also because it presents an excellent example of the type of performance achievable. This highly three-dimensional motion is then broken down into its more practical two-dimensional constituents: plunging (vertical), rowing (horizontal), and pitching (rotational), with combinations considered separately in Section 1.3.5.

1.3.1 Nature

The efficacy of flapping-flight is evident through its abundance within nature. Of the known 13,000 vertebrates, 10,000 are airborne (9,000 birds, 1,000 bats) [37]. This genetic abundance of flapping mammals combined with over 300 million years of evolution has allowed nature to hone flight to such an extent that it can outperform man-made aircraft in every field except altitude and absolute maximum speed. For example, in terms of relative speed a human being is capable of 4 body lengths per second, a cheetah 18, and an SR-71 'blackbird' 32. In comparison the common pigeon can manage 50 and some swifts 140. In terms of manoeuvrability the picture is similar; a highly aerobatic aircraft can achieve roll rates of 720 °/s, whereas a barn swallow rolls at 5000°/s creating loads in the region of 14G [6]. These feats are achievable through three key facets: i) very lightweight structures; ii) complex control systems; iii) unsteady aerodynamic phenomena. Since birds and insects operate in a similar Reynolds number range (5 to 200000 [38]), with similar requirements, and under similar conditions to MAVs, the understanding of these characteristics potentially presents a great wealth of useful knowledge. Of the three it is only the last, the unsteady aerodynamic phenomenon, which is of interest to this thesis.

The various examples of flapping flight can be observed for three principal animal types: birds, insects and fish. Fish propulsion is not included because it is primarily for thrust production with lift forces being neglected [39, 40] and therefore not directly applicable. To be succinct insect and bird aerodynamics will be considered as one. This is justifiable because although there are differences, the similarities are more apparent. In essence both types rely on similar mechanisms, but in differing proportions.

a) Wing Kinematics

The wing kinematics of insects and birds is a complex combination of flexing, twisting, bending, rotating and feathering throughout the flapping cycle [1]. The motion is produced both actively through muscular actuation, as well as to a lesser extent passively through aeroelastic effects and flow control techniques. A typical flapping cycle can generally be summarized as four phases: downstroke, supination, upstroke, and pronation (see Fig. 1.5).

The downstroke is, as the name implies, the downward translation of the wing. It has been found that as much as 80% of the lift is produced during this phase (in combination with the latter part of the upstroke [1, 41, 42]) through the action of a Leading Edge Vortex (LEV). Supination follows the downstroke; it involves rotating the wing to increase its angle of attack so as to reduce the moment of inertia and the drag. Following supination, the upstroke resets the wing to its original position. Pronation then acts to reset the wing's angle of attack, effectively unravelling the wing in preparation for the down-stroke so as to maximise the surface area and strength of the LEV. It is important to note that the period of time for each phase will be highly unbalanced and asymmetrical, and will vary according to the species and phase of flight [43].

b) Lift Generation

During the latter part of the 20th century it became clear that the lift achieved in nature is far greater than that achievable under steady or quasi-steady conditions. It is therefore reasonable to suppose that natural flyers employ unsteady mechanisms to overcome the deteriorating aerodynamic performance of steady-state mechanisms at low Reynolds numbers. The role in nature of these unsteady-mechanisms is increasingly being understood and a brief outline is given below, for full reviews see Dickinson [38], Sane [44], Ho et al. [1], Lehmann [45], and Michelson & Naqvi [41].

Leading Edge Vortex - for a flapping wing at reasonable effective angles of attack (~ 10°) flow will separate from the leading edge of the wing but reattach before the trailing edge [46]. In the separation zone a LEV forms in a similar manner to the dynamic stall vortex [42] as seen in Fig. 1.6. The majority of the lift force in

natural flight is attributed to the action of the LEV through the creation of a region of low pressure above the wing, although it can also be thought of as augmenting the circulation around the wing. For three-dimensional sections the LEV was found to be smaller and more stable. This effect has been attributed [1, 39, 42, 44, 47-50] to axial flow which is driven by a strong spanwise pressure gradient dissipating the vorticity and momentum, and thereby stabilizing the vortex in a similar manner to delta wings [36]. This explanation for the apparent stability of the leading-edge vortex however remains inconclusive [44, 51]. An alternative explanation is that a minimum time (typically four chord lengths travel) is required for an LEV to form and shed from a translating wing. Most natural flyers use wing strokes less than this [52], thereby avoiding the shedding process.

Wing-Wing Interference – also termed Clap & Fling or Weis-Fogh, shown in Fig. 1.7. Alternative versions are near-clap-and-fling and clap-and-peel. Although only observed for some insects in certain flight modes it has been shown to produce as much as 25% extra lift. Following the description of Sane [44]: during the clap phase the leading edges meet and gradually close the gap until the trailing edges meet. This has two effects, firstly a jet of air is created, and secondly the touching of the trailing edges diminishes the TE vorticity for the next stroke, therefore attenuating the Wagner effect and enhancing lift. The fling mechanism involves the wings separating at the leading edge whilst remaining attached at the trailing edge creating a V shape. This creates a low-pressure void and also strong stable LEVs as the air rushes to fill it. However it has been observed by Sane [44] that the clap and fling mechanism is not ubiquitous amongst free-flying birds and insects but is in fact only observed for tethered ones, perhaps indicating that it is an extreme response induced by the tethered flyer reacting to its restraint by maximizing lift through maximum stroke amplitude.

Kramer Effect (rotational circulation) – following the description of Sane [44]: pitching an airfoil whilst also translating it causes the flow to deviate from the Kutta condition so that the stagnation region moves away from the trailing-edge. Additional circulation must be created to correct this instability so the fluid creates a rotational circulation to counter the effects of rotation. The re-establishment of the Kutta condition however requires time and so if pitching continues this extra circulation will continue also. Circulation is therefore developed proportionally to

the angular velocity of rotation with its sign determined by the direction of rotation. It is not equivalent to the Magnus force for blunt bodies, as blunt bodies have no surface singularities where the Kutta condition can hold.

Wing-Wake Interference - at the end of the upstroke the LEV and TEV are shed and used to create a 'jet' of flow angled at the under-surface of the wing as in Fig. 1.8. However the evidence for the significance of this is contradictory [44].

Added-Mass - when the wing accelerates it also accelerates the surrounding fluid and as predicted by Newton's laws any acceleration generates a force. It is effectively a force created due to the inertia of the surrounding fluid. When averaged over a complete cycle this force will equal zero.

Wagner Effect - when an airfoil starts from rest its circulation does not instantaneously rise to its steady state value but instead there is a latency due to both viscous action delaying the establishment of the Kutta condition, and the time taken for formation and shedding of the trailing edge starting vortex. As a result the lift will be lower than in the steady-state case. Once the starting vortex has moved sufficiently downstream the effect is diminished. For normal fixed-wing aircraft this is not a problem, however, for flapping wings only a few chord lengths pass before the flapping direction is reversed. Recent studies with both 2D and 3D wings have shown it to be not very strong at the Reynolds numbers typical of insects [44, 46].

c) Thrust Generation

A bluff-body placed in a flow will usually create a wake as indicated in Fig. 1.9. The characteristic feature of this flow is two approximately symmetric vortices that roll inwards towards the object. This form of wake is known as a Kármán vortex street. It is drag-indicative due to the time-averaged velocity deficit left in the wake.
A static airfoil will behave in the same manner as a bluff body, producing a Kármán vortex street. If the airfoil is then oscillated with increasing amplitude and/or frequency, the sense of these vortices will be gradually inverted thereby producing a reverse-Kármán vortex street (see Fig. 1.10). Due to the relative position of the vortices they produce a self-advection velocity in the freestream direction greater than the freestream [53] thereby creating a time-averaged ‘jet’ of flow [54]. It is therefore generally taken to be thrust-indicative. The effect responsible for the production of the reverse-Kármán vortex street is termed the Knoller-Betz effect.

The transition between a drag and thrust indicative wake for a NACA 0012 airfoil at $\alpha = 0°$ occurs in the region of $Sr_A \sim 0.13$ [12, 55] with most efficient thrust production in the region of $Sr_A = 0.2$ to 0.4 [56-58]. This description of thrust production is a simplistic one but still applicable to nature. Indeed for many aquatic species the non-dimensional plunge velocity of operation lies in the region 0.25 to 0.35 [56] closely correlating with the experimental values.

1.3.2 Plunging

Plunging motion is the oscillation of a wing in the vertical direction. Due to its direct applicability to flapping wing MAVs, studies of plunging airfoils are numerous and cover a wide variety of parameters. The majority of these studies are however motivated by the concept of a flapping wing as a propulsor and treat the lift properties, if at all, as an aside.

a) Flow Field

i) Leading Edge

In a similar manner to natural flapping-flight, several studies [59-63] have identified leading edge vortices which form even at low to moderate plunge velocities, typically $Sr_A \approx 0.11$ [63]. The vortex forms on the leeward surface, rolls up and is convected downstream interacting with trailing edge vortices. This LEV contributes to thrust whilst upstream of the point of maximum airfoil-thickness but as it is convected downstream it begins to detract from the thrust due to the rearward facing surface [60]. For higher plunge velocities ($Sr_A = 0.25$ and 0.32) Lewin & Haj-Hariri [62] found that the LEV is not always shed. Instead the LEV remains attached and loses its coherency through interaction with the airfoil in an effect termed vortex 'shredding'.

ii) Wake

The wakes of oscillating airfoils are typically characterised as being drag-producing, neutral or thrust-producing with the type being determined by the frequency and amplitude of oscillation (see Section 1.3.1). The transition from drag to thrust-producing (neutral wake) has been shown not to be smooth [55, 64, 65]. Rather, around the neutral band a number of transitional forms are observed; an example is shown in Fig. 1.11. It has been suggested [66] that these transitional

forms are a result of vortex lock-in. Essentially, due to the low Reynolds numbers a static NACA 0012 airfoil is subject to separation even at $\alpha = 0°$. It therefore acts as a bluff body and sheds vortices at the natural shedding frequency. Young & Lai [66] suggest that at low plunge velocities this natural frequency is dominant. With increasing plunge velocity however the forcing frequency begins to dominate and the natural shedding frequency becomes a harmonic of it, see Fig. 1.12. It is important to note that the vortex lock-in boundary does not depend on a constant plunge velocity; just that the natural frequency dominates at lower plunge velocities and forcing frequency at higher plunge velocities.

In addition to the three wake structures already described, at high plunge velocities several authors [12, 62, 67-70] have identified a fourth wake structure where the reverse-Kármán vortex is vertically deflected. The deflection is a result of pairing of the TEVs [70] to create a vortex dipole which due to the relative position of the vortices has a self-advective velocity at an angle to the horizontal thereby producing a deflected time-averaged jet. Thus at high enough Strouhal numbers there is the possibility of asymmetric flow fields and non-zero lift even at zero degrees angle of attack.

Jones et al [12] and Lai and Platzer [55] identified the existence of deflected jets both numerically [12] and experimentally [12, 55] for a plunging NACA 0012 airfoil at zero degrees angle of attack for $Sr_A > 0.32$. Numerically the deflected jets were stable. Experimentally however the deflected jets were unstable and prone to random (nonperiodic) switching. Likewise Lewin and Haj-Hariri [62] observed unstable deflected jets for an elliptic airfoil oscillating at $Sr_A \approx 0.48$, and Heathcote and Gursul [67] observed jet switching for a NACA 0012 airfoil oscillated in still fluid. In the latter case however the jet switching was observed to be periodic with a period on the order of 100T. In contrast to these papers for unstable deflected jets, von Ellenreider and Pothos [69] observed stable deflected jets to commence in the range $0.434 < Sr_A < 0.455$ for a NACA 0012 airfoil plunging at $\alpha = 0°$ and $a/c = 0.215$. The direction, upwards or downwards, was established when the heaving motion was initiated and remained the same as long as the motion is continued. It was also hypothesized, but not experimentally substantiated, that the lift resultant from deflected jets would be $L \approx T\tan\varphi$ where T is the thrust force and φ is the angle of

the deflected jet to the horizontal. Deflected jets have also been observed for pitching airfoils [68, 70] with onset around $Sr_A \approx 0.40$. This value is very approximate because the actual value of onset was found to be highly amplitude dependent. It was also conjectured [68] that as natural flyers typically operate in the range $0.2 < Sr_A < 0.4$ animals using flapping-based propulsion could exploit deflected jets for maneuvering. Indeed Wang [71] identified downward deflected vortex dipoles as a possible method of lift generation in hovering insect flight.

To the author's knowledge no previous study has measured the effect on force coefficient of deflected jets, nor how the initial conditions determine the direction of the deflected jet. Furthermore all previous studies have considered an airfoil oscillated at a mean zero effective angle of attack, which is practically not achievable or desirable for a MAV.

b) Parameters

i) Plunge Velocity (Frequency / Amplitude)

The exact form of the thrust and efficiency will be dependent on a variety of parameters, however, the most influential is generally accepted as plunge velocity. Plunge velocity can take many forms but all are proportional to Sr_A. It is important to note that plunge velocity oscillates periodically during a cycle and these terms actually represent peak plunge velocity. Fig. 1.13 demonstrates the general trend for thrust and efficiency with plunge velocity that has been demonstrated in numerous studies. Fig. 1.13a shows that with increasing plunge velocity there is decreasing drag and increasing thrust resulting in a switch from drag to thrust in the region of $Sr_A = 0.05$. Fig. 1.13b shows that in terms of efficiency, a peak occurs in the region of $Sr_A = 0.1$. Depending on the case this will generally appear between $0.1 < Sr_A < 0.4$ which is in close agreement with the values observed in nature. For frequencies below the most effective, viscous forces, leading-edge separation and leading-edge vorticity detract from efficiency [60]. For frequencies above the most effective, the reduced efficiency is due to the combination of greater spacing in the shedding of trailing edge vorticity [60], and vortices remaining nearer to the airfoil for a greater portion of each cycle due to the reduced wavelength with increasing frequency [62].

Plunge velocity combines two independent variables, frequency and amplitude, into one that according to Garrick approximations is the most influential parameter in determining thrust coefficient. In reality, however, this is not true. Fig. 1.14 shows the interdependence of thrust, plunge velocity and wake-structure for a plunging NACA 0012 airfoil. The thrust, as derived from computational potential flow theory, is demonstrated by the dark dashed lines representing a constant thrust value. The plunge velocity is represented by the lighter dashed line representing a constant plunge velocity. One can observe that for this case there is reasonable correlation between the two but that they are not identical. Within experiments one therefore has to treat frequency and amplitude as separate variables. Indeed Wang [72] computationally investigated the optimal frequency-amplitude combination for an airfoil in combined pitch-plunge. The thrust coefficient and propulsive-efficiency were calculated for a range of Sr_A and Sr_c. It was found that Sr_A was determined to give the greatest effective angle of attack possible. Given this Sr_A, the optimal Sr_c is determined by maximising the time during a single stroke in which thrust is produced. This is associated with two intrinsic time scales. The lower bound is associated with the growth of the TEV which is significant for higher frequencies. The upper bound is associated with the shedding of the LEV which is significant for lower frequencies. The optimal Sr_c was found to be $Sr_c \sim 0.7$ for $Sr_A > 0.2$, but became dependent on Sr_A for lower values. There is limited data to support this.

Also shown on Fig. 1.14 are the wake-structure regions for the three basic forms of wake with their limits approximately demarcated by the solid lines. Region A represents a drag-indicative wake (Kármán vortex street), Region C is thrust-indicative (reverse-Kármán vortex street) and Region B the intermediate (neutral) phase. As shown by the dotted lines these regions do not directly follow either constant plunge velocity or constant thrust coefficient. The description of them as drag or thrust indicative, as commonly used within the literature, is therefore misleading. The reason for the distinction between wake structure and thrust performance can be explained by the theoretical equation shown below for the thrust created by a reverse-Karman vortex street[53]:

$$\mathbf{T = -\frac{|\Gamma|^2}{2\pi a} + \frac{|\Gamma| b}{a}(1 + 2u_v)} \qquad \textbf{(1.1)}$$

Where Γ is the intensity of the vortices, a is their spacing in the horizontal direction, b their spacing in the vertical direction, and u_v the self-advection velocity of the vortices, which can be estimated for an infinite vortex street as [53]:

$$\mathbf{u_v = \frac{|\Gamma|}{2a}\tanh(\frac{\pi b}{a})} \quad \textbf{(1.2)}$$

The thrust is therefore derived from two distinct terms. In the case of a reverse-Karman vortex street the second will always be positive due to positive b, the first however will remain negative regardless. The discontinuity between wake structure and thrust behaviour can therefore be attributed to this first term [53] since as long as the first term remains larger than the second, it is possible to have a reverse-Kármán vortex street coinciding with drag. This discontinuity is also supported by the measurements of Bohl and Koochesfani [73], which showed that extra momentum flux was required to overcome the pressure reduction downstream of the airfoil; this pressure reduction was a result of transverse velocity fluctuation (v_{rms}).

ii) Reynolds Number

A quick summary of the relevant studies is:

- Re = 20 to 200,000 – Ashraf et al. [74] computationally found a very strong dependence, Ct and η varied from approximately -0.8 and -0.5 at low Reynolds numbers to 0.5 and 0.25 at high Reynolds numbers.
- Re = 1000 to 8000 – Young & Lai [64] found a strong dependence for a computationally modelled NACA 0012 in pure-plunge with laminar flow assumed.
- Re = 1500 to 10,000 – Ohmi et al. [75] concluded that as far as the fundamental fluid dynamics of vortices and the general aspects of wakes are concerned, the effect of Reynolds number is less important than other parameters.
- Re = 3000 to 36,000 – Buchholz [76] found thrust to be Reynolds independent but efficiency to be dependent.
- Re = 10,000 to 30,000 – force measurements by Heathcote et al. [57] found a slight Reynolds dependence of efficiency.

From these studies it can be inferred that the Reynolds number will have to be altered significantly (order of magnitude) for a significant effect, and that this effect will primarily be for propulsive efficiency rather than thrust. The effect on lift has not been studied but given that thrust and lift are components of the same force

vector derived from the same pressure and viscous forces, it is reasonable to assume that lift will behave in a similar manner to thrust.

iii) Angle of Attack

The effect of angle of attack is particularly important as a central point of the current study is lift generation, and to create lift it is necessary to have asymmetry in the flowfield. The simplest method of achieving this is a nonzero angle of attack. The first study of a plunging airfoil at nonzero angle of attack was that of Freymuth [77]. It consisted of smoke flow visualizations which showed a leading edge vortex forming during the downstroke, then convecting along the upper surface, and interacting with trailing-edge vortices to reinforce the clockwise trailing-edge vortex. Similar behaviour was observed by Rival et al. [78] for pure-plunge of an SD7003 at $\alpha = 8°$, for one frequency ($Sr_c = 0.080$) and one amplitude ($a/c = 0.50$). PIV measurements demonstrated an LEV growing during the downstroke, 'pinching' off at $t/T \sim 0.333$, and then interacting with vorticity shed at the trailing edge to form a vortex-pair that convects into the wake. Neither of these studies measured the forces or considered more than one parameter combination.

Andro & Jacquin [79] considered computationally, a NACA 0012 at $Re = 1000$ and $\alpha = 15°$. Multiple plunge velocities were tested and the resultant forces presented. It was concluded that three fundamental mechanisms govern the forces over an airfoil: i) suction by the LEV, ii) added mass reaction (which averages to zero over a cycle), iii) wake capture. This emphasizes that the main contributing factor to time-averaged lift is the LEV and how it interacts with the airfoil (wake capture). As a result of wake capture a clear peak in the time-averaged lift was observed at $Sr_c = 0.4$.

c) Three-Dimensionality

In three dimensions the vortical patterns observed for two-dimensional foils must connect with each other and the foil producing them to form vortex rings [39], as shown in Fig. 1.15. Parker et al. [80-82] showed that for a wing of aspect ratio three, these three dimensional effects are confined to the tip of the wing and are negligible in the mid-plane. In terms of the forces created by three-dimensional flapping wings, several authors [39, 76, 83, 84] have reported that with reducing aspect ratio the propulsive performance decreases due to the role the tip vortex plays in drag production [85]. This effect is diminished at higher frequencies [39].

d) Simulations

In 1936 Garrick published a set of equations for the thrust and efficiency of a flat plate oscillating in inviscid flow. These equations modelled pure plunge, pure pitch and coupled plunge-pitch but only for the limiting case of small amplitude oscillations. In 1976 Chopra extended Garrick's theory to oscillations of arbitrary amplitude. These inviscid methods only apply in the case of high Reynolds number, low effective angle of attack cases where separation does not occur. At the Reynolds numbers and angles of attacks encountered in birds, insects, and MAVs leading edge separation is common. Navier-Stokes codes are therefore more practical in modelling the leading edge separation, vortex formation and shedding, and the consequent merging of the LE vortices into the TE vortex system [57]. A brief summary of the various numerical methods is given below, for further detail see Rozhdestvensky & Ryzhov [86].

- *Linear Theory* - Linear theory was devised by Garrick[87]. It is an incompressible, inviscid, 2-D model suitable only for small amplitude oscillations without separation [83]. It predicts the thrust and efficiency for pure plunge, pure pitch and coupled plunge-pitch.
- *Panel Method* - Panel methods assume an incompressible and inviscid flow, therefore Mach and Reynolds numbers do not feature. They are however able to model airfoils of finite aspect ratio and thickness in large-amplitude motion. The panel method follows a potential flow approach in which a thick airfoil is constructed from a number of panels, each with a point source and vorticity. Boundary conditions, including the Kutta condition, are then applied to generate a solution [83].
- *Navier-Stokes Method* - Navier-Stokes allows one to model viscous effects. It is therefore more accurate for near zero-net-thrust cases where the panel method is unable to predict the drag forces due to the bluff-body Kármán-Vortex street. It does however require significantly more computing power [83].

1.3.3 Pitching

Pitching motion at high angles of attack induces a well established phenomenon known as dynamic stall. Dynamic stall refers to lift increases beyond the $C_{l,max}$ experienced by a dynamically pitching airfoil exceeding the stall angle, and thereby

creating a hysteresis loop that is characterized by large increases followed by sharp falls in lift. It is suggested [88] that two different flow phenomena are responsible for the force hysteresis; stall-delay due to time-lag and boundary-layer improvement effects, and the action of a leading edge vortex termed the Dynamic Stall Vortex (DSV).

The most common application of dynamic stall theory is rotor aircraft. During forward flight the retreating blade has a lower relative velocity and therefore requires a higher angle of attack to maintain balanced flight, the airfoil therefore periodically pitches. With increasing flight speed the retreating blade is required to pitch to greater and greater angles until the static stall angle is exceeded. The resultant moment variations are considered the most crucial factor limiting a helicopter's forward flight performance [89]. In more recent years increased attention has been paid to dynamic stall on wind turbine blades due to the detrimental effect it has on the blades' fatigue life and aeroelastic stability [89]. The majority of studies are therefore for higher Reynolds numbers and lower Strouhal numbers than applicable to MAV flight. A brief overview of dynamic stall is given below, for more detail see Carr [90], and McCroskey [91], and Lee & Gerontakos [88].

a) Dynamic Stall

The dominant feature of dynamic stall is the DSV. According to the description of Greenblatt et al.[92] the DSV develops in four stages:

- *Stage I* - a layer of reversed flow forms in the leading-edge region, in which fluid particles are driven in the reverse direction due to a very strong adverse pressure gradient.
- *Stage II* - the faster moving particles from Stage I collide with the slower moving particles ahead of them resulting in vertical movement forming a primary recirculation region.
- *Stage III* - a counterclockwise secondary recirculation region.
- *Stage IV* - the primary and secondary recirculation regions interact, ejecting fluid in an eruptive plume from the wall thereby initiating the breakaway and rollup of the DSV.

The DSV is usually on a comparable scale to the chord length and convects downstream at $0.39U_\infty$ [93] creating a suction 'wave' over the upper surface [94]. The

shedding of the DSV triggers the formation of a shed counter-rotating vortex at the trailing edge [93] which (for Sr_c = 0.06-0.12) combine to form a 'mushroom' structure measuring three chord-lengths in diameter just three chord lengths downstream from the trailing edge [95]. The effect of the DSV on the measured forces is demonstrated in Fig. 1.16. This model is in agreement with the PIV and flow visualization results of Panda & Zaman [95], NACA 0012 results of Carr [96], DPIV and numerical simulations of Shih et al. [93], and results of McCroskey [91].

The degree to which the DSV forms depends heavily on the degree of stall and consequently α_{mean} and pitching amplitude. It can therefore be divided into three regimes determined by α_{mean} and pitching amplitude [91]:

- *Stall onset* - the maximum unsteady lift that can be obtained with no significant penalty in moment or drag (the maximum useful lift). Further increases induce dynamic stall.
- *Light stall* - α_{max} is sufficiently small that the scale of the viscous-inviscid interaction is on the order of the airfoil thickness. Any changes are therefore closely related to the boundary-layer separation characteristics, which are in turn dependent on: airfoil shape, reduced frequency, maximum incidence and Mach number.
- *Deep stall* - experienced at stall angles well in excess of the static one. Characterised by strong vortex like interactions. The scale of the viscous interaction zone is large (on the order of the airfoil chord). Deep stall experiences large amounts of hysteresis and if the Mach number is low then these features are relatively insensitive to airfoil shape, motion and Reynolds number.

The light stall behaviour of both plunging and pitching airfoils can differ greatly, whilst the deep stall behaviour is generally similar. A brief summary of the parameters which effect dynamic stall are:

- *Airfoil Shape* - the most significant effect [96], particularly for light stall [91]. The leading-edge geometry determines the point of boundary-layer separation. Sharper leading edges promote leading-edge separation and therefore create a relatively concentrated vortex which causes abrupt changes in C_l, C_d and C_m.

- *Reduced Frequency* - very significant effect [91]. Its effect will depend on the type of boundary layer separation and stall-regime and is therefore not easily predictable.
- *Mean Angle* - significant effect [91] as separation is a prerequisite for dynamic stall. In combination with pitching amplitude it will determine the type of stall (stall onset, light stall or deep stall).
- *Amplitude* - significant effect [91], it will tend to determine the strength and timing of the shed DSV. For example a small amplitude will tend to form a mild DSV which is only shed at the maximum angle of oscillation, whereas larger amplitude causes a stronger vortex that is shed earlier in the cycle.
- *Mach number* - has a small effect below $M_\infty = 0.2$ [91].
- *Reynolds number* - small effect at low M_∞ according to McCroskey [91] and Carr[96] however these studies were for high Reynolds numbers. Oshima & Ramaprian [97] showed that Reynolds number ($Re = 5.4x10^4$ and $1.5x10^5$) can have strong effect on C_{lmax} because early transition to turbulence causes the DSV to form at later, more abruptly. In addition Lee et al. [98] showed that a pitching NACA 0012 airfoil at $Re = 1.95x10^5$ was firmly within the region of laminar-turbulent transition. Therefore at the bottom of the pitching motion the flow is laminar until near the trailing edge, as the airfoil pitches upward the transition point then moves forwards.

1.3.4 Rowing

Rowing motion is an oscillatory motion parallel to the freestream (forward-backward). Compared to plunging and pitching motion there are relatively few studies of rowing behaviour as the potential performance gains are perceived as less significant. The studies that have been conducted can be divided into two sub-categories, natural and experimental.

a) Nature

All natural flapping flight incorporates a combination of plunging, pitching and rowing motion to a greater or lesser extent. Rowing motion is most apparent in aquatic locomotion, however Walker & Westneat [99] concluded that: “Flapping appendages proved to be more mechanically efficient than rowing appendages at all

swimming speeds", raising the question why does rowing motion occur at all? Three possible explanations are:

- Rowing could be more effective at low Reynolds numbers (<100).
- Semi-aquatic mammals have to function in both land and water, and a rowing appendage can be more effective on land.
- Rowing is more effective at generating maximum thrust. Large forces are necessary for manoeuvring behaviours such as accelerations, turning and braking, which suggests that rowing should be found in slow-swimming animals that frequently manoeuvre. This is in agreement with the observed patterns of behavioural variation among rowing and flapping vertebrates.

b) Experimental

Maresca et al. [100] performed experiments on a NACA 0012 in a forced oscillation parallel to the freestream. Across a wide variety of cases there was a significant increase in lift, the greatest observed being 300% over the value for a static airfoil. The improvement was found to be limited in the pre-static-stall range but significant post-stall. This increase in lift accompanied an increase in drag and nose-down pitching moment which were attributed to the increase in width of the wake. The experiments were however across a wide range of Reynolds numbers with Reynolds number, amplitude and frequency interdependent. It is therefore not possible to directly compare individual parameters. Despite this limitation an empirical formula was derived to estimate the lift performance of a rowing NACA 0012. Using this formula a rowing NACA 0012 at conditions typical of the current study (U_∞ = 0.1 m/s, c = 0.1 m, a/c = 0.15 and f = 1 Hz, at an angle of 15° with static stall at 10°), would produce approximately 110% more lift than the steady-state case.

A similar study by Gursul & Ho [101] demonstrated similar results for an oscillating freestream. An increase in C_{lmax} as high as 170% and a clear optimum of Sr_c = 0.35 to 0.40 for a variety of amplitudes. The increase in lift was attributed to a LEV with the optimum determined by the vortex convection speed of approximately $0.35U_\infty$ to $0.40U_\infty$, the suggestion being that a vortex which remains over the chord of the airfoil for a greater portion of the cycle will contribute more to lift.

1.3.5 Special Cases

a) Combined Plunge-Pitch

Previously only pure plunge and pure pitch have been considered, another possible case is coupled plunge-pitch. This hybrid form more closely mimics the wing-kinematics of nature and could therefore produce similar benefits in terms of efficiency and manoeuvrability.

The most significant early work on coupled plunge-pitch is that of Anderson et al. [61] who used a NACA 0012 to produce 'optimal' performance (maximum C_t or η). They concluded that the efficiency optimum was for: Sr_A = 0.25 to 0.4, large amplitude ~ c, large α_{max} ~ 15° to 25°, and a phase angle between plunge and pitch of ~75° (depending upon the centre of pitch). The optimal efficiency case corresponded to the formation of moderately strong leading edge vortices which amalgamate with trailing edge vortices to form a reverse-Kármán vortex street. At higher Strouhal numbers the LEV begins to interfere with the TEV; at lower Strouhal numbers the LEV does not form. At larger pitch angles a 'piston' mode with four vortices formed per cycle appears; lower pitch angles and the wake does not form distinct patterns. The amplitude controlled the strength of the LEVs. The optimal phase angle is determined so as to minimise flow separation and increase efficiency through the constructive interaction of leading and trailing edge vortices [102].

A more detailed study was later performed by Schouveiler et al. [103] resulting in contour plots of force and efficiency against Sr_A and α_{max}, see Fig. 1.17. Thrust was shown to continuously increase with Sr_A with local optimum α_{max} for a given Sr_A. Efficiency however demonstrates a clear peak at Sr_A = 0.25 and α_{max} = 15°. For this study the phase angle was set to 90° as this had previously been found to be optimal [61, 104].

A second interesting aspect studied by Schouveiler et al. [103] was the lift force created by a nonzero mean pitch angle. Using this nonzero mean pitch angle time-averaged lift coefficients as great as 3.2 were created for Sr_A = 0.45 and α_{mean} = 40°. However, the thrust force was significantly reduced as a result. This is in agreement with Tuncer & Kaya [63] who concluded that for maximum propulsive efficiency the

pitch must be reduced so as to inhibit large scale vortex formation at the leading edge. Hence the large scale leading edge vortices required for lift can also inhibit thrust. Similar experiments for a wider range of parameters [104] demonstrated time-averaged lift coefficients of up to five. Given the steady-state value of $C_{lmax} < 1$ this is a very significant increase. These increases in lift do however incur the penalty of increased drag, the largest stated being $C_d = 3.04$ compared to $C_d \sim 0.20$ for a static airfoil. These results are in approximate agreement with the computational results of Soueid et al. [102].

Oyama et al. [105, 106] performed a CFD based aerodynamic optimization routine for a NACA 0002 in combined pitch-plunge with a pitch offset (analogous to a mean fixed angle of attack). The optimization was applied to three problems: maximum thrust, maximum lift, and minimum required power. For maximum thrust a large but relatively symmetrical variation in effective angle of attack was required to produce leading-edge vortices which acted to enhance thrust. For maximum lift a large but asymmetrical variation in effective angle of attack was required so that strong upper-surface vortices were created but no lower-surface vortices. For minimum power the effective angle of attack is held to a minimum so as to minimise separation and thus minimise any force.

The influence of planform (sinusoidal, square, or sawtooth) was studied experimentally by Hover et al. [107]. Phase angle was not considered; however it was evident that a sinusoidal waveform was superior across the spectrum considered. An optimisation routine to the same effect was performed by Kaya & Tuncer [108]. To maximize thrust fast pitch accelerations at the minimum and maximum plunge positions were required. To maximize propulsive efficiency a sinusoidal motion for both plunge and pitch was required.

b) Combined Pitch-Roll

Triantafyllou et al. [109] reported the effect on time-averaged lift and thrust coefficient of a mean incidence superimposed onto a pitching and rolling three-dimensional foil. The motion is therefore highly three-dimensional. Fig. 1.18 demonstrates that flapping motion can produce lift and thrust coefficients far in

excess of the static values with increasing performance for increased amplitude and or frequency. There is also the intuitive trade-off between lift and drag.

c) Passive-Pitch

Tinar & Cetiner [110] performed acceleration and PIV measurements for self-induced pitching vibrations of a NACA 0012 using three different levels of spring stiffness, three different freestream velocities and four pre-angle settings. The results demonstrated that significant variations of angle of attack could be passively produced through the action of a LEV. The effect of this motion on lift, drag and efficiency were however not considered.

d) Passive-Plunge

Murray & Howle [111] used an inviscid flow model to investigate the potential of passive-plunge motion as a thrust enhancement mechanism. The motion was created by a pitching zero-thickness airfoil with spring stiffness to control the plunging motion. It was found that a less stiff spring produced greater thrust at lower frequencies (Sr_c<0.4) but less thrust beyond this. The efficiency was improved for all frequencies considered. The limitations of both the model and the limited range of stiffnesses considered mean however that the results are of limited use.

1.3.6 Flapping Flight Summary

Natural flapping flight presents an excellent example of the type of performance desirable for MAVs. It is achieved through a mixture of lightweight structures, complex control systems, and unsteady aerodynamics. The latter primarily refers to the previously described lift-enhancing mechanisms, the most important being the leading-edge vortex. This leading-edge vortex is responsible for creating a large region of low pressure over the upper surface and is primarily created during the downstroke phase of the flapping cycle with the other phases used to reset the wing ready for the downstroke in the most efficient manner possible.

Both experimental and computational studies have identified the presence and importance of vortical action in force production for large amplitudes. Given that the strongest parameter has been identified as nondimensional plunge velocity, one can reasonably expect similar forces for small-amplitude high-frequency motion, as large-amplitude low-frequency motion.

1.4 LITERATURE REVIEW SUMMARY

Section 1.1 described MAVs and identified the three principal types of MAV and their comparative advantages and disadvantages. From this it became evident that the only type to be nearing readiness is the fixed-wing design. However, further gains in the efficiency of thrust and / or lift generation are required before this can become feasible, thus necessitating a flow control methodology.

Section 1.2 described the state of the art in flow control methodologies applicable to MAVs. From this it became clear that standard methods such as blowing / suction, and plasma actuators are inappropriate at MAV-scales. This leaves the field open to more novel methods such as membrane wings and wing oscillations, the latter being the subject of the current study.

Section 1.3 described the effect of flapping motion in both natural flight and under experimental conditions. It was shown that even though the dependence is not perfect for a given Reynolds number the most significant parameter in determining the performance is generally accepted as the plunge velocity, $Sr_A = fA/U_\infty$. The forces and flowfields created by large-amplitude, low-frequency motion can therefore be extrapolated to small-amplitude, high-frequency motion; the latter being more suited to electrical actuators, and as a stable sensor platform. For large-amplitude motion the LEV has been identified as the primary lift enhancement mechanism, responsible for very large lift increases over steady-state mechanisms. Under experimental conditions it has been demonstrated that lift coefficients as great as five can be created but these tend to incur a drag penalty. In a similar manner drag reduction can be enacted through vortical action by means of a reverse-Kármán vortex street, which involves the pairing of trailing-edge vortices to create self-advecting pairs that impart momentum to the flow.

1.5 OBJECTIVES

The three objective of the current study are:

i) Quantify the effect on thrust and lift of small-amplitude high-frequency motion. For lift creation it is necessary that the wing have a non-zero mean angle of attack, if not, the symmetry of the motion will likely create a symmetric flowfield and thus

zero lift (bar the deflected jet case). The current experiments will therefore consider a two-dimensional airfoil at a fixed post-stall angle of attack, undergoing an actively created small-amplitude pure-plunging motion.

ii) Quantify the effect on thrust and lift coefficients of deflected jets, investigate whether they form at non-zero angles of attack, the effect of starting position and garner greater understanding of why deflected jets form.

iii) Investigate the effect of geometry on the efficacy of small-amplitude high-frequency motion. Typically, stationary flat plates produce more lift than stationary airfoils so this is a suitable comparative geometry.

1.6 FIGURES

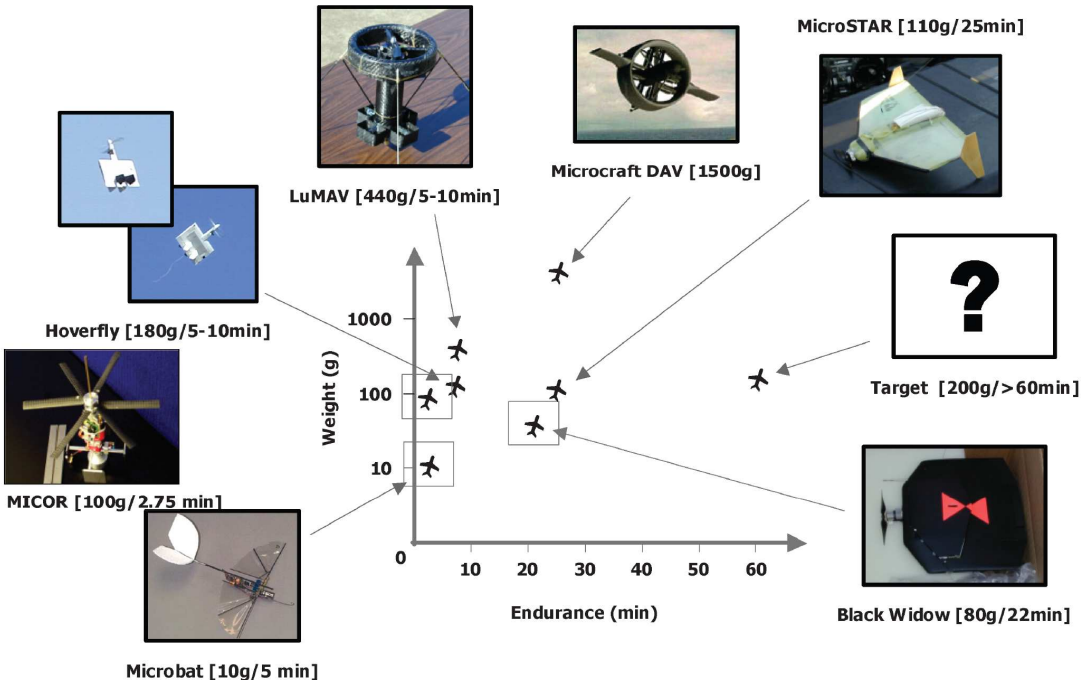

Fig. 1.1 Endurance or hover time of current MAV designs. From Pines & Bohorquez [5].

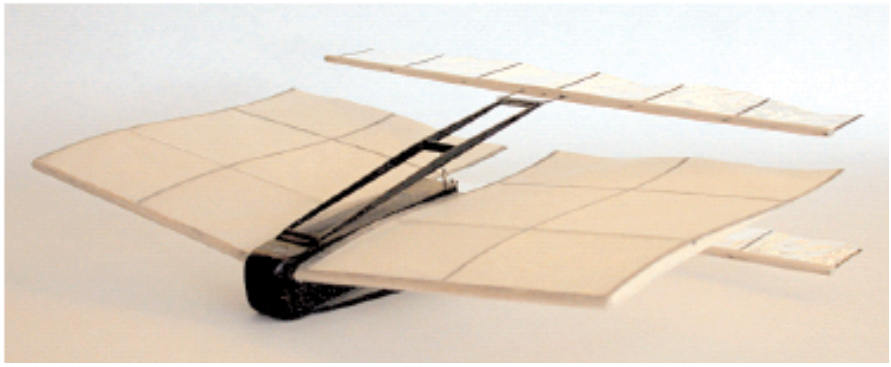

Fig. 1.2 NPS design, from Jones et al. [3].

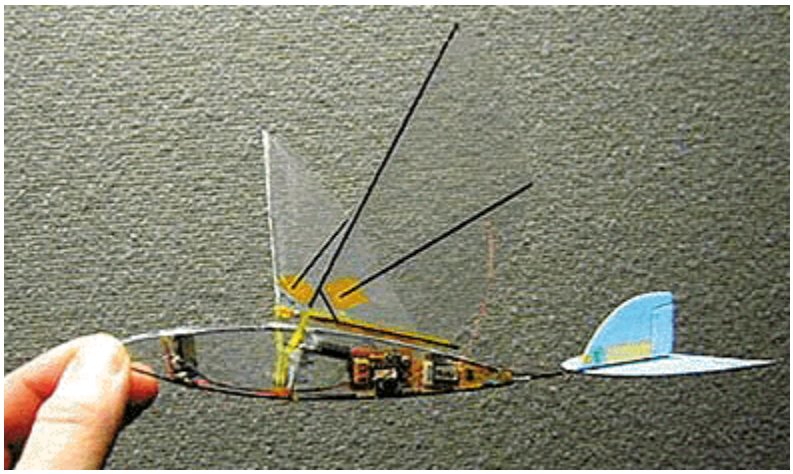

Fig. 1.3 Microbat.

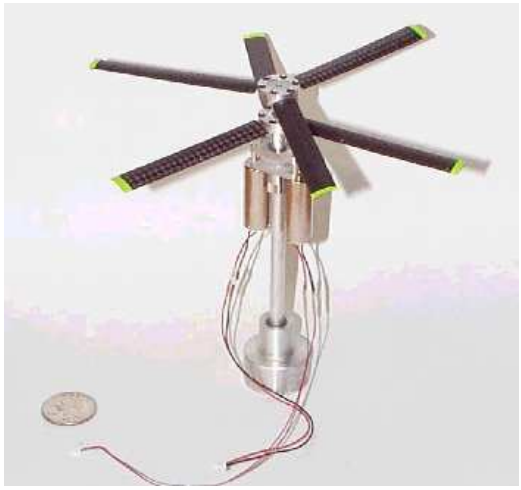

Fig. 1.4 MICOR NPS rotary wing, from Bohorquez et al. [15].

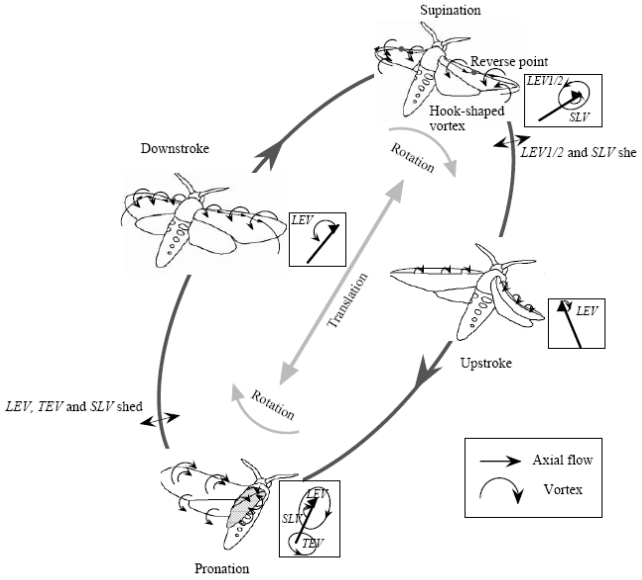

Fig. 1.5 Stages of flapping flight. From Liu et al. [42].

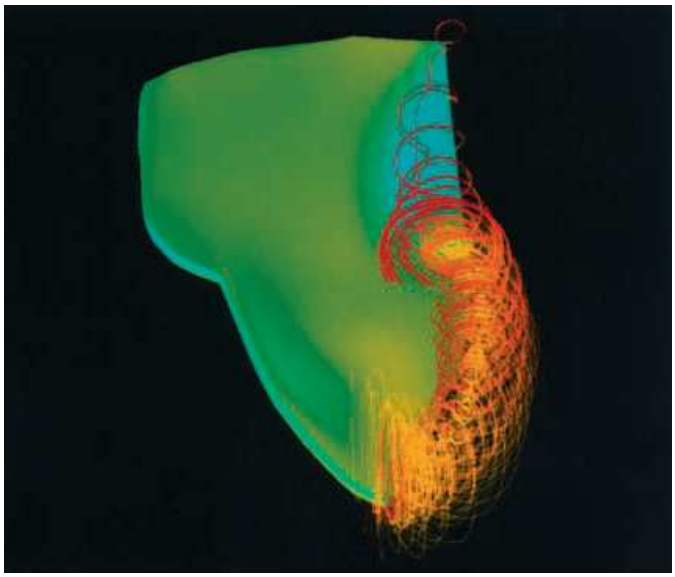

Fig. 1.6 LEV of a hovering hawkmoth. From Liu et al. [42].

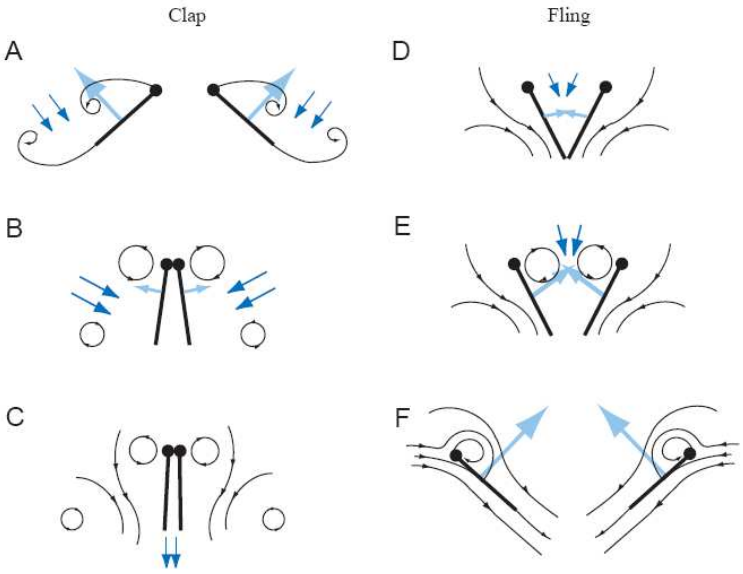

Fig. 1.7 Clap and fling lift production [44].

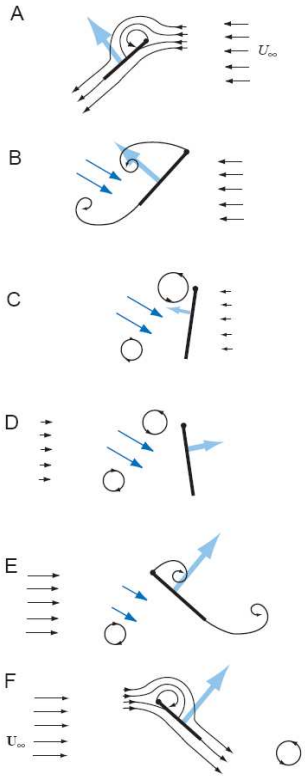

Fig. 1.8 Wing-wake interference [45].

Fig. 1.9 Kármán vortex street. From van Dyke [112].

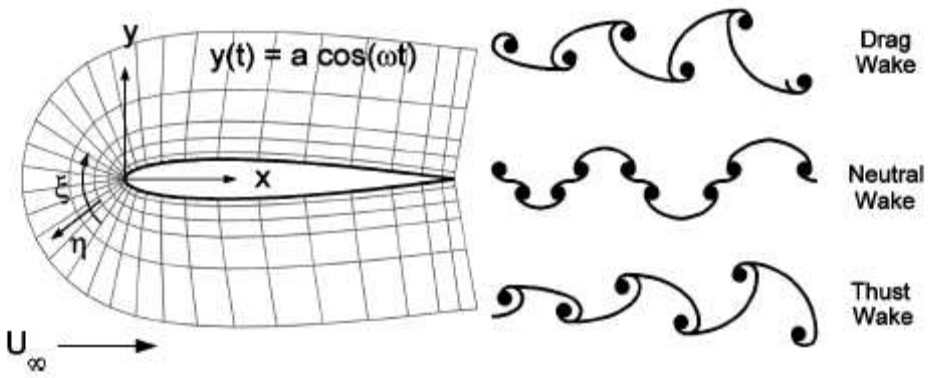

Fig. 1.10 Wake-force relationship. From Young & Lai [64].

Fig. 1.11 Neutral wake, from Young & Lai [66].

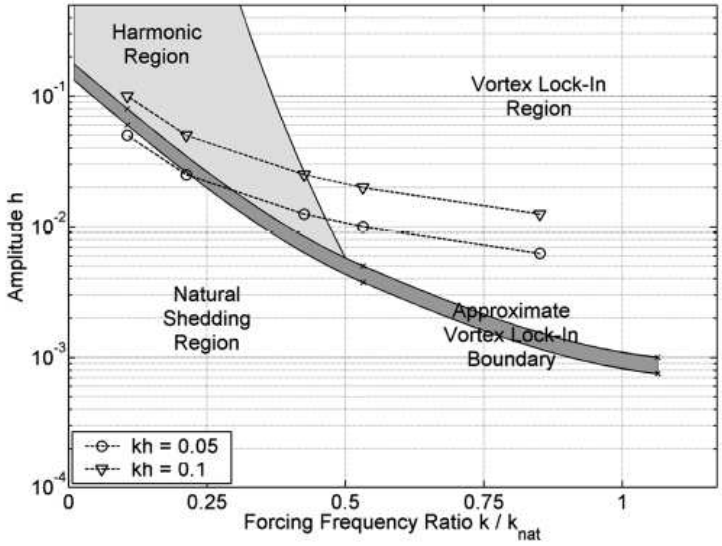

Fig. 1.12 Vortex lock-in for NACA 0012 at Re = 20,000, from Young & Lai [66].

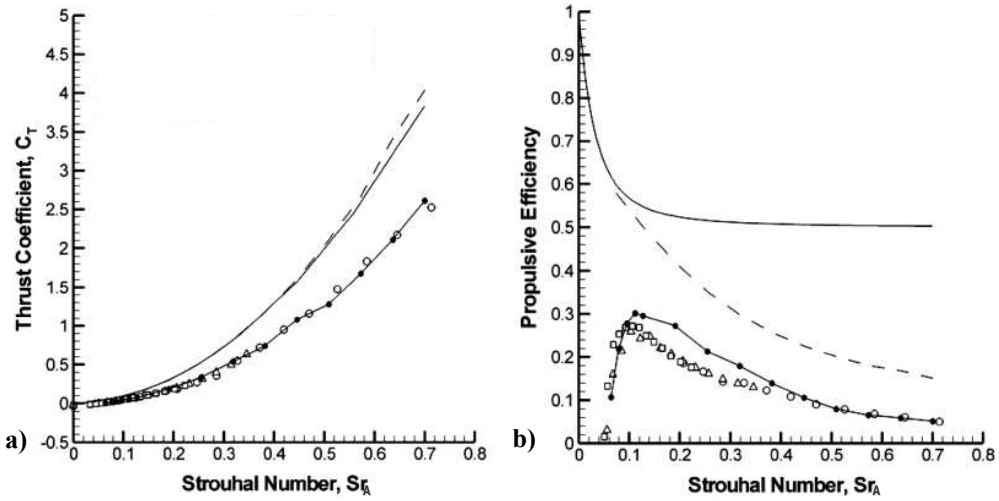

Fig. 1.13 Dependence of thrust coefficient and propulsive efficiency on Sr_A, adapted from Heathcote et al. [57] Open circles represent experimental results of Heathcote et al.; dashed lines are panel method; solid lines are Garrick approximations; lines with filled circles are Navier-Stokes computational results of Young [64].

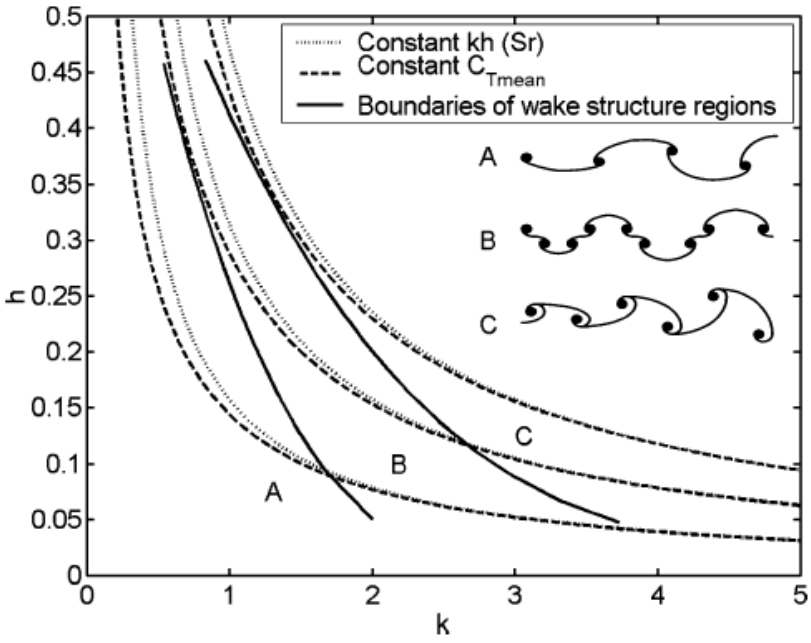

Fig. 1.14 Variation of constant average thrust coefficient, from Young & Lai [64].

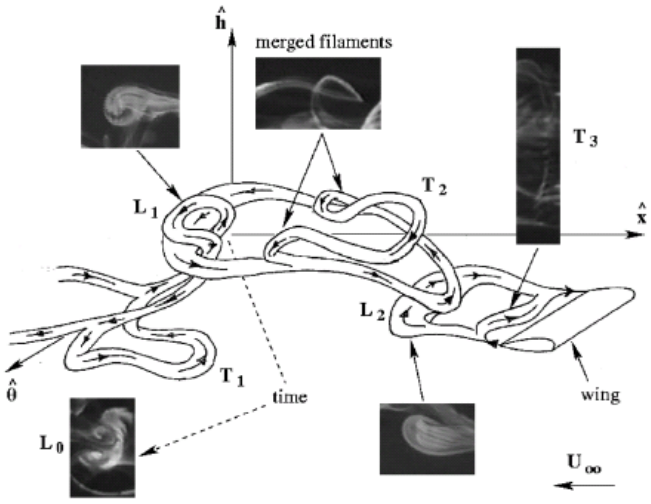

Fig. 1.15 Three-dimensional vortex structure, from von Ellenreider et al. [113].

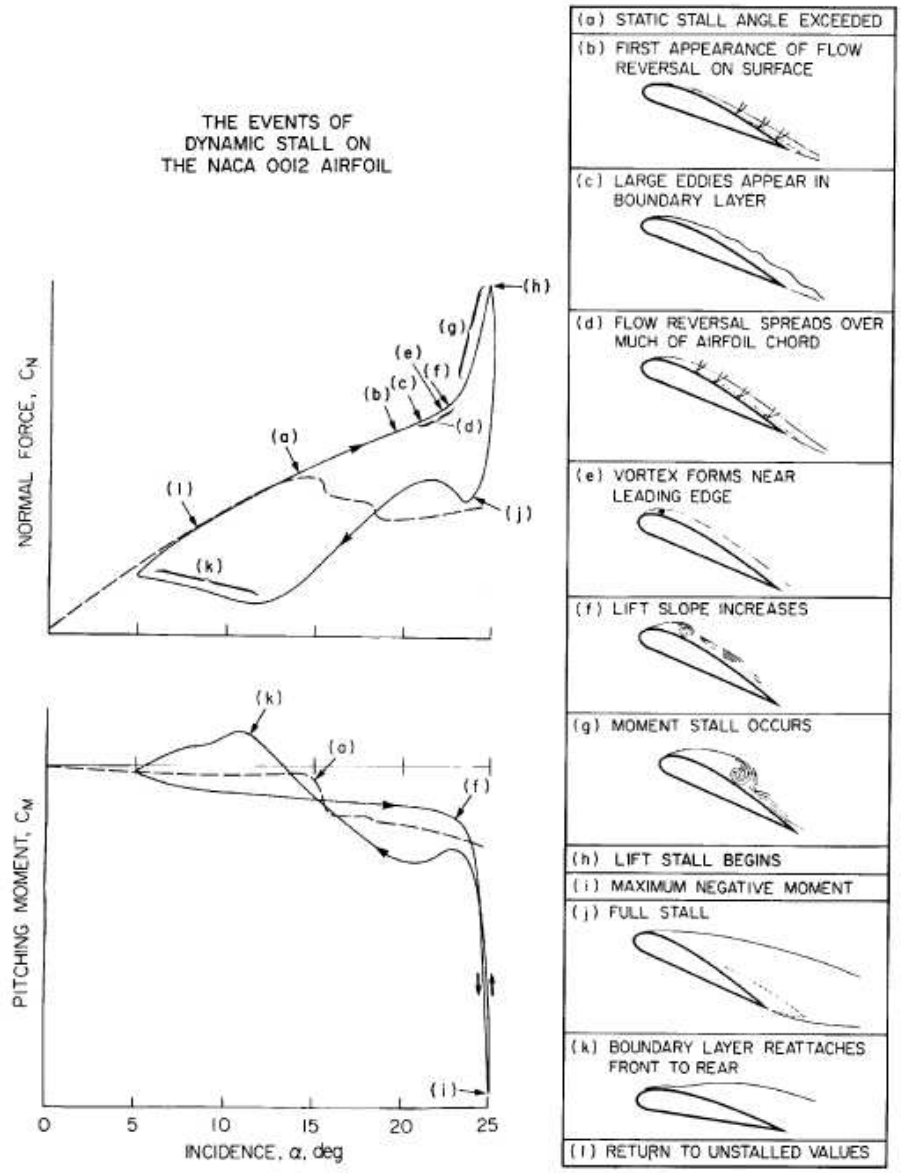

Fig. 1.16 Dynamic stall for a NACA 0012, from Carr et al. [96].

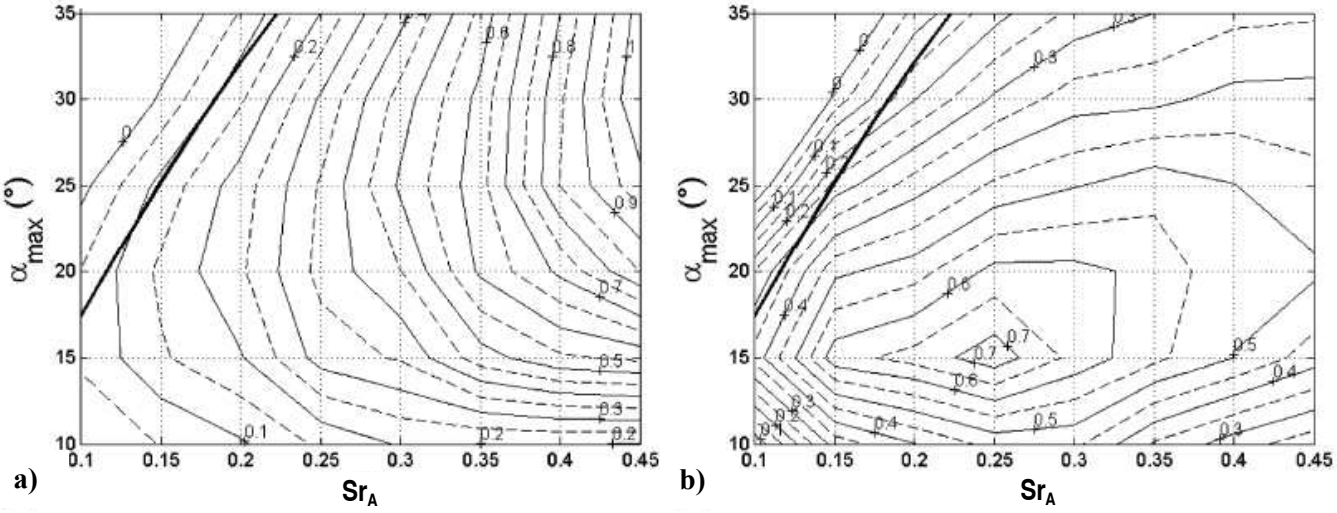

Fig. 1.17 a)Thrust coefficient, and b) propulsive efficiency for a NACA 0012 in combined plunge-pitch, from Schouveiler et al. [103].

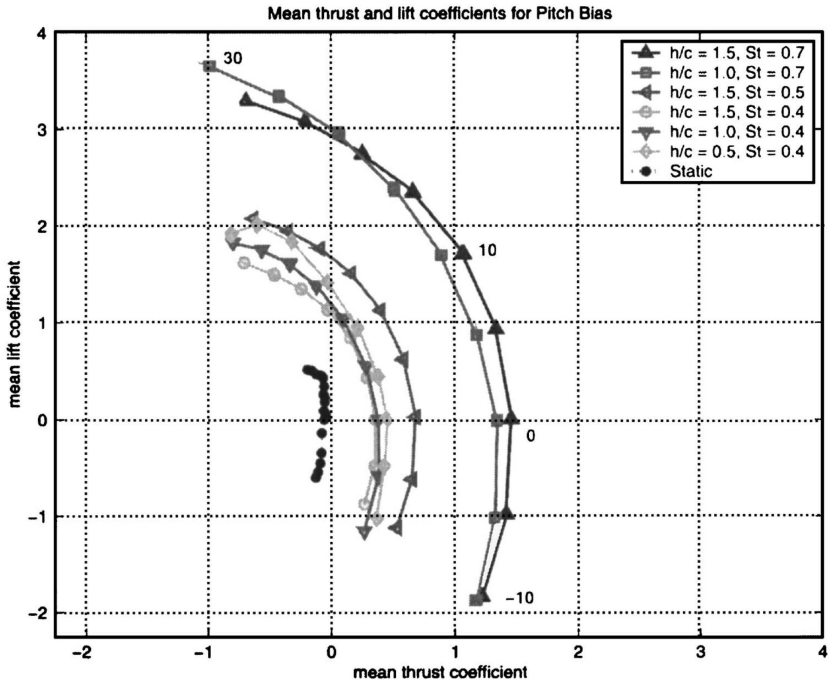

Fig. 1.18 Compromise between lift and drag coefficient for a three-dimensional heaving and pitching foil, from Triantafyllou et al. [109].

CHAPTER 2. EXPERIMENTAL METHODOLOGY

2.0 INTRODUCTION

Force, PIV, and hot film measurements were conducted on a plunging airfoil mounted vertically in a closed-loop water tunnel. The experimental parameters and their ranges are shown in Table 2. Uncertainties are calculated based on the methods of Moffat [114] incorporating both bias and precision errors.

Table 2 Experimental parameters

Variable	Range Presented	Uncertainty
Re	10,000 to 40,000	+/- 200
α	0 to 20°	+/- 0.5°
a/c	0.025 to 0.200	+/- 0.003
Sr_c	0 to 3	+/- 2.33%

2.1 EXPERIMENTAL SETUP

The experiments were conducted in a free-surface closed-loop water tunnel (Eidetics Model 1520) at the University of Bath. The water tunnel is capable of flow speeds in the range 0 to 0.5 m/s and has a working section of dimensions 381 mm x 508 mm x 1530 mm. The freestream velocity was controlled through a frequency controller attached to the motor. The freestream velocity was calibrated relative to the frequency controller through PIV measurements of an area one chord upstream of the leading-edge of the stationary wing. This was repeated as necessary and the variation between calibrations was found to be small (< 0.5%).

The water temperature was measured on a daily basis before testing to an accuracy of ±0.25°C. This temperature was used to calculate the water density, ρ, and dynamic viscosity, μ, used in determining the freestream velocity required for the desired Reynolds number. The drift in water temperature across a day was always small (<0.5°C).

The wing was of dimensions 0.1 m chord x 0.3 m span and was mounted vertically in a 'shaker' mechanism, as shown in Fig. 2.1. The NACA 0012 airfoil was

constructed by selective laser sintering from Duraform Polyamide. The flat plate was constructed from 4 mm mild steel with a rounded leading and trailing edge, see Fig. 2.2. Both wings were placed between upper and lower end plates, with clearances maintained at less than 2 mm. The oscillations were supplied via a Motavario 0.37 kW three-phase motor, 5:1 wormgear and IMO Jaguar Controller. The position of the root of the airfoil was measured through a rotary encoder attached to the spindle of the worm gear shaft. The rotary encoder was also used to trigger the PIV system.

2.2 FORCE MEASUREMENT

According to Mueller & DeLaurier [115] p.103: "Obtaining good experimental data for oscillating and flapping wings is a considerable challenge because the inertial-reaction forces can often obscure the relatively small thrusts being measured." This effect is further compounded in the case of lift measurements as inertia acts in the y direction. To acquire accurate results therefore necessitated exhaustive measurements.

The forces applied in both the streamwise and cross-stream directions were measured via two-component aluminium binocular strain gauge force balances [116]. One of the major deficiencies of this design is that to function a strain must be produced, thereby introducing flexibility. Due to inertia forces being dominant and approximately proportional to the frequency squared, the forces experienced at Sr_c = 3 are approximately nine times those at Sr_c = 1. A force balance designed for use at Sr_c = 1 would therefore produce excessively large trailing edge displacements at Sr_c = 3 (as the airfoil is supported in a similar manner to a cantilevered beam); and one designed for Sr_c = 3 would be inaccurate at Sr_c = 1. Up to three force balances of varying rigidities were therefore used for the dynamic force measurements, and a fourth more sensitive one was used for the stationary measurements. Data was taken across the entire range for each force balance, but only data from each force balance's acceptable range was used (i.e., $Sr_c < 1$ for the least rigid, $Sr_c < 2$ for the moderately rigid, and $Sr_c < 3$ for the most rigid. Within these ranges the agreement between the three was generally very good, for a typical example see Fig 2.3.

The signal from the strain gauges was amplified by a Wheatstone bridge circuit and sampled at either 2 kHz for 20,000 samples (stationary cases), or 360 samples per cycle for a minimum of 50 cycles (dynamic cases). This signal was then time-averaged across a number of complete cycles so as to remove the inertia component, leaving only the aerodynamic component, and converted into a force through linear calibration curves. To minimize uncertainty the calibration curves consisted of twenty three points, and were performed daily before and after testing. Each data set was repeated a minimum of three times for each force balance. The force measurements were then nondimensionalized through:

$$C_l = \frac{\overline{F_y}}{0.5\rho bcU_\infty^2} \quad \textbf{(2.1)}$$

$$C_d = \frac{\overline{F_x}}{0.5\rho bcU_\infty^2} \quad \textbf{(2.2)}$$

$$C_p = \frac{\overline{F_y u_y}}{0.5\rho bcU_\infty^3} \quad \textbf{(2.3)}$$

The uncertainty associated with these force measurements was calculated following the methods of Moffat [114, 117, 118]. It encompasses all possible sources of error including calibration errors, standard deviation errors, etc. These can be divided into two types, 'fixed' which are independent of Strouhal number, and 'variable' which approximately scale with the square of the Strouhal number, for further details see Appendix 1. For a typical case the lift uncertainty therefore increases from $C_l \pm 0.03$ at $Sr_c = 0$, to $C_l \pm 0.35$ at the maximum Strouhal number, see Fig 2.4. The large uncertainty in lift coefficient in the range $C_l = 1.2$ to 1.35 is due to hysteresis in the Strouhal number at which the sudden reduction in lift occurs, as will be discussed in Chapter 4. Taking into account that this uncertainty tends to scale with the inertia, and therefore according to a power law trend, and that time-averaged lift coefficient typically varies in the range $C_l = -4$ to 4 this value of uncertainty is reasonable. Furthermore the fixed component of the uncertainty will be constant across all data sets and therefore does not affect any trends identified. The drag uncertainty likewise increases from $C_d \pm 0.02$ to $C_d \pm 0.09$ compared to typical values of drag coefficient in the range $C_d = -1.6$ to 0.3. The power uncertainty increases from $C_p \pm 0.0$ to $C_p \pm 3.0$ compared to typical values of power coefficient in the range $C_p = 0$ to 50.

2.3 PIV

The flow was seeded with TSI 8 μm to 12 μm hollow glass spheres. Following the methods of Prasad [119] to estimate whether these particles are suitable for the application the settling velocity was calculated:

$$u_s = \frac{g d_p^2 (\rho_p - \rho)}{18\mu} \tag{2.4}$$

Where d_p is the particle diameter, and ρ_p and ρ the particle and fluid density respectively. The density of the particles used was ρ_p = 1050 to 1150 kg/m^3. This gives a settling velocity range of $u_s = 1.5*10^{-6}$ m/s to $10.2*10^{-6}$ m/s. This value is negligibly small in comparison with the freestream velocity, $U_\infty \approx 0.1$ m/s.

The velocity of these particles was measured using a TSI inc. 2D-PIV system incorporating a dual ND:YAG 120 mJ pulsed laser, 2MP Powerview Plus 12 bit CCD camera and TSI Model 610034 synchronizer. For measurements over the upper surface of the airfoil, the laser was positioned behind as shown in Fig. 2.1a. The shadow created by the airfoil therefore obscured the lower surface. For measurements over the lower surface the laser was positioned near the side wall of the tunnel, as in Fig. 2.1b. In both cases, the camera was located under the tunnel. The phase-averaged data is derived from 100 pairs for the upper surface and between 100 and 250 pairs (as required) for the lower surface. The PIV images were analyzed using the software Insight 3G. A recursive FFT correlator was selected to generate a vector field of 99 x 73 vectors giving a 1.22 mm spatial resolution for the upper surface, and 0.88 mm for the lower surface. Where necessary the upper and lower surface data were later merged through interpolation of the upper surface data onto the lower surface grid in MATLAB.

To calculate the circulation from the phase-averaged data, first the vortex is located using a vortex identification algorithm [120, 121] with the search centered on the point of maximum or minimum vorticity as appropriate. The radius of the vortex is then determined by continually expanding from the centre, one spatial resolution unit at a time, until the increase in circulation is negative or small (<1%). The circulation calculation itself is done using both line integral (see Eq. 2.5), and vorticity surface methods (see Eq. 2.6) [70]. The agreement between the two was generally very

good. All circulation results presented herein are derived from the average of the two methods (so as to minimize discretization error), normalized according to Eq. (2.7):

$$\Gamma = -\oint_C V \cdot ds \tag{2.5}$$

$$\Gamma = -\iint_S (\nabla \times V) \cdot dS \tag{2.6}$$

$$\hat{\Gamma} = \frac{\Gamma}{U_\infty c} \tag{2.7}$$

It was not possible to perform circulation calculations for lower Strouhal numbers because the vortex was too weak or indistinct.

2.4 HOT FILM

Hot film measurements were performed in the wake of the airfoil to measure both the natural shedding frequency and the level of cross-correlation between two probes separated in the spanwise direction. As both measurements are concerned with the frequency content of the flow it is not necessary to calibrate the velocity of the probes as long as the probes are operated at a low overheat ratio and therefore with a linear proportionality between velocity and voltage. This effect is demonstrated through a comparison of a cross-correlation measurement performed on the raw voltage signal and calibrated velocity signal shown in Fig. 2.5.

The signal was recorded for three minutes at a rate of 60 Hz and then processed using a Welch based PSD for the natural shedding frequency, and the MATLAB function xcorr for the cross-correlation with the normalization option set to 'coeff'. The xcorr function calculates the cross-correlation of two signals for a series of lags using the equation:

$$R_{xy}(m) = \frac{1}{N} \sum_{n=1}^{N-m-1} y(n)x(n+m) \tag{2.8}$$

The 'coeff' option then normalizes this, such that the autocorrelations at zero lag are equal, using:

$$R(m) = \frac{R_{xy}[m]}{[R_{xx}[0] * R_{yy}[0]]^{\frac{1}{2}}} \tag{2.9}$$

For all results presented herein a zero lag of m = 0 is used.

2.5 EXPERIMENTAL CONDITIONS

2.5.1 NACA 0012

The NACA 0012 airfoil was selected as the primary airfoil for this study due to its symmetry, wide general use, and 'standard' shape. There exists an extensive database of information for NACA 0012 airfoils under a wide range of conditions, see [96, 122]. The most significant paper for the current study is that of Huang & Lin [123] due to its low Reynolds numbers (<120,000). In contradiction of the common assertion [23, 124] that the NACA 0012 is a leading-edge stall airfoil, at Reynolds numbers less than 20,000 Huang & Lin observed trailing-edge stall to commence at angles of attack in the region of 1°, becoming fully stalled once the angle exceeded ~10°. The difference can be attributed to the low Reynolds number. Indeed Huang & Lin observed that at higher Reynolds numbers trailing edge stall would develop but at a specific angle of attack the boundary layer would trip into turbulence forming a laminar separation bubble. With increasing Reynolds number this laminar separation bubble moves towards the leading-edge. One would anticipate that with further increases in Reynolds number this laminar separation bubble would shrink in size creating a bubble typical of leading-edge stall. This description is in agreement with the results of Kim et al. [125] and the computations of Visbal et al. [126] for an SD 7003 airfoil under similar conditions.

Fig. 2.6 shows force measurements for a stationary NACA 0012 airfoil. These curves are in general agreement with those [127-131] in the literature for comparable Reynolds numbers. The changing stall behaviour with Reynolds number is apparent through the significantly different lift curve at a Reynolds number of 10,000 and changing C_{lmax}. It can be surmised that for all Reynolds numbers considered, stall commences in the region 10° to 11°. The angles of attack under consideration in this study can therefore be considered as: $\alpha = 0°$, 5° is pre-stall, $\alpha = 10°$ is around stall, and $\alpha = 12.5°$, 15°, 20° are post-stall.

Once the boundary layer becomes separated, the airfoil will begin shedding vortices in a similar manner to a bluff body. For a Reynolds number of 10,000 these vortices will be laminar up to $\alpha \approx 5°$, becoming subcritical till $\alpha \approx 10°$, and transitional beyond [123]. Within the laminar regime the vortices will be strongly periodic giving a clear peak. Within the subcritical regime the strength of this peak will be marginally diminished due to the action of instabilities developed in structures upstream of the separation point. Within the transitional regime the shed vortices lose coherency resulting in a disorganized wake with no clear power spectra peak. If one were to significantly increase either Reynolds number or angle of attack from within this region one would anticipate that it would enter the supercritical regime where the vortices become periodic again with fluctuations superimposed.

The trend of vortex shedding frequency with Reynolds number is shown in Fig. 2.7. One observes a strong Reynolds dependence below fifteen degrees as a result of the transitional nature of the flows below this angle of attack. This is in general agreement with the results of Young & Lai [66] and Koochesfani [65] for a NACA 0012 but rather surprisingly deviates at higher angles of attack from the results for a flat plate [132].

2.5.2 Flat Plate

Lift coefficient for the flat plate is compared to that for the NACA 0012 airfoil in Fig. 2.8 for a Reynolds number of 10,000. Within the pre-stall region the lift coefficient of the flat plate is very linear in agreement with previous measurements [133, 134]. Due to the steep gradient of this linear region the flat plate experiences significantly higher lift coefficients across all angles of attack. Stall occurs at $\alpha \approx 10°$. The description of $\alpha = 0°, 5°$ as pre-stall, $\alpha = 10°$ as around stall, and $\alpha = 12.5°, 15°, 20°$ as post-stall is therefore valid for both flat plate and NACA 0012 airfoil. The vortex shedding behaviour of flat plates has been studied in detail [132, 135]. The established range of vortex shedding frequencies for a flat plate is $Sr_d = 0.16$-0.22.

2.5.3 Reynolds Number

The Reynolds number for this study will usually be maintained at 10,000, although other values are also considered. This Reynolds number was selected as being relevant to MAV scale flight and experimentally convenient. The effect of Reynolds number so far presented for plunging (section 1.3.2), and pitching (section 1.3.3) airfoils presents an often contradictory impression. One can however infer that it requires a significant (order of magnitude) variation of Reynolds number to produce a noticeable effect.

2.5.4 Tunnel Interference Effects

Following the text of Pankhurst & Holder [112] tunnel interference effects for a stationary wing can be subdivided into five sources:

1. *Solid blockage* – the increase in velocity caused by the presence of the airfoil section. Using the methods of Pankurst & Holder one would anticipate for this case a stationary NACA 0012 at 15° angle of attack would induce a 0.8% error in the tunnel to free-flight velocity.

2. *Wake blockage* – the increase in velocity caused by the presence of the airfoil wake. As one would anticipate the wake blockage is more significant at greater angles of attack. Again based on the methods of Pankhurst & Holder, the wake blockage would induce a 1.6% error in tunnel to free-flight velocity.

3. *Lift effect* – in a wind tunnel an airfoil would be expected to produce less lift than that in free-flight as the tunnel walls limit the streamline curvature. The difference for the stationary $\alpha = 15°$ case between free-air and closed loop tunnel would be [112] $\sim 2.8\%$.

4. *Static-pressure gradient* – a static pressure gradient may arise throughout the length of the tunnel due to acceleration of the fluid created by both the wake and the developing tunnel-wall boundary layer. The drag force as measured on the force balance should therefore be corrected accordingly. This is not possible at the current time as the value of dp/dx required for the calculations is unquantifiable in a water tunnel. The drag force however is of secondary concern in the current study so this is not a serious hindrance.

5. *Wall boundary-layer interference* – the boundary-layers created by the two side walls (end plates) if turbulent can interfere with the flow over the tips of the airfoil section. This effect should be minimal because the end plates begin 0.015 m upstream of the leading edge and the required distance for transition under these conditions would be 2 m (based on a critical Reynolds number = $2x10^5$); the wall boundary layer can therefore be taken as laminar. Boundary-layer theory predicts that at its thickest (trailing edge) the boundary-layer will be ≈ 5 mm thick. The anticipated effect of a laminar boundary-layer developing from 0 to 5 mm at either tip will be minimal.

For a dynamic pitching wing Carr et al. [96] observed that the wing-wall interaction for AR = 1.62 had negligible effect once $Sr_c > 0.032$, contrary to the static cases. In addition, blockage ratio ceased to have an effect once $Sr_c > 0.050$. The current study is primarily concerned with comparing the forces and fluid dynamic structures of an oscillating wing for Strouhal numbers in the range $Sr_c < 3$. The tunnel interference will therefore be comparatively small for a static wing, and negligible for a dynamic wing.

2.5.5 Turbulence Intensity

The turbulence intensity has previously been measured [83] to be less than 0.5%. It has previously been shown [130] that freestream turbulence at a Reynolds number of 80,000 can energise the boundary layer and therefore delay stall by 4° (so that C_{lmax} increased from ~0.85 to ~1.05) for a static airfoil. But this required substantial levels of turbulence ~5% and the effect diminished with the wing undergoing pitching oscillations. Mueller [134] found that more reasonable turbulence intensities of <1.3% had a negligible effect on stationary lift coefficient. The anticipated effect of a turbulence intensity of 0.5% on a stationary or plunging airfoil is therefore negligible.

2.6 FIGURES

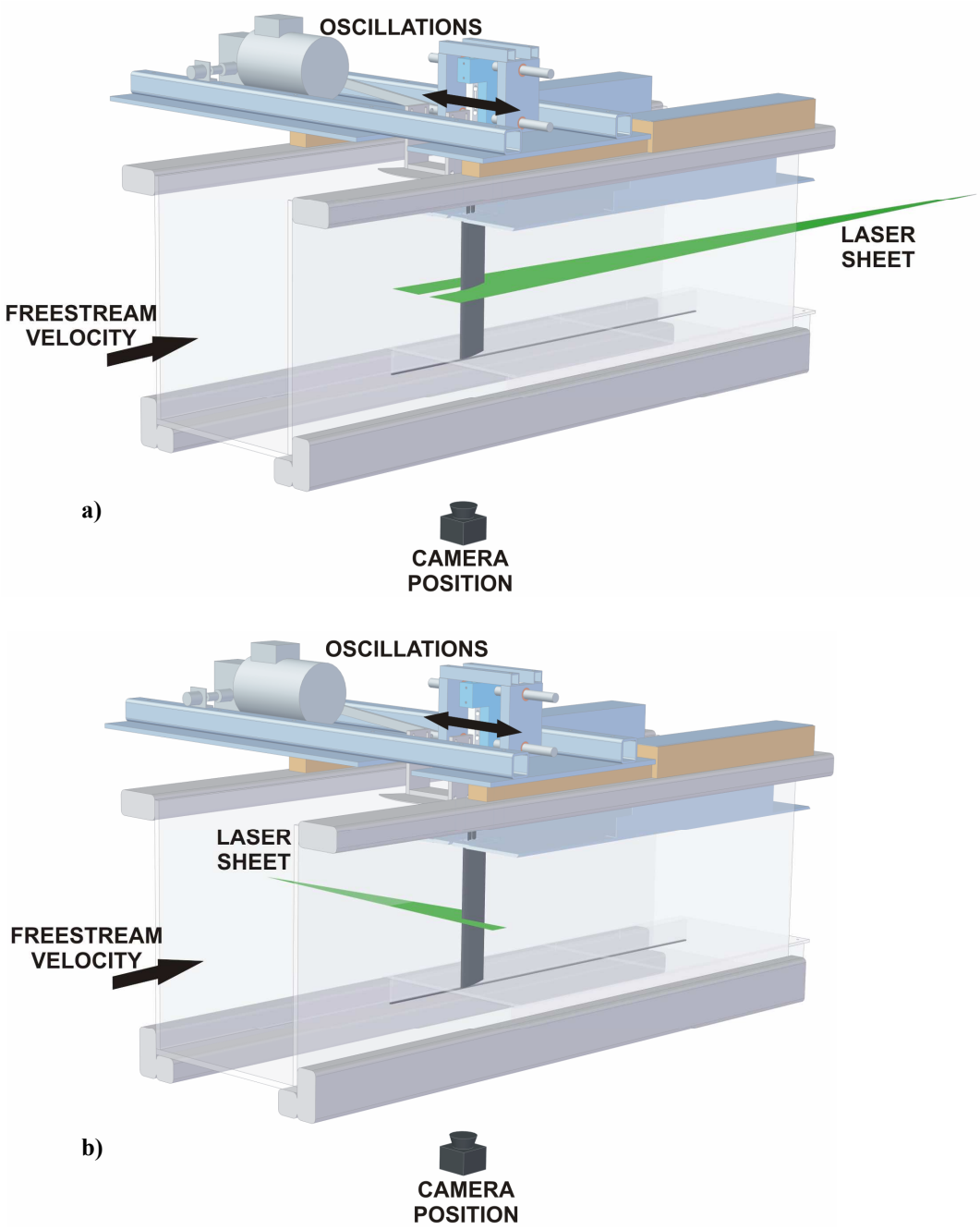

Fig. 2.1 Experimental setup a) for PIV measurements over the upper surface, and b) for PIV measurements over the lower surface.

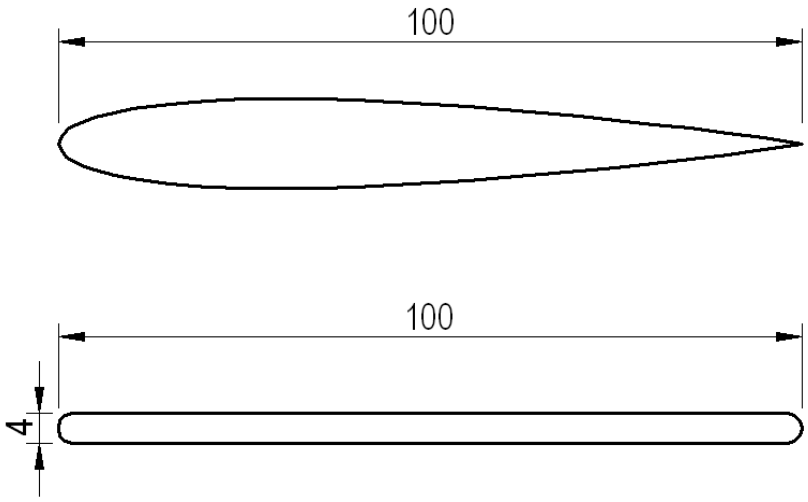

Fig. 2.2 Wing cross-section showing: NACA 0012 airfoil (top) and flat plate (bottom).

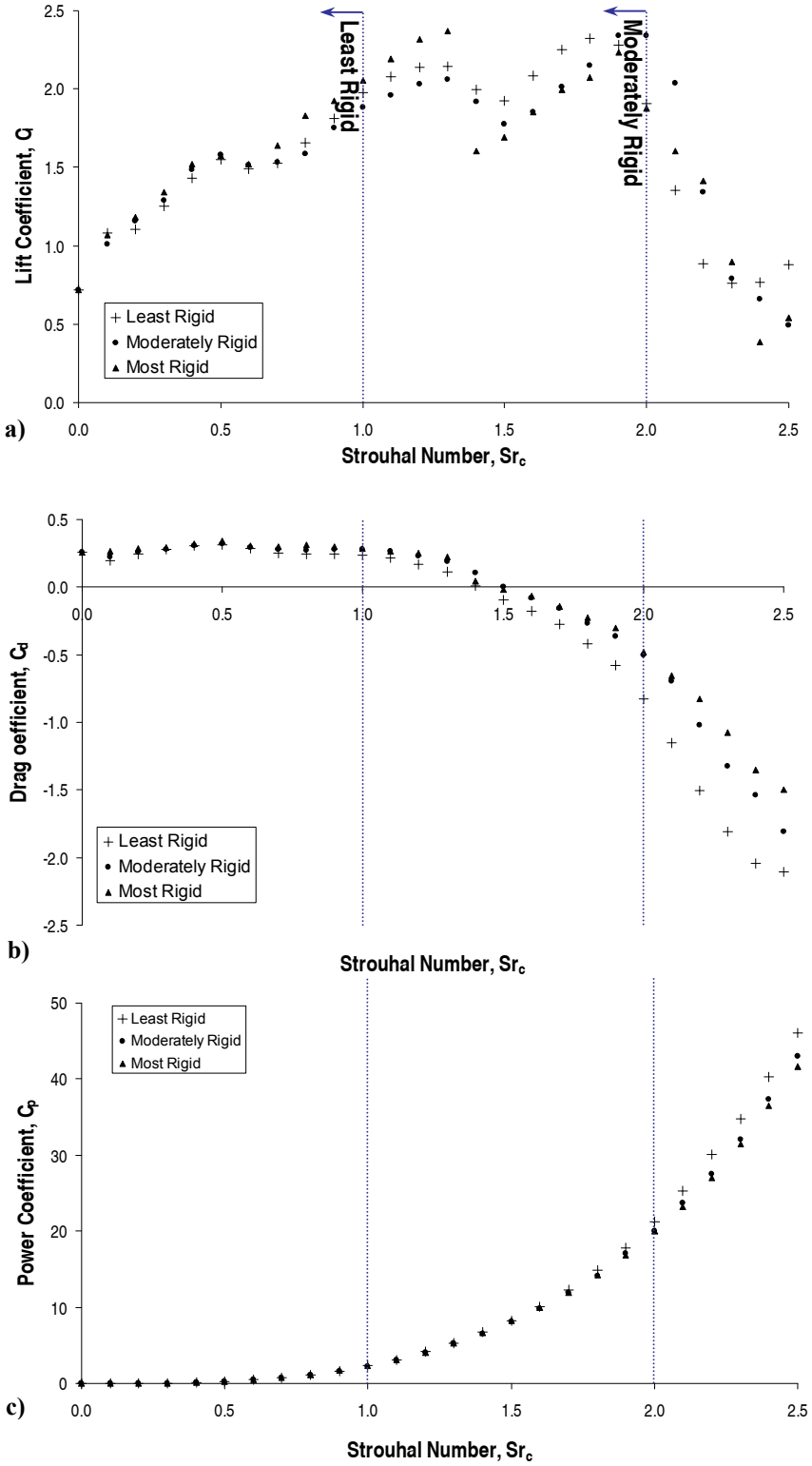

Fig. 2.3 Example force measurements for the three force balances including their relevant ranges for α = 15° and a/c = 0.10: a) lift coefficient, b) drag coefficient, and c) power coefficient.

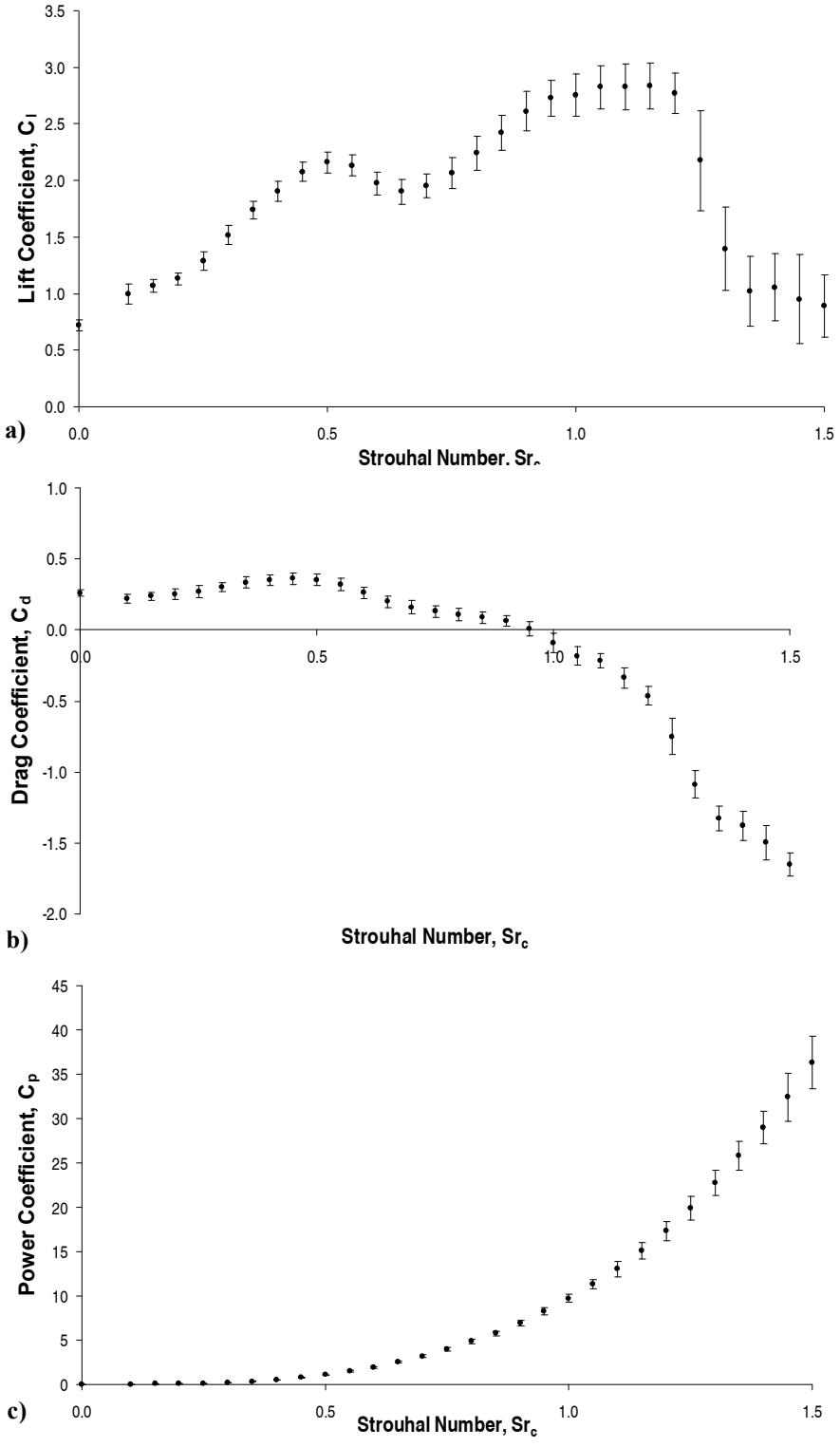

Fig. 2.4 Example uncertainties for a typical case, α = 15° and a/c = 0.20, showing: a) lift coefficient, b) drag coefficient, and c) power coefficient.

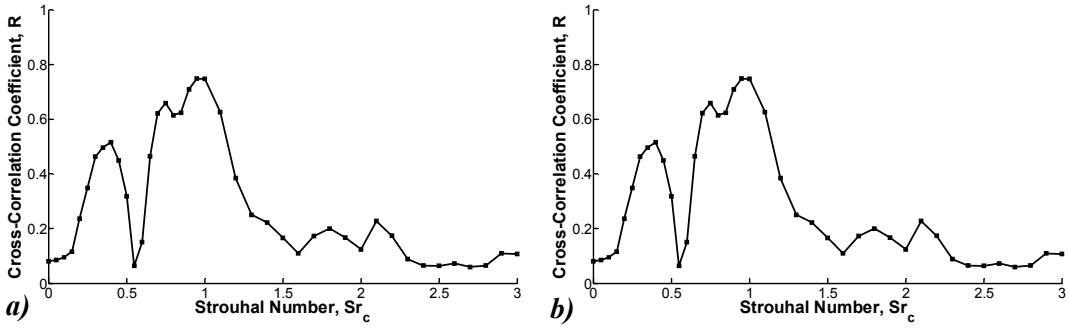

Fig. 2.5 Cross-correlation measurements using: a) raw voltage signal; b) calibrated velocity signal.

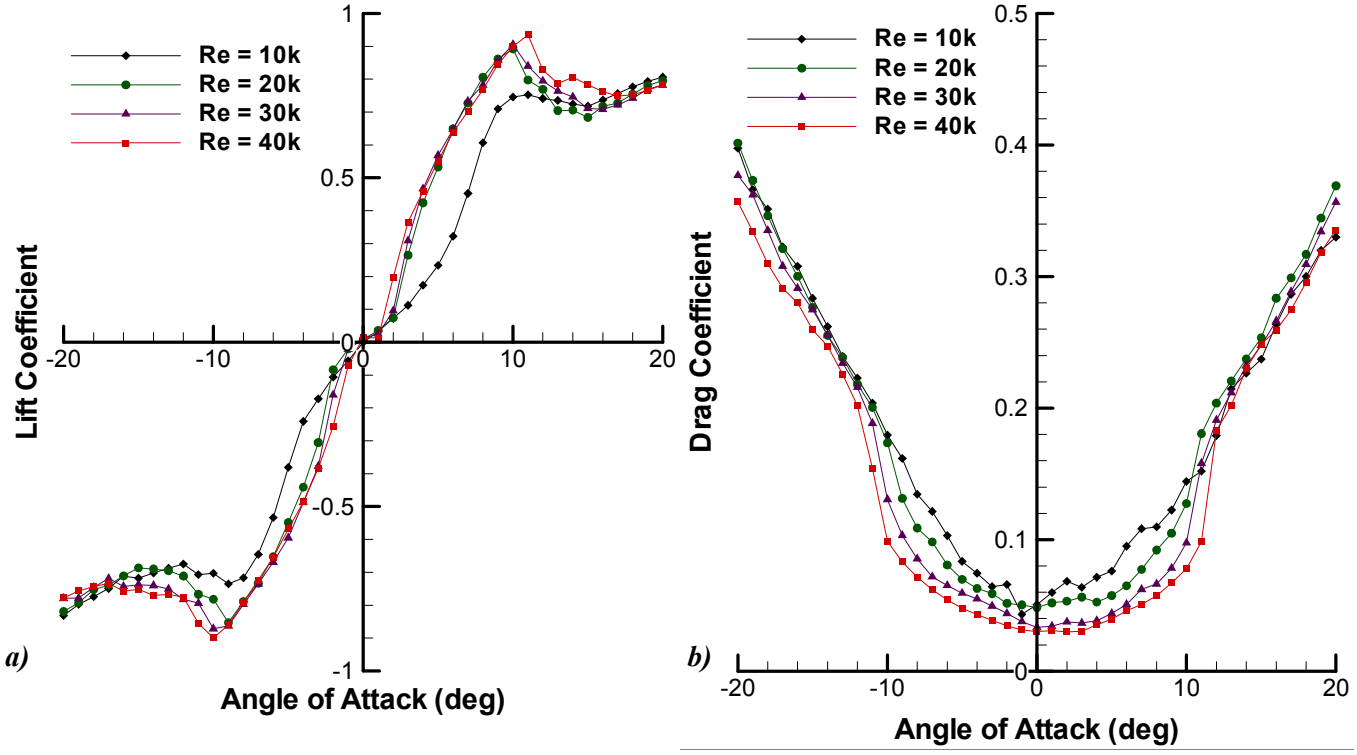

Fig. 2.6 Static force measurements: a) lift coefficient; b) drag coefficient.

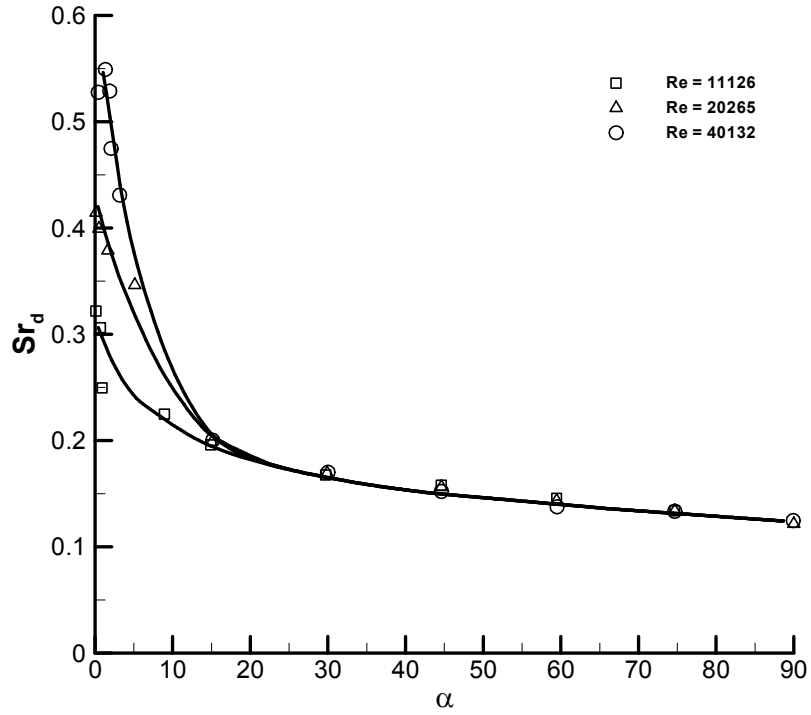

Fig. 2.7 Variation of natural vortex shedding frequency with α and Reynolds number. From Huang & Lin [123].

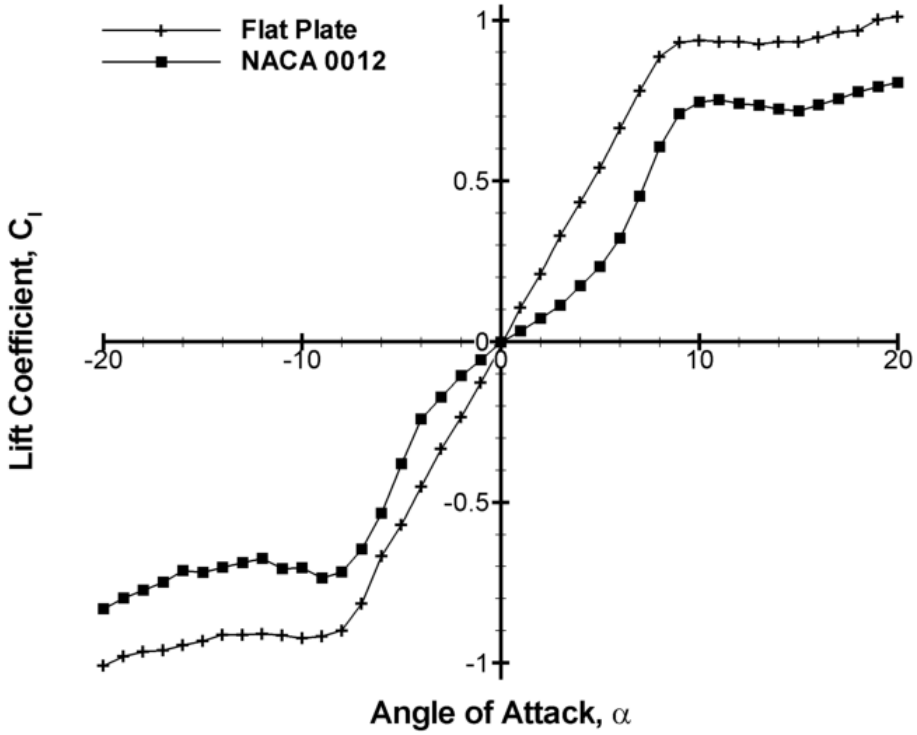

Fig. 2.8 Lift coefficient for the stationary flat plate and NACA 0012 airfoil at a Reynolds number of 10,000.

CHAPTER 3. PERFORMANCE ENHANCEMENT THROUGH SMALL-AMPLITUDE AIRFOIL OSCILLATIONS

3.0 SUMMARY

To investigate the potential for performance improvement through small-amplitude high-frequency motion the lift and thrust performance of a NACA 0012 oscillating with a fixed post-stall angle of attack ($\alpha = 15°$), small amplitude ($a/c \leq 0.2$), and range of Strouhal numbers has been studied experimentally. PIV, force and hot film measurements were taken to quantify the performance improvement and understand why. The force measurements demonstrated a significant increase in time-averaged lift of up to 305% and significant reduction in drag resulting in thrust production. The drag decrease was shown to be associated with the formation of a reverse-Kármán vortex street. Time-averaged lift was shown to increase approximately proportionally with plunge velocity. PIV measurements showed the lift increase to be associated with the growth of leading-edge vortices. Superimposed onto this linear trend were several peaks in lift coefficient at constant Strouhal numbers, independent of amplitude. Hot film measurements showed these to be due to lock-in with the natural shedding frequency, its harmonics, and subharmonics. At high plunge velocities the linear trend was broken due to the combined effect of the dissipation of the upper surface leading edge vortex and the development of a strong lower surface leading edge vortex resulting in a significant fall in lift. It was therefore concluded that the most effective method of performance enhancement was to oscillate at a moderate plunge velocity with the frequency selected to be the natural shedding frequency, or its harmonics, and subharmonics.

3.1 RESULTS

3.1.1 Force Measurements

The lift, drag and power coefficient for a NACA 0012 airfoil oscillating at a fixed angle of attack of $\alpha = 15°$, a range of amplitudes, $a/c = 0.025$ to 0.200, and range of Strouhal numbers based on chord is shown in Fig. 3.1. Strouhal number based on

chord can be considered as non-dimensional frequency of oscillation. Shown in Fig. 3.2 is the same force measurements but versus Strouhal number based on amplitude. Sr_A can be considered as non-dimensional plunge velocity.

Starting with lift coefficient versus Strouhal number based on chord as shown in Fig. 3.1a, the value for a stationary airfoil is represented by the value at $Sr_c = 0$ of $C_l = 0.72$. With increasing Strouhal number the lift coefficient increases substantially, with greater effect for greater amplitude. The maximum observed is therefore $C_l = 2.91$ for the largest amplitude, a/c = 0.20. This represents an increase of 305% over the value for a stationary airfoil. The nature of this dependence on amplitude suggests that a more appropriate parameter is nondimensional plunge velocity Sr_A, see Fig. 3.2a. This demonstrates that at low Sr_A there is a very approximate linear trend between Sr_A and lift augmentation which is independent of amplitude. At high Sr_A however there is a significant fall in lift which breaks from this trend. This occurs at $Sr_A \approx 0.400$ for a/c = 0.100, $Sr_A \approx 0.4275$ for a/c = 0.150, and $Sr_A \approx 0.46$ for a/c = 0.200, suggesting that the fall occurs in the region of $Sr_A \approx 0.45$ and is delayed by larger amplitude. For the smaller amplitudes the maximum Sr_A studied was therefore insufficient ($Sr_A < 0.30$ for a/c = 0.2, and $Sr_A < 0.15$ for a/c = 0.1) for the fall in lift to occur. The cause of the fall in lift is analysed in more detail in section 3.1.4.

Returning to Fig. 3.1a a further interesting feature is the presence of several peaks in the lift curves for all amplitudes. These occur at consistent values of Sr_c independent of amplitude, i.e., $Sr_c \approx 0.45$, 0.90, and 2.10. To verify that the cause of the peaks was aerodynamic and therefore dependent on Sr_c, and not experimental and therefore dependent on f, the force measurements for a/c = 0.20 were repeated at a higher Reynolds number of Re = 20,000, see Fig. 3.1a. The measurements for both Reynolds numbers match to within the bounds of experimental uncertainty. It can therefore be concluded that it is an aerodynamic phenomenon. The cause of these peaks will be analysed in more detail later in section 3.1.3.

The effect of small-amplitude oscillations on time-averaged drag coefficient is shown in Fig. 3.1b. For all amplitudes there is a general decrease in drag coefficient

with increasing Strouhal number. The exception to this is a small peak in the region of $Sr_c \approx 0.45$ reflecting the first peak observed in lift coefficient, further evidence that the peak is due to an aerodynamic phenomenon. The effect of Reynolds number is negligible. As a result of the decreasing drag one observes, for $a/c > 0.025$, a drag to thrust switch. As before for lift coefficient, drag coefficient demonstrates greater effect for greater amplitude. The occurrence of the drag-thrust switch is therefore also amplitude dependent, i.e., $Sr_c \sim 2.45$ for $a/c = 0.05$, $Sr_c \sim 1.50$ for $a/c = 0.10$, $Sr_c \sim 1.20$ for $a/c = 0.15$, and $Sr_c \sim 0.975$ for $a/c = 0.20$. This amplitude dependence again suggests the possibility of Strouhal number based on amplitude as a significant parameter, see Fig. 3.2b. When compared against Sr_A the curves collapse into a smaller band but are not constant. In contradiction to Garrick approximations, for the same Sr_A smaller amplitudes produce more thrust. This contradiction is feasible given the large degree of separation present at the large effective angles of attack which invalidate Garrick approximations.

The effect of small-amplitude oscillations on time-averaged power coefficient is shown in Fig. 3.1c. Power coefficient demonstrates a power law trend with a strong amplitude dependence, these results are in good qualitative agreement with those of Heathcote et al. [57]. Thus for a given Strouhal number smaller amplitude results in a smaller power coefficient. The effect of Reynolds number is negligible. Indeed the two Reynolds numbers match so closely the points overlie each other, see Fig. 3.1c. Again this amplitude dependence suggests Sr_A as a more important parameter, see Fig. 3.2c. Fig. 3.2c demonstrates that for a given Sr_A larger amplitude is preferable. Larger amplitude is therefore preferable to minimise power, smaller amplitude is preferable to maximise thrust, and any amplitude is acceptable to maximise lift although the Sr_c should be tuned to the natural shedding frequency and larger amplitudes may delay the fall in lift.

3.1.2 Performance Improvement

Fig. 3.3a presents the streamlines and the magnitude of the time-averaged velocity vector for the stationary NACA0012 airfoil. There is a large region of separation over the suction surface of the airfoil. The airfoil can therefore be classified as fully

stalled in agreement with the force measurements presented in Chapter 2.5.1 and previous studies [127, 136] at low Reynolds numbers, Re = 4,000 – 31,000.

Fig. 3.3b demonstrates that oscillation even at small amplitude (a/c = 0.025) and low frequency (Sr_c = 0.50) significantly reduces this separated region. It is worth noting that due to the nature of time-averaged measurements the motion of the airfoil obscures a region in the direct vicinity of the airfoil. This makes the separated region appear smaller than is necessarily true. It is therefore preferable to consider the mean position of the airfoil (shown as a solid line) when comparing with the stationary case. Even taking this into account the separation reduction is still significant. With increasing Strouhal number (Fig. 3.3c to 3.3g) the reduction in separation region increases so that for Sr_c = 3 the separated region is almost completely eliminated in a time-averaged sense.

A second interesting feature is the region of high velocity over the leading-edge of the airfoil. With increasing Strouhal number this region increases in size and magnitude. As will be shown later this region coincides with the formation and shedding of leading-edge vortices. A third feature is the region in the vicinity of the trailing-edge for Sr_c = 2.5, see Fig. 3.3f. A region of low velocity is observed above the trailing-edge accompanying a region of high velocity below the trailing-edge. It will be shown later that these two features coincide with the formation of trailing-edge vortices. It will also be shown that once formed these trailing-edge vortices may form a reverse-Kármán vortex street responsible for the weak time-averaged 'jet' observed in Fig. 3.3g.

Relating this to the time-averaged force measurements the reduction in time-averaged separation and high velocity leading-edge region correlate well with an increasing lift coefficient, from C_l = 0.72 up to C_l = 1.62; and the weak time-averaged jet correlates well with the reduced drag, from C_d = 0.26 to C_d = 0.12. However the reason for the various peaks is not apparent in the time-averaged PIV suggesting that they are related to a phase-locked, instantaneous or three-dimensional phenomenon.

At the increased amplitude of a/c = 0.050 shown in Fig. 3.4 there are the same three flow features (reduced separation, high velocity near the leading-edge region, and time-averaged 'jet' downstream of the trailing-edge), but with greater effect for the same Strouhal number. Indeed the reduction in separation is such that for Strouhal numbers above $Sr_c = 1.5$ (Fig. 3.4e to 3.4g) there is no discernible separation region. Likewise for the same Strouhal number the high velocity leading-edge region is enhanced by the greater amplitude but with the crucial difference that for $Sr_c > 2$ (Fig. 3.4f and 3.4g) it begins to shrink in size. It will be shown later that this reduction coincides with a new mode of leading-edge vortex behaviour.

The trailing-edge flow behaviour is similarly enhanced by the larger amplitude of airfoil oscillation. For example the time-averaged jet is first apparent at $Sr_c = 1.5$ and grows in strength with increasing Strouhal number such that for $Sr_c = 3$ it contains peak time-averaged velocities of three times the freestream (as measured a half-chord downstream of the trailing-edge). Due to this time-averaged jet, the airfoil becomes thrust producing for $Sr_c \geq 2.5$.

This greater effect for greater amplitude mirrors what is observed in the force measurements, i.e., a maximum time-averaged lift coefficient of $C_l = 2.45$ and minimum drag coefficient of $C_d = -0.334$. Again the reason for the various peaks in the time-averaged lift coefficient is not apparent in the time-averaged PIV measurements.

With further increase in amplitude to a/c = 0.100 (Fig. 3.5), a/c = 0.150 (Fig. 3.6), and a/c = 0.200 (Fig. 3.7), there are the same three flow features but with greater effect for greater amplitude, i.e., reduced separation, a high velocity leading-edge region that initially grows then shrinks, and a time-averaged jet that develops at higher Strouhal numbers. The only significant qualitative difference is in the width of the time-averaged jet which appears to vary in direct proportion to the peak to peak amplitude of the oscillation, in agreement with the assumption of Lai & Platzer [55].

Moving on to the phase-averaged flowfield, Fig. 3.8 shows the phase-averaged contour plots of normalized vorticity at the top (left column), and bottom (right column) for the same amplitude and Strouhal numbers as Fig. 3.3c to g. The region directly below the airfoil is not visible due to the shadow created by the airfoil. For $Sr_c = 1.0$ (Fig. 3.8a) multiple clockwise leading-edge vortices and multiple counter-clockwise trailing-edge vortices form during the downward motion. During the upward motion these vortices gradually diffuse in a phase-averaged sense as they convect downstream.

With the Strouhal number increased to $Sr_c = 1.5$ (Fig. 3.8b) the multiple leading and trailing-edge vortices have become a single LEV / TEV of greater strength. The convected clockwise LEV interacts with the counter-clockwise TEV resulting in its dissipation. One would anticipate that during the upward motion a clockwise trailing-edge vortex should form, however due to the low plunge velocity there is none or it is very weak.

With the Strouhal number increased to $Sr_c = 2.0$ (Fig. 3.8c), the maximum and minimum effective angles of attack are $\alpha_{eff,max} = \alpha + \tan^{-1}(U_{pl}/U_\infty) = 32.4°$ and $\alpha_{eff,min} = \alpha - \tan^{-1}(U_{pl}/U_\infty) = -2.4°$. As such there is now a weak clockwise vortex shed at the trailing-edge during each cycle (visible below the counter-clockwise trailing-edge vortex in the left column). The interaction between leading and trailing edge vortex is visible at the top of the motion. A single clockwise LEV is formed during the downward motion and convects along the upper surface. On reaching the trailing edge this leading edge vortex interacts with the counter-clockwise trailing edge vortex causing it to divide into two weaker vortices. This strong interaction between convected leading edge vortex and trailing edge vortex becomes more evident with greater Strouhal number, see Fig. 3.8d and e. Also evident in Fig. 3.8e is the formation of a secondary leading-edge vortex due to vortex-boundary interaction. This can be seen as a small positive region of vorticity upstream of the primary leading-edge vortex. The significance of this secondary vortex will be made clear later.

For an increased amplitude of a/c = 0.050 (Fig. 3.9) similar behaviour is observed but as before with greater effect for greater amplitude. For example the formation of the secondary vortex observed at $Sr_c = 3.0$ for a/c = 0.025 is first observed at $Sr_c = 1.5$ for a/c = 0.050, and for the same Strouhal number the vortices are larger with greater maximum absolute vorticity. As a result for $Sr_c \geq 2$ new behaviour not witnessed for the smaller amplitude begins to emerge.

At a Strouhal number of $Sr_c = 2.0$ (Fig. 3.9c), there is a strong clockwise leading-edge vortex which forms during the downstroke and has an accompanying secondary vortex of opposite sign. The primary LEV is shed at the bottom of the downstroke and convected over the upper surface. At the trailing edge there is one strong counter-clockwise and one weak clockwise trailing-edge vortex shed per cycle. It is the interaction of these trailing edge vortices with the convected leading edge vortex that produces the interesting 'dual-branch' wake pattern. The upper branch is formed by the clockwise leading edge vortex merging with the stronger clockwise trailing-edge vortex (just visible in left column). This merged vortex forms a dipole with the weak counter-clockwise vortex from the trailing edge. This dipole convects downstream above the trailing-edge (clearly seen in right column). Meanwhile, the lower branch is formed by the stronger counter-clockwise trailing-edge vortex creating a dipole with the weak clockwise trailing edge vortex. This second dipole convects downstream below the trailing edge. The resultant dual-branch wake bears a strong resemblance to the neutral wakes of Lai and Platzer [55] that are created during the transition from drag to thrust. Indeed the corresponding time-averaged flowfield (Fig. 3.4e) shows a negligible time-averaged jet further downstream, and the time-averaged drag coefficient has a negative gradient leading to the drag to thrust transition at $Sr_c = 2.5$, in agreement with this description.

At $Sr_c = 2.5$ (Fig. 3.9d) the flowfield has changed significantly. The leading-edge vortex again forms during the downward motion but remains close to the leading-edge for a greater portion of the cycle and therefore impinges with the airfoil during the upward motion and loses its coherency. It remains nearer the leading-edge due to the reduced wavelength of the vortices. This can be seen in the reduced vortex spacing with increasing Strouhal number shown in the right hand column of Fig. 3.9.

The reduced wavelength is due to a combination of the decreasing period with increasing Strouhal number and the vortex convection velocity remaining approximately constant (~$0.75U_\infty$). There is one strong clockwise and one counter-clockwise trailing-edge vortex formed per cycle. As there is no interference from a convected LEV, the two TEVs combine to create a vortex dipole. The resultant reverse-Kármán vortex street is responsible for the strong time-averaged 'jet' observed in Fig. 3.9f, and the previously noted drag to thrust switch.

At $Sr_c = 3.0$ (Fig. 3.9e) this effect is further enhanced. In this case the leading-edge vortex is formed during the downward motion and loses its coherency entirely during the upward motion so that there is no discernible convected leading-edge vortex. As a result one observes a strong reverse-Kármán vortex street with peak phase-averaged velocities of six times the freestream.

Fig. 3.10 shows eight phase averaged vorticity contour plots throughout the cycle for the same case ($a/c = 0.050$, $Sr_c = 3.0$) as in Figures 3.4g and 3.9e. It demonstrates that the LEV is formed late in the downward motion (Figures 3.10d and e) so that it is strongest at the bottom of the motion (Fig. 3.10e). During the upward motion the LEV appears to be sucked around the leading edge of the airfoil in a similar manner to the mode-1 of Lu et al. [51]. As the distance between the LEV and the airfoil is small, the details of the interaction during the upward motion are difficult to resolve. This interaction is therefore discussed for a larger amplitude later.

As would be expected the downward motion of the trailing edge creates the counter-clockwise TEV whereas the upward motion creates the slightly smaller, weaker, clockwise TEV. These two vortices become paired and convect downstream along a path approximately parallel to the chordline of the airfoil. Figure 3.11 shows that these TEVs induce large velocities, the maximum being over six times the freestream (contour scale limited to four). In addition, Fig. 3.11 demonstrates that the large region of separation witnessed for a stationary NACA0012 (Fig. 3.3a) is eradicated for almost the entire oscillation cycle. The only region of separation observed is at the maximum displacement (Fig. 3.11a) and relatively small, from x/c

= 0.7 to the trailing edge. This low velocity region coincides with the region of formation of a clockwise TEV.

During the downward motion (Figures 3.11b to 3.11e) the streamlines curve around the forming LEV and downwards into the airfoil. The streamlines therefore imply the flow is into the airfoil however it is important to note that the airfoil is in motion. Likewise during the upward motion (Figures 3.11f to 3.11a) the streamlines curve upwards out of the airfoil. The formation of an LEV is noticeable in all phases except a. Given the strong LEV, lack of separation, and strong reverse von Kármán vortex street, one would anticipate significant improvements in both lift and drag performance.

To investigate the details of the aforementioned interaction of the LEV with the airfoil, PIV measurements were performed for a larger amplitude (a/c = 0.10) over both upper and lower surfaces for Sr_c = 1.75. In Fig. 3.12, the upper surface demonstrates the same behaviour as for the previous cases; an LEV forms during the downward motion (Figures 3.12a to 3.12e), and is not convected despite being a reasonable distance from the airfoil (Fig. 3.12e), but instead appears to be sucked around the leading edge (Figures 3.12g to 3.12h). The lower surface measurements show however that this is not the case. Indeed the only negative vorticity observed over the lower surface is that created at the stagnation point during the formation of the LEV (Fig. 3.12c). It is therefore concluded that the LEV is not sucked around the leading edge but destroyed through impingement with the upward moving airfoil.

Hereafter this form of wake (no convected leading-edge vortex) will be termed a mode-2 flow field; mode-1 refers to a leading-edge vortex which is shed and convected over the upper surface of the airfoil as in Fig. 3.9c. Intermediate flow fields i.e. those with a weak convected LEV as in Fig. 3.9d, will be termed mixed. Based on these definitions one can compare the occurrence of the different flow fields for a wide variety of amplitudes thereby producing Fig. 3.13. The shaded area represents the boundary between the two mode types derived from phase-averaged measurements of the flow field (see Appendix 2), mixed flowfields therefore lie within this band. This demonstrates that the switch from mode-1 to mode-2 depends

upon both amplitude and frequency. The trend of decreasing Strouhal number with increasing amplitude suggests a constant plunge velocity or angle of attack as being responsible. Superimposed onto Fig. 3.13 are therefore lines of constant maximum effective angle of attack. These lines can also be considered lines of constant normalized plunge velocity ($Sr_A = fA/U_\infty = f2a/U_\infty$), as:

$$\alpha_{eff,\max} = \alpha + \tan^{-1}\frac{U_{pl}}{U_\infty} = \alpha + \tan^{-1}\frac{2\pi fa}{U_\infty} = \alpha + \tan^{-1}\pi Sr_A \qquad \textbf{(3.1)}$$

Since the mode-switch band occurs in the approximate range of $\alpha_{eff,max} = 48°$ to $\alpha_{eff,max} = 68°$, or alternatively $Sr_A = 0.20$ to $Sr_A = 0.43$, one can conclude that the mode-switch does not bear a strong correlation with either constant effective angle of attack or constant Strouhal number based on amplitude. So in a similar manner to the observations of Young and Lai [64] for drag, neutral and thrust wakes, wake structure regions do not follow lines of constant Strouhal number based on amplitude.

The drag-to-thrust switch locations are also shown in Figure 3.13. These points are for the four amplitudes where zero drag was observed. It is clear that a mode-2 flowfield is beneficial to thrust production. It is suggested that the mode-2 flowfield may facilitate thrust production through a stronger reverse-Kármán vortex street created by a combination of greater shedding of vorticity at the trailing-edge and no destructive interference from the convected leading-edge vortex. This effect is emphasized in Fig. 3.14, where the time-averaged drag coefficient is plotted as a contour plot with the mode-switch boundary superimposed. The agreement between the mode boundary and the shape of the drag contours is excellent, thus demonstrating that even though neither flow field nor force measurements depend on a constant plunge velocity, they do depend on each other.

In a similar manner the effect of the mode-switch boundary on lift coefficient is shown in Fig. 3.15. A modified time-averaged lift coefficient is used because as Strouhal number or amplitude are increased, the plunge velocity is also increased. Therefore, from an active flow control point of view, excitation level is not constant.

In order to take this into account, a modified lift coefficient based on the vector sum of the freestream velocity and maximum plunge velocity is used:

$$\hat{C}_l = \frac{L}{\frac{1}{2}\rho(U_\infty^2 + U_{pl}^2)c} \tag{3.2}$$

Fig. 3.15 demonstrates two interesting features. Firstly there is a substantial fall in lift at higher Strouhal numbers which roughly follows the mode-switch boundary. This fall in lift can result in values of modified lift coefficient even smaller than that for a stationary airfoil. Hence, even though the mode-2 flowfield is beneficial to thrust production it inhibits lift production, this will be returned to later. The second interesting feature is the three regions of optimal excitation condition which appear to be amplitude independent, see $Sr_c \approx 0.5$, 1.0, and 2.0. It is interesting that the three regions are located on a constant plunge velocity of $U_{pl}/U_\infty = 0.5$ shown with a dashed line in Fig. 3.15. The optimum plunge velocity is therefore approximately half the freestream velocity. These two features, the peaks in lift coefficient and fall in lift coefficient are dealt with in the following subsections.

3.1.3 Peaks

Wu et al. [137] demonstrate the effectiveness of the vortex lock-in phenomenon in flow control, when the excitation frequency is equal to the natural frequency of vortex shedding in the wake and its first harmonic. They also report that subharmonic resonance with vortex shedding led to the largest lift increase in their numerical simulations. In an experimental study, Miranda et al. [138] also confirmed the effectiveness of excitation at the subharmonic and fundamental frequency of the wake natural shedding frequency for an airfoil with a sharp leading-edge. To investigate if this was the cause of the peaks observed here, the natural shedding frequency was measured by means of a hot-film placed in multiple locations in the wake of the airfoil. The signal was recorded and the frequency spectra were calculated for various locations. A typical example is shown in Fig. 3.16, the inset shows an instantaneous flow field measured by PIV and the location of the hot-film probe. Measurements repeated at different locations suggest that the average of the dominant peaks is at $Sr_c = 0.89$ for a streamwise station one chord length

downstream of the trailing-edge. The dominant frequency corresponds to a Strouhal number based on frontal distance $Sr_d = fc \sin\alpha / U_\infty = 0.23$, which agrees well with the previous results (in the range $Sr_d = 0.16$-0.22) for flat plates and airfoils [123, 132, 135, 138]. Hence, the peak in lift at $Sr_c \approx 1.0$ in Fig. 3.15 could correspond to the natural vortex shedding frequency in the wake. The peak at $Sr_c \approx 0.5$ would therefore be the subharmonic, and the peak at $Sr_c \approx 2.0$ the first harmonic of the natural shedding frequency.

The suitability of using the natural shedding frequency for a stationary airfoil to describe the behaviour for an oscillating airfoil is however questionable due to the changing flowfield with increasing oscillation frequency, see Fig. 3.17. Through oscillation, a time-averaged momentum deficit at $Sr_c = 0$, becomes a time-averaged momentum surplus at $Sr_c = 1$. A second method of validation is therefore required. One would expect that oscillation at the natural shedding frequency, its harmonics or subharmonics, will result in the wake becoming more ordered and synchronized in a similar manner to vortex lock-in of oscillating cylinders [139], resulting in an increase of spanwise correlation of the flow. Cross-correlation measurements were therefore performed in the wake of the oscillating airfoil, see Fig. 3.18. The measurement position in the x-y plane is marked in the inset and the hot-film probes were separated by a distance of 1.3c about the mid-span in the spanwise plane. Fig. 3.18 shows the variation of the correlation coefficient as a function of Strouhal number for $a/c = 0.025$, and $\alpha = 15°$. It is seen that there are strong peaks at $Sr_c \approx 0.45$ and $Sr_c \approx 1$, in close agreement with the lift coefficient measurements, and a weaker peak around $Sr_c \approx 2$. Hence we conclude that the peaks in the lift are due to the resonance with the fundamental, subharmonic and first harmonic of the natural vortex shedding in the wake.

3.1.4 Fall in Lift Coefficient

To demonstrate the cause of the fall in lift coefficient a single amplitude, $a/c = 0.15$, is considered in detail. The lift and drag coefficient for this amplitude are shown in Fig. 3.19. Superimposed onto Fig. 3.19 are lines demarcating Strouhal number regions, phase-averaged flowfields associated with each of these regions are shown

in Fig. 3.20 through to Fig. 3.23. These phase-averaged flowfields show normalized vorticity at the top (left column) and bottom (right column) of the motion.

Fig. 3.19 demonstrates significant lift enhancement with increasing Strouhal number until a sudden fall in lift at higher Strouhal numbers. Before the fall in lift occurs two peaks in the time-averaged lift are observed as described in Chapter 3.1.3. These peaks are reflected in the time-averaged drag coefficient. In addition the drag coefficient demonstrates the well documented [12, 56, 64] switch from drag to thrust at $Sr_c \sim 1.15$.

Fig. 3.20a is for a Strouhal number of $Sr_c = 0.125$. This Strouhal number is associated with a significant increase in lift coefficient when compared to the stationary value, but still relatively small when compared to higher Strouhal numbers. The flow field exhibits an oscillating shear layer of negative vorticity emanating from the leading edge, and one of positive vorticity emanating from the trailing edge. With the frequency increased to $Sr_c = 0.250$, the oscillating shear layer rolls up into multiple coherent vortices. The animations show these multiple vortices amalgamating so that at mid-way through the downstroke only two remain (not shown here). The passing of these two vortices over the trailing edge initiates the formation of two trailing edge vortices (TEVs) of opposite sign; the first of which is shown in Fig 3.20b at the bottom of the motion and the second is shown at the top of the motion.

With increasing Strouhal number the size and strength of the leading-edge and trailing-edge vortices continue to increase as demonstrated for $Sr_c = 0.375$ and $Sr_c = 0.500$ by Fig 3.20c and d. This is reflected in the continued increase in C_l which levels out at $Sr_c = 0.500$ creating a local maximum.

The continued rise in C_l beyond $Sr_c = 0.625$ is associated with the increasing strength of the LEV as demonstrated in Fig. 3.21, and quantified through the circulation calculations shown in Fig. 3.24. Figure 3.24a and 3.24b show the circulation of the upper surface LEV from its inception at the leading-edge until it reaches the trailing-edge. For the lower Strouhal numbers shown in Figure 3.24a, the growth of the LEV

is apparent in the range t/T = 0.125 to 0.375. One contributory factor to the increasing lift across this Strouhal number range is the increasing strength of the LEV. This is apparent through the increasing peak circulation at t/T = 0.375 with increasing Strouhal number. A second contributory factor is the increasing 'lifespan' of the vortex (the time taken for the vortex to pass beyond the trailing-edge or to be dissipated), which varies from a minimum of $\Delta t/T = 0.750$ at $Sr_c = 0.500$ to a maximum of $\Delta t/T = 1.500$ at $Sr_c = 1.125$. The maximum of $\Delta t/T = 1.500$ means that for half of every cycle, two vortices exist over the upper surface; one forming at the leading edge, and a second nearing the trailing edge from the previous cycle. Fig. 3.21 demonstrates the same effect through the position of the LEV over the upper surface, i.e., in Fig. 3.21a (left) the LEV is approximately at 1c, Fig. 3.21b it is at ~0.8c, Fig. 3.21c it is at ~0.6c, and Fig 3.21d it is at ~0.5c. The position of the LEV therefore implies a nearly constant vortex convection time scale, which is substantiated through detailed vortex tracking calculations. As a result of the increased lifespan, each LEV would contribute towards lift for a greater proportion of the cycle.

This trend of increasing LEV circulation and further upstream LEV position with increasing Strouhal number continues until $Sr_c = 1.250$ where there is a marked change, see Fig. 3.22b. The LEV now remains over the upstream portion of the airfoil for the entire cycle. Consequently it is destroyed through impingement with the upward moving airfoil in the same manner as previously described for a mode-2 flow field. Fig. 3.24b demonstrates this effect through the rapid decrease in circulation to near-zero values at time t/T = 0.875 for $Sr_c \leq 1.750$. Furthermore with increasing Strouhal number the onset of the vortex dissipation becomes earlier in the cycle so that for $Sr_c > 1.750$ the near-zero circulation values commence at t/T = 0.750.

At the trailing-edge there is also a marked change in the flow structure, see Fig. 3.23. With increasing Strouhal number the TEVs remain closer to the trailing-edge. Consequently their proximity satisfies the vortex-dipole formation criteria described by Godoy-Diana et al. [70]. The two vortices therefore form a dipole pair which convects away from the airfoil at an angle to the horizontal, thereby forming a

deflected wake [12, 67, 69, 70]; this can be seen in the left column of Fig. 3.23 and the animations for $Sr_c \geq 1.250$ (not shown here). Due to the direction of the deflected wake, it draws fluid from the lower surface of the airfoil thereby accelerating the fluid over the lower surface and aiding in the formation of a lower surface LEV. Similar flowfields, deflected jets resulting in very large negative or positive lift coefficients, will be shown in chapter 4.

As demonstrated in the circulation values shown in Fig. 3.25 and Fig. 3.26 the strength of this lower surface LEV grows substantially with increasing Strouhal number. Fig. 3.25 shows that the lower surface LEV begins to form at the bottom of the motion, t/T = 0.500, growing in strength during the upward motion before reaching a maximum at t/T = 0.875, and then being dissipated in a similar manner to the upper surface LEV through impingement with the airfoil. The peak circulation shown in Figure 3.26 demonstrates the strength of the lower surface LEV increases significantly with Strouhal number so that the rate of increase exceeds that of the upper surface LEV. In addition, the lifespan of the upper surface LEV is decreasing within this range. Consequently when the effects of increasing lower surface LEV circulation and the dissipation of the upper surface LEV are combined, the result is a pronounced and sudden fall in time-averaged lift coefficient. Indeed at $Sr_c = 1.75$ (shown in Fig. 8) the strength of the lower surface LEV has grown to such an extent that it negates the time-averaged lift enhancement entirely, returning the lift coefficient to a value approximately equal to the stationary one.

As previously discussed the mode-2 flow field does however have a beneficial effect on the drag and thrust characteristics as shown in Fig. 3.19b. Until $Sr_c \sim 1$, any change in drag coefficient is relatively small, but for $Sr_c > 1$ the coefficient of drag decreases substantially, turning negative at $Sr_c \sim 1.2$, and then becoming thrust producing. $Sr_c \sim 1.2$ coincides with the beginning of the mode-2 wake.

3.2 CONCLUSIONS

Force, hot film and particle image velocimetry measurements have been performed for a NACA 0012 oscillating with small-amplitude at a geometric angle of attack of

fifteen degrees. These measurements showed that significant lift enhancement and drag reduction were achievable.

For a given Strouhal number the drag reduction was shown to be consistently greater for greater amplitude, but without dependence on normalized plunge velocity. For larger amplitudes a switch to negative drag (thrust) was therefore observed. This switch was shown to closely rely on a flowfield that was classified as mode-2. Mode-1 refers to a flowfield where an upper surface leading-edge vortex formed during the downward motion is shed and convected over the upper surface. Mode-2 refers to a flowfield where the upper surface leading-edge vortex again forms during the downward motion but is dissipated through impingement with the upward moving airfoil. Once the mode-2 flowfield forms, greater shedding of vorticity occurs at the trailing-edge, associated with a strong downwards deflected jet. The mode-2 flowfield is beneficial to thrust production through two means: a stronger reverse-Kármán vortex street resulting from greater shedding of vorticity at the trailing-edge combined with no destructive interference from a convected leading-edge vortex, and the diminished drag enhancing effect of a convected leading edge vortex on the upper surface.

The lift enhancement is also shown to be amplitude dependent but loosely dependent on normalized plunge velocity until the occurrence of a fall in lift. The greatest recorded increase was 305% over the value for a stationary airfoil. For lower Strouhal numbers the lift enhancement was shown to be associated with growing strength and longevity of the upper surface leading-edge vortex. Within this range several peaks in the force measurements were observed which were shown to be amplitude and Reynolds number independent. Hot film measurements showed these peaks to be due to oscillation at the natural shedding frequency, its harmonics and subhamonics. The fall in lift at higher plunge velocity was shown to be due to a combination of the onset of the mode-2 flowfield and the sudden growth of a lower surface leading-edge vortex. The mode-2 flowfield is significant because it results in reduced longevity of the upper surface leading-edge vortex diminishing its positive lift enhancing effect. The lower surface leading-edge vortex is significant because it

counters the effect of the upper surface vortex resulting in lift coefficients approximately equal to that of the stationary airfoil.

3.3 FIGURES

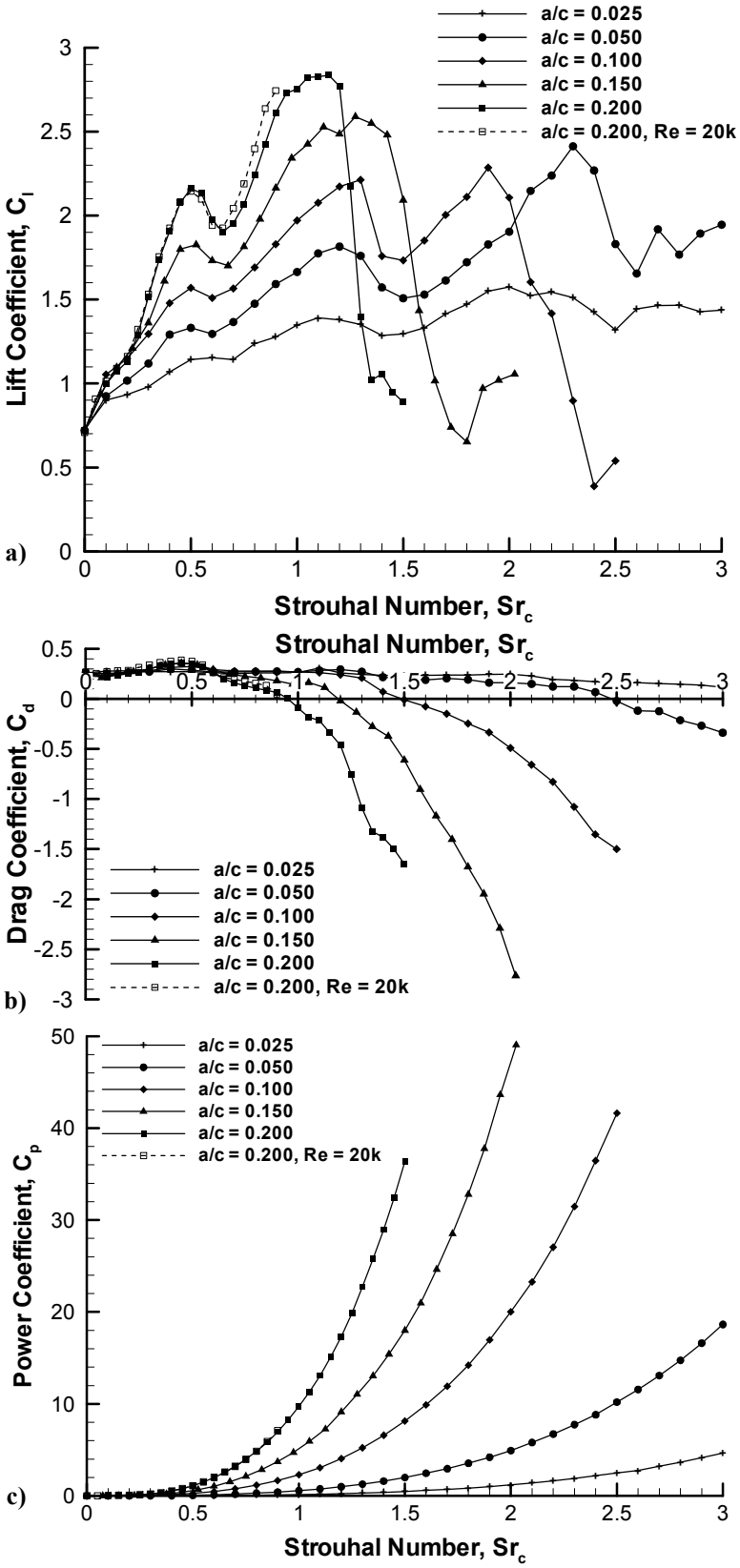

Fig. 3.1 Time-averaged a) lift, b) drag, and c) power coefficient for α = 15°, Re = 10, 000 and different amplitudes versus Strouhal number based on chord.

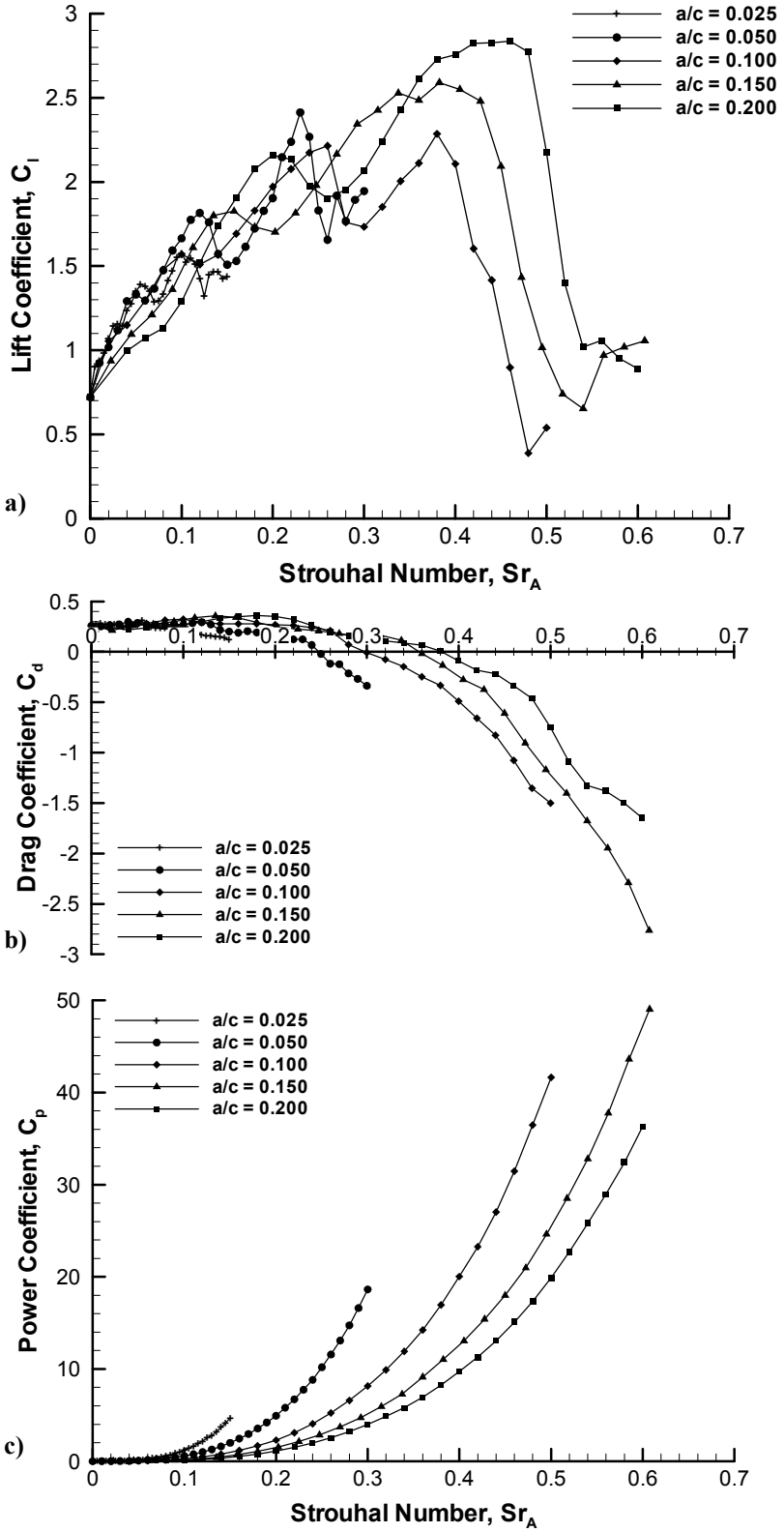

Fig. 3.2 Time-averaged a) lift, b) drag, and c) power coefficient for α = 15°, Re = 10, 000 and different amplitudes versus Strouhal number based on amplitude.

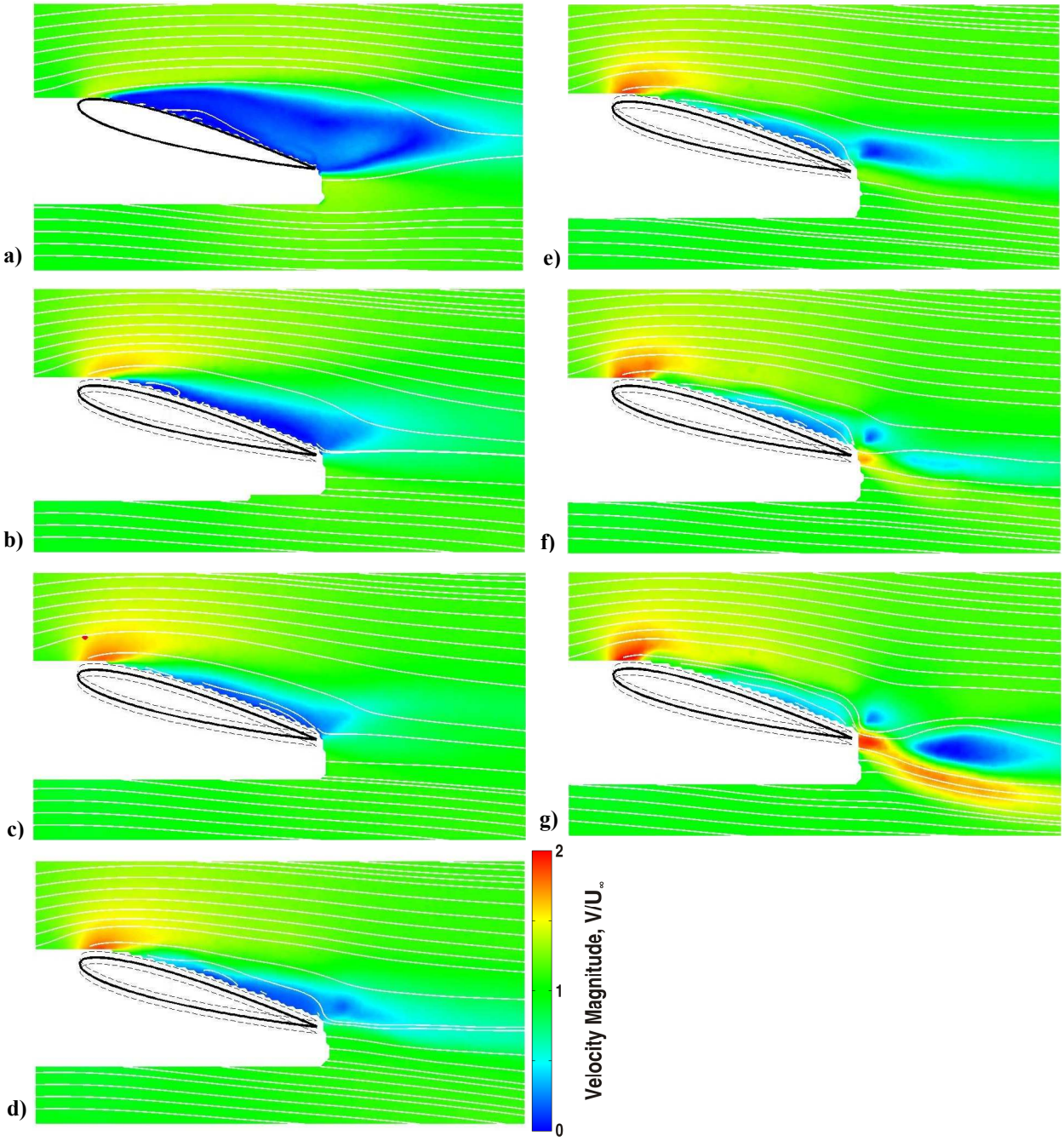

Fig. 3.3 Magnitude of time-averaged velocity for a/c = 0.025: a) stationary; b) $Sr_c = 0.5$; c) $Sr_c = 1.0$; d) $Sr_c = 1.5$; e) $Sr_c = 2.0$; f) $Sr_c = 2.5$ and g) $Sr_c = 3.0$.

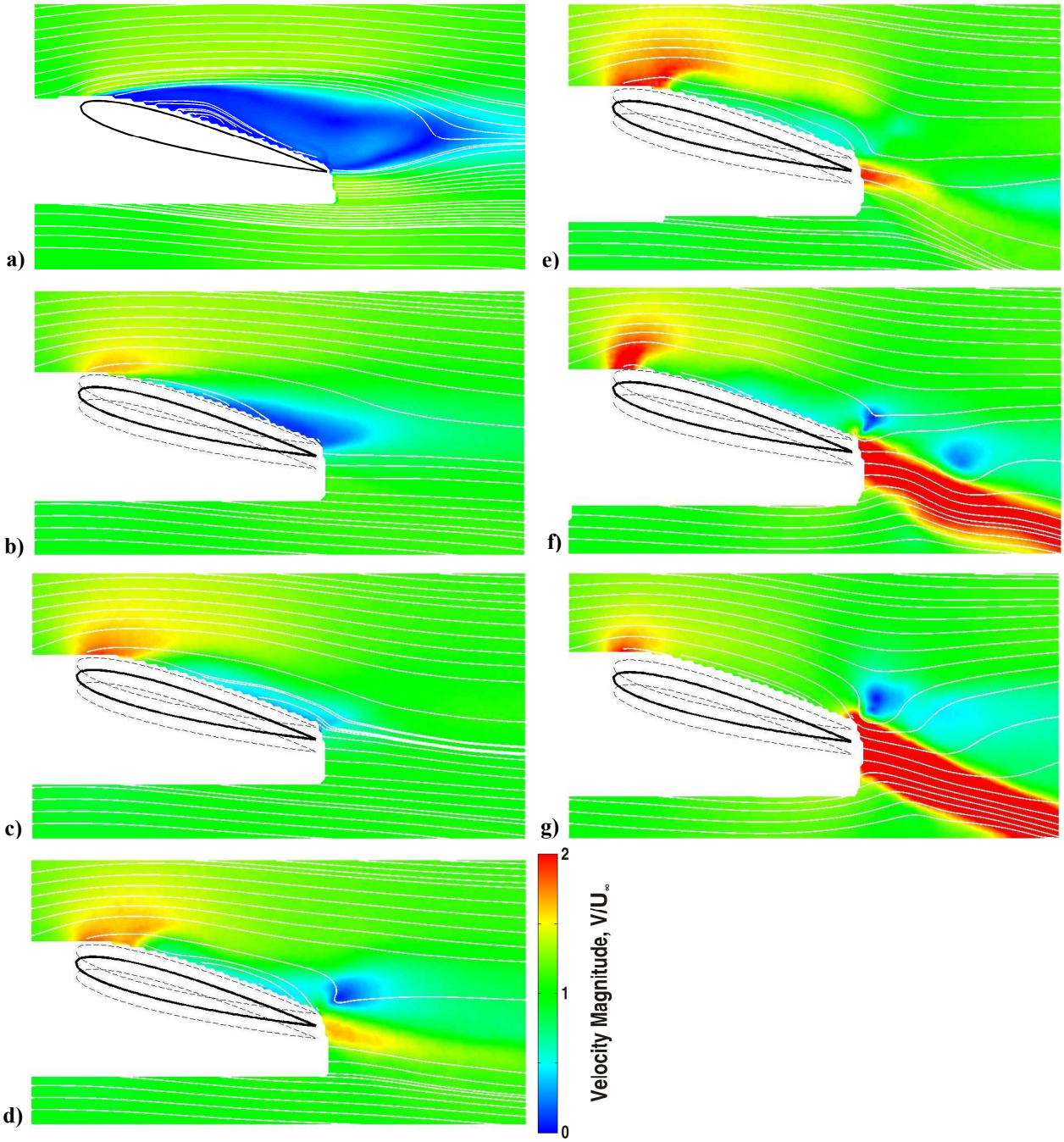

Fig. 3.4 Magnitude of time-averaged velocity for a/c = 0.050: a) stationary; b) $Sr_c = 0.5$; c) $Sr_c = 1.0$; d) $Sr_c = 1.5$; e) $Sr_c = 2.0$; f) $Sr_c = 2.5$ and g) $Sr_c = 3.0$.

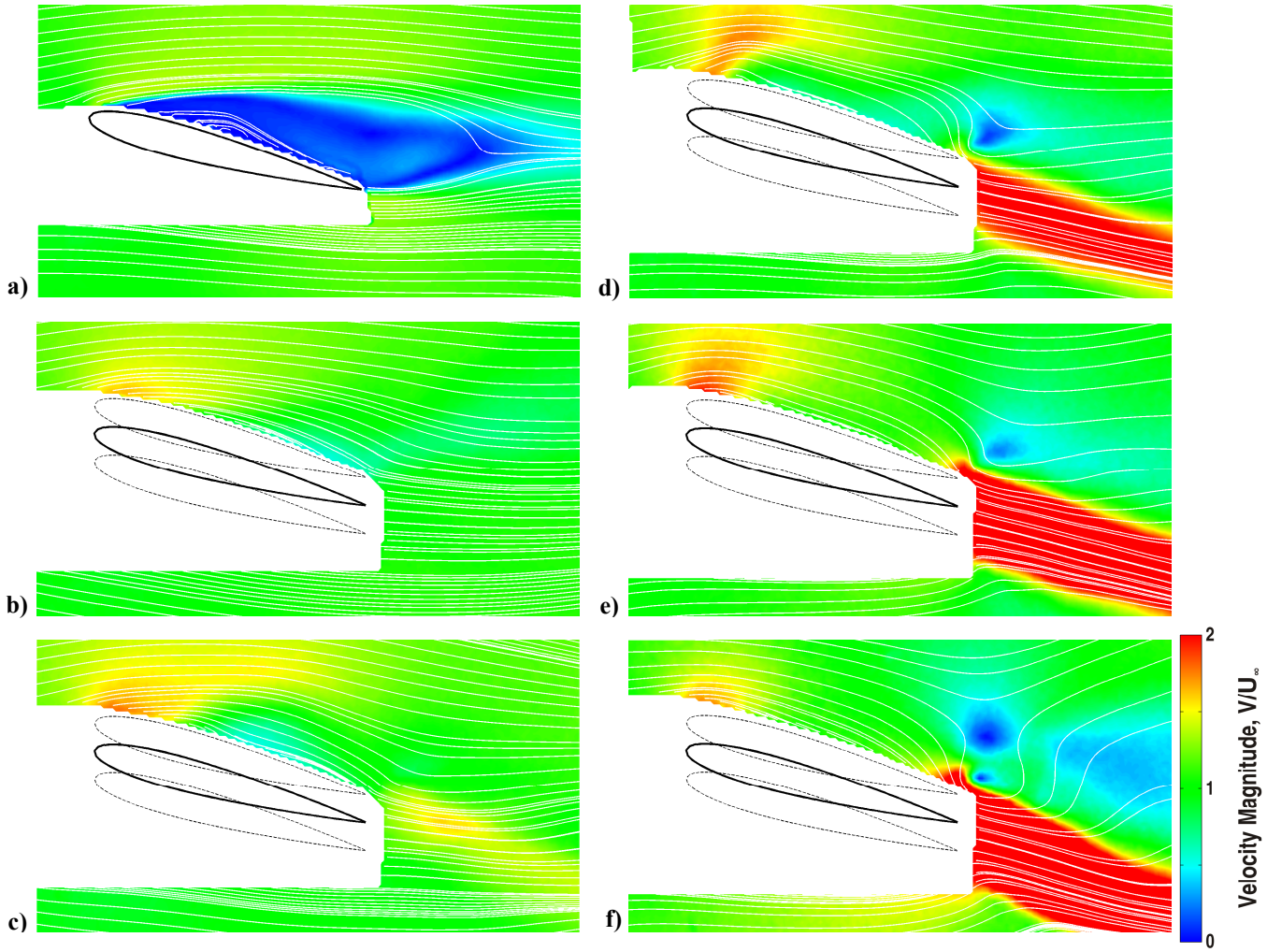

Fig. 3.5 Magnitude of time-averaged velocity for a/c = 0.100: a) stationary; b) $Sr_c = 0.5$; c) $Sr_c = 1.0$; d) $Sr_c = 1.5$; e) $Sr_c = 2.0$; and f) $Sr_c = 2.5$.

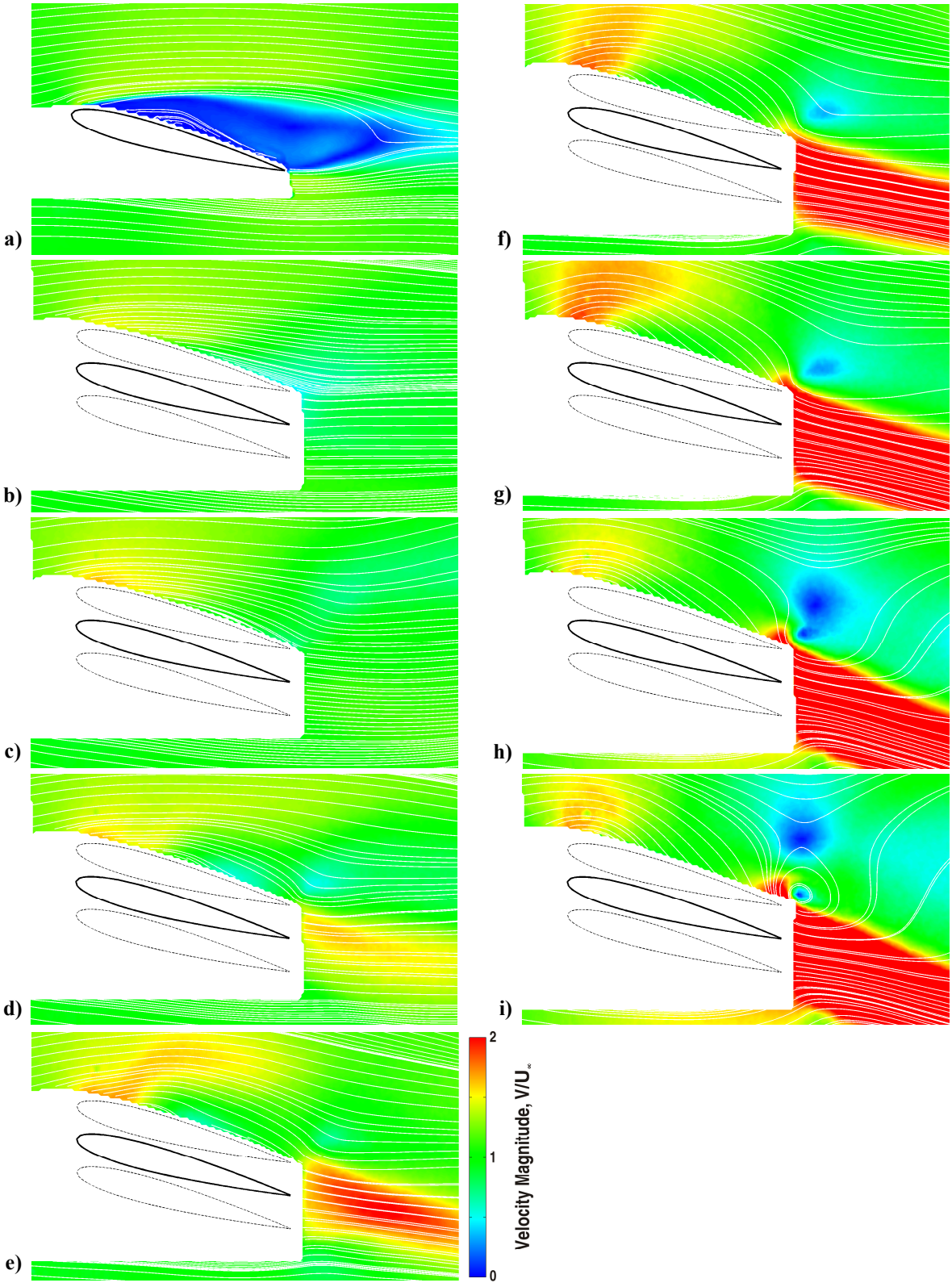

Fig. 3.6 Magnitude of time-averaged velocity for a/c = 0.150: a) stationary; b) $Sr_c = 0.25$; c) $Sr_c = 0.50$; d) $Sr_c = 075$; e) $Sr_c = 1.00$; f) $Sr_c = 1.25$; g) $Sr_c = 1.50$; h) $Sr_c = 1.75$; and i) $Sr_c = 2.00$.

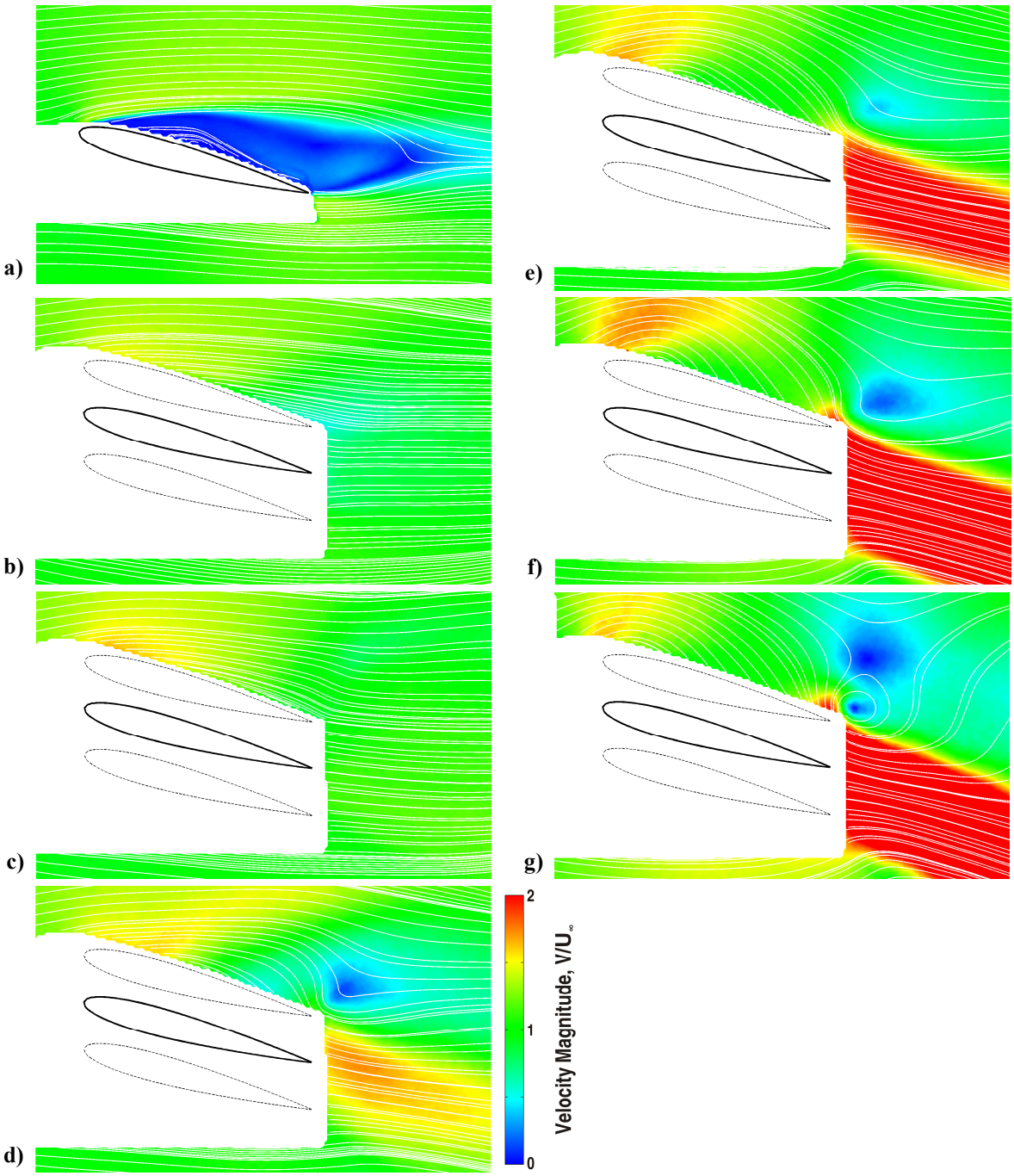

Fig. 3.7 Magnitude of time-averaged velocity for a/c = 0.200: a) stationary; b) $Sr_c = 0.25$; c) $Sr_c = 0.50$; d) $Sr_c = 075$; e) $Sr_c = 1.00$; f) $Sr_c = 1.25$; and g) $Sr_c = 1.50$.

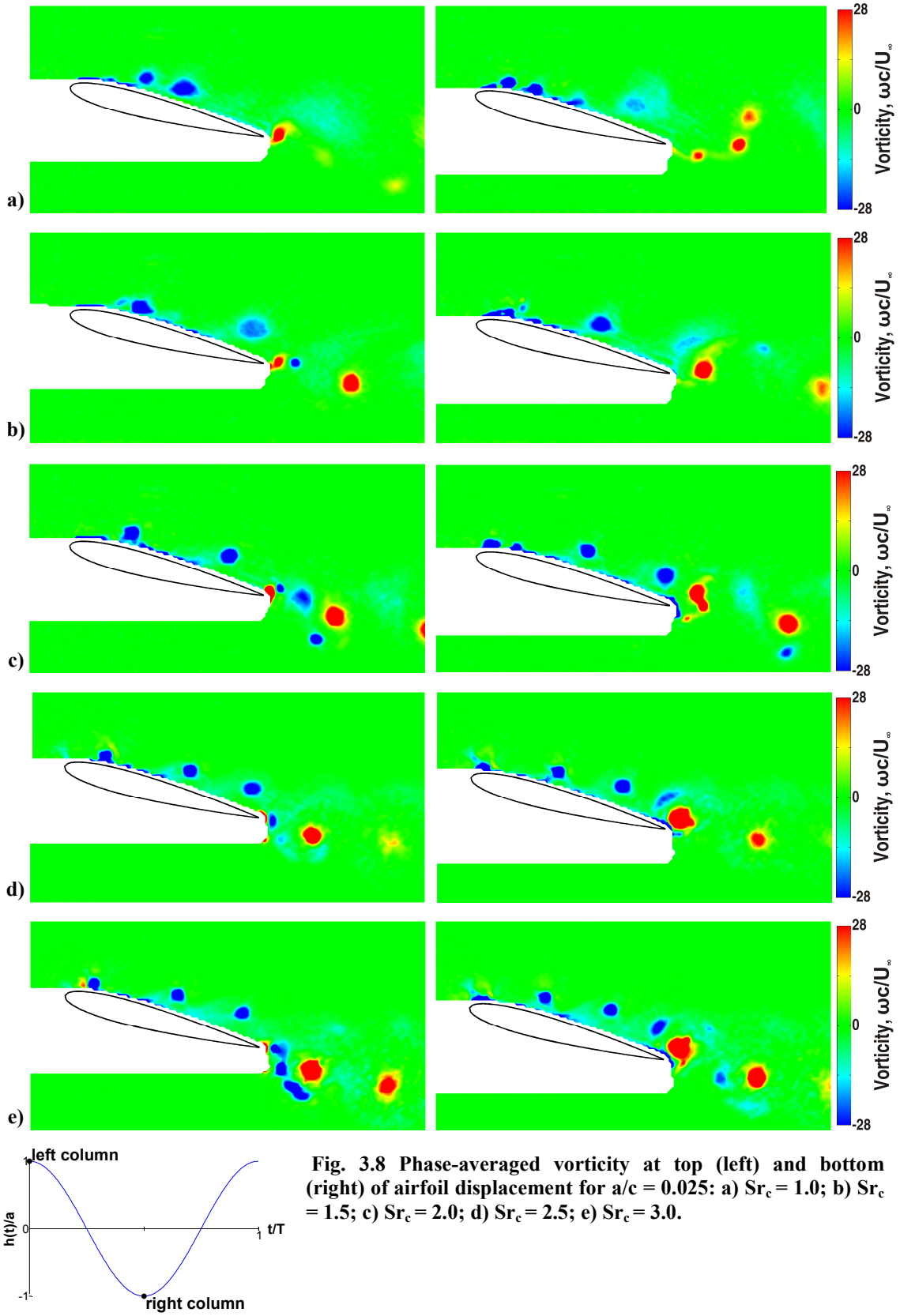

Fig. 3.8 Phase-averaged vorticity at top (left) and bottom (right) of airfoil displacement for a/c = 0.025: a) $Sr_c = 1.0$; b) $Sr_c = 1.5$; c) $Sr_c = 2.0$; d) $Sr_c = 2.5$; e) $Sr_c = 3.0$.

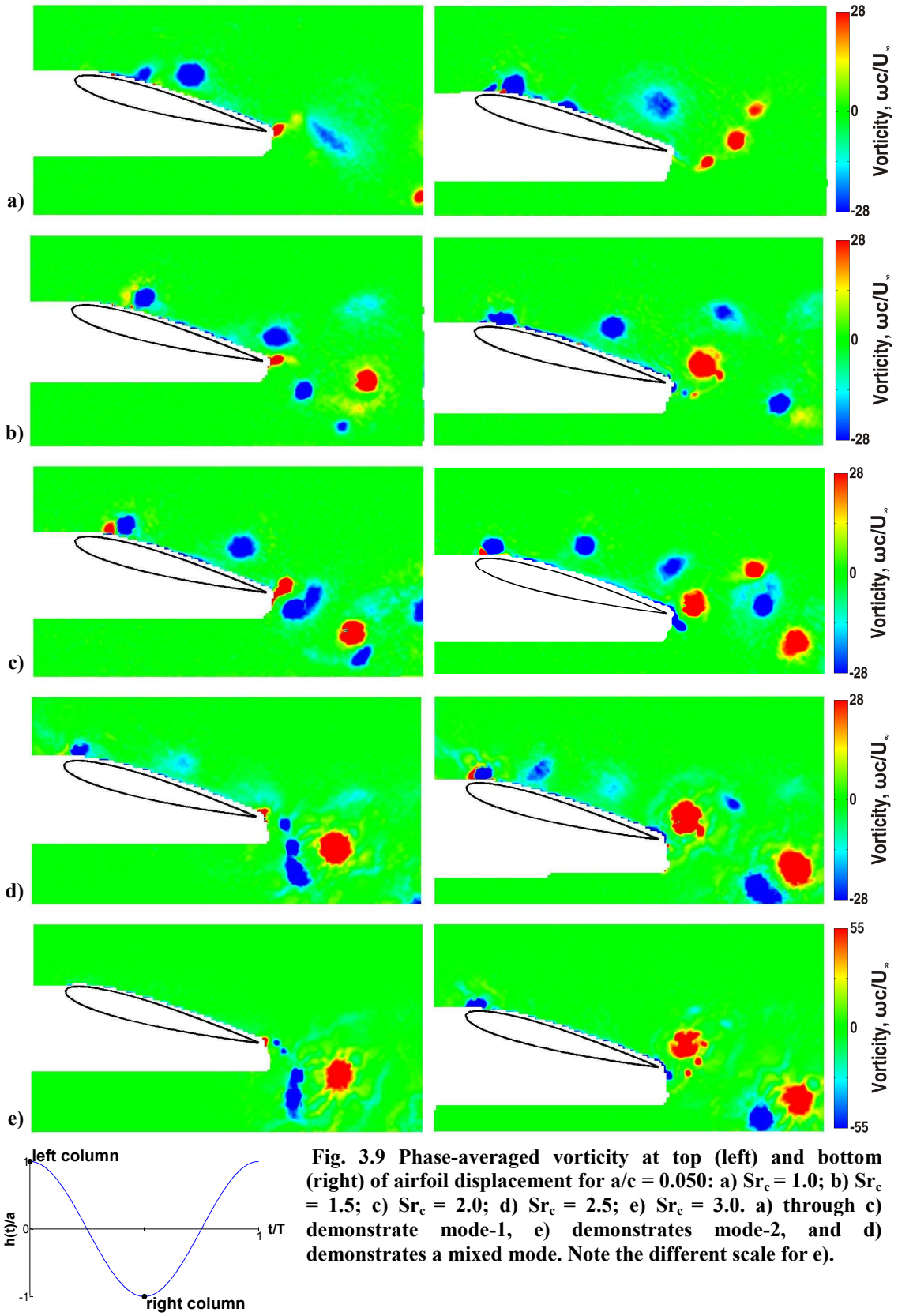

Fig. 3.9 Phase-averaged vorticity at top (left) and bottom (right) of airfoil displacement for a/c = 0.050: a) Sr_c = 1.0; b) Sr_c = 1.5; c) Sr_c = 2.0; d) Sr_c = 2.5; e) Sr_c = 3.0. a) through c) demonstrate mode-1, e) demonstrates mode-2, and d) demonstrates a mixed mode. Note the different scale for e).

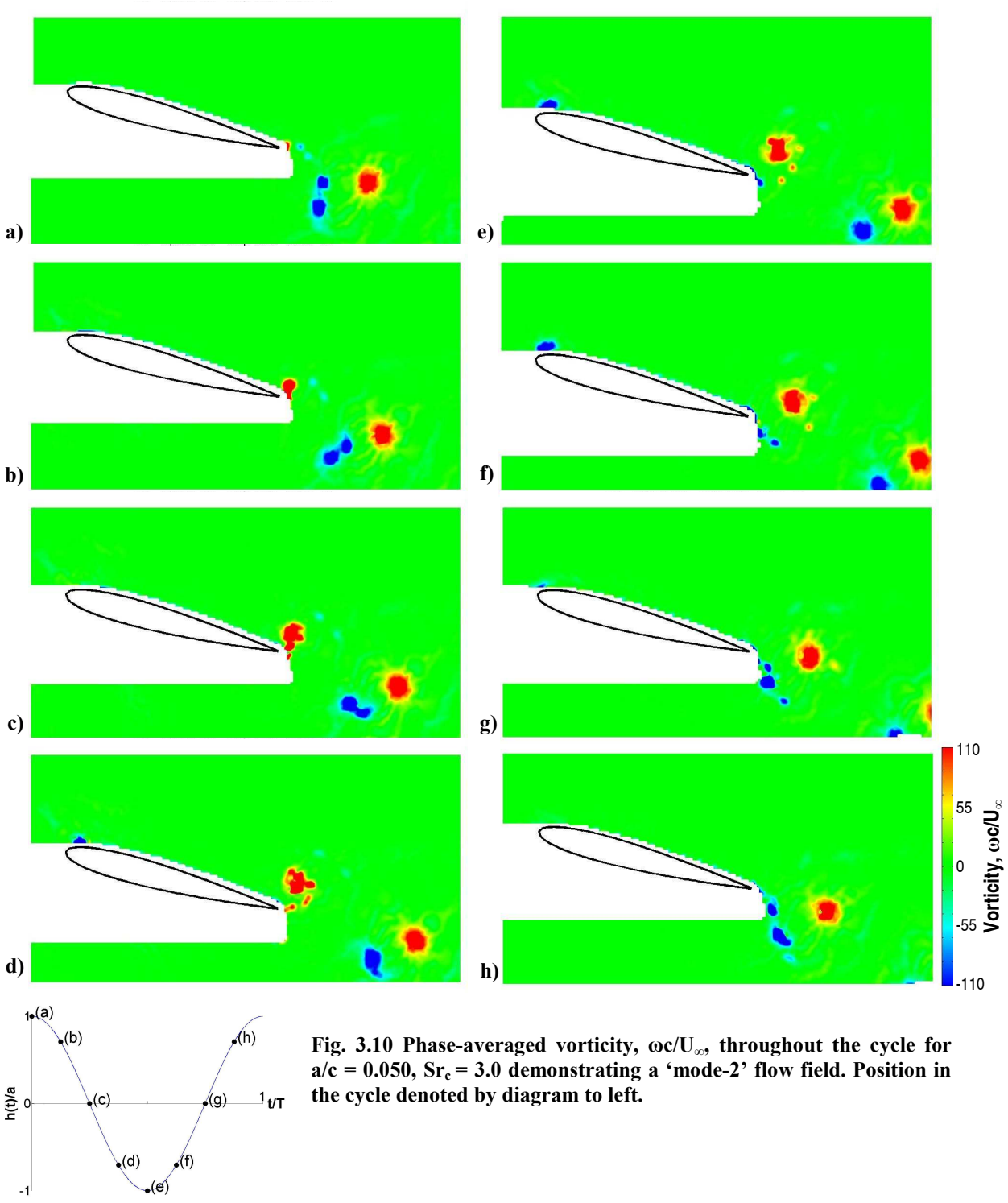

Fig. 3.10 Phase-averaged vorticity, $\omega c/U_\infty$, throughout the cycle for a/c = 0.050, $Sr_c = 3.0$ demonstrating a 'mode-2' flow field. Position in the cycle denoted by diagram to left.

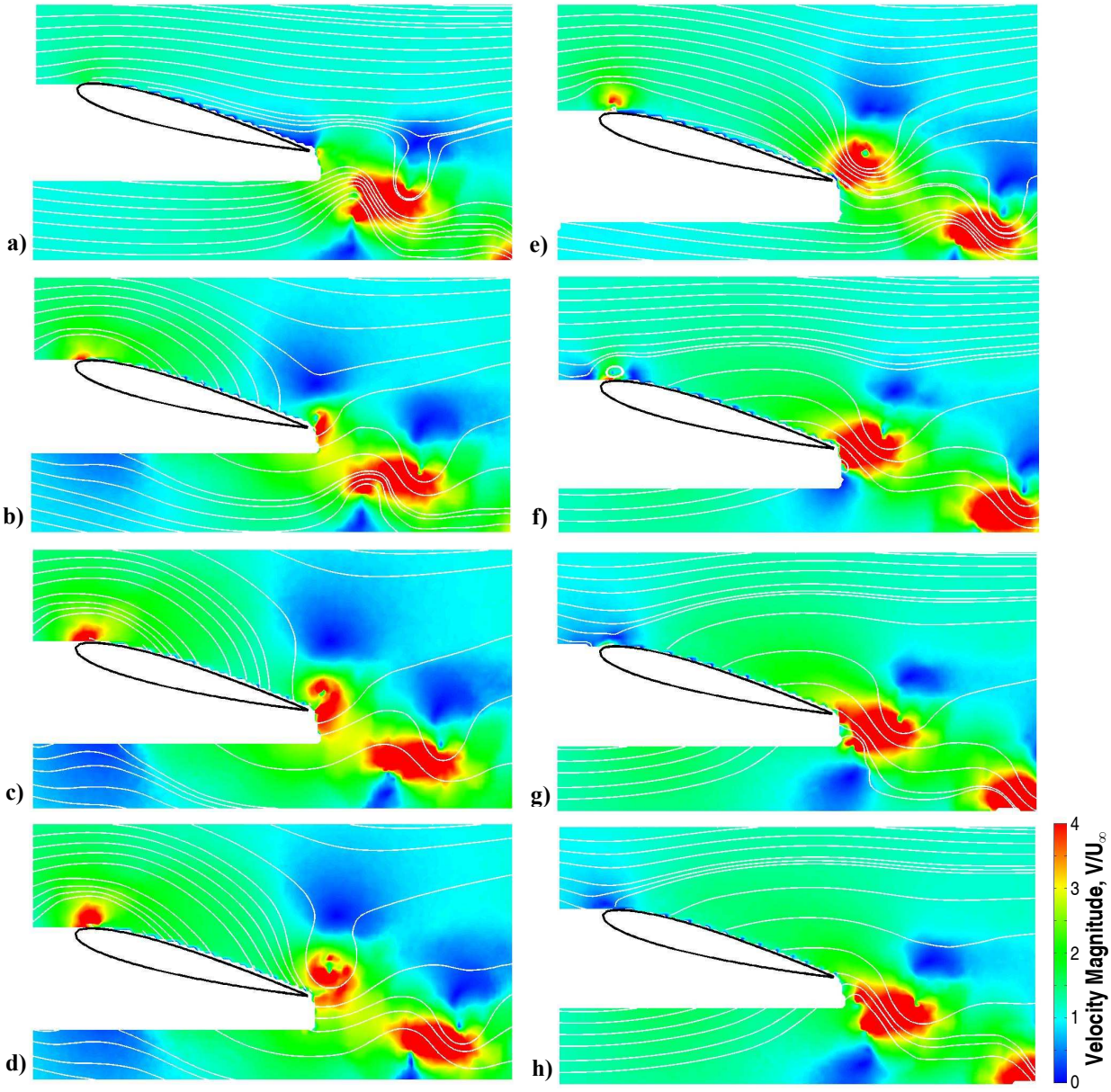

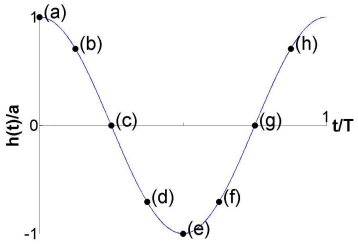

Fig. 3.11 Magnitude of phase-averaged velocity throughout the cycle for a/c = 0.050 and Sr_c = 3.0, demonstrating a 'mode-2' flow field. Position in the cycle denoted by diagram to left.

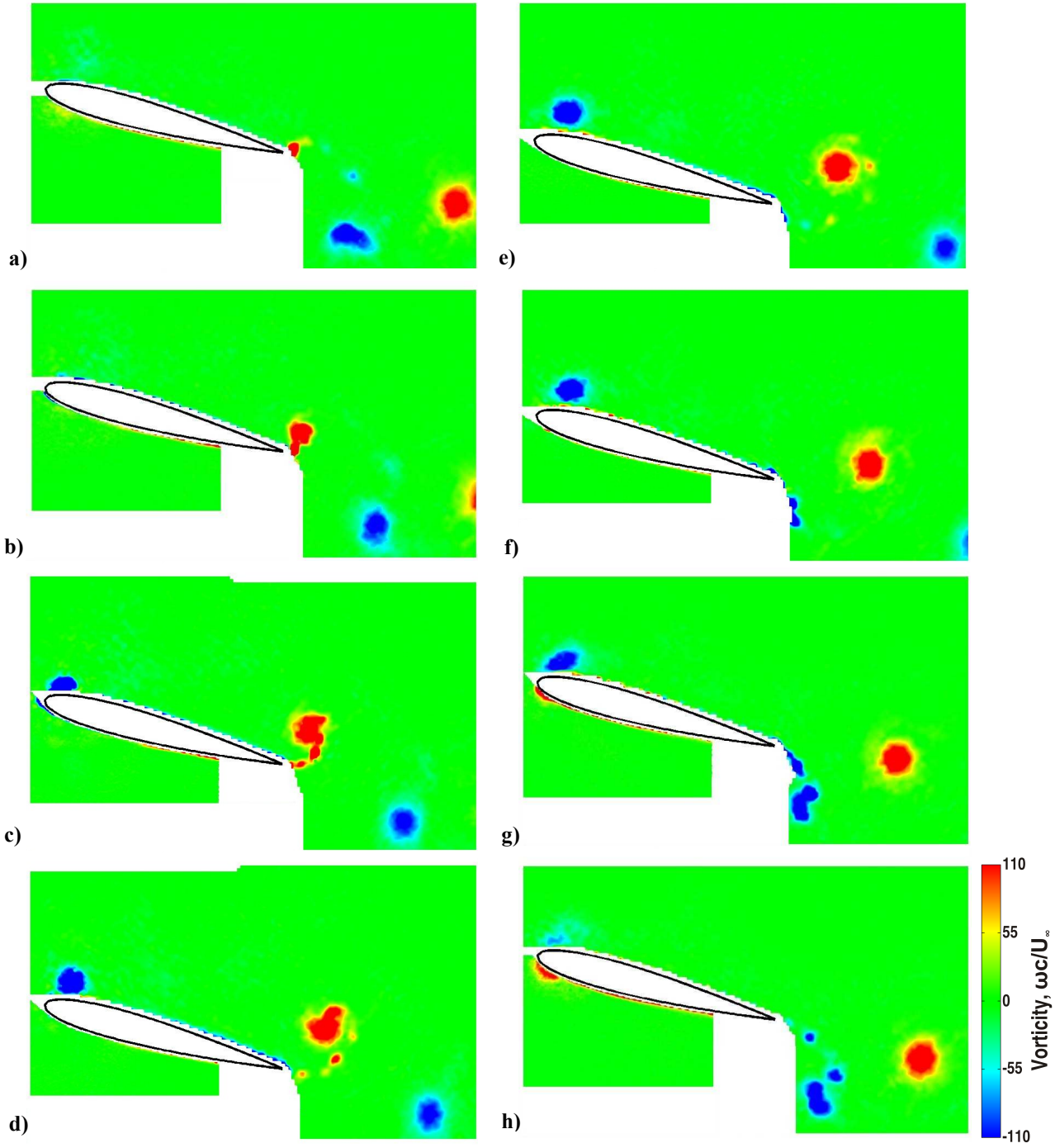

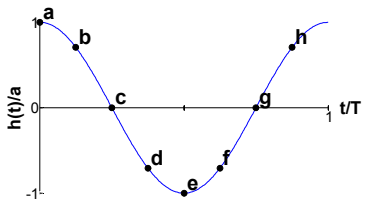

Fig. 3.12 Phase-averaged vorticity for both the upper and lower surface of a mode-2 flow field: a/c = 0.10 and Sr_c = 1.75. Position in the cycle denoted by diagram to left.

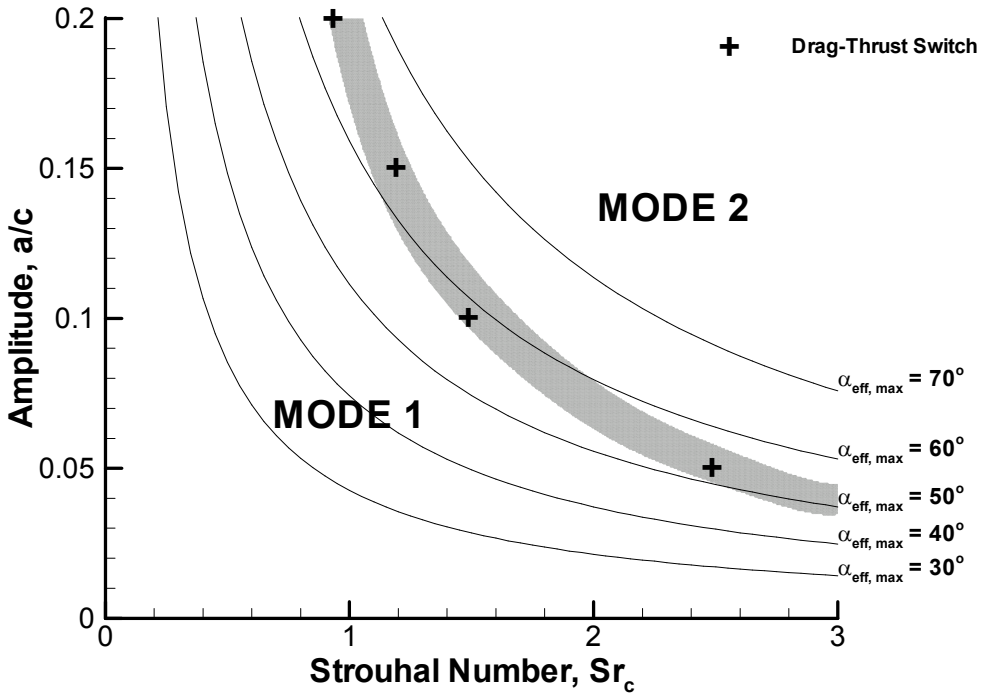

Fig. 3.13 Mode diagram derived from phase-averaged flow fields. The mode-switch boundary is represented by the shaded area.

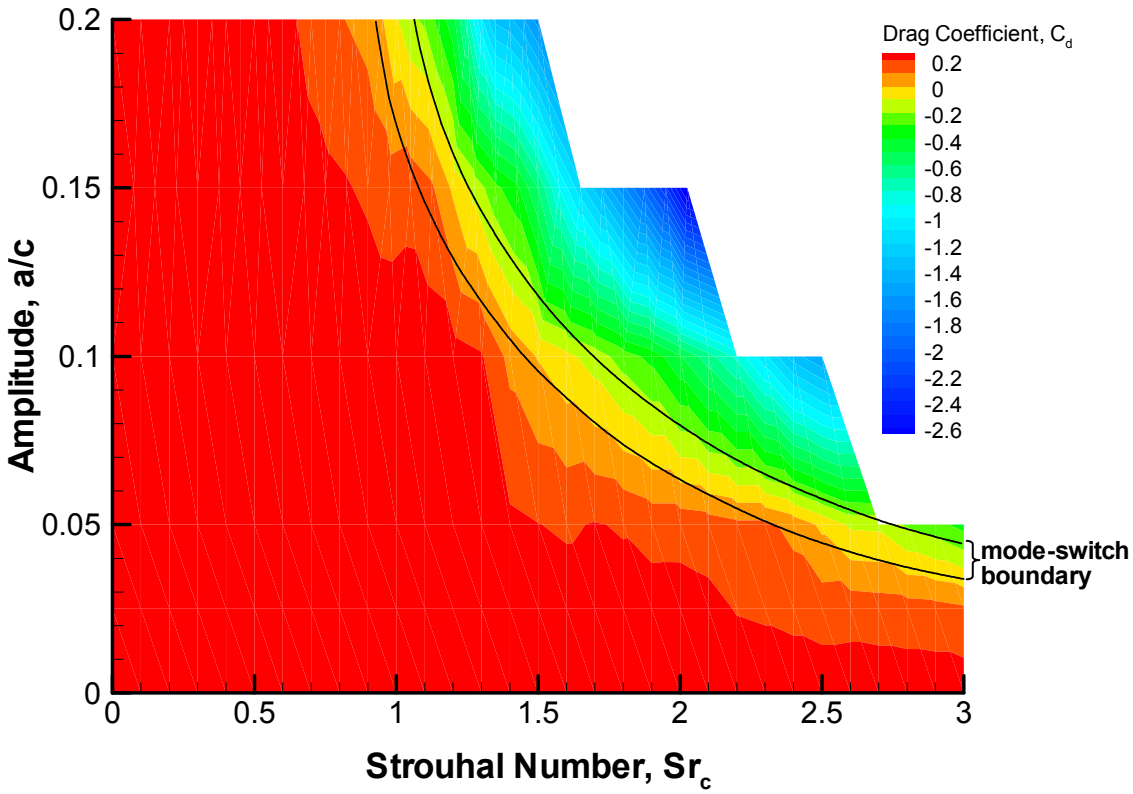

Fig. 3.14 Contour plot of drag coefficient. Mode-switch boundary from Fig. 3.13.

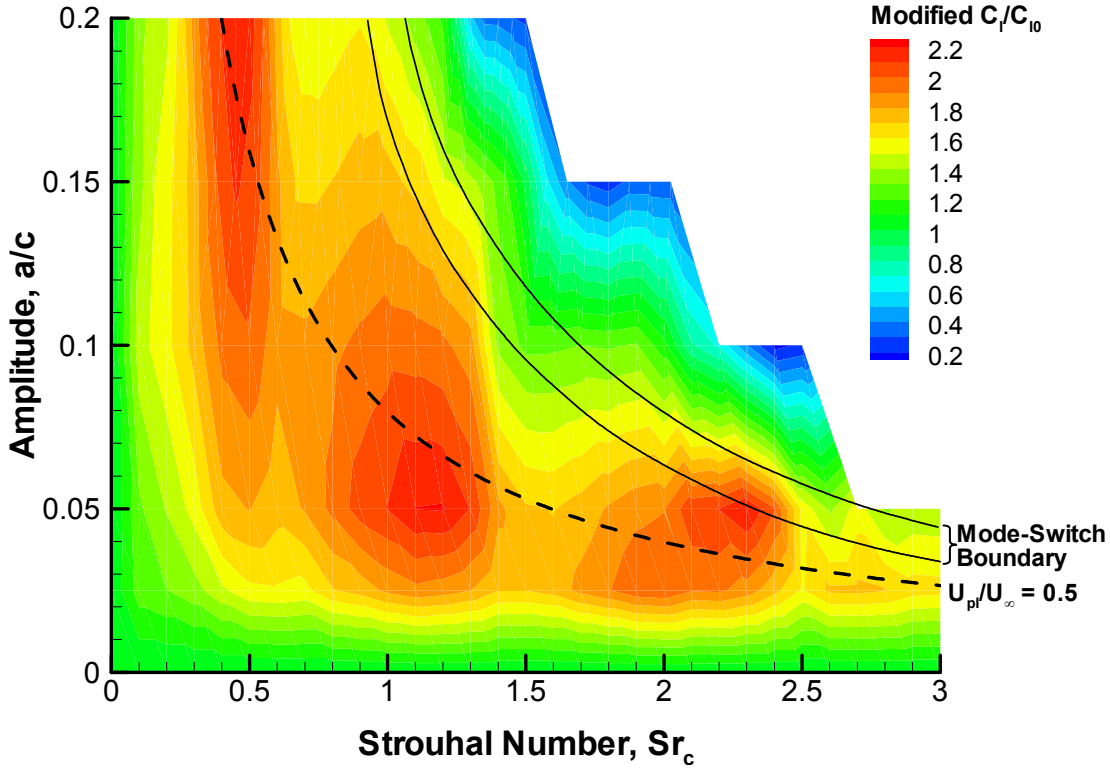

Fig. 3.15 Contour plot of modified lift coefficient normalized by the value for a stationary airfoil. Dashed lines represent the mode-switch boundary from Fig. 3.13. Solid line represents a constant normalized plunge velocity.

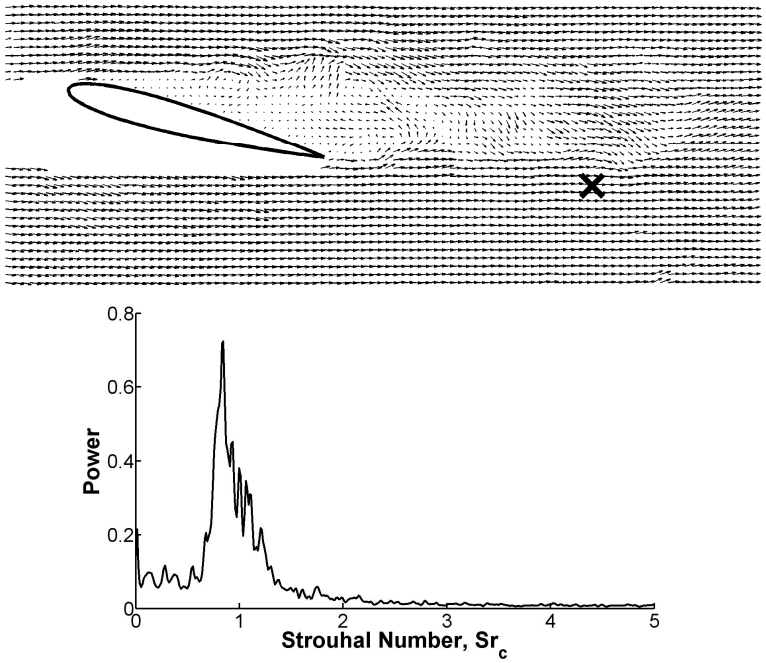

Fig. 3.16 Typical frequency spectra for a hot-film placed in the wake of the stationary airfoil. The position of the hot-film in the x-y plane is shown in the vector arrow plot above, in the z-plane it was positioned in the mid-span.

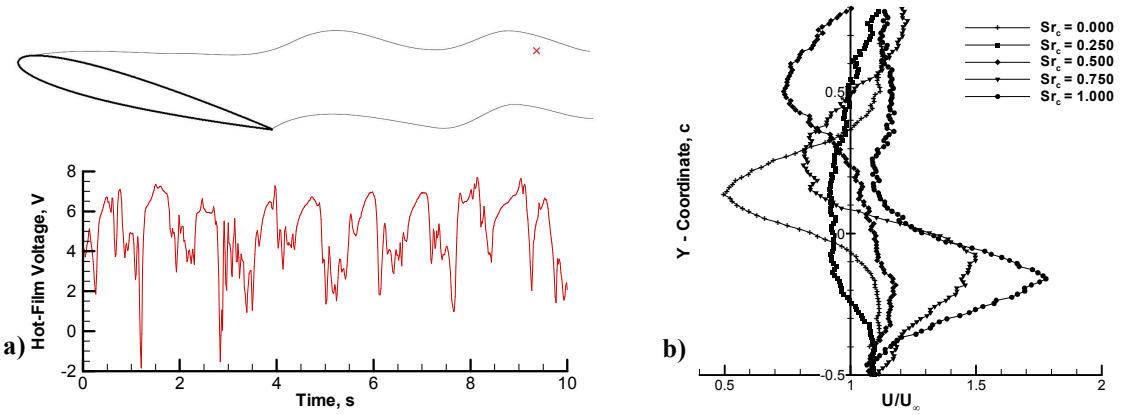

Fig. 3.17 a) Hot-film signal in the wake of the stationary airfoil; cross denotes the location of measurement, b) time-averaged streamwise velocity measured through PIV 0.75c downstream of the trailing edge, Y-coordinate is relative to the trailing edge.

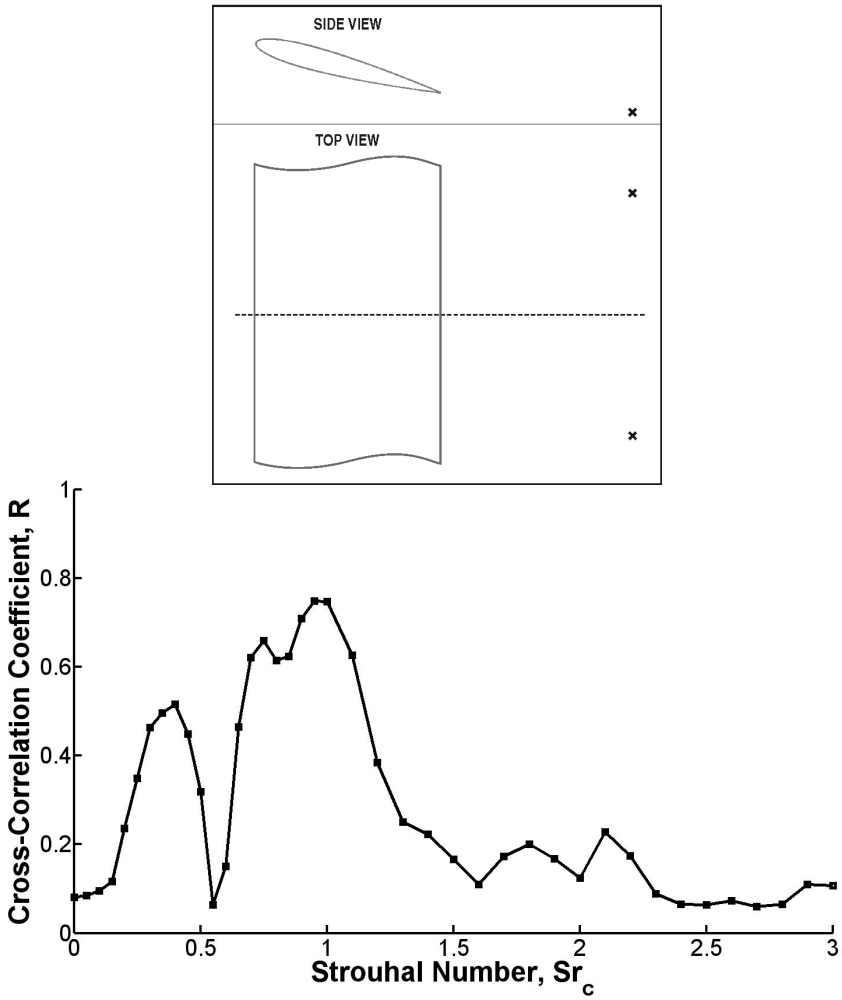

Fig. 3.18 Cross-correlation measurements in the wake of the plunging airfoil for a/c = 0.025. The hot films were positioned in the x-y plane as shown above and separated in the z-plane symmetrically about the mid-span by 1.3c.

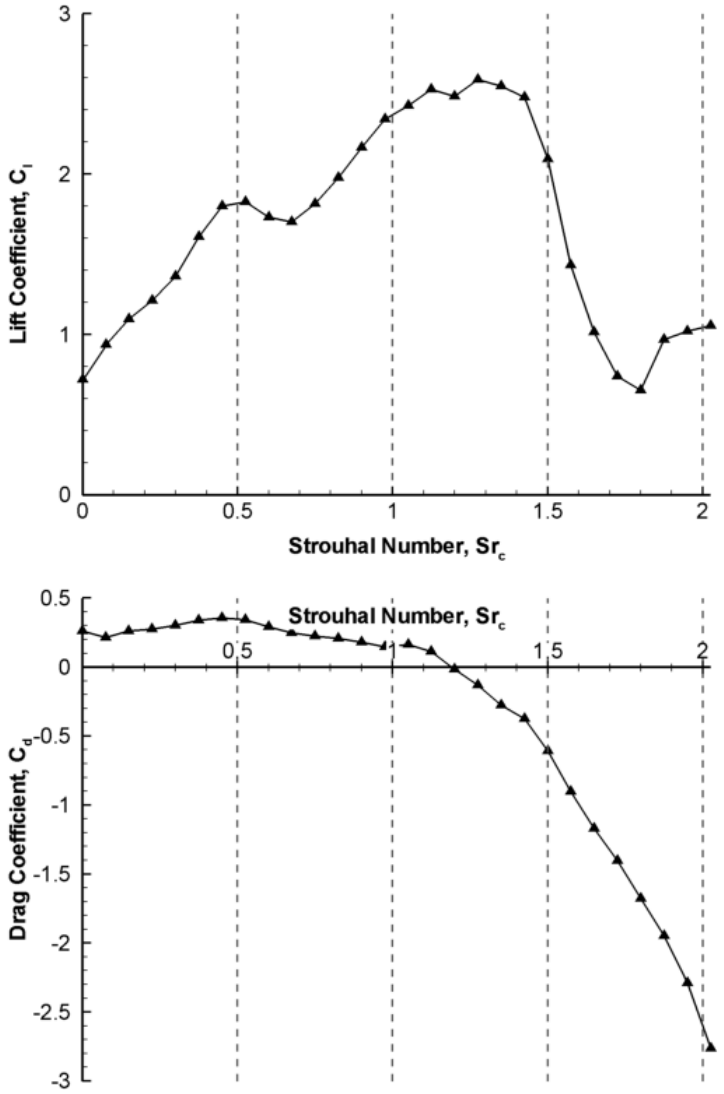

Fig. 3.19 Lift and drag coefficient for a/c = 0.15, α = 15°, and Re = 10,000. Grey dashed lines demark the limits of the regions shown in Figures 3.20 to 3.23.

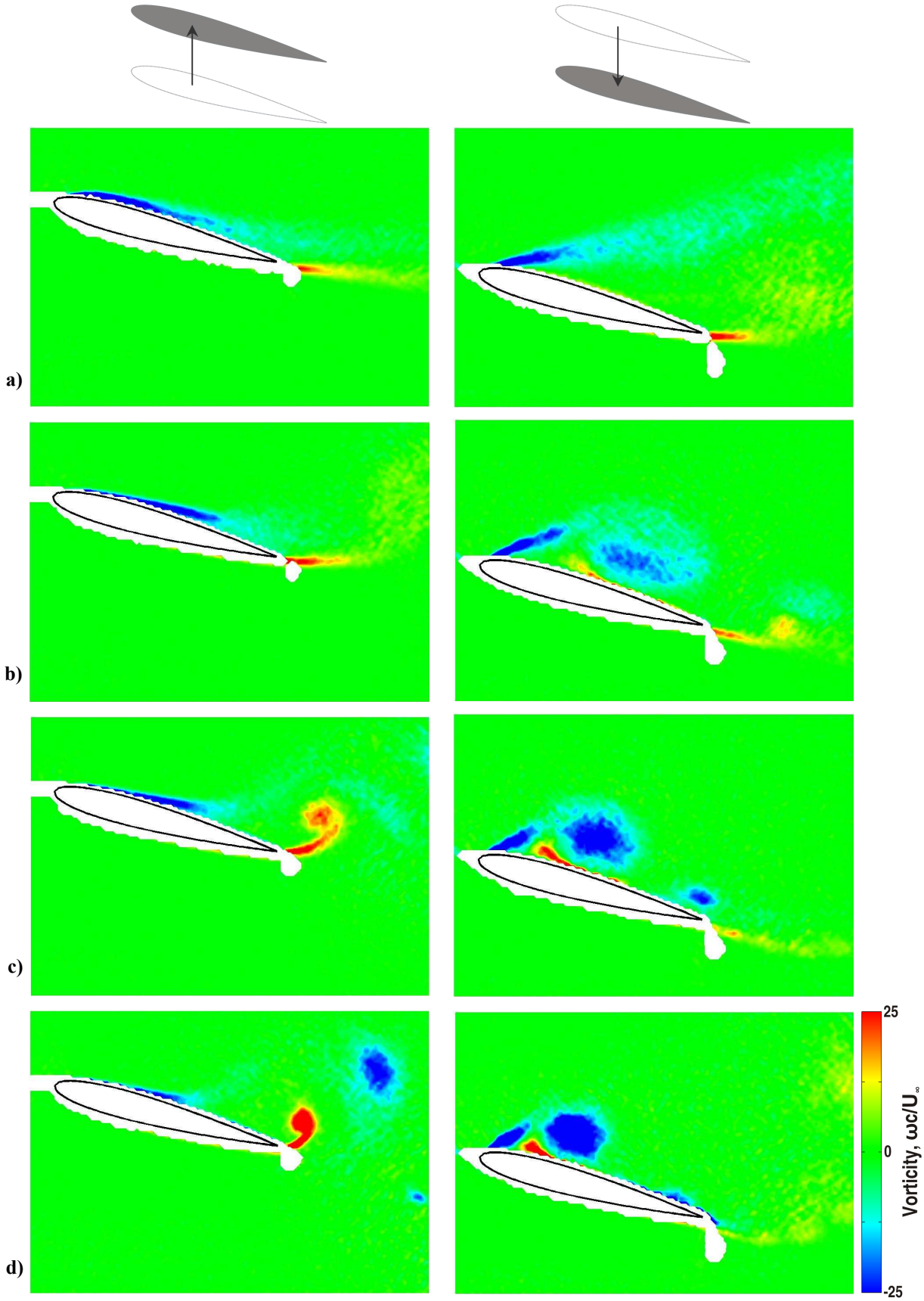

Fig. 3.20 Normalized vorticity at maximum (left) and minimum (right) of motion with a/c = 0.15, α = 15°, Re = 10,000, for: a) Sr_c = 0.125, b) Sr_c = 0.250, c) Sr_c = 0.375, d) Sr_c = 0.500.

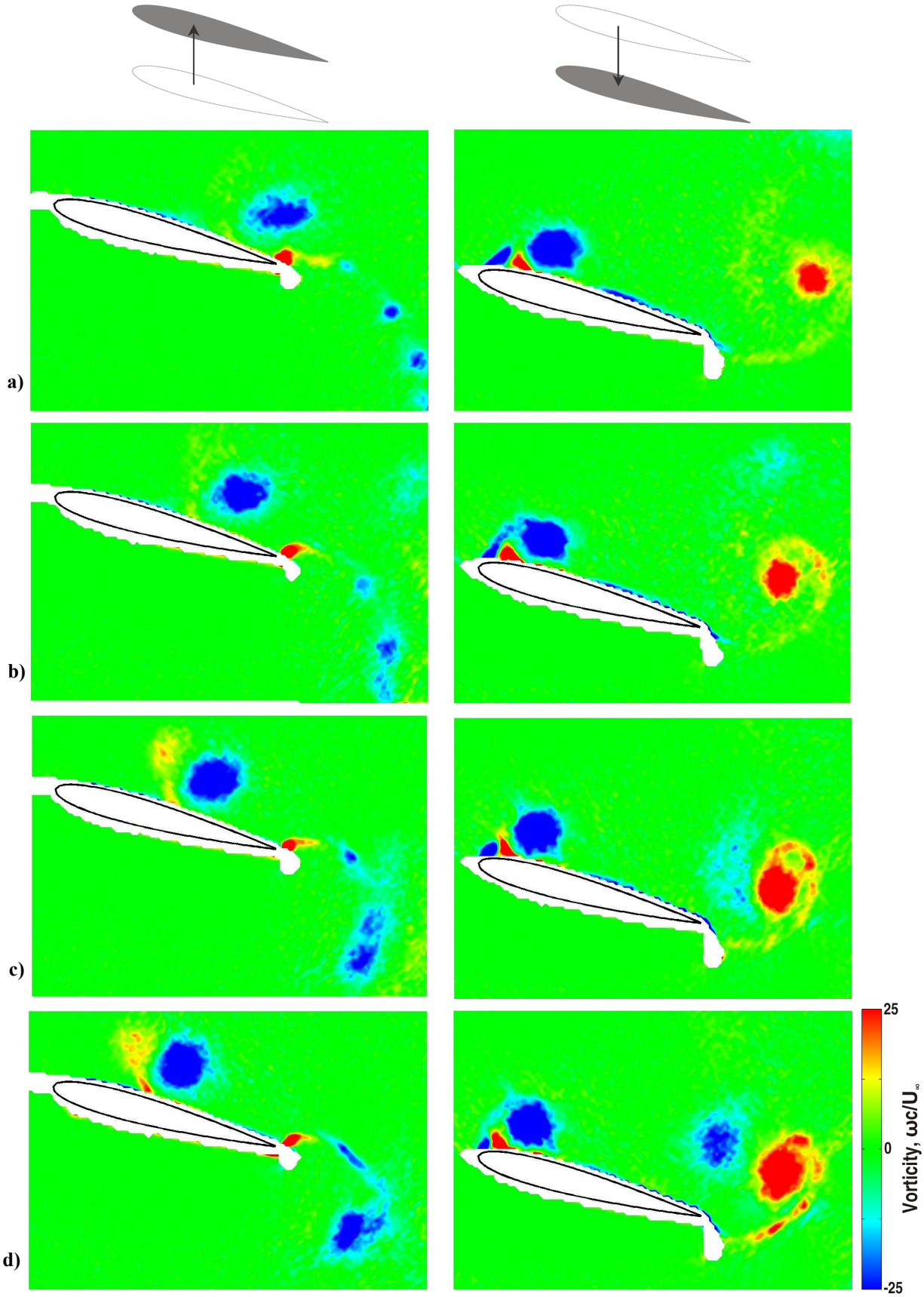

Fig. 3.21 Normalized vorticity at maximum (left) and minimum (right) of motion with a/c = 0.15, α = 15°, Re = 10,000, for: a) Sr_c = 0.625, b) Sr_c = 0.750, c) Sr_c = 0.875, d) Sr_c = 1.000.

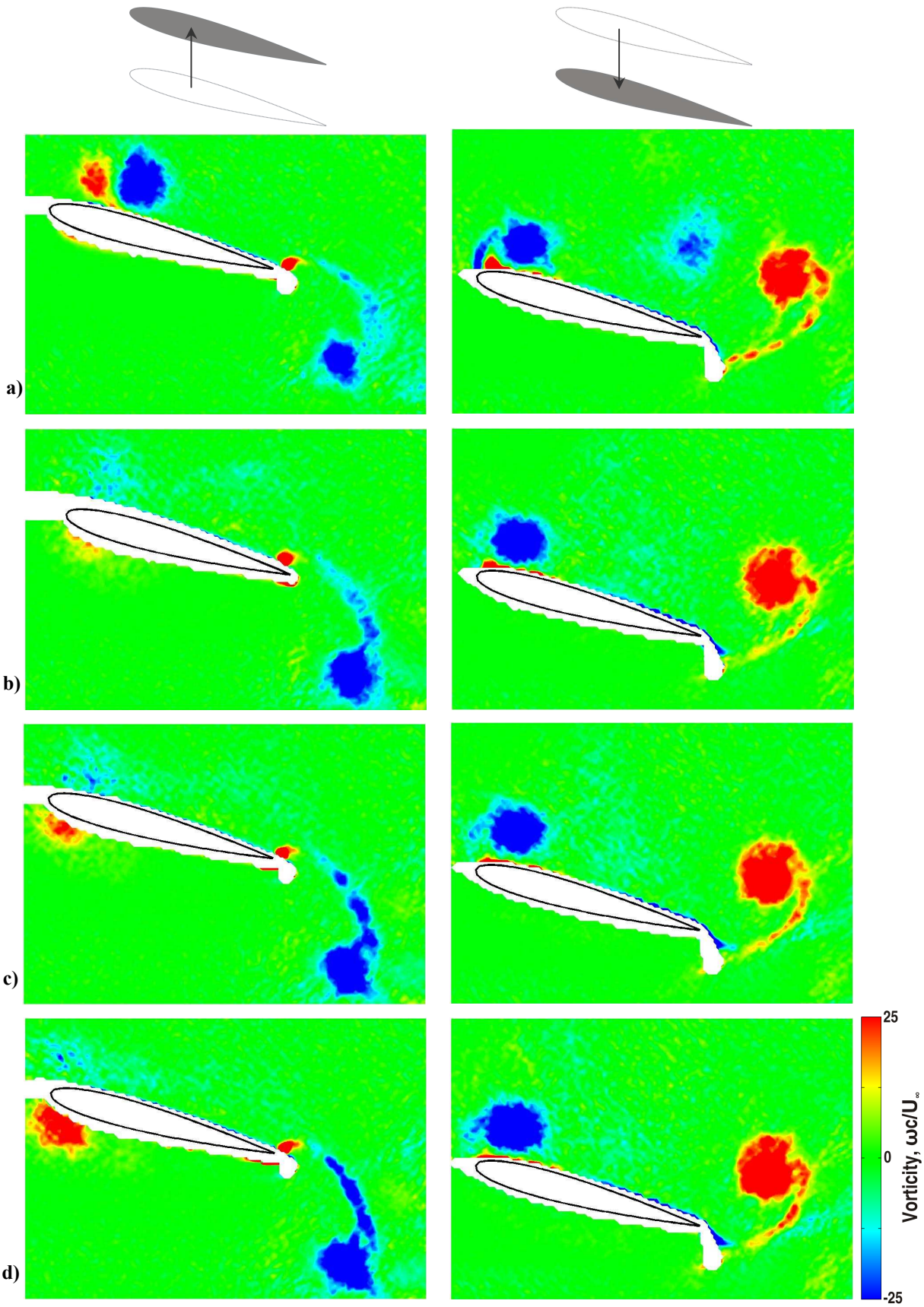

Fig. 3.22 Normalized vorticity at maximum (left) and minimum (right) of motion with a/c = 0.15, α = 15°, Re = 10,000, for: a) Sr_c = 1.125, b) Sr_c = 1.250, c) Sr_c = 1.375, d) Sr_c = 1.500.

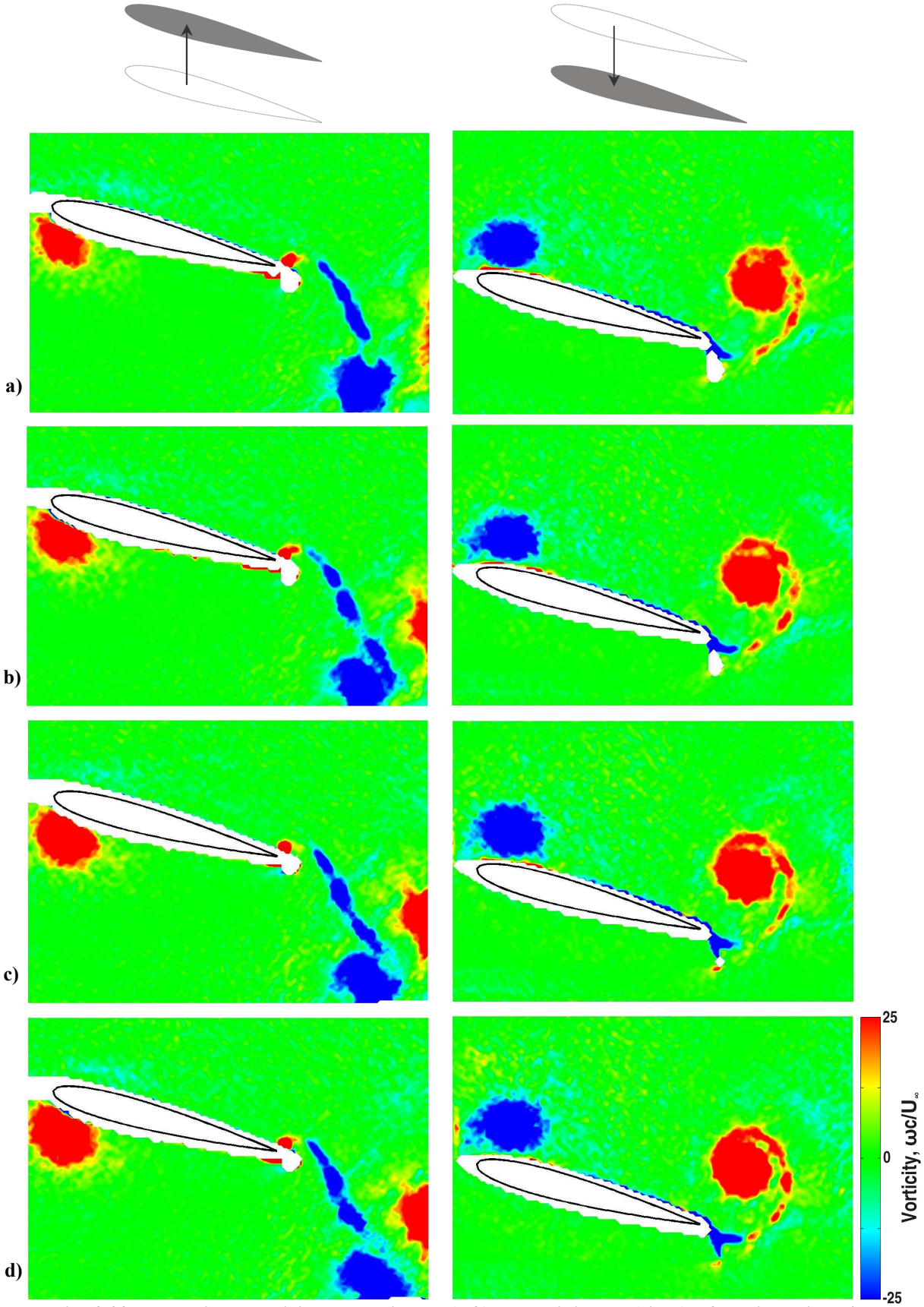

Fig. 3.23 Normalized vorticity at maximum (left) and minimum (right) of motion with a/c = 0.15, α = 15°, Re = 10,000, for: a) Sr_c = 1.625, b) Sr_c = 1.750, c) Sr_c = 1.875, d) Sr_c = 2.000.

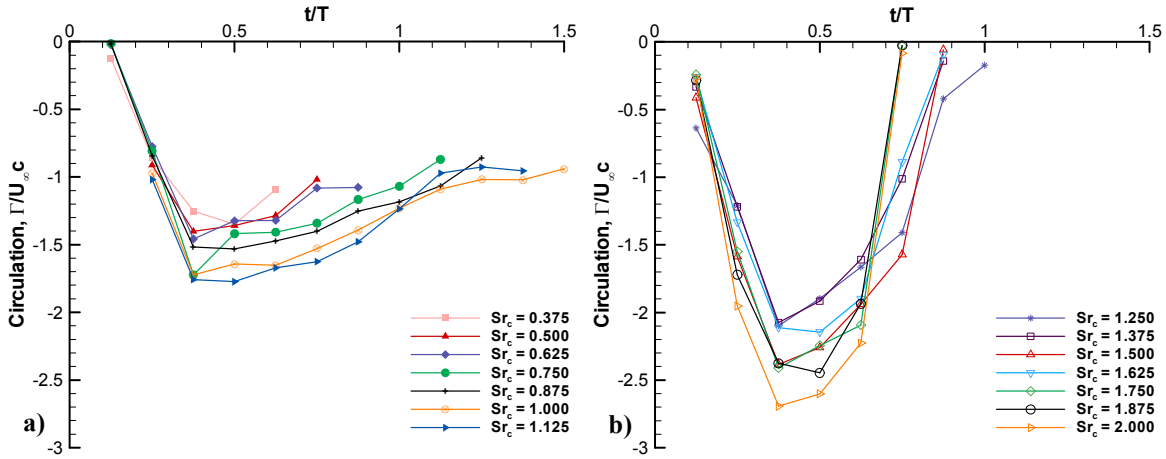

Fig. 3.24 Normalized circulation of the upper surface leading edge vortex for a/c = 0.15, α = 15°, Re = 10,000, and: a) $Sr_c \leq 1.125$, and b) $Sr_c \geq 1.250$.

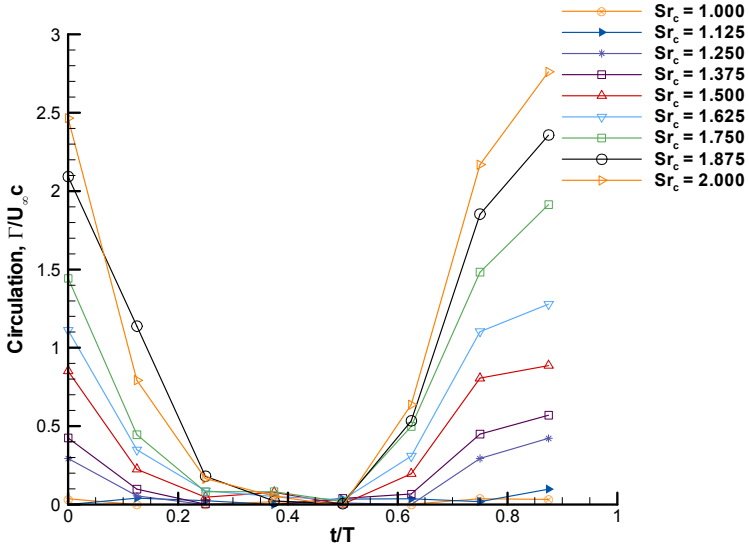

Fig. 3.25 Normalized circulation of the lower surface leading edge vortex for a/c = 0.15, α = 15°, Re = 10,000, and Src ≥ 1.

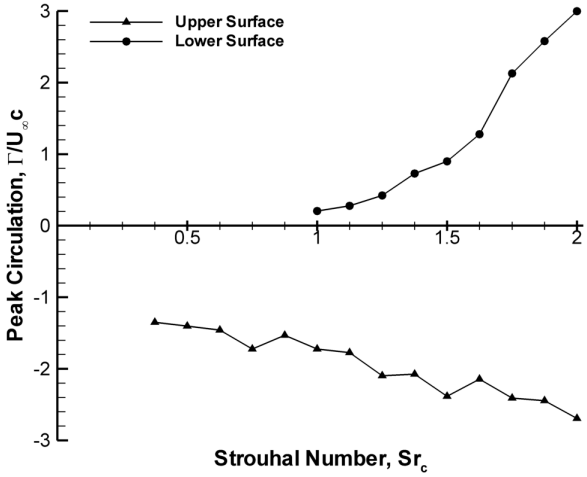

Fig. 3.26 Peak normalized LEV circulation for upper and lower surface for a/c = 0.15.

CHAPTER 4. BIFURCATING FLOWS AT HIGH STROUHAL NUMBERS

4.0 SUMMARY

The lift and thrust performance of a NACA 0012 oscillating at a range of fixed angles of attack (α = 0 to 20°), small amplitude ($a/c \leq 0.2$), and range of Strouhal numbers has been studied. The objective was to investigate the existence of deflected jets and the effect of Reynolds number, angle of attack, and amplitude on them. For $\alpha = 0°$ deflected jets were observed to occur at higher plunge velocities resulting in very large positive lift coefficients when upwards deflected, and conversely very large negative lift coefficients when downwards deflected. The direction, upwards or downwards, was determined by the initial conditions resulting in a bifurcation in lift coefficient. With the frequency gradually increasing from zero either direction is possible although an upwards deflected jet was more common due to slight asymmetries in the experimental setup. With the frequency decreasing and the airfoil impulsively started at the top of the motion an upward deflected jet occurs; with the frequency decreasing and the airfoil impulsively started at the bottom of the motion a downward deflected jet occurs. Deflected jets were shown to exist across Reynolds numbers in the range Re = 2,500 to 15,000.

The bifurcations were shown only to occur for angles of attack in the range $\alpha \leq 10°$, above this only a downwards deflected jet is observed. Starting position was shown to have an effect through the action of the first trailing edge vortices. With the airfoil impulsively started at the top of the motion and $\alpha = 10°$ as opposed to $\alpha = 0°$ the first counter-clockwise vortex is weaker and therefore the first clockwise vortex pairs with the second counter-clockwise vortex instead advecting in a downwards direction. Thereafter all future vortex pairs are ‘locked-in’ to the same direction.

4.1 RESULTS

4.1.1 Bifurcations

Shown in Fig. 4.1a is the time-averaged lift coefficient for a NACA 0012 airfoil oscillating at an amplitude of a/c = 0.15, and $\alpha = 0°$. A solid line represents data collected by starting at $Sr_c = 0$ (stationary), and then increasing the Strouhal number accumulating data at discrete points along the way. A dashed line represents data collected by impulsively starting at the maximum Strouhal number, and then decreasing the Strouhal number accumulating data at discrete points along the way. There are three curves: one for increasing frequency, and two for decreasing frequency, where two airfoil starting positions are considered: $h_i = +a$ (solid symbol, dashed line) and $h_i = -a$ (open symbol, dashed line). With the experiments carried out on different occasions these curves were highly repeatable. Up to $Sr_c = 1.5$ all three match closely. They all begin at $C_l = 0$ and continue along $C_l = 0$ until $Sr_c > 1.25$ where all three become slightly positive suggesting a slight asymmetry developing. After $Sr_c = 1.5$ the three curves diverge significantly producing two distinct results: increasing and decreasing ($h_i = a$) frequency produce very large positive lift coefficients; decreasing ($h_i = -a$) frequency produces very large negative lift coefficients. Hence for the same experimental conditions two entirely different results are possible; indeed the two results are approximately mirror images of each other in the x-axis. Hereafter where two distinct results exist for the same experimental conditions it shall be termed a dual-flow, with the positive lift coefficient branch termed mode A and the negative branch termed mode B.

Figures 4.1b and 4.1c show the time-averaged drag coefficient and power coefficient for the same three cases. Across the entire range studied these curves match to within the bounds of experimental uncertainty. Hence there is no sign of the bifurcation observed in the time-averaged lift coefficient.

Fig. 4.2 and 4.3 show PIV measurements for a/c = 0.15, and $\alpha = 0°$ demonstrating pre-bifurcation, mode A, and mode B flow fields. In Fig. 4.2 these are in the form of time-averaged velocity magnitude. Fig. 4.2a, for a pre-bifurcation flow field, clearly shows a time-averaged jet aligned horizontally. The associated phase-averaged

vorticity fields in Fig. 4.3 (left column) demonstrate this jet to be the result of a reverse-Kármán vortex street. During the downward motion (a to c) a counter-clockwise vortex forms and sheds from the trailing-edge; during the upward motion (c to a) a clockwise vortex forms and sheds. Both of these vortices convect along a path approximately aligned with the horizontal with equidistant spacing. At the leading-edge an upper surface clockwise vortex forms during the downward motion (see c) and is dissipated during the upward motion through impingement with the upward moving airfoil as previously described by Visbal [140] and Cleaver et al. [141]. Conversely during the upward motion a counter-clockwise leading-edge vortex forms (see a) which is dissipated during the downward motion. The flow field as a whole is characterized by symmetry about the horizontal plane justifying the near-zero time-averaged lift coefficient.

With the Strouhal number increased into the dual-flow regime this symmetry is broken, see Figures 4.2b and 4.2c. For mode A the time-averaged jet is deflected upwards and there is a high velocity region over the upper surface. For mode B the inverse is true, a downwards deflected jet and a high velocity leading-edge region over the lower surface. The phase-averaged vorticity shown in Fig. 4.3 identifies the cause to be trailing-edge vortex dipole formation. For mode A (centre column) the clockwise trailing-edge vortex (TEV) forms during the upward motion (c to a) and 'loiters' near the airfoil during the downward motion (a to c) during which the counter-clockwise TEV forms. As a result of their proximity the vortices form a dipole that due to the relative positions of the vortices has a self-induced velocity in the upwards direction, thereby creating an upwards deflected jet. For mode B (right column) the inverse is true, i.e., the counter-clockwise TEV loiters, creating a vortex dipole with a downwards self-induced velocity and therefore a downwards deflected jet. The mode B flow field therefore appears mirrored in the horizontal and 180 degrees out of phase with the mode A flow field, compare Fig. 4.3c (centre) with Fig. 4.3a (right).

Due to the asymmetry of the flow near the trailing-edge, asymmetry is also created near the leading-edge. Mode A has a strong upper surface LEV (Fig. 4.3c centre), and comparatively weak lower surface LEV (Fig. 4.3a centre), explaining both the

high time-averaged velocity above the upper surface observed in Fig. 4.2b and also the very high positive time-averaged lift coefficient, $C_l \approx 3.4$. For mode B the inverse is true, i.e., a weak upper surface LEV and strong lower surface LEV resulting in a large negative lift coefficient. This effect is quantified in the circulation measurements shown in Fig. 4.4. In Fig. 4.4 purely for convenience mode A is treated as a continuation of the pre-bifurcation flowfield and therefore represented as solid lines and closed symbols, mode B is represented by dashed lines and open symbols. For the mode B case all four of the primary vortices are shifted (comparatively) to more positive circulations. This means a comparatively stronger lower surface LEV, and therefore negative lift coefficient.

It is interesting to note that an upwards deflected jet (mode A) is associated with high lift and a downwards deflected jet (mode B) is associated with low / negative lift. This relationship between the direction of the lift and deflected jet is contrary to what one would intuitively expect based on a simple control volume argument, see Fig. 4.2. As the deflected jet represents a momentum, one would expect a reaction force opposite to its direction, hence lift is expected to be opposite to the direction of the deflected jet. However, this simple analysis neglects the velocity fluctuations and the pressure difference in the near wake. It can therefore be concluded that although momentum in the deflected jet may make a small contribution to the lift force, the lift force is instead dominated by the effect the deflected jet has on the flow over the airfoil surfaces, i.e., the region of high velocity flow over the upper / lower surface in Fig. 4.2. This is consistent with the simulations performed at much lower Reynolds numbers (Re = 200 in Emblemsvag et al. [142]; Re = 1,850 in Liang et al. [143]). Nevertheless the lack of bifurcation in time-averaged drag coefficient (see Fig. 4.1b) is explicable through a momentum argument. Since the deflected jet observed in Fig. 4.2 is mirrored about the horizontal axis in the mode A and mode B cases, the horizontal component will be the same and the drag coefficient identical.

4.1.2 Effect of Reynolds Number

The results presented for a plunging airfoil so far were for Re = 10,000. Fig. 4.5 shows the effect of Reynolds numbers in the range Re = 2,500 to 15,000 on deflected jets. We found that bifurcation occurs for Sr_c = 2.00-2.25 for $\alpha = 0°$ and a/c = 0.15.

Although there are minor differences in the shape and size of some of the vortices the wake as a whole is very similar, and crucially the deflected jet is still apparent for all Reynolds numbers. The phenomenon of deflected jets and their associated force bifurcations are therefore applicable to a wide range of Reynolds numbers.

4.1.3 Effect of Angle of Attack

Shown in Fig. 4.6 is the time-averaged lift coefficient for a NACA 0012 airfoil oscillating at an amplitude of a/c = 0.15, and six different angles of attack. A solid line represents data collected by starting at $Sr_c = 0$ (stationary), and then increasing the Strouhal number accumulating data at discrete points along the way. A dashed line represents data collected by impulsively starting at the maximum Strouhal number, and then decreasing the Strouhal number accumulating data at discrete points along the way. The results for $\alpha = 0°$ have already been discussed in section 4.1.1.

With the angle of attack increased to $\alpha = 5°$ there are similarly two distinct results determined by the initial conditions. Increasing frequency results in mode A, and decreasing frequency results in mode B. As will be discussed in more detail later, for the decreasing case given a suitable h_i either mode can be produced; however for conciseness only a single starting position ($h_i = 0$, moving upwards) that produces mode B is considered here. Initially both increasing and decreasing frequency demonstrate a gradual increase in lift coefficient with increasing Strouhal number. At around $Sr_c = 1.5$ the two cases bifurcate, increasing frequency leads to mode A and decreasing frequency leads to mode B. Due to the non-zero angle of attack the two cases are not symmetrical about the x-axis. Mode A results in a maximum lift coefficient of $C_l = 5.3$; and mode B results in a minimum lift coefficient of $C_l = –2.0$.

At an angle of attack of $\alpha = 10°$ there are similar trends. Initially both curves match, gradually increasing until the bifurcation at around $Sr_c = 1.5$. Again increasing frequency results in mode A and decreasing frequency mode B with the asymmetry further accentuated. The associated lift coefficients are respectively $C_l = 4.3$ and $C_l = –0.4$.

At $\alpha = 12.5°$ there are no longer two distinct results, instead both increasing and decreasing frequency result in a negative lift coefficient. In the low Strouhal number range the match is very close. At $Sr_c = 1.63$ increasing and decreasing frequency diverge slightly remerging at $Sr_c = 1.88$. The behaviour in this range can be considered as a hysteresis loop. Regardless of hysteresis, both increasing and decreasing frequency result in significant fall from $C_l \approx 2.5$ to $C_l \approx -0.3$.

At $\alpha = 15°$ there is similar behaviour to $\alpha = 12.5°$ except the fall in lift does not result in a negative lift coefficient. Again there is small hysteresis between the increasing and decreasing frequency cases around $1.43 < Sr_c < 1.73$ but it is much reduced in comparison with $\alpha = 12.5°$. The features associated with this post-stall angle of attack and enhanced time-averaged lift were discussed in chapter 3. The general rise in lift was associated with the growth of an upper surface leading-edge vortex and its convection along the surface. The peaks were attributed to resonance with the natural wake shedding frequency, its harmonics or subharmonics. The fall in lift at $Sr_c \approx 1.5$ was attributed to the disintegration of the upper surface LEV (due to a strong vortex-airfoil interaction) combined with the growth of a lower surface LEV.

With the angle of attack increased to $\alpha = 20°$ there is no longer a fall in lift at $Sr_c \approx 1.5$, instead there is a continued increase in lift coefficient with Strouhal number. Superimposed onto this are several peaks which can be attributed to resonance with the natural wake shedding frequency as for $\alpha = 15°$. The crucial point is that both increasing and decreasing frequency curves match, and there is no hysteresis or bifurcation.

In summary, for angles of attack up to the stall angle, $\alpha \leq 10°$, dual flows are possible resulting in extremely different and potentially very large time-averaged lift coefficients. Which flow field is created is dependent upon the initial conditions. With increasing frequency and $0° < \alpha \leq 10°$ only mode A is achievable. With decreasing frequency, either mode may be obtained depending upon the starting position and angle of attack. In the post-stall region, $10° < \alpha < 20°$, except some minor hysteresis loops, both increasing and decreasing frequency match. While the convected leading-edge vortices enhance time-averaged lift in the post-stall region,

in the pre-stall region there is the possibility of even higher lift. As will be shown below, the mechanism for this high lift is deflected (thrust producing) jets at high Strouhal numbers.

Both Fig. 4.2 and Fig. 4.3 are for zero degree angle of attack where symmetry about the horizontal plane simplifies the problem. However, as suggested by the force measurements shown in Fig. 4.6, similar dual flows exist for nonzero angles of attack. Fig. 4.7 therefore shows phase-averaged vorticity contours for mode A and Fig. 4.8 for mode B for the three angles of attack that exhibit dual flows. In both figures the left column is the top of the motion and the right the bottom. For mode A, Fig. 4.7 shows that qualitatively the wake structure is independent of angle of attack in this range. In all cases there is a TEV dipole, which, due to the vortex positions, convects upwards. For mode B Fig. 4.8 shows that the same is true except the wake structure is inverted. There is a vortex dipole at the top of the motion which convects downwards to create a downwards deflected jet. It can therefore be concluded that the same phenomenon, deflected jets, is responsible for the lift force bifurcations observed for $\alpha \leq 10°$.

4.1.4 Effect of initial conditions

The initial conditions can be divided into two broad categories: increasing and decreasing frequency. For increasing frequency, the starting position is always the stationary case, and the result is the same for all three angles of attack, mode A. This is unexpected for $\alpha = 0°$, as symmetry means that logically mode B is equally likely. Practically however symmetry is impossible to achieve experimentally, and in practice the mode B case only occurred once in twelve occasions (and is therefore not presented here). From this it can be concluded that for increasing frequency the direction of the deflected jet is extremely susceptible to even slight asymmetry.

For decreasing frequency the situation is more complicated. For $\alpha = 0°$, symmetry means either case is equally possible and it has previously been shown [69] that starting position is the determining factor. This is further complicated because there are an infinite number of possible starting positions in the range $-a \leq h_i \leq a$, and because experimentally a true impulsive start (meaning an infinite acceleration to

full frequency) is not physically possible. For the purposes of this study the acceleration time is measured to be less than the full period as demonstrated in the insets of Fig. 4.9 and Fig. 4.10, and only the two extreme starting positions are considered in detail: $h_i = a$, and $-a$. The effect of these starting positions on whether mode A or B is produced is shown in Table 3. These are derived from ten repeats for each starting position. For all angles of attack and amplitudes starting with a position of $h_i = -a$, produces mode B (downwards deflected jet). Starting with a position of $h_i = a$ is more complicated. For $\alpha = 0°$ and 5° this starting position consistently produces mode A (upwards deflected jet), but at $\alpha = 10°$ it only produces an upwards deflected jet at a single amplitude and only 20% of the time. In all other cases a mode B case is produced. This suggests that the direction of the deflected jet is determined by competing asymmetries, i.e., starting position versus angle of attack. It is important to note that for $\alpha > 0°$ in figures 4.6, 4.7 and 4.8 a starting position of $h_i = 0$ (up) was used to guarantee a mode B flow field.

Table 3 Effect of starting position on the mode produced.

		Angle of Attack, α				
		0°	5°		10°	
	a/c:	0.15	0.15	0.10	0.15	0.20
Starting Position, h_i	a	A	A	B	B (80%)	B
	-a	B	B	B	B	B

To investigate how starting position and angle of attack influence the direction of the deflected jet, phase-locked instantaneous PIV measurements were performed for the first five cycles of an impulsive start from $h_i = a$ with a/c = 0.15, $\alpha = 0°$ and $\alpha = 10°$, see Fig. 4.9. For $\alpha = 0°$ a mode A (upward jet) is produced, and for $\alpha = 10°$ a mode B (downward jet) is produced. In this figure, the instantaneous velocity field shown in each image when the airfoil is at the bottom of the motion. For $\alpha = 0°$, the first counter-clockwise TEV can be seen above the trailing-edge in Fig. 4.9a (left), and can again be seen below the vortex dipole in Fig. 4.9b (left). This vortex dipole is formed from the first clockwise TEV and second counter-clockwise TEV, and due to the vortex positions convects upwards creating an upwards deflected jet. As only two trailing-edge vortices are created in each cycle, one clockwise and one counter-clockwise, all future cycles will now be 'locked-in' to this mode of vortex pairing

creating a stable upwards deflected jet, see Fig. 4.9c through e (left). The starting process for $\alpha = 10°$ is shown in the right column of Fig. 4.9. As before a counter-clockwise vortex forms during the first downward motion but in this case it is only partially visible at the bottom of Fig. 4.9b where it appears to have paired with the first clockwise TEV. In Fig. 4.9c to e the flow field is now clearly representative of a stable downwards deflected jet. From Fig. 4.9 it can be concluded that the direction of the deflected jet is determined in the first two cycles, and the motion of the first counter-clockwise trailing-edge vortex is crucial.

To give more detail of the startup process, shown in Fig. 4.10 are selected instantaneous PIV images from the first two cycles. For $\alpha = 0°$ the first counter-clockwise vortex can be seen as CCW1 in A, and then again at the top of the next cycle next to the first clockwise vortex (CW1) in B. During the course of the next cycle it can be seen that the first counter-clockwise vortex has little effect on the outcome as the first clockwise vortex pairs with the second counter-clockwise vortex instead. As a result the first vortex dipole convects upwards. By contrast for $\alpha = 10°$ the first clockwise vortex pairs with the first counter-clockwise vortex drawing it downwards, see B through F (right). This results in a flow field, where the counter-clockwise TEV 'loiters' and pairs with the clockwise TEV to give a downwards deflected jet. The reason for the increased effect of the first counter-clockwise vortex at $\alpha = 10°$ is its increased strength. This is quantified through the absolute circulation measurements shown in Fig. 4.11. For $\alpha = 0°$ (solid lines), there is a very large difference between the circulation of the first counter-clockwise and clockwise TEV. This is due to the aforementioned acceleration time which results in the airfoil moving slower in the first downwards motion than the first upwards. For $\alpha = 10°$ the gap in vortex strengths is reduced due to the positive bias in the effective angle of attack. This enables the first clockwise TEV to pair with the first counter-clockwise and therefore create a downward deflected jet. It is therefore important to note that different acceleration rates could cause different results.

4.1.5 Effect of amplitude

Shown in Fig. 4.12 is time-averaged lift coefficient for five amplitudes, at four angles of attack $\alpha = 0°$, 5°, 10°, and 15°. Fig. 4.12a shows the data for $\alpha = 0°$; and for

each amplitude three initial conditions are considered: increasing frequency, decreasing frequency with $h_i = a$, and decreasing frequency with $h_i = -a$. Both a/c = 0.025 and 0.050 do not exhibit bifurcation behaviour. For $a/c \geq 0.10$ however bifurcation behaviour is evident. For all three amplitudes initially the three curves match following $C_l \approx 0$. Then at a critical Strouhal number these three curves bifurcate with increasing and decreasing ($h_i = a$) frequency consistently becoming mode A, and decreasing ($h_i = -a$) consistently becoming mode B. The Strouhal number of the onset of bifurcation is delayed by smaller amplitude, hence the bifurcation occurs at Sr_c = 1.25, 1.50, and 2.00 for a/c = 0.20, 0.15, and 0.10 respectively. Similarly for $\alpha = 5°$ and 10° (see Figures 4.12b and 4.12c), bifurcation only occurs for $a/c \geq 0.10$, with increasing frequency becoming mode A and decreasing frequency becoming mode B. Again the point of bifurcation is amplitude dependent but slightly delayed from that for $\alpha = 0°$. The bifurcation points for $\alpha = 5°$ are therefore Sr_c = 1.30, 1.58, and 2.00 for a/c = 0.20, 0.15, and 0.10 respectively; and for $\alpha = 10°$ are Sr_c = 1.30, 1.58, and 2.10 for a/c = 0.20, 0.15, and 0.10 respectively. These points are however approximate as how to define the bifurcation point is subjective and therefore accurate to a measurement interval. For $\alpha = 15°$ across all amplitudes there is no significant bifurcation. There is some minor hysteresis at the higher Strouhal numbers as previously described for a/c = 0.15 but this behaviour is not indicative of dual flows.

The time-averaged drag coefficient for the same cases as in Fig. 4.12 is shown in Fig. 4.13. For $\alpha = 0°$ (Fig. 4.13a), generally there is decreasing drag coefficient with increasing Strouhal number, with greater effect for greater amplitude as predicted by Garrick approximations and previously observed in other studies [64, 144, 145]. For this angle of attack for all amplitudes all three curves (increasing and decreasing frequency) match to within the bounds of experimental uncertainty across the entire Strouhal number range. Hence, there is no sign of the bifurcation behaviour observed in the associated lift coefficient (Fig. 4.12a). As previously discussed this is a consequence of the symmetry at $\alpha = 0°$ which means that in terms of horizontal force there is no difference between upwards / downwards deflected jet because they are mirror images of each other in the horizontal plane and therefore create the same horizontal force component. With the angle of attack increased to $\alpha = 5°$ this

symmetry is broken and a bifurcation is therefore observed, see Fig. 4.13b. As observed in the lift coefficient, this only occurs for a/c ≥ 0.10, and is amplitude dependent with the onset being at the same Strouhal numbers as observed in the lift coefficient. As a result of the bifurcation, the decreasing frequency case (downwards deflected jet) consistently produces more thrust. The thrust enhancing nature of the downwards deflected jet is a result of the strong lower surface vortex which acts on the forward facing lower surface of the airfoil. The magnitude of this difference in drag is small in comparison with that observed in the lift coefficient, i.e., $\Delta C_d \approx 0.5$ versus $\Delta C_l \approx 7.0$. Increasing the angle of attack to $\alpha = 10°$ amplifies this difference, $\Delta C_d \approx 0.75$. The onset of bifurcation is again amplitude dependent reflecting the points observed in the lift coefficient. With the angle of attack increased to $\alpha = 15°$ (Fig. 4.13d), there is no longer a bifurcation at any amplitude, again reflecting the trends observed in lift coefficient.

To confirm that deflected jets are responsible for the force bifurcations at all amplitudes phase-averaged vorticity contour plots at the top (left) and bottom (right) of the motion for a/c = 0.10, 0.15, and 0.20 and $\alpha = 0°$ are shown in Fig. 4.14 and 4.15. The Strouhal numbers are the maximum tested in the force measurements and therefore demonstrate post-bifurcation wakes. Fig. 4.14 is for mode A and therefore demonstrates an upwards deflected jet as is visible in the right column. Fig. 4.14 also excellently demonstrates the previously discussed LEV asymmetry, compare the weak lower surface LEV in the left column with the strong upper surface LEV in the right column. The only significant difference between amplitudes is the increased spacing between the TEVs in the dipole with increasing amplitude, see right column. For the mode B case shown in Fig. 4.15 the inverse is generally true, i.e., the jet is deflected downwards and the lower surface LEV is the stronger. Across all amplitudes the cause of the force bifurcation is therefore the same phenomenon, deflected jets.

As further confirmation of the existence of deflected jets for all cases where bifurcation occurs, the angle of the deflected jet was measured by tracking the motion of the trailing-edge vortices in phase-averaged PIV measurements, see Fig. 4.16. Fig. 4.16a for $\alpha = 0°$ reaffirms that in the pre-bifurcation regime the vortices

convect approximately along the horizontal. After bifurcation, for mode A, the vortex trajectory angle becomes negative indicative of an upwards deflected jet, for mode B the vortex trajectory angle becomes positive indicative of a downward deflected jet. Figures 4.16b and 4.16c confirm similar trends for $\alpha = 5°$ and $\alpha = 10°$ but with a bias towards positive vortex trajectory angles due to the nonzero angle of attack.

4.1.6 Bifurcation criteria

In this section several criteria to predict the onset of bifurcation will be introduced. To this end shown in Fig. 4.17 are the points of bifurcation in the amplitude-Strouhal number domain. Also shown is a power law curve fit of the drag to thrust switch points as derived from Fig. 4.13. These show that the location of the switch from drag to thrust is highly amplitude dependent with earlier zero drag for greater amplitude. The point of zero drag is also delayed by increasing angle of attack, mostly due to the increased drag of the stationary airfoil which must be overcome, but also to a lesser extent by the drag enhancing effect of the convecting upper surface vortex acting on the rearward facing upper surface. The single-dual flowfield boundary is likewise delayed to higher Strouhal numbers by increasing angle of attack but the effect is not as pronounced. Extrapolation of these curves to smaller amplitudes and higher Strouhal numbers shows that dual-flow was not observed at the smaller amplitudes (a/c = 0.025 and a/c = 0.05) because the maximum Strouhal number studied was insufficient.

The trend of increasing Strouhal number with decreasing amplitude suggests the possibility of a constant plunge velocity or effective angle of attack as criteria for the onset of bifurcation. Fig. 4.18 therefore shows the bifurcation onset points as symbols plotted against both Strouhal number based on amplitude and effective angle of attack. Effective angle of attack varies in a range, so the limits of this range ($\alpha_{eff,min}$ and $\alpha_{eff,max}$) are used in Fig. 4.18. The points representing the onset of bifurcation fall within the range $Sr_A = 0.45 \pm 0.05$ which is in very close agreement with the range $0.434 < Sr_A < 0.455$ suggested by von Ellenreider and Pothos [69]. The trend of decreasing Sr_A with decreasing amplitude and angle of attack means however that this cannot be considered a universal criterion. In terms of effective

angle of attack the points fall within the range $\alpha_{eff,max} = 60° \pm 9°$, however again due to the trend of decreasing effective angle of attack with amplitude and angle of attack this cannot be considered a universal criterion. In addition, neither plunge velocity nor effective angle of attack give an adequate explanation as to why there is no bifurcation at larger angles of attack ($\alpha > 10°$).

As a simple universal criterion cannot be defined from the controllable experimental parameters it is necessary instead to derive a criterion from the flow field measurements. As deflected jets are a direct result of TEV dipole formation the logical choice is a criterion based on the strength of the trailing-edge vortices. Shown in Fig. 4.19 is therefore the circulation of the TEVs for $\alpha = 0°$, 5°, 10° and 15°, for a/c = 0.05, 0.10, 0.15, and 0.20. Clockwise TEVs are denoted by solid lines and counter-clockwise TEVs by dashed lines. The pre-bifurcation case is denoted by solid symbols, with the mode A treated as a continuation of this, and the mode B denoted by open symbols. For $\alpha = 0°$ both trailing-edge vortices grow almost identically with increasing Strouhal number until the point of bifurcation. After the point of bifurcation the asymmetric wake creates asymmetry in the strengths of the clockwise and counter-clockwise vortices. For mode A the clockwise vortex becomes stronger than the counter-clockwise vortex, and vice-versa for mode B. Note that this does not include all circulation shed into the wake and therefore does not contravene Kelvin's circulation theorem. There is a strong amplitude dependence of the trailing-edge vortex strength. For $\alpha = 5°$ the same basic trend is observed except that the clockwise circulation curve is shifted downwards and the counter-clockwise curve is shifted upwards. This is due to the greater mean angle of attack causing greater asymmetry in the effective angle of attack as demonstrated in Fig. 4.18. The gap between clockwise and counter-clockwise vortex is further enhanced by $\alpha = 10°$.

For $\alpha = 15°$ this trend of increased counter-clockwise vortex circulation and reduced clockwise trailing-edge vortex circulation is continued, however now only a single mode is observed, one with a stronger counter-clockwise vortex than clockwise vortex. The circulation measurements for the smaller angles of attack demonstrate that this is typical of a mode B flow field. Indeed when comparing the flow field for

α = 15° with the mode B flow field for α = 5° and α = 10° (see Fig. 4.20), it bears all the hallmarks of a mode B flow field and yet without a point of bifurcation it is not possible to classify it as such. In summary, the increasing geometric angle of attack causes greater asymmetry in the effective angle of attack which causes an imbalance in the trailing-edge vortex strengths, inclining the wake towards a downward deflected jet. To characterize this asymmetry a new parameter is suggested based on the angular velocity of a vortex pair [146]:

$$\frac{(\Gamma_{T+} + \Gamma_{T-})}{d^2} \tag{4.1}$$

where d is the distance between the vortices. This is made dimensionless as:

$$\frac{(\Gamma_{T+} + \Gamma_{T-})c}{U_\infty d^2} \tag{4.2}$$

This represents a non-dimensional trailing-edge vortex asymmetry parameter. Our data suggests that the mode A flow field is not possible once this asymmetry parameter exceeds a critical value, as will be discussed further.

In a similar manner, it is possible to consider the minimum plunge velocity criteria in terms of the experimentally measured circulation. Shown in Fig. 4.21 is the average absolute circulation of the two trailing-edge vortices versus Strouhal number. The average circulation is used so as to minimize and separate out any asymmetry effects. For the different angles of attack the curves collapse onto a nearly parabolic trend with the gradient determined by the amplitude. The points of bifurcation are identified through the grey dashed line. This shows that a minimum threshold trailing-edge vortex circulation is required for bifurcation to occur. The trend with amplitude suggests that bifurcation requires larger trailing-edge vortex circulation at larger amplitudes. This is rational since larger amplitude leads to larger trailing-edge vortex spacing which inhibits vortex-pairing. If this trend is extrapolated to higher Sr_c, it is clear that for a/c = 0.05 the level of trailing-edge vortex circulation is insufficient for bifurcation (within the Strouhal number range tested).

Combining the asymmetry parameter and the normalized circulation parameter produces Fig. 4.22. Both a horizontal boundary separating the single and dual modes, and a vertical boundary separating mode A and mode B is shown. The question of

why there is no bifurcation at low amplitudes is therefore answered by the circulation threshold, and the question of why there is no mode A at large angles of attack is answered by the asymmetry boundary, i.e., all the points for α = 15° lie to the mode B side of the boundary.

The threshold circulation displayed in Fig. 4.22 is however not perfect, as seen by the scatter. As the airfoil is in effect acting as a vortex generator with the strength determined by the plunge velocity, plunge velocity is a more logical normalizing variable. Shown in Fig. 4.23 is this alternative circulation parameter with the same asymmetry parameter. As expected the data points have collapsed down to a smaller band, but more importantly there is now a clear boundary between the single and dual modes with minimal scatter of the data. The critical value of circulation normalized by plunge velocity corresponding to the bifurcation points is $\bar{\Gamma}/U_P c$ = 1.85. When compared to Fig. 4.22 the collapse of the data into a smaller band in Fig. 4.23 elucidates the importance of plunge velocity.

Alternatively, Fig. 4.24 shows all the trailing-edge vortex circulations for all amplitudes and angles of attack plotted against Sr_A. This figure demonstrates the three possible bifurcation strength criteria: Sr_A = 0.45±0.05 on the x-axis, $\bar{\Gamma}/U_\infty c$ = 2.6±0.3 on the y-axis, and $\bar{\Gamma}/U_P c$ = 1.85 as a straight line with its gradient determined by:

$$\frac{\bar{\Gamma}}{U_P c} = \frac{\bar{\Gamma}}{\pi U_\infty Sr_A c} = 1.85 \qquad (4.3)$$

therefore,

$$\frac{\bar{\Gamma}}{U_\infty c} = 1.85\pi Sr_A \qquad (4.4)$$

This line passes through the points of bifurcation with the values above being dual mode and the values below single mode, reinforcing the significance of $\bar{\Gamma}/U_P c$ in determining the onset of deflect jets and bifurcation.

The circulation normalized by the plunge velocity, $\bar{\Gamma}/U_P c$, can be interpreted as the inverse of a modified Strouhal number based on the dipole velocity Γ/a, the frequency and chord length. Initial distance between the trailing-edge vortices of

opposite sign is on the order of peak-to-peak amplitude 2a, which is physically more meaningful than the distance once the dipole is formed. The $\overline{\Gamma}/U_p c$ strength parameter can therefore also be viewed as the inverse of a modified Strouhal number, which is the ratio of two time scales.

4.2 CONCLUSIONS

Time-averaged force measurements on a periodically plunging NACA 0012 airfoil have identified significant bifurcations at high Strouhal numbers for angles of attack smaller than and equal to the stall angle. These bifurcations were observed when the frequency of oscillation was increased slowly up to a maximum and the motion stopped, then restarted impulsively at the maximum frequency and the frequency decreased. It was found that below a critical frequency, lift force and flow fields were identical independent of initial conditions; however, above this bifurcation frequency, dual flows and significantly different lift forces were observed. These dual flows were characterized by thrust producing deflected jets. The deflected jets were produced by a trailing-edge vortex loitering over the airfoil to form a vortex dipole with the opposite sign vortex. The deflected jets also modify the leading-edge vortices resulting in very high lift coefficients. The lift direction is the same as the direction of the vertical component of the deflected jet. With the frequency increasing, the deflected jet is always deflected upwards leading to high lift; with the frequency decreasing either direction is possible depending on the angle of attack and starting position. For decreasing frequency the direction of the deflected jets is determined in the first two cycles by the first trailing-edge vortex. Bifurcation and deflected jets were observed for a wide range of Reynolds numbers.

Effective angle of attack due to the plunging motion or the Strouhal number based on amplitude has some correlation to the onset of bifurcation. However better agreement and insight into the flow physics were derived from flow field measurements. Analysis of the trailing edge vortices led to two parameters which describe the wake behaviour. Firstly, an asymmetry parameter is derived from the difference in circulation of the clockwise and counter-clockwise trailing-edge vortex. This parameter determines whether the deflected jet is deflected upwards or downwards. It also explains why dual flows are not observed at larger angles of

attack as the greater asymmetry in the effective angle of attack causes an imbalance in the trailing-edge vortex strengths, which gives a natural tendency towards a downwards deflected jet. Secondly, a strength parameter is derived from the average of the circulations of the trailing edge vortices. From the measured values of circulation, this parameter can be expressed as circulation normalized by the freestream velocity or circulation normalized by the plunge velocity. It was shown that a minimum value of the strength parameter is necessary for bifurcation to occur. The bifurcation was therefore not observed at small amplitudes or low frequencies, due to insufficient trailing-edge vortex strength. Circulation normalized by the plunge velocity gives the best data collapse, which can be interpreted as the inverse of a modified Strouhal number.

4.3 FIGURES

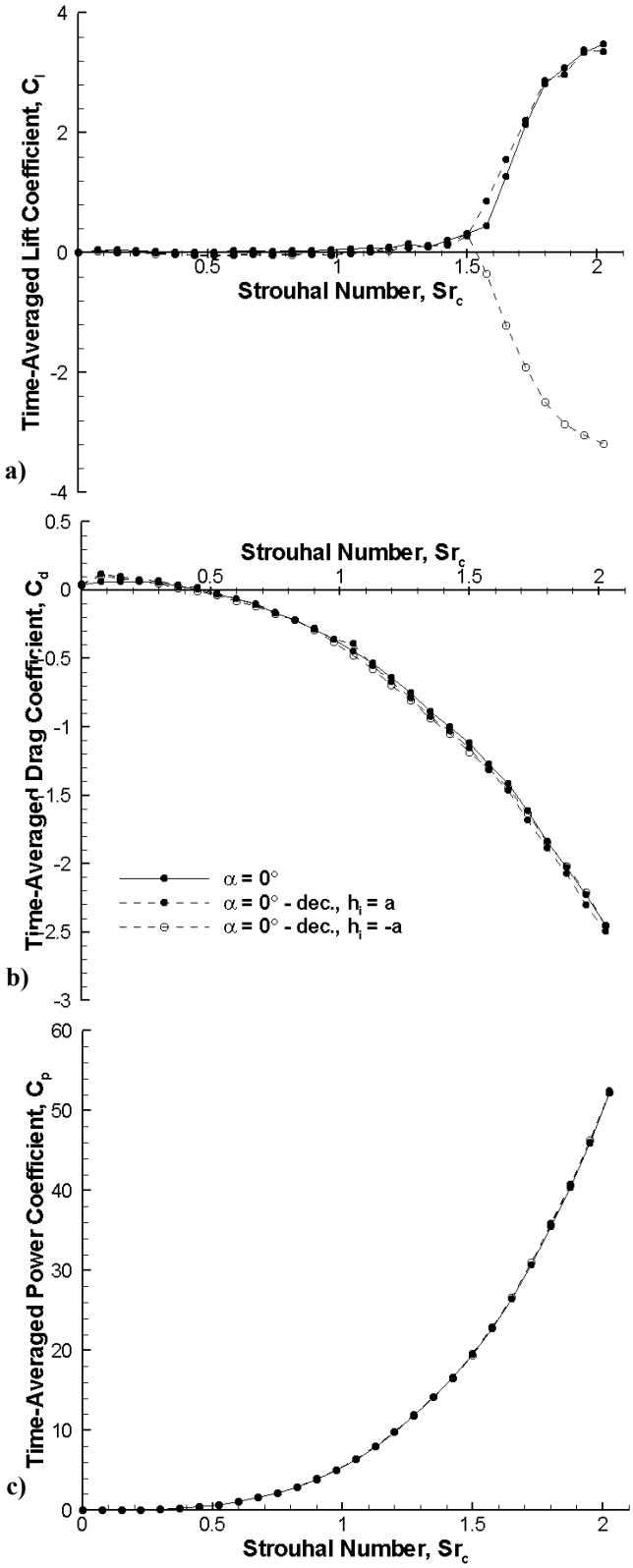

Fig. 4.1 Time-averaged a) lift coefficient, b) drag coefficient, and c) power coefficient for a/c = 0.15 and α = 0°. Solid line represents increasing frequency, dashed line represents decreasing frequency with a starting position of $h_i = \pm a$ as appropriate.

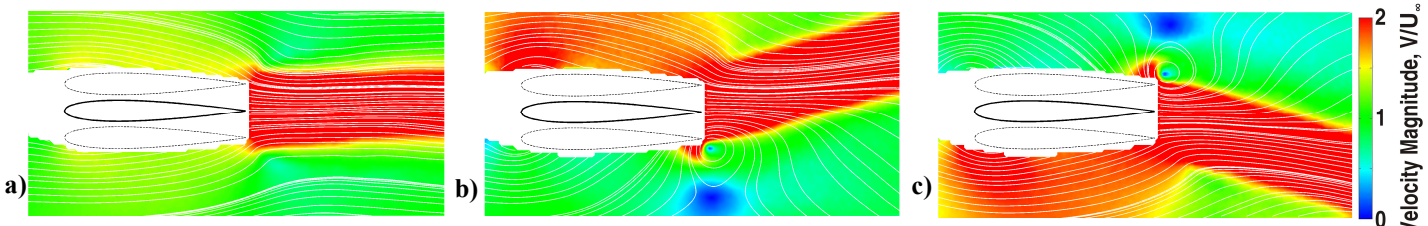

Fig. 4.2 Time-averaged velocity magnitude for a/c = 0.150, α = 0°, and: a) Sr_c = 1.500 - pre-bifurcation, b) Sr_c = 2.025 – mode A, and c) Sr_c = 2.025 – mode B.

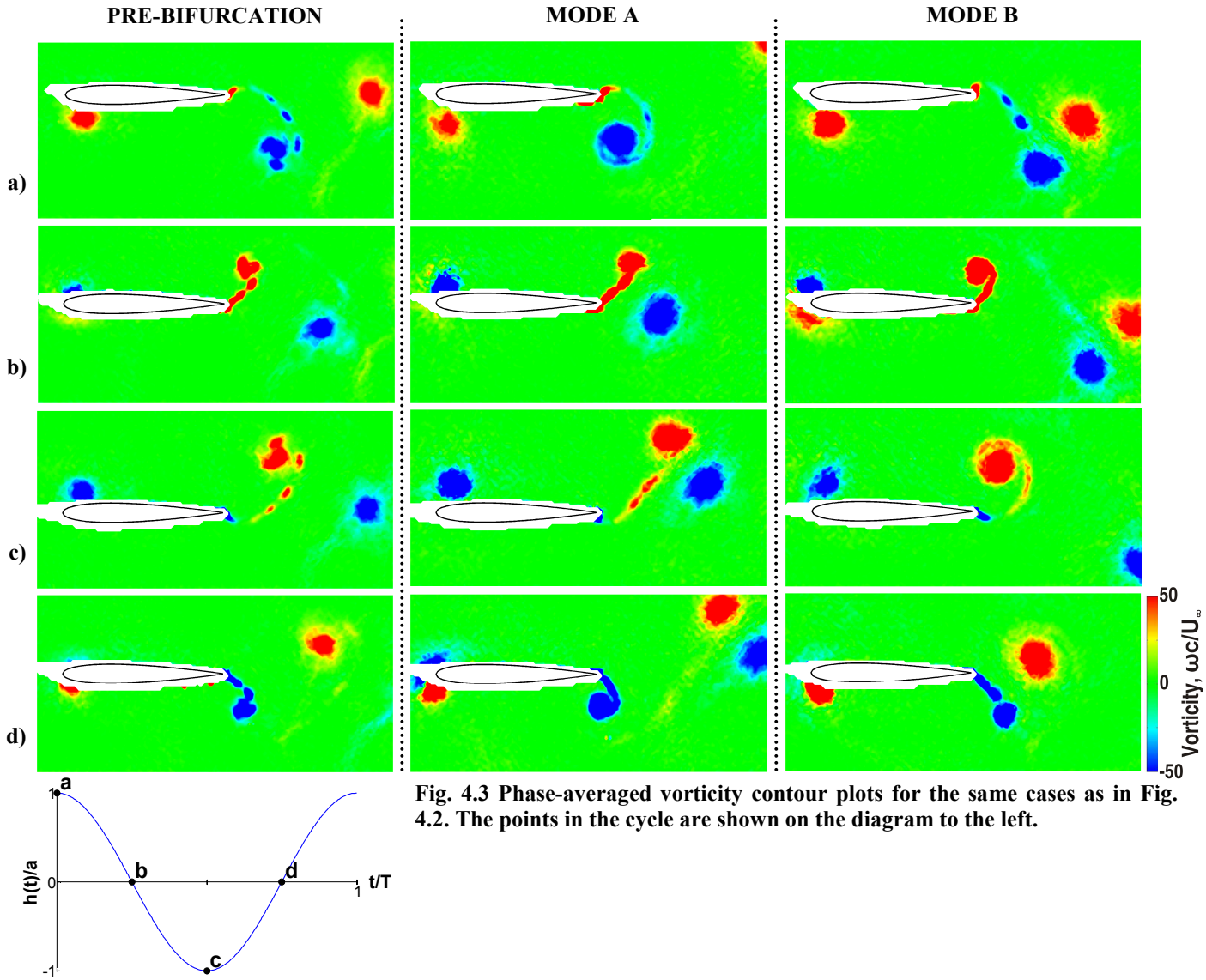

Fig. 4.3 Phase-averaged vorticity contour plots for the same cases as in Fig. 4.2. The points in the cycle are shown on the diagram to the left.

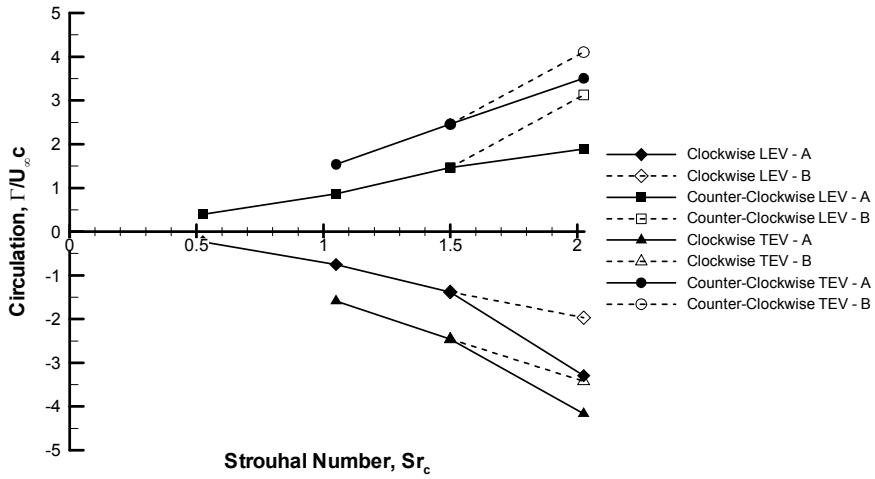

Fig. 4.4 Normalized peak circulation for both LEVs, and both TEVs for: a/c = 0.150, α = 0°.

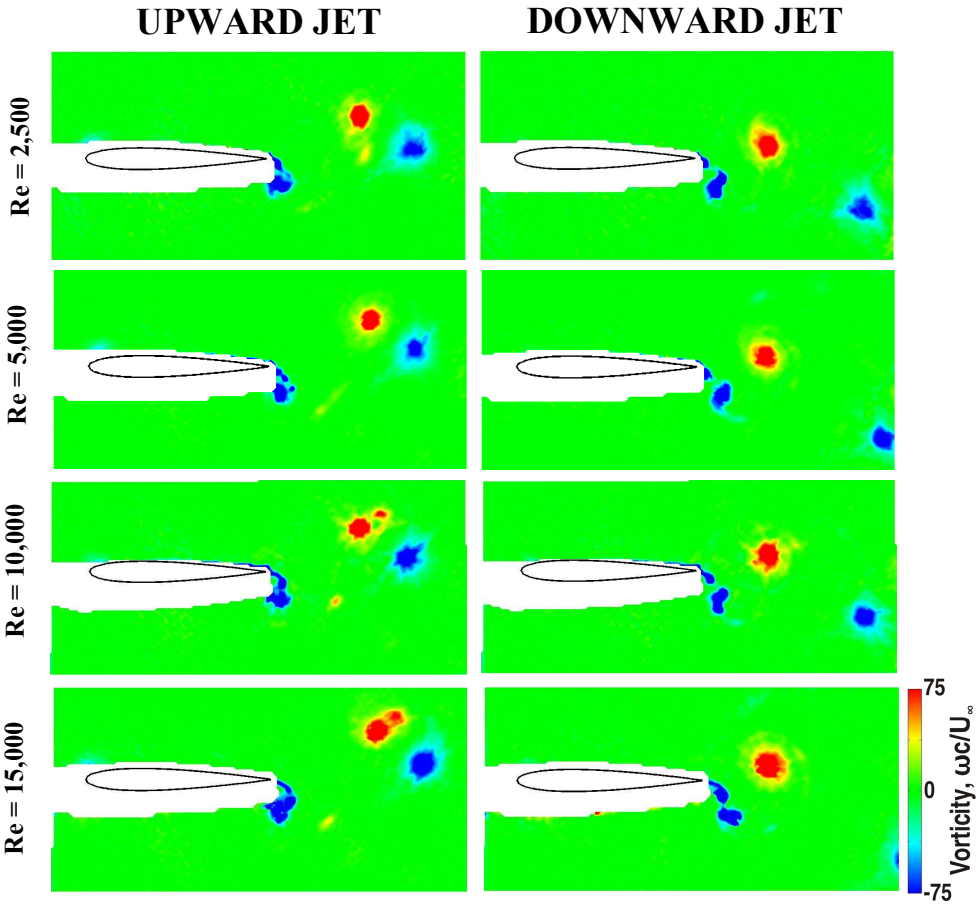

Fig. 4.5 Normalized vorticity for multiple Reynolds numbers. The Strouhal numbers were selected so as to demonstrate post-bifurcation wakes.

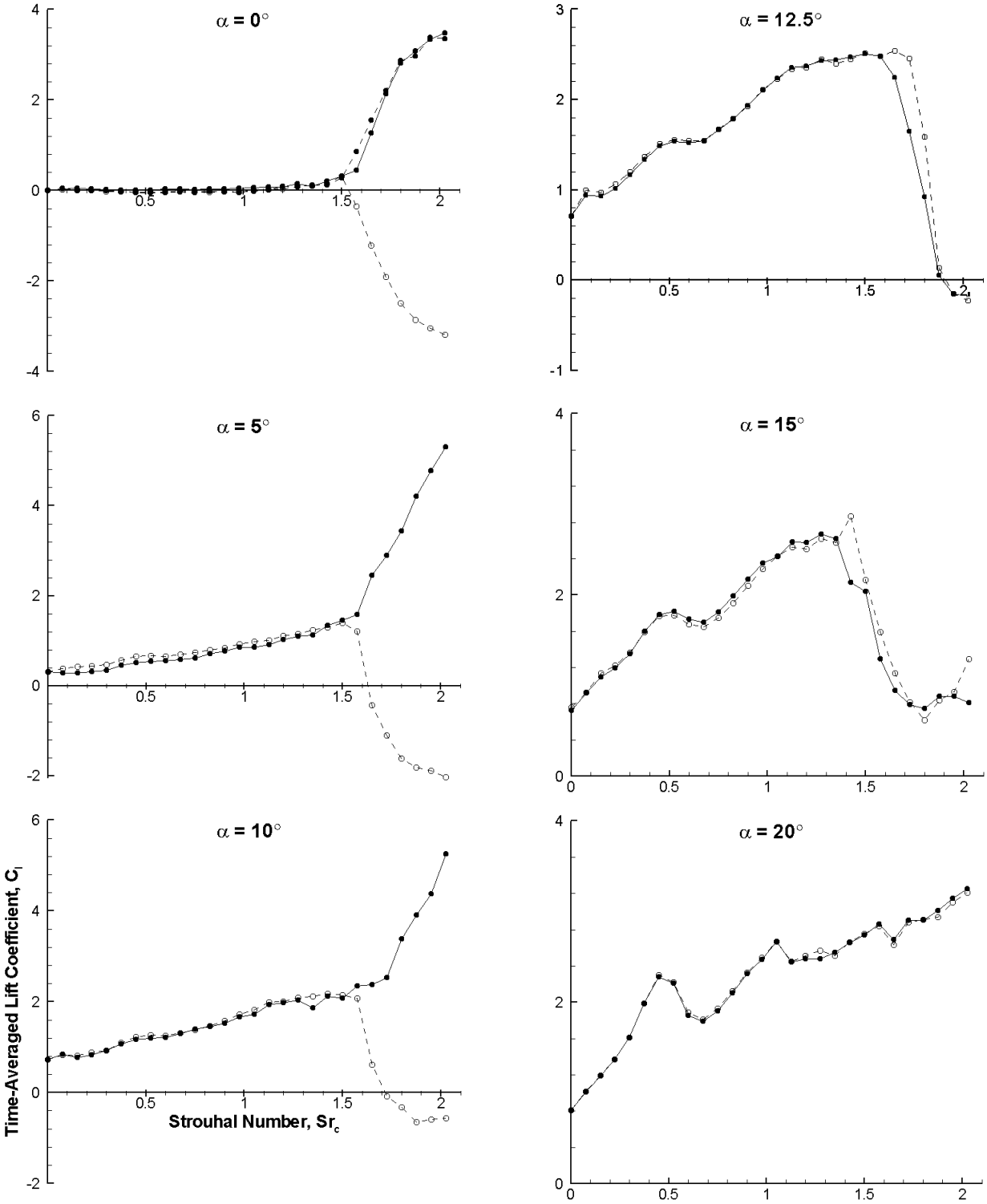

Fig. 4.6 Time-averaged lift coefficient for a/c = 0.15 and all angles of attack considered. Solid line represents increasing frequency, dashed line represents decreasing frequency with a starting position for α = 0° of $h_i = \pm a$, and for α > 0° $h_i = 0$ ($t_s/T = 0.75$).

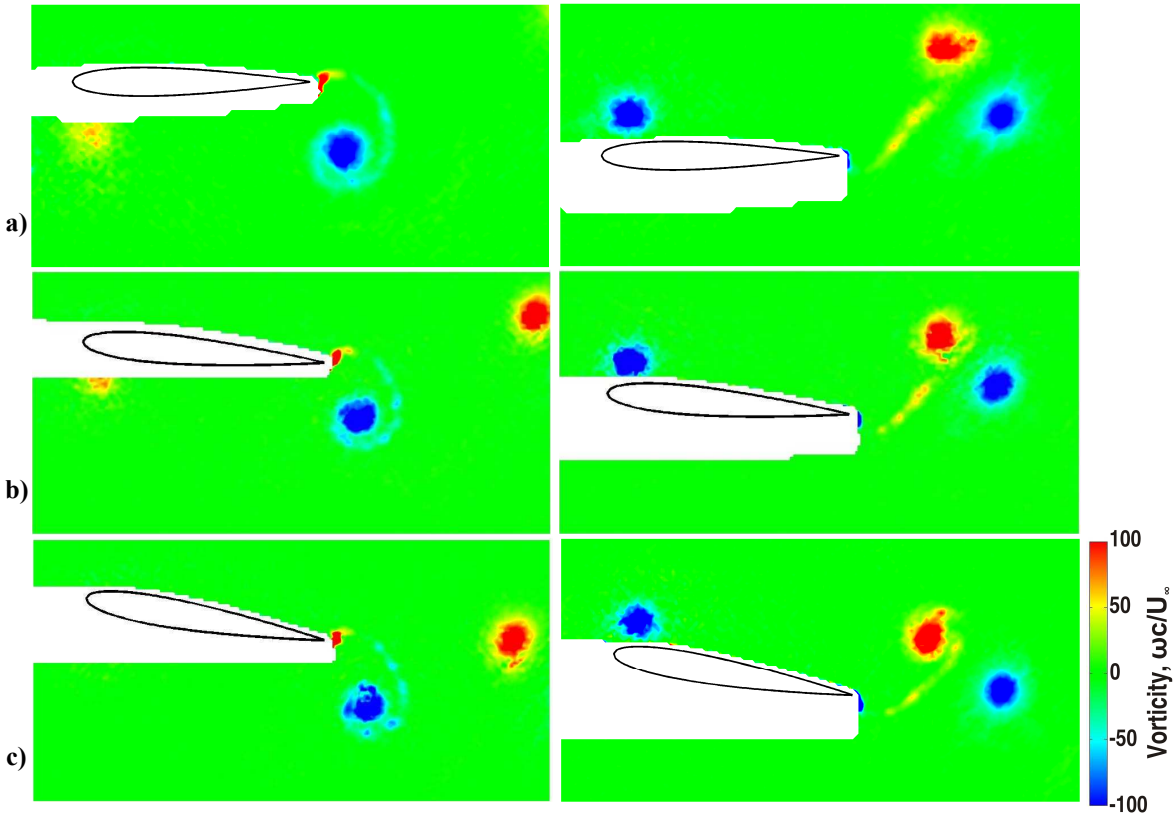

Fig. 4.7 Phase-averaged vorticity contour plots at the top (left) and bottom (right) of the motion comparing the mode A flowfield for a/c = 0.10, Sr_c = 2.50 and: a) α = 0°, b) b = 5°, and c) α = 10°.

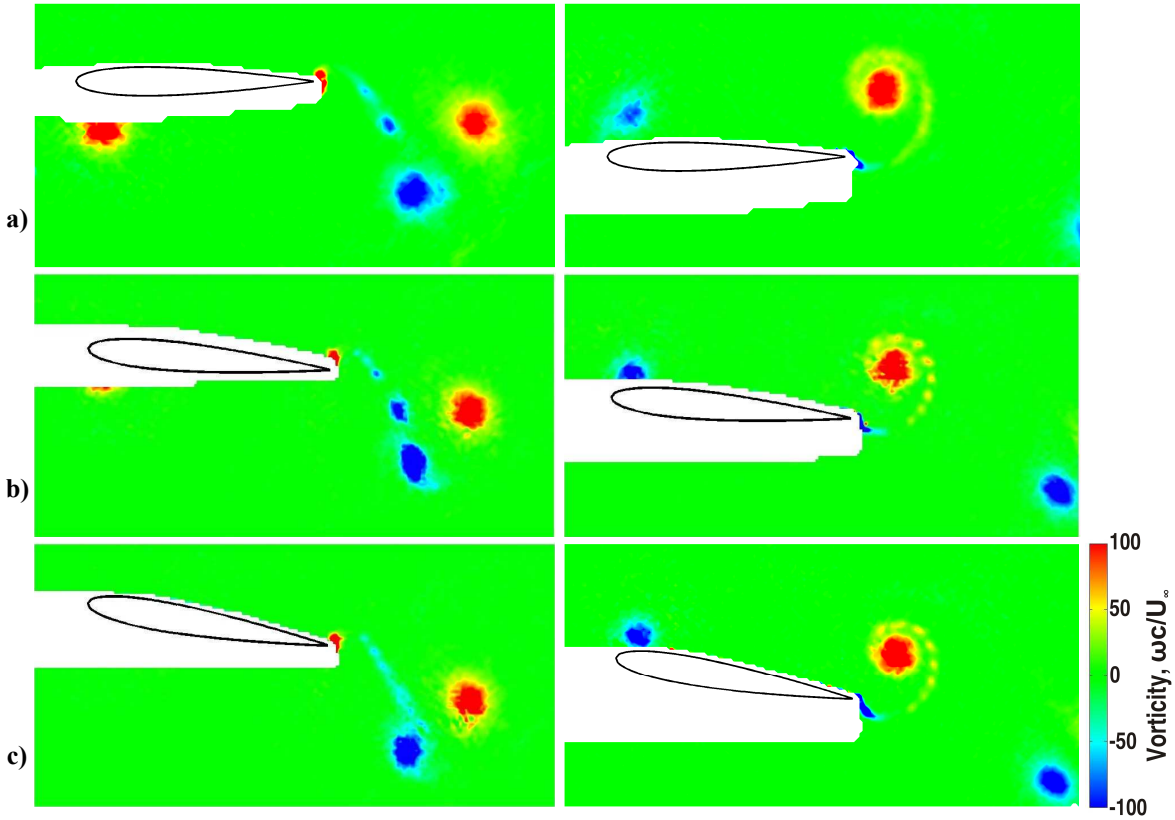

Fig. 4.8 Phase-averaged vorticity contour plots at the top (left) and bottom (right) of the motion comparing the mode B flowfield for a/c = 0.10, Sr_c = 2.50 and: a) α = 0°, b) b = 5°, and c) α = 10°

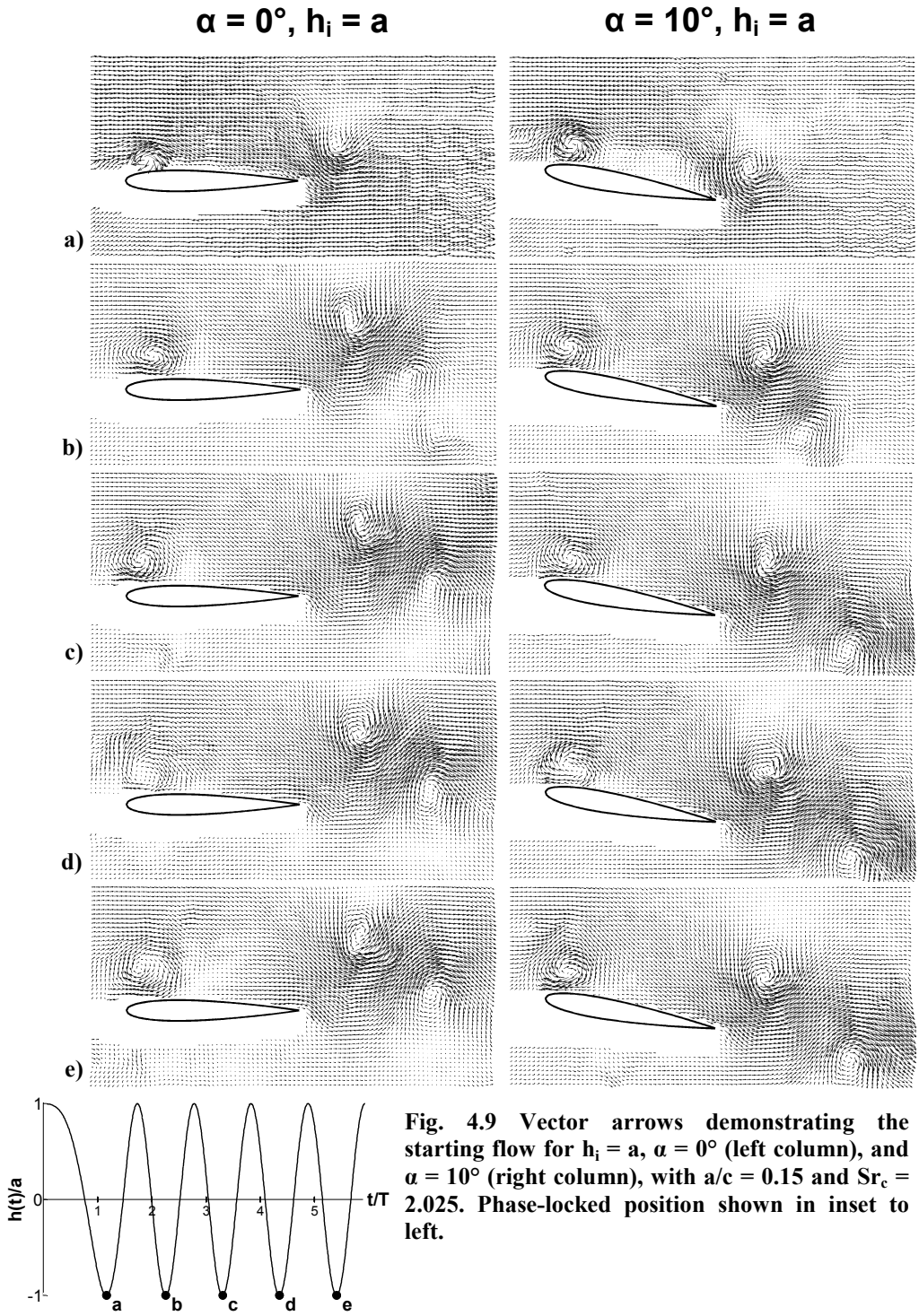

Fig. 4.9 Vector arrows demonstrating the starting flow for $h_i = a$, $\alpha = 0°$ (left column), and $\alpha = 10°$ (right column), with $a/c = 0.15$ and $Sr_c = 2.025$. Phase-locked position shown in inset to left.

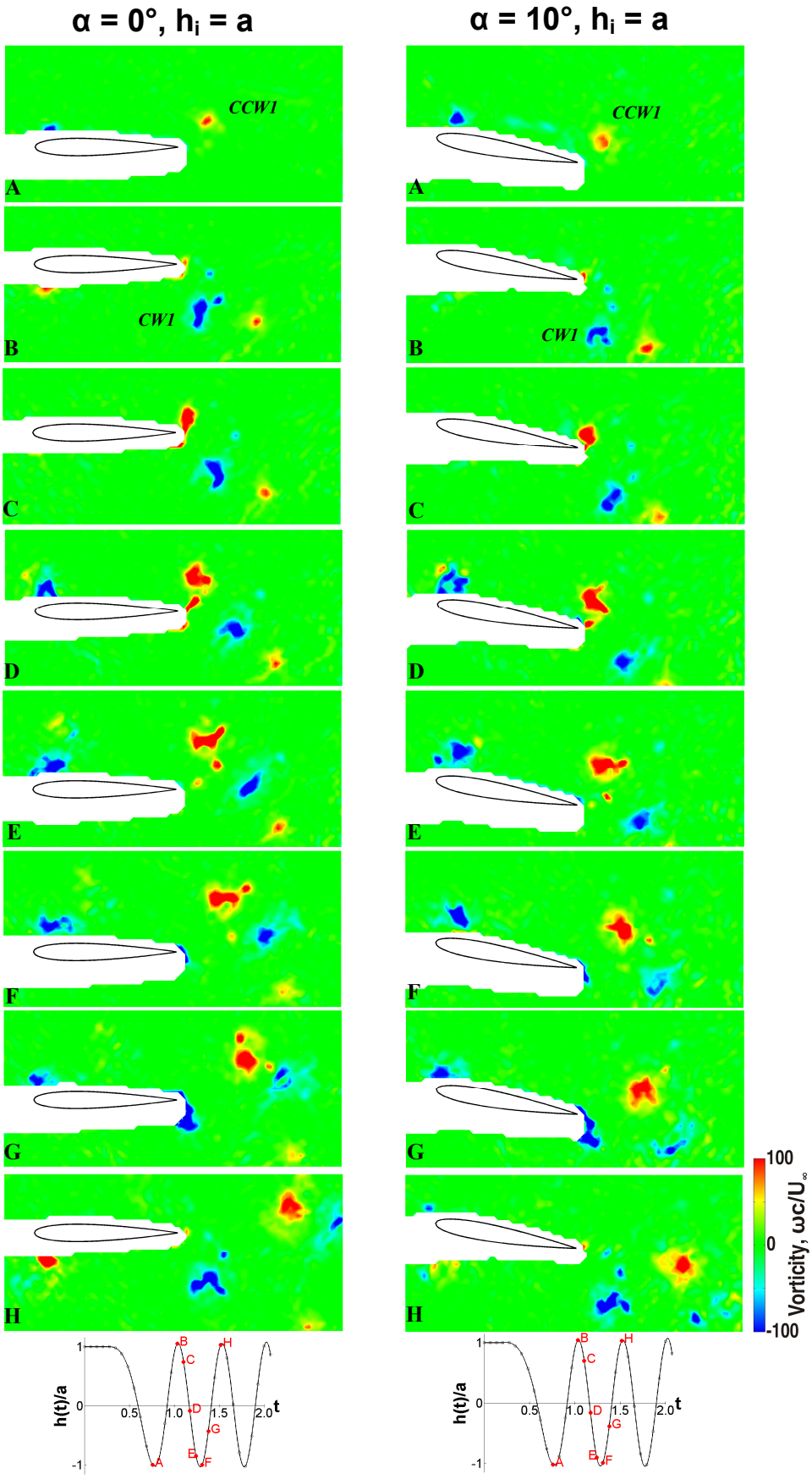

Fig. 4.10 Normalized vorticity of the instantaneous flow field for a/c = 0.15, and Sr_c = 2.025. Note the stronger first counter-clockwise vortex (CCW1) in the α = 10° case. This pairs with the first clockwise vortex, drawing it downwards and thereby creating a downward deflected jet.

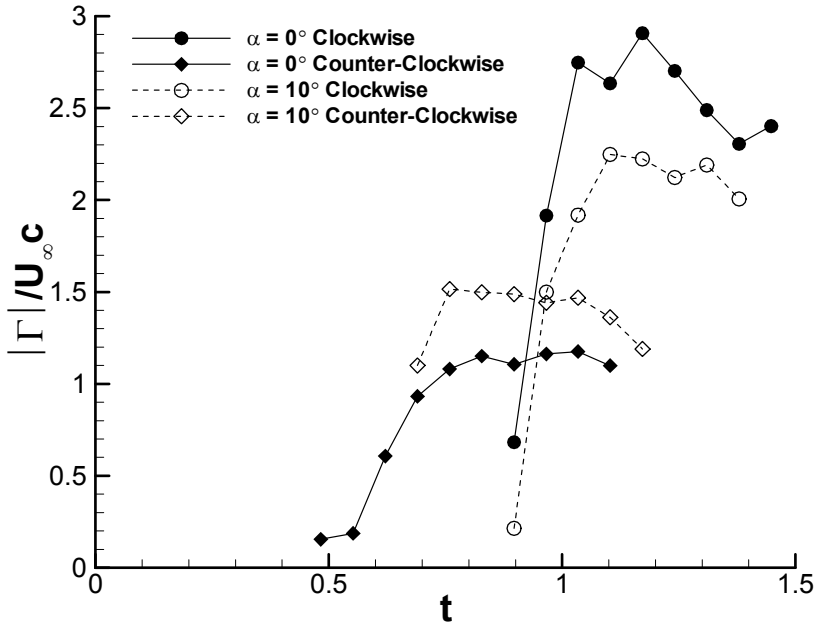

Fig. 4.11 Normalized circulation of the first two trailing edge vortices formed during the starting process from $h_i = a_s = 0$, for $\alpha = 0°$ and $\alpha = 10°$.

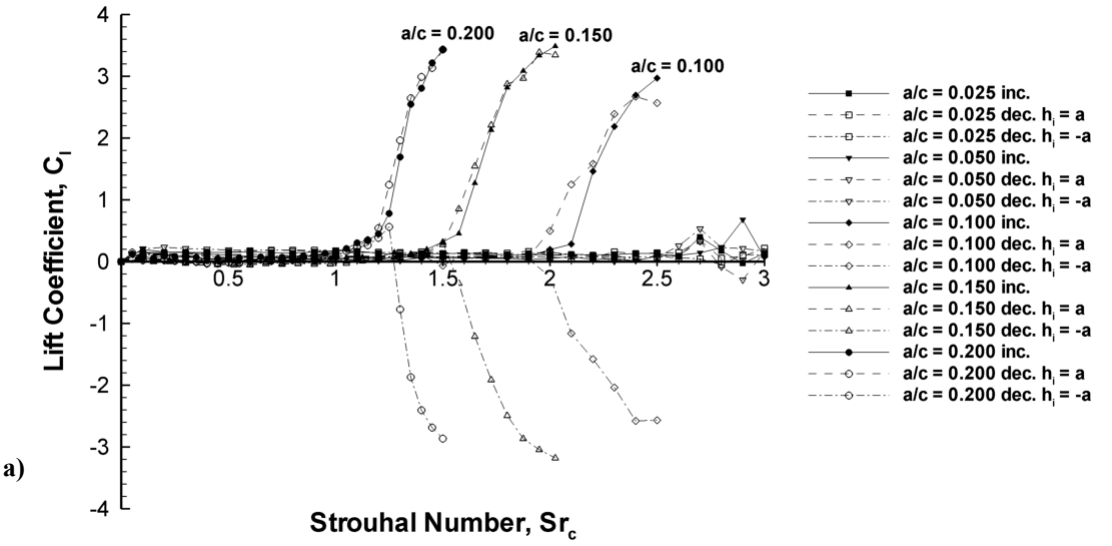

a)

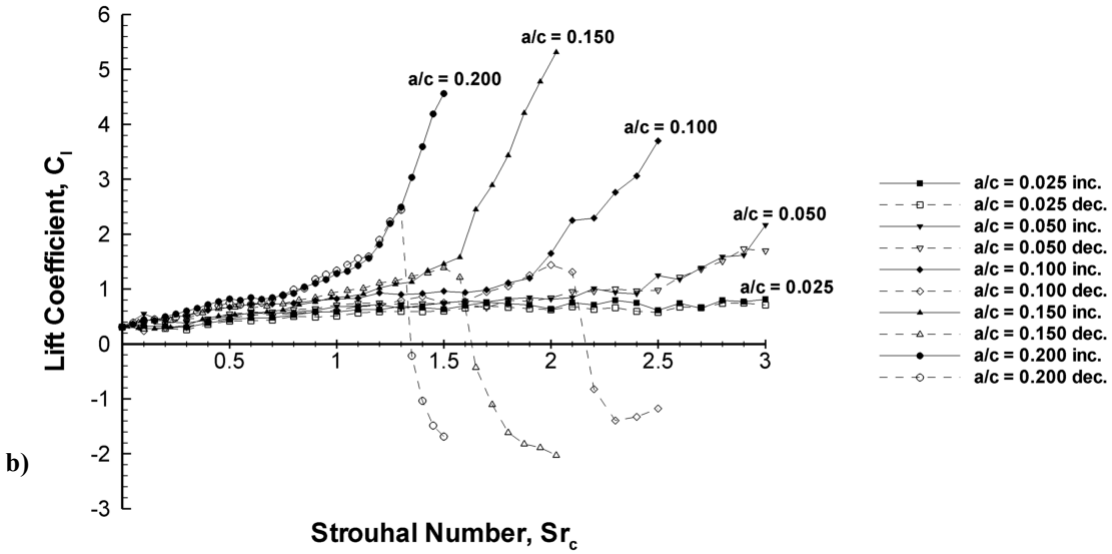

b)

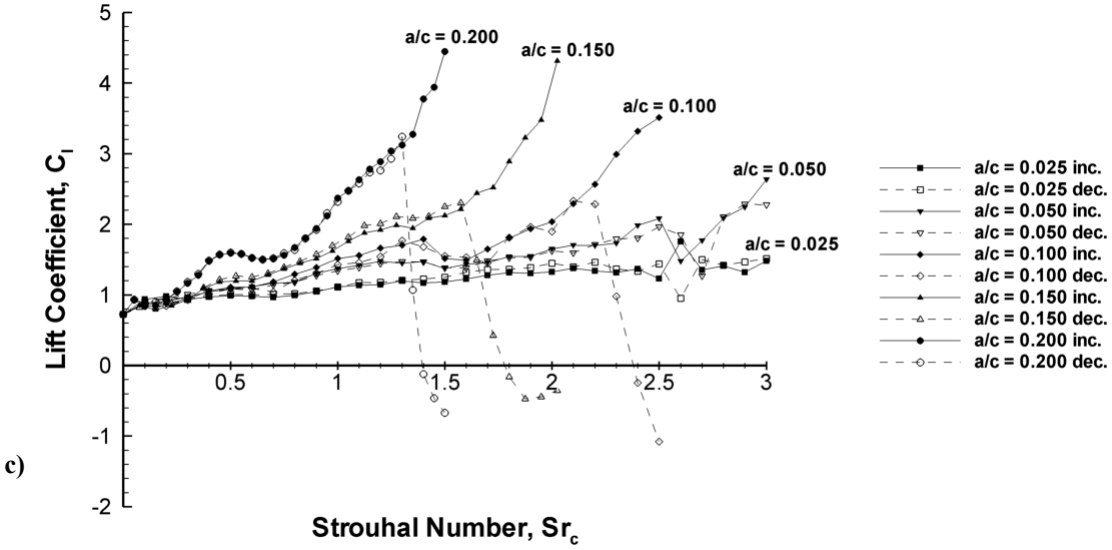

c)

Fig. 4.12 Lift coefficient as a function of Strouhal number for: a) α = 0°, b) α = 5°, c) α = 10°, and d) α = 15°. Increasing frequency: solid lines and full symbols; decreasing frequency: dashed lines and open symbols. Unless stated in the legend the starting position for decreasing frequency is $h_i = 0$ ($t_s/T = 0.25$). Continued on next page.

d)

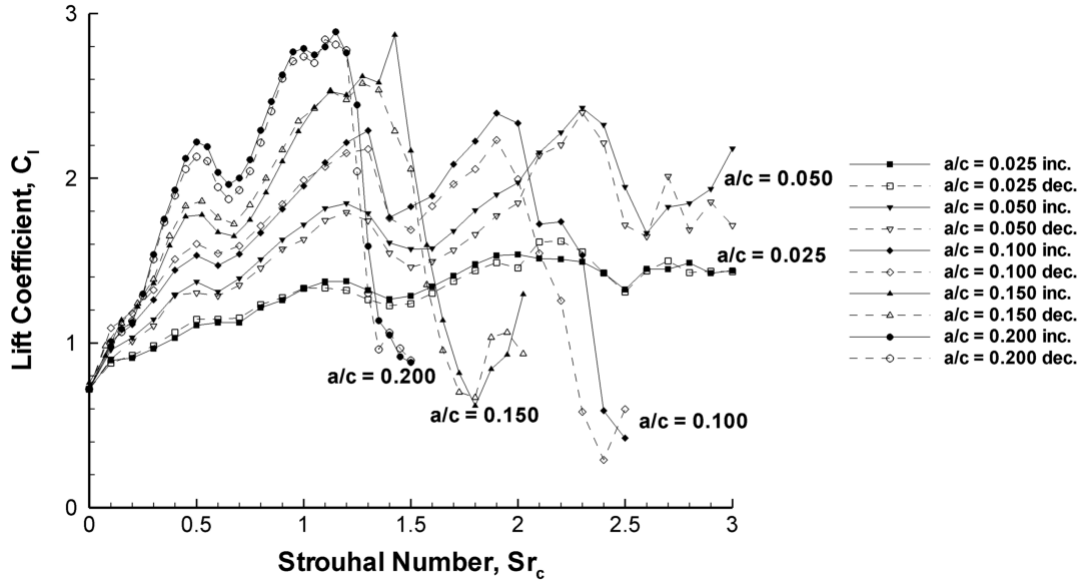

Fig. 4.12. Continued

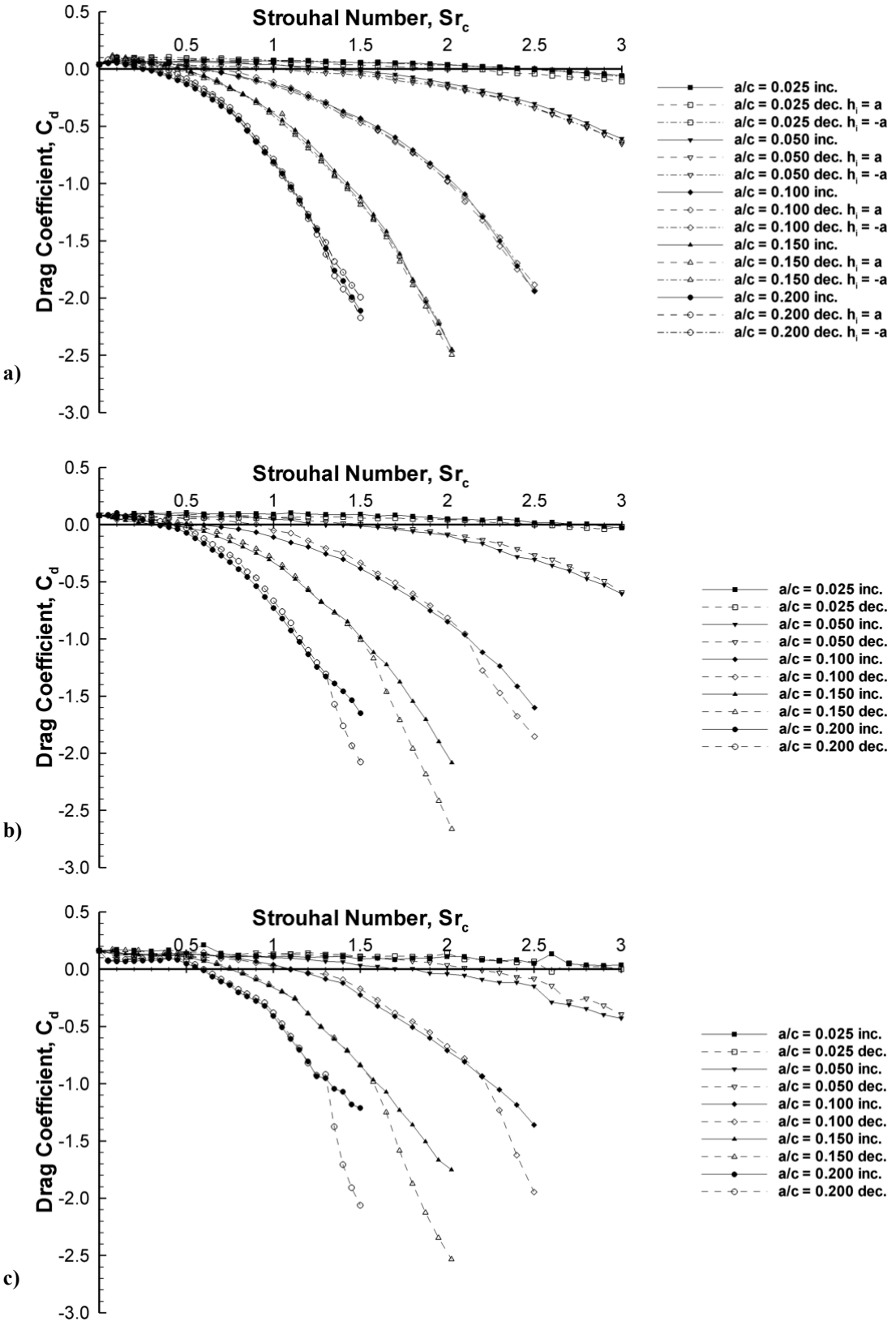

Fig. 4.13. Drag coefficient as a function of Strouhal number for: a) α = 0°, b) α = 5°, c) α = 10°, and d) α = 15°. Increasing frequency: solid lines and full symbols; decreasing frequency: dashed lines and open symbols. Unless stated in the legend the starting position for decreasing frequency is $h_i = 0$ ($t_s/T = 0.25$). Continued next page.

d)

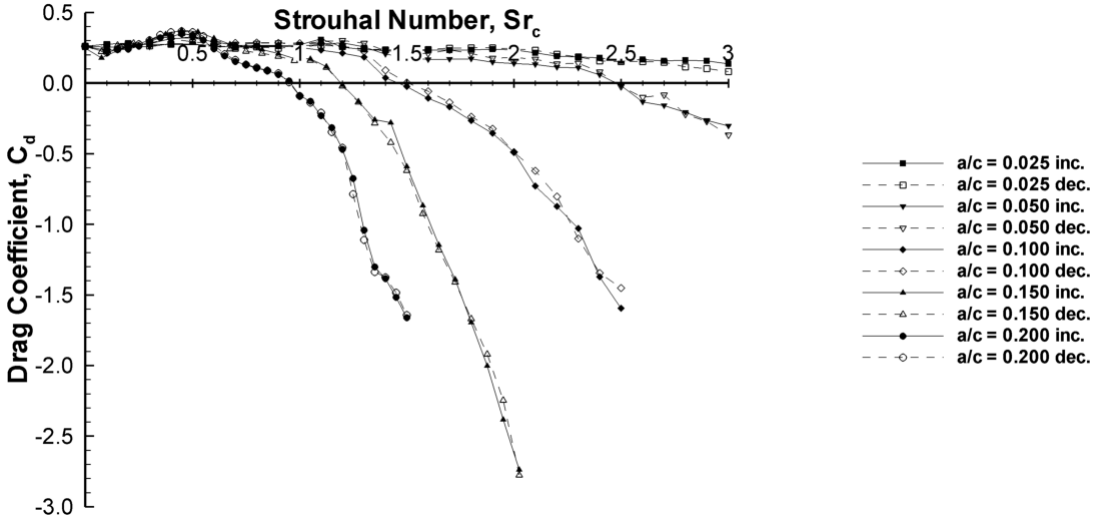

Fig. 4.13. Continued

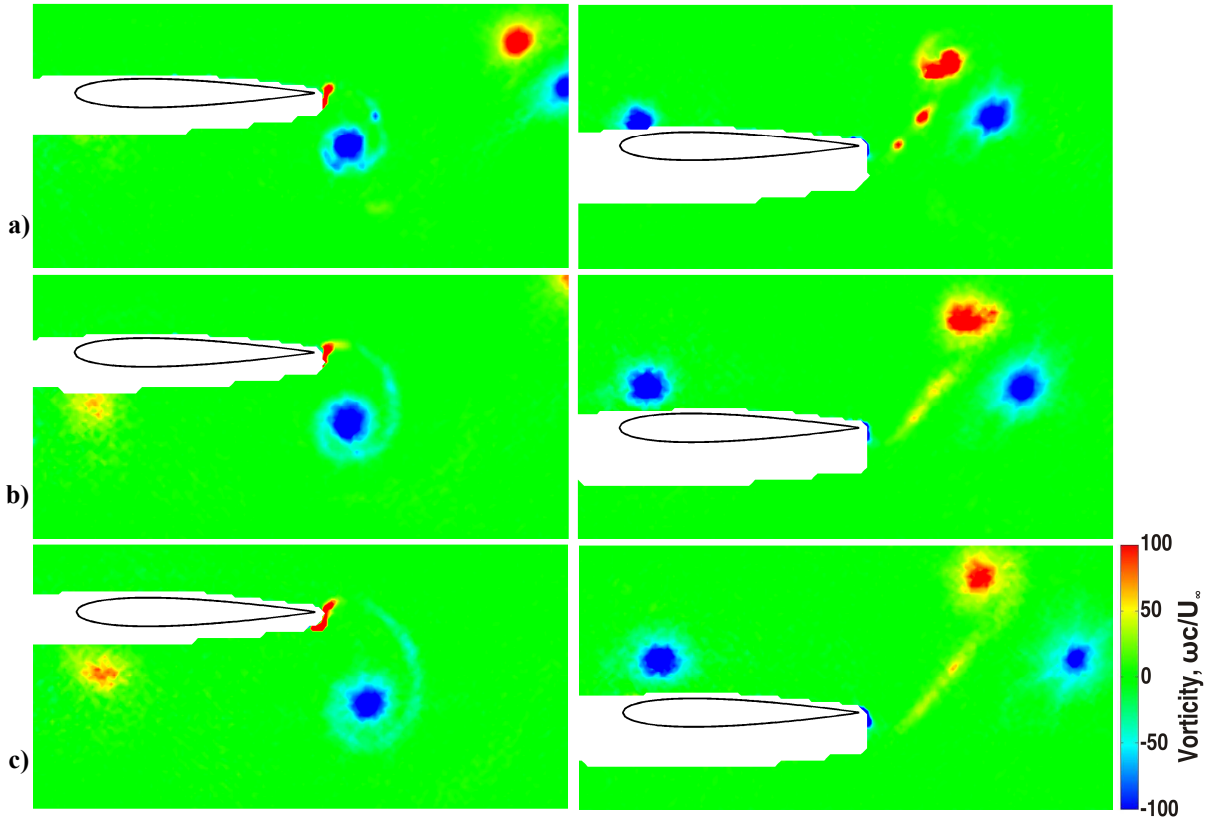

Fig. 4.14 Phase-averaged vorticity contour plots at the top (left) and bottom (right) of the motion comparing the mode A flowfield for α = 0°, and: a) a/c = 0.10, Sr_c = 2.5, b) a/c = 0.15, Sr_c = 2.025, and c) a/c = 0.20, Sr_c = 1.5.

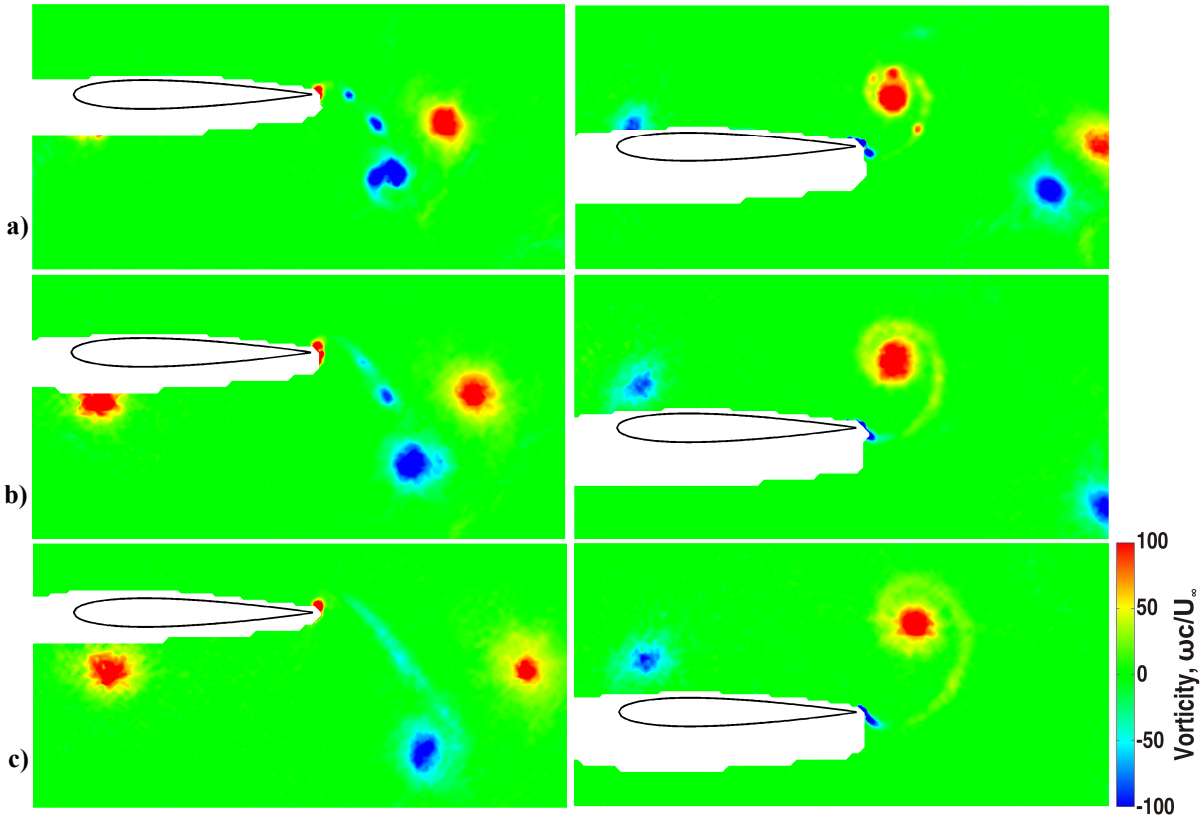

Fig. 4.15 Phase-averaged vorticity contour plots at the top (left) and bottom (right) of the motion comparing the mode B flowfield for $\alpha = 0°$, and: a) $a/c = 0.10$, $Sr_c = 2.5$, b) $a/c = 0.15$, $Sr_c = 2.025$, and c) $a/c = 0.20$, $Sr_c = 1.5$.

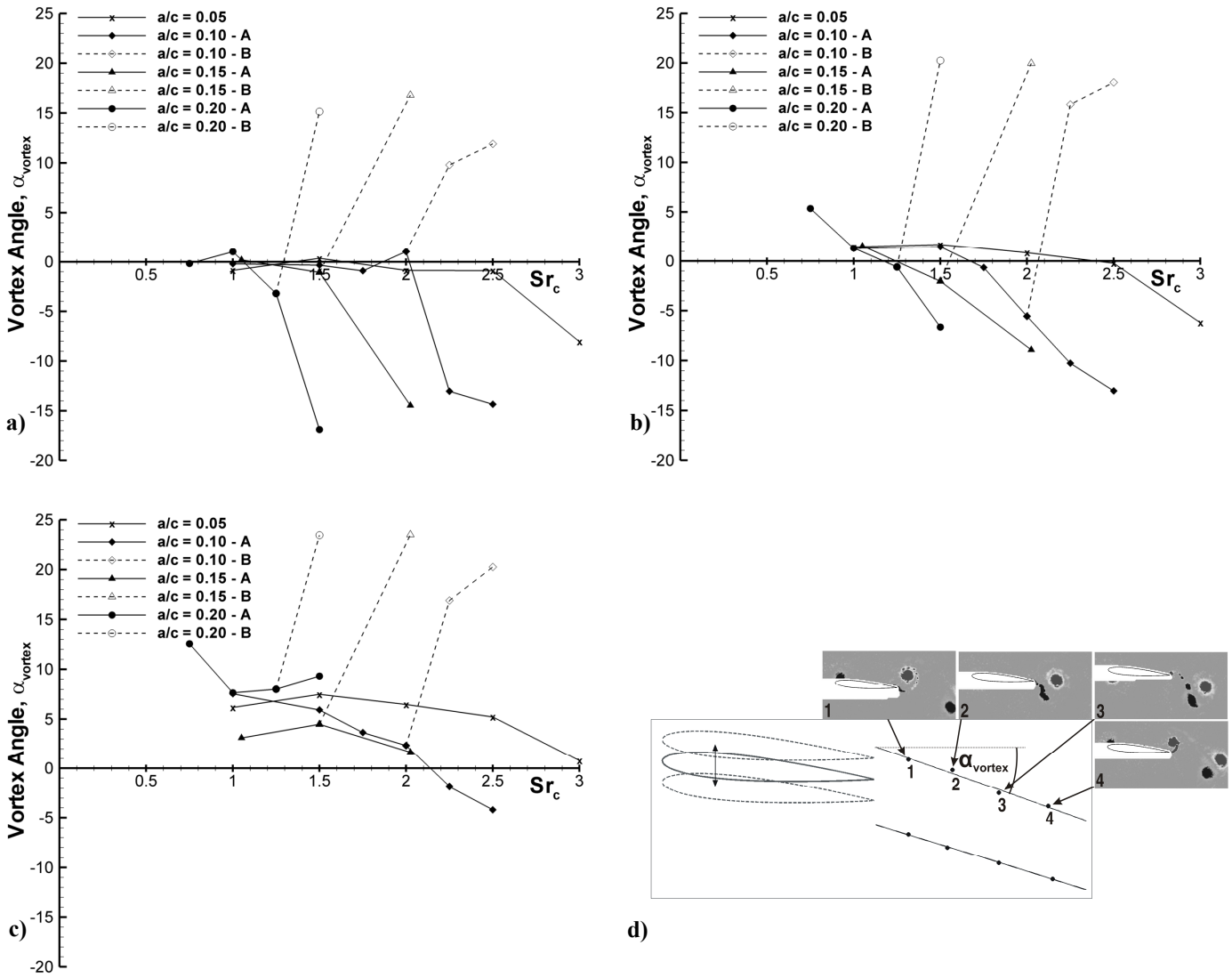

Fig. 4.16 Trailing edge vortex trajectory angle for: a) α = 0°, b) α = 5°, and c) α = 10°; and d) method used to determine α_{vortex} for the counter-clockwise TEV. It is first located in the phase-averaged data, a line of best fit is then applied giving a gradient related to α_{vortex}. α_{vortex} is negative for an upwards deflected jet, and positive for a downwards deflected jet.

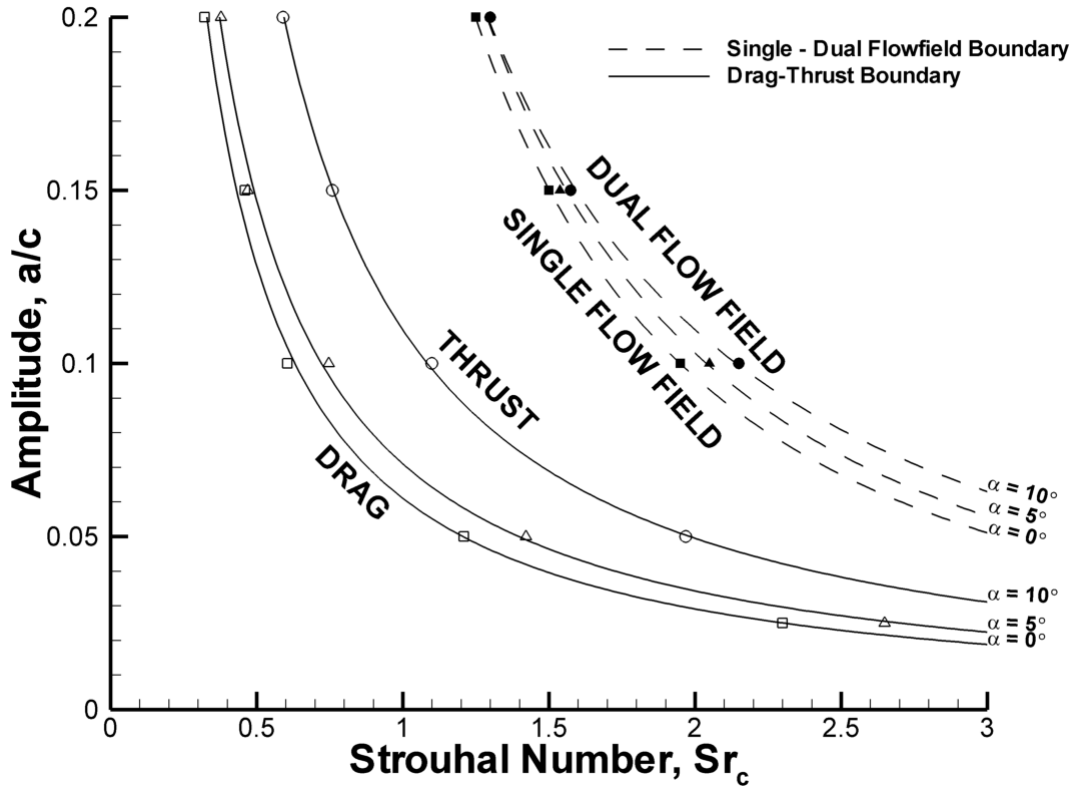

Fig. 4.17. Boundary between drag / thrust producing and single / dual flowfield for: α = 0° (square), α = 5° (triangle), and α = 10° (circle). Lines are power law curve fits.

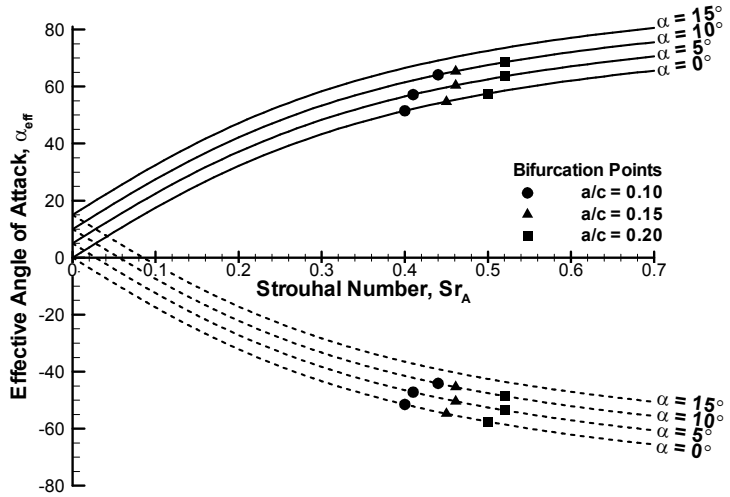

Fig. 4.18 Effective angle of attack as a function of Strouhal number based on amplitude. Solid line: $\alpha_{eff,max}$, dashed line: $\alpha_{eff,min}$. Symbols denote the point of bifurcation as determined from the force measurements.

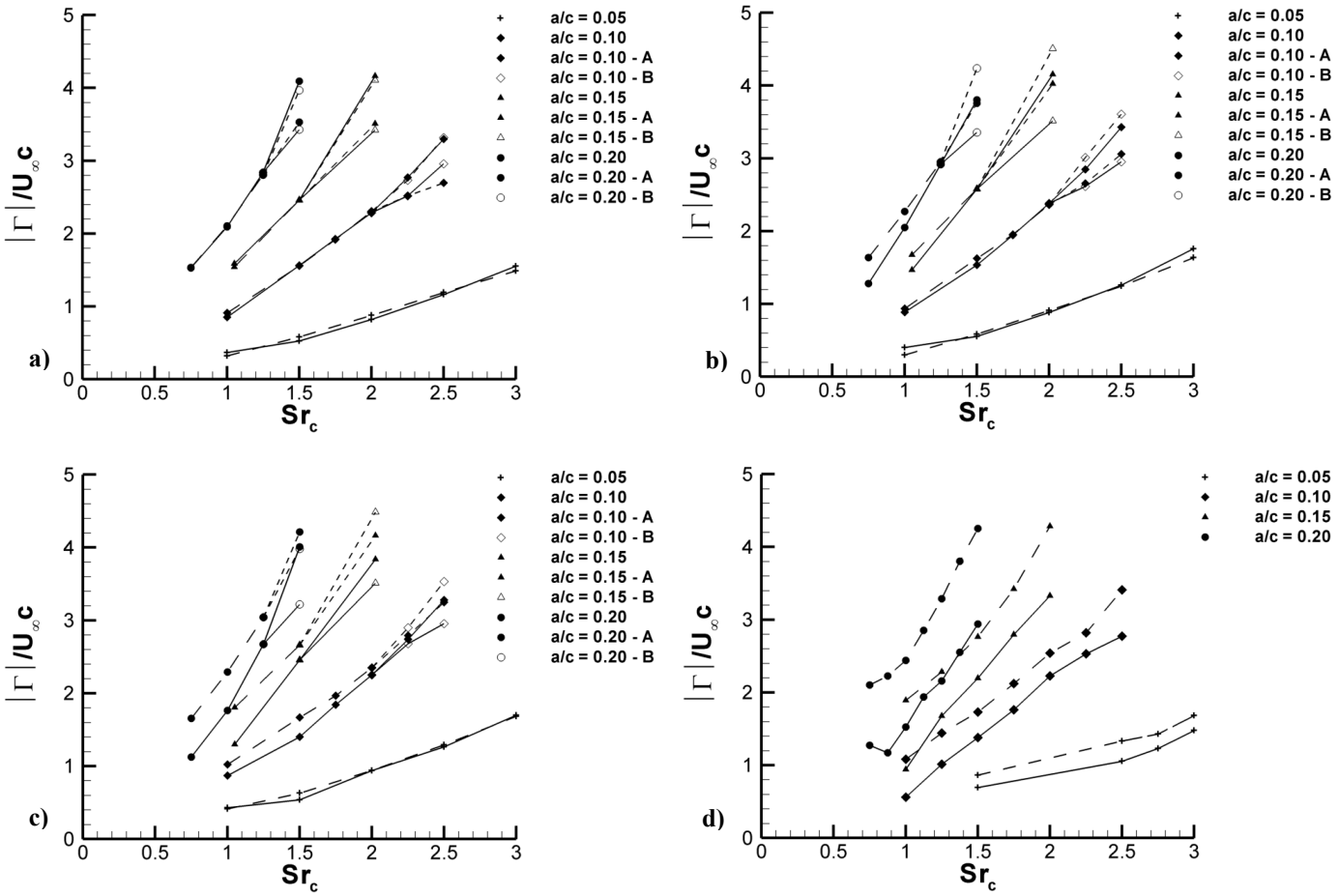

Fig. 4.19 Absolute circulation for: a) α = 0°, b) α = 5°, c) α = 10°, and d) α = 15°. Solid line represents the clockwise TEV, and dashed line the counter-clockwise TEV.

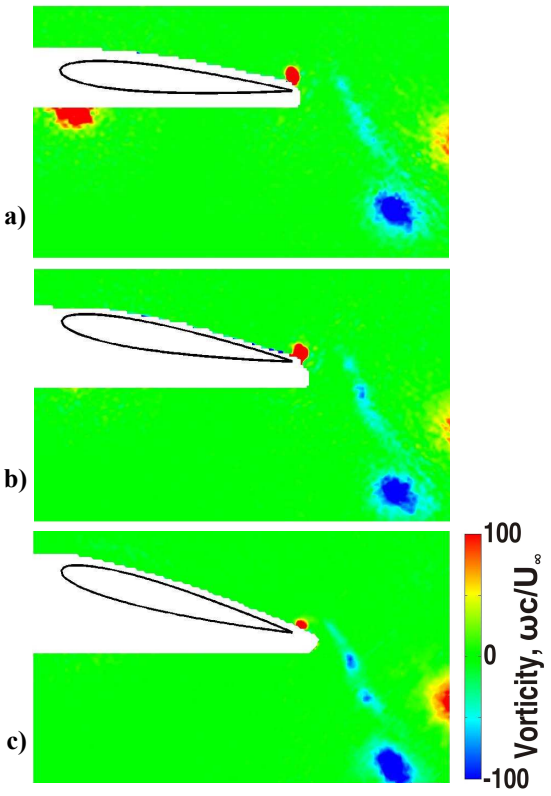

Fig. 4.20 Vorticity contours showing the similarity of flowfields across different angles of attack for a/c = 0.150, Sr_c=2.025 and: a) α = 5° - mode B, b) α = 10° - mode B, and c) α = 15°.

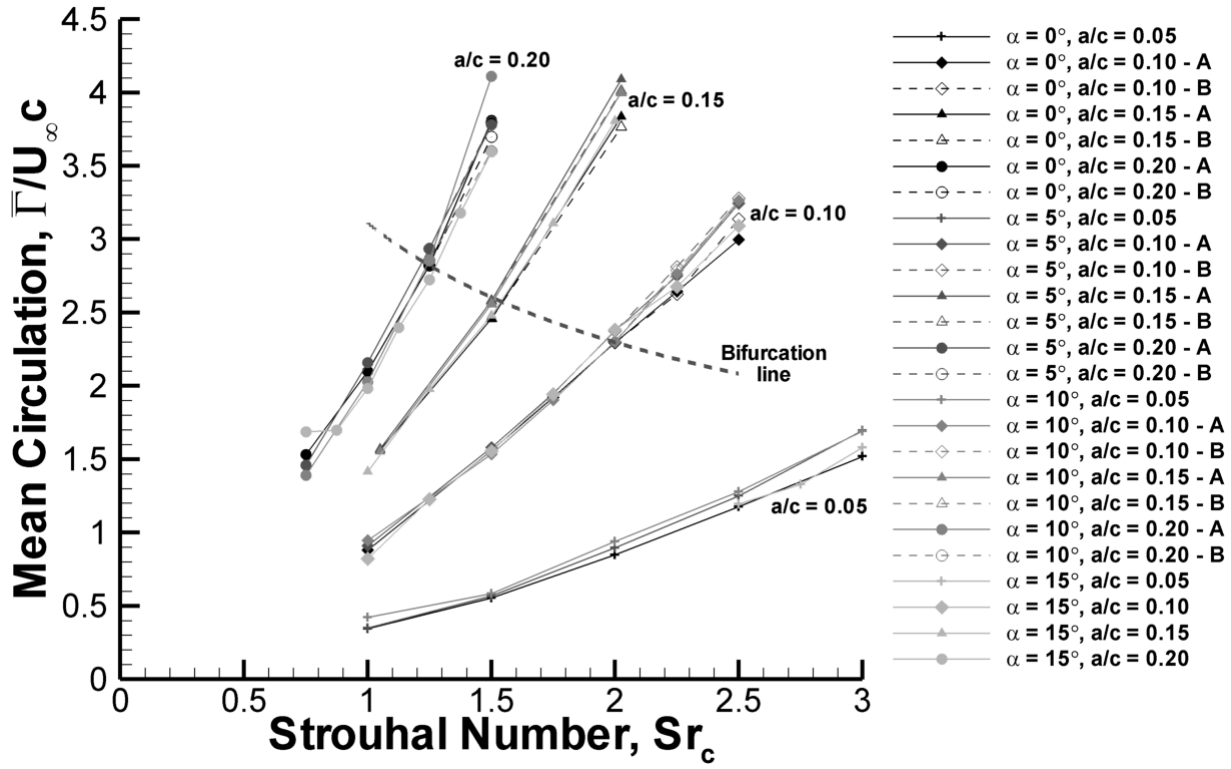

Fig. 4.21 Average absolute TEV circulation as a function of Strouhal number.

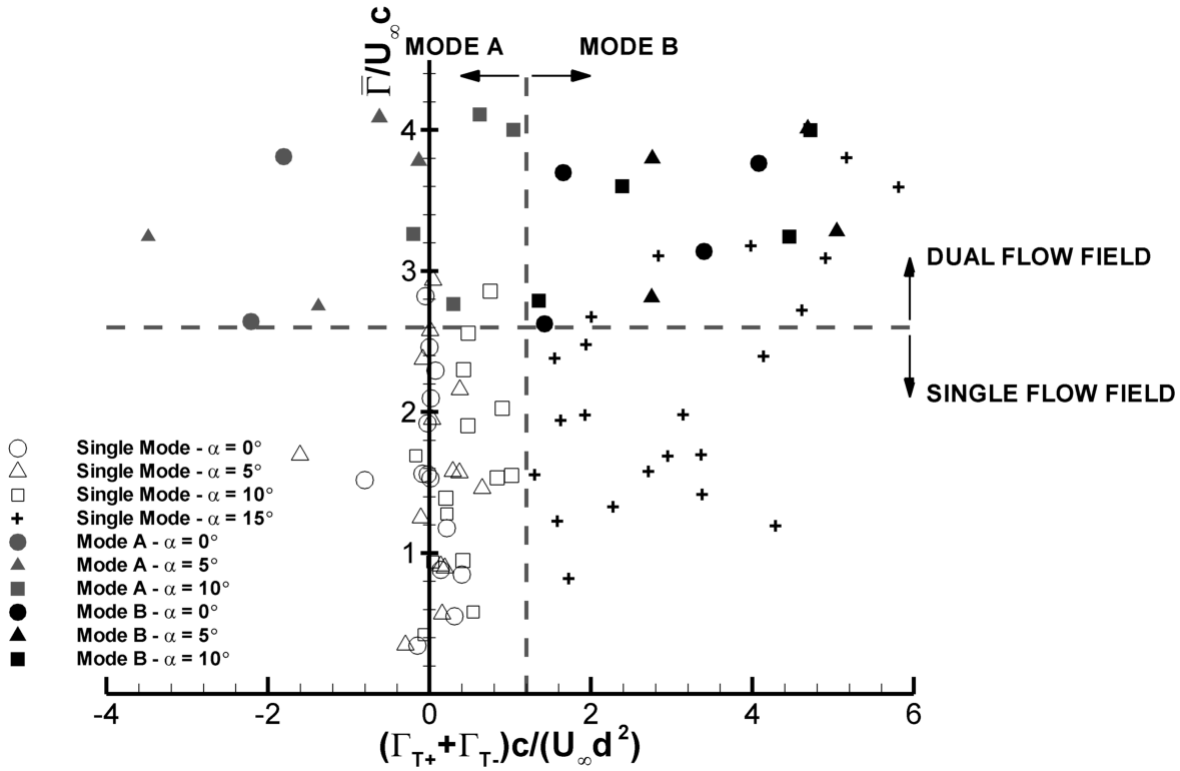

Fig. 4.22 Normalized circulation as a function of asymmetry parameter.

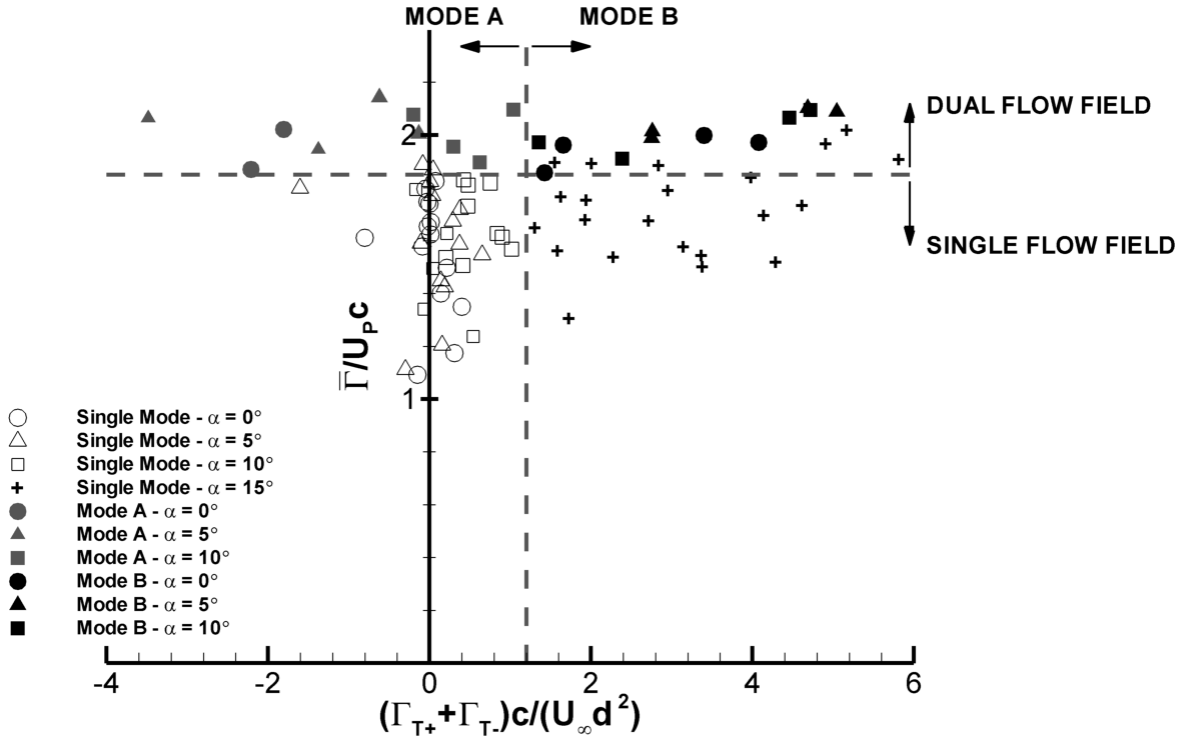

Fig. 4.23 Circulation normalized by plunge velocity as a function of asymmetry parameter.

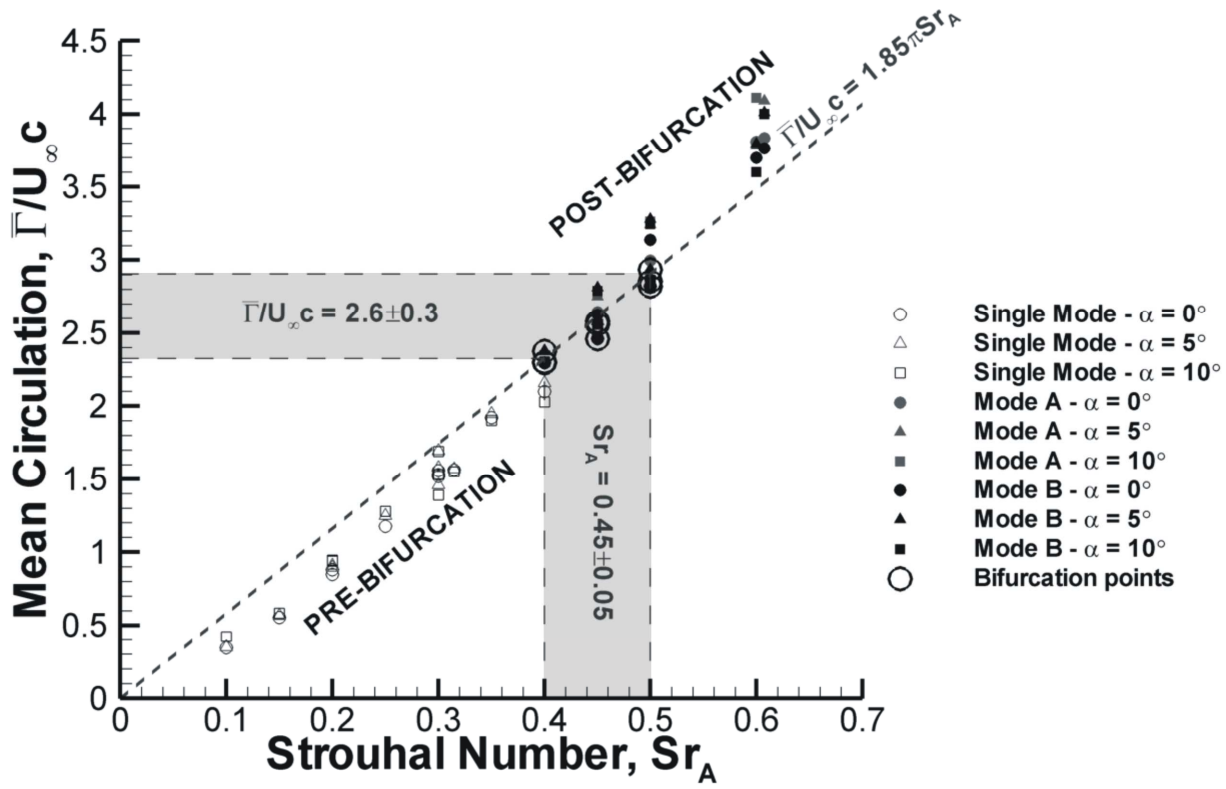

Fig. 4.24 TEV normalized circulation as a function of Strouhal number based on amplitude. Orange circles highlight the points of bifurcation. Grey dashed line of gradient 1.85π represents the bifurcation constant derived from Fig. 4.23.

CHAPTER 5. EFFECT OF GEOMETRY

5.0 SUMMARY

The effect of geometry is studied through comparison of the forces and flow fields associated with small-amplitude plunge oscillations of a NACA 0012 airfoil and flat plate at a Reynolds number of 10,000 and two angles of attack: zero degrees and fifteen degrees (post-stall). For zero degrees at high Strouhal numbers the NACA airfoil experiences stable deflected jets, whereas the flat plate experiences deflected jets that are prone to near sinusoidal oscillation in direction resulting in oscillation of the lift coefficient with a period on the order of 100 cycles. For fifteen degrees the flat plate is shown to produce a comparable increase in lift up to a Strouhal number of one, but after this the lift performance deteriorates. This deterioration is due to a new mode of LEV behaviour. Instead of the mode 2 flow field observed for the NACA 0012 airfoil, the flat plate upper surface LEV pairs with the lower surface LEV to form a dipole that self-advects normal to the free stream and is rapidly destroyed. The result is increased time-averaged separation and thus deteriorating lift performance and high drag.

5.1 RESULTS

In this section the effect of small-amplitude oscillations on the forces and flow fields of a flat plate and NACA 0012 airfoil will be considered for two angles of attack, α = 0° and 15°. Some of the results for the NACA 0012 airfoil have previously been presented in Chapters 3 and 4 but are repeated here to allow direct comparison. Where this occurs a brief summary of the relevant points will be given, for more detail see the applicable chapter.

5.1.1 Zero Degrees Angle of Attack

Shown in Fig. 5.1a is the time-averaged lift coefficient for a NACA 0012 airfoil oscillating at a range of Strouhal numbers, amplitude of a/c = 0.150, and α = 0°. These results are for the same case as previously used in Fig. 4.1a except with the individual runs shown so as to demonstrate repeatability. The solid line represents data collected by starting at $Sr_c = 0$ (stationary), and increasing the Strouhal number,

accumulating data at discrete points along the way. Dashed lines represent data collected by impulsively starting at the maximum Strouhal number, and then decreasing the Strouhal number, accumulating data at discrete points along the way. There are therefore three types of curves: one for increasing frequency; and two for decreasing frequency where starting positions of $h_i = +a$ and $h_i = -a$ are considered. Up to $Sr_c = 1.5$ all the curves match closely. After $Sr_c = 1.5$ the curves bifurcate producing two distinct results: the runs for increasing and decreasing ($h_i = a$) frequency produce very large positive lift coefficients; decreasing ($h_i = -a$) frequency produces very large negative lift coefficients. As discussed in chapter 4, the large positive lift coefficients are due to a mode-A flowfield. This is characterized by an upwards deflected jet created by the clockwise TEV loitering over the airfoil to pair with the counter-clockwise TEV and thereby form a vortex dipole with an upwards inclination. The large negative lift coefficients are associated with a mode-B flow field which is the inverse, i.e., the counter-clockwise vortex loiters to form a downward inclined vortex dipole and thereby a downwards deflected jet.

Fig. 5.1b shows the same measurements except for the flat plate. Up until $Sr_c = 1.5$ all curves match closely following similar trends to those observed for the NACA 0012 airfoil. After $Sr_c = 1.5$ however the curves diverge significantly giving very erratic results with no repeatability. Despite the apparent randomness, these results fall within an upper and lower bound which bear a strong resemblance to those for the NACA 0012 airfoil, and with the same point of divergence. This suggests that deflected jets are also responsible in this case but that their direction is unstable, in a similar manner to the jet switching phenomenon observed by Heathcote et al. [67].

Force measurements were therefore performed over a much larger time period for the flat plate; however instead of averaging over the whole time period, the signal is averaged over individual cycles, see Fig. 5.2. Fig. 5.2 demonstrates that the lift force oscillates approximately sinusoidally with amplitude of $C_l \approx 5$ and period on the order of 100 plunge cycles. Using a sample size of 60 cycles, as in Fig. 5.1, is therefore insufficient to accurately capture an average. 6000 cycles would be more appropriate but experimentally inconvenient. The period of this oscillation correlates

well with the values observed by Heathcote et al. for periodic jet switching of rigid and flexible airfoils oscillating in still fluid.

To capture the phenomenon responsible for the oscillatory lift coefficient phase-locked instantaneous PIV measurements were performed in conjunction with simultaneous force measurements, a selection are shown in Fig. 5.3. The flow field in the top row shows a vortex dipole pairing that due to its position would result in a downwards deflected jet. The cycle-averaged lift coefficient in this case is C_l = -5.1. The correlation between downward deflected jet and large negative lift coefficient mirrors that observed for the NACA 0012 airfoil. In the next row the TEV behaviour is significantly different. The vortices are not paired and instead convect approximately horizontally. The lift coefficient for this case is C_l = -1.1. In the next row there is now an established upwards deflected jet with close vortex pairing which coincides with a lift coefficient of C_l = 5.5. Fig. 5.3 thus demonstrates that jet switching is responsible for the oscillation in lift coefficient with the downward deflected jet associated with very large negative lift coefficients and the upwards deflected jet associated with very large positive lift coefficients. Animations of the process show the transition from one to the other to be gradual, not distinct, justifying the approximately sinusoidal variation in lift coefficient observed in Fig. 5.2 and Fig. 5.3.

As further evidence of the existence of jet switching the position and circulation of the trailing-edge vortices in the instantaneous phase-locked PIV results was measured, see Fig. 5.4. Fig. 5.4a shows the vertical position of both the clockwise and counter-clockwise TEV, see Fig. 5.4c for more detail. The position of both clockwise and counter-clockwise TEV clearly oscillates almost sinusoidally with a period on the order of 100T. Indeed a sine curve fitted to the clockwise vortex Y_{TEV} position gives a period of 102T. Likewise the normalized circulation of the TEVs also oscillates with a period of approximately 100T although the trend is not as sinusoidal, see Fig. 5.4b. Using these instantaneous measurements it is possible to make a direct comparison between the NACA 0012 bifurcation modes and their flat plate equivalents. The equivalents are defined by the position, Y_{TEV}, of the clockwise vortex (see Fig. 5.4a). The 50 instantaneous flowfields (10%) with the largest

clockwise Y_{TEV} values are defined as mode A equivalent (upward deflected jet); inversely the 50 instantaneous flowfields (10%) with the smallest clockwise Y_{TEV} values are defined as mode B equivalent (downward deflected jet). Using this definition a comparison of typical instantaneous NACA flowfields and their flat plate equivalents is shown in Fig. 5.5.

Fig. 5.5 demonstrates that despite the differences in geometry the flowfields are qualitatively similar. For mode A for both geometries the vortex pairing is indicative of an upwards deflected jet, and for mode B the vortex pairing is indicative of a downwards deflected jet. The position and strength of the vortices is similar between the two flowfields, this is quantified in Table 4.

Table 4 Comparison of the mean instantaneous trailing-edge vortex characteristics for the NACA 0012 bifurcation flowfields and their flat plate equivalents for the single phase h = -a.

		Clockwise TEV			Counter-Clockwise TEV		
		X_{TEV}	Y_{TEV}	$\Gamma/U_\infty c$	X_{TEV}	Y_{TEV}	$\Gamma/U_\infty c$
A	**NACA 0012**	0.68	0.15	-4.12	0.44	0.48	3.62
	Flat Plate	0.67	0.14	-3.71	0.40	0.41	3.90
B	**NACA 0012**	1.04	-0.35	-2.98	0.16	0.31	4.33
	Flat Plate	0.94	-0.37	-2.81	0.16	0.26	4.55

Time-averaged lift coefficient measurements similar to those in Fig. 5.1 are shown for three further amplitudes in Fig. 5.6. For a/c = 0.025, all three cases approximately follow $C_l = 0$ suggesting that the maximum Strouhal number tested was insufficient for deflected jets to occur. For a/c = 0.10 and 0.20 there is however a clear point of bifurcation which closely correlates with those observed for the NACA 0012 airfoil. After bifurcation the lift curves are erratic with a slight preference towards positive lift coefficients. The erratic nature of the curves suggests that unstable deflected jets also occur at these amplitudes.

The core question is therefore what aspect of the flat plate geometry makes it subject to jet switching when the NACA 0012 airfoil at the same conditions is not. The obvious choice would be the rounded trailing-edge however as will be shown in the next section the leading-edge behaviour of the flat plate is also significantly different and so cannot be excluded as a possibility.

5.1.2 Post-Stall Incidence, α = 15°

Shown in Fig. 5.7 is the time-averaged lift, drag, and power coefficient for a NACA 0012 airfoil (left column) and flat plate (right column) oscillated at a post-stall angle of attack of α = 15°, range of amplitudes and range of Strouhal numbers. The results for the NACA 0012 airfoil have previously been discussed in detail in chapter 3. In summary: at low Strouhal numbers small-amplitude airfoil oscillations increase lift coefficient significantly with greater effect for greater amplitude. The largest increase observed is therefore for the largest amplitude of a/c = 0.2 and 305% over the value for a stationary airfoil. It was shown that lift coefficient increases approximately proportionally to the non-dimensional plunge velocity, $Sr_A = fA/U_\infty$, and that superimposed onto this linear trend are local optima. These can be seen as the peaks at $Sr_c \approx 0.5$, 1, and for smaller amplitudes $Sr_c \approx 2$. Hot-film measurements showed these to be due to resonance with the natural shedding frequency, its harmonics and subharmonics. At higher Strouhal numbers this linear trend is broken by a significant fall in lift, this can be seen around $Sr_c \approx 1.15$ for a/c = 0.2, $Sr_c \approx 1.5$ for a/c = 0.15, and $Sr_c \approx 2.0$ for a/c = 0.1. The cause of this fall has been shown to be a combination of the dissipation of the upper surface LEV and formation of a lower surface LEV. Small-amplitude airfoil oscillations can also improve drag performance significantly with greater effect for greater amplitude, see Fig. 5.5b left. The improvement is such that for the four larger amplitudes thrust is observed at higher Strouhal numbers. The switch from drag to thrust was shown to be highly dependent on the formation of what was termed a mode-2 flow field. This is characterized by the formation of an upper surface leading-edge vortex during the airfoil's downward motion and then its dissipation during the upward motion, as opposed to its convection into the wake in a mode-1 flow field. Power coefficient demonstrates a similar trend to that previously observed by Heathcote et al. [57]. Again there is greater effect for greater amplitude.

Now considering the force measurements for the flat plate, see Fig. 5.7 right column, lift coefficient demonstrates the first two peaks at the same Strouhal numbers as for the NACA 0012 airfoil, $Sr_c \approx 0.5$ and 1. This would be expected as when the flow is fully separated the natural shedding frequency is determined by the frontal area [123, 132, 135, 138] and for α = 15° this is almost identical for the NACA 0012 airfoil and

flat plate. A second interesting feature is that although the lift performance of the NACA 0012 airfoil and flat plate are similar at low Strouhal numbers, at higher Strouhal numbers the lift performance of the flat plate deteriorates significantly. Furthermore in contrast to the sudden fall in lift observed for the NACA 0012 airfoil, this deterioration is gradual with its onset around $Sr_c = 1$. As a result it is experienced at all amplitudes whereas the sudden fall in lift observed for the NACA 0012 airfoil is delayed to higher Strouhal number by smaller amplitude, and is therefore not observed for the two smaller amplitudes.

Drag coefficient demonstrates significantly worse performance for the flat plate. Indeed in comparison with the NACA 0012 airfoil there is essentially no reduction in drag coefficient, and as a result there is no switch from drag to thrust for any amplitude.

Power coefficient demonstrates similar trends to those observed for the NACA 0012 airfoil, with steeper gradient for greater amplitude. However for the same amplitude the gradient is steeper for the flat plate. For any amplitude-Strouhal number combination the flat plate therefore requires greater power-input. One can therefore conclude that by every measure of performance the flat plate is generally worse than the NACA 0012 airfoil; it generally produces the same or less lift, always produces more drag, and always requires more power.

Shown in Fig. 5.8 is the time-averaged velocity magnitude for both the NACA 0012 airfoil (left column) and flat plate (right column) for $\alpha = 15°$, $a/c = 0.025$ and range of Strouhal numbers. Fig. 5.8a left presents the streamlines and the magnitude of the total velocity vector for the stationary NACA0012 airfoil at an angle of attack, $\alpha = 15^o$. There is a large region of separation over the suction surface of the airfoil. The airfoil can therefore be classified as fully stalled in agreement with the force measurements already presented, and other authors [136, 138]. The flat plate experiences a similar region of separation, although due to the smaller radius of curvature at the leading-edge the point of separation is closer to the leading-edge. Oscillation even at small amplitude ($a/c = 0.025$) and low frequency ($Sr_c = 0.25$ and 0.50) significantly reduces this separated region, see Fig. 5.8b and c. It is worth

noting that due to the nature of time-averaged measurements the motion of the airfoil obscures the region in its direct vicinity. This makes the separated region appear smaller than is necessarily true. It is therefore preferable to consider the mean position (shown with solid line) when comparing with the stationary case. Even taking this into account the separation reduction is still significant for both NACA 0012 airfoil and flat plate. The reduction is however greater for the flat plate, which is reflected in the measured lift coefficient, $\Delta C_l = 0.5$ vs $\Delta C_l = 0.38$ for $Sr_c = 0.50$. For both geometries there is also a high velocity leading-edge region suggesting LEV formation.

With the Strouhal number increased to $Sr_c = 1$ the high velocity leading-edge region is enhanced for both NACA 0012 airfoil and flat plate. For the NACA 0012 airfoil the reduction in separation has continued however for the flat plate, although the nature of the separation has changed there is no further noticeable reduction. For Strouhal numbers larger than $Sr_c = 1$ the flat plate experiences generally deteriorating lift performance whilst the NACA 0012 airfoil experiences generally improving lift performance. This trend is reflected for $Sr_c = 1.25$ to 3 in Fig. 5.8f to m. In contrast to the reducing separation of the NACA 0012 airfoil, the flat plate experiences increasing separation with increasing Strouhal number. In addition the high velocity leading-edge region becomes smaller for the flat plate and further from the upper surface. This trend of increased separation and decreased high velocity leading-edge region for the flat plate continues up to $Sr_c = 3$. At $Sr_c = 3$ (Fig. 5.8m) for the first time for the NACA 0012 airfoil there is a time-averaged jet. This is indicative of thrust creation due to the action of a reverse-Kármán vortex street which is reflected in the drag coefficient measurements shown in Fig. 5.7b. By contrast the flat plate does not demonstrate a reverse-Kármán vortex street and therefore experiences higher drag coefficient.

Fig. 5.9 shows similar time-averaged velocity magnitude measurements for the larger amplitude: $a/c = 0.050$. For $Sr_c \leq 1$ (Fig. 5.9a to e) the behaviour is qualitatively similar to that previously described for $a/c = 0.025$. With increasing Strouhal number both the NACA 0012 airfoil and the flat plate generally experience decreasing separation and increasing size of the high velocity leading-edge region.

For $Sr_c > 1$ (Fig. 5.9f to m) the behaviour of the NACA 0012 airfoil and flat plate diverges. The NACA 0012 airfoil generally experiences reduced separation, increasing high velocity leading-edge region (up to $Sr_c = 2.25$), and time-averaged jet (after $Sr_c = 2.25$). By contrast the flat plat experiences increased separation, diminishing high velocity leading-edge region, and a very weak time-averaged jet (after $Sr_c = 2.25$).

To explain why there is such a difference between the geometries for $Sr_c > 1$, phase-averaged vorticity contour plots are shown in Fig. 5.10 at the top of the motion, and Fig. 5.11 at the bottom of the motion for the same amplitude as Fig. 5.8. Starting with $Sr_c = 1$ at the top of the motion, Fig. 5.10a. For this case the increase in lift coefficient and reduction in separation is comparable for the NACA 0012 airfoil and flat plate, the phase-averaged flow fields however show significant differences. For the NACA 0012 airfoil there are two small clockwise LEVs close to the upper surface; whereas for the flat plate there is a single, larger, more diffuse clockwise LEV slightly further from the upper surface. In both cases these upper surface LEVs are formed during the downward motion (see Fig. 5.11a) before being shed and convected over the upper surface. The decreasing effective angle of attack in the second half of the upward motion combined with the action of the passing clockwise LEV initiates the formation of the counter-clockwise TEV seen at the trailing-edge in Fig. 5.10a.

With the Strouhal number increased to $Sr_c = 1.5$ the lift performance and separation reduction of the two has diverged. The phase-averaged flow fields (Fig. 5.10b and Fig. 5.11b) show the NACA 0012 airfoil to form a single clockwise LEV per cycle. This LEV is small, concentrated, and convects close to the surface. Conversely the flat plate also has a single clockwise LEV except it is larger, more diffuse, and convects further from the upper surface. Likewise the number of TEVs is similar for both geometries but they are generally larger, and more diffuse in the case of the flat plate.

With further increase in Strouhal number to $Sr_c = 2.0$ (Fig. 5.10c and Fig. 5.11c) these characteristics continue. There is a single LEV formed during each cycle but

for the flat plate the vortex is larger, more diffuse, convects more slowly (as demonstrated by the vortex spacing), and convects further from the upper surface. Due to the large vertical distance between the convecting LEV and trailing-edge they do not interact with the TEVs to create the dual-branch wake observed for the NACA 0012 airfoil. It is also interesting to note that the LEV for the flat plate has a strong secondary vortex. Due to this secondary vortex the vortex pair remains nearer to the leading-edge for a greater proportion of the cycle.

Further increase in Strouhal number to $Sr_c = 2.5$ (Fig. 5.10d and Fig. 5.11d) and $Sr_c = 3.0$ (Fig. 5.10e and Fig. 5.11e) and the difference is further enhanced. For the NACA 0012 airfoil the LEVs are small, concentrated and convect very close to the upper surface interacting at the trailing-edge with the TEVs. Conversely for the flat plate the LEVs are larger, more diffuse, with a much stronger secondary vortex, and convect further from the upper surface. The reason for the deteriorating lift performance of the flat plate at high Strouhal numbers can therefore be attributed to the convection path of the LEV. As it is further from the airfoil surface, its lift enhancing effect will be significantly weakened and there will be greater time-averaged separation.

Similar measurements are shown for a larger amplitude, a/c = 0.15 in Fig. 5.12 and Fig. 5.13. For this larger amplitude, larger plunge velocities are experienced, $Sr_A \leq 0.6$ vs $Sr_A \leq 0.15$, therefore new types of flow behaviour are observed. The results for the NACA 0012 airfoil have previously been discussed in detail in Chapter 3. In summary the increasing lift performance is associated with increasing circulation of the upper surface LEV which forms during the downward motion, see Fig. 5.13. This continues until the combination of the onset of the mode-2 flowfield and formation of a strong lower-surface LEV mean that the asymmetry between upper-surface and lower-surface vortex strengths is lost and the lift coefficient returns to approximately that of the stationary airfoil.

For $Sr_c \leq 1$ the principal differences are the same as for the smaller amplitude previously discussed. For both geometries an upper surface LEV forms during the downward motion, but for the flat plate it is more diffuse, and convects further from

the upper surface. For $Sr_c > 1$ one begins to observe new behaviour, instead of the vortex dissipation typical of a mode-2 flowfield, the upper-surface LEV never appears to form for the flat plate, see Fig. 5.13c and Fig. 5.13d. The only visible clockwise vorticity is a vague region above the leading-edge that appears as a 'plume'.

Further detail of this process is shown in Fig. 5.14 for the maximum Strouhal numbers studied for the three largest amplitudes. The largest amplitude of a/c = 0.2 (right column) shows the clearest detail. At the top of the motion there is a strong lower surface counter-clockwise vortex which is mostly obscured by the laser shadow. This vortex is not visible for the smaller amplitudes however this does not preclude its existence. As the airfoil moves down a strong counter-clockwise TEV and strong clockwise LEV form. Also just visible to the left of the LEV is a region of counter-clockwise vorticity partnering the LEV. Considering the presence of this vorticity in combination with the motion of the LEV (vertically and upstream) this would suggest that the upper-surface clockwise LEV has partnered with the lower surface counter-clockwise LEV to form a dipole that self-advects upwards. In the next phase the upper-surface vortex has lost its coherency and can be seen as the plume of clockwise vorticity above the leading-edge. A similar process is observed for the smaller amplitudes, see Fig. 5.14 left and central column.

To capture this LEV destruction process more detailed phase-averaged PIV measurements were performed for a/c = 0.15 and $Sr_c = 2$, see Fig. 5.15. These show that the counter-clockwise lower-surface LEV formed during the upward motion remains near the leading-edge during the downward motion, pairing with the clockwise upper surface LEV to form a strong vortex dipole. Due to the position of the vortices within this dipole it convects upstream rapidly, leading to the rapid dissipation of both vortices. It is also interesting to note that the interaction of the lower surface vortex with the upper surface vortex results in it pinching off prematurely, i.e. before the point of maximum effective angle of attack. It is therefore significantly weaker than the equivalent LEV for the NACA 0012 airfoil.

Similar LEV pairing is also observed at the smallest amplitude: a/c = 0.025, see Fig. 5.16. The lower surface LEV forms during the upward motion (Fig. 5.16c to a), before circumventing the leading-edge to form a vortex dipole with the upper surface LEV (Fig. 5.16a). Due to the position of the vortices, this dipole will have a self-advective velocity away from the upper surface. This gives a good explanation for the large region of separation (Fig. 5.8m) and poor lift performance (Fig. 5.7a) observed for the flat plate. In comparison with the larger amplitude shown in Fig. 5.15, the effect of this LEV dipole is comparatively small. This is a result of the smaller Sr_A at this smaller amplitude which results in weaker LEVs. The same phenomenon, LEV pairing, is however responsible regardless of amplitude.

5.2 CONCLUSIONS

Experiments were performed to compare the forces and flow fields of both a NACA 0012 airfoil and flat plate oscillating with small-amplitude at angles of attack of 0° and 15°. For 0° at high Strouhal number the NACA airfoil is subject to stable deflected jets resulting in very large negative or positive lift coefficients with the direction determined by initial conditions. The flat plate is likewise subject to deflected jets however the direction oscillates approximately sinusoidally between upwards and downwards with a period on the order of 100 cycles. The lift coefficient is therefore also unstable and oscillatory.

For $\alpha = 15°$ at low Strouhal number the performance of the NACA airfoil and flat plate are similar. Both experience significant increase in lift coefficient with greater effect for greater amplitude and local optima due to resonance with the natural shedding frequency, its harmonics and subharmonics. This increase is associated with reduced time-averaged separation and a high velocity leading-edge region due to LEV formation. After a Strouhal number of approximately one, the performance of the flat plate and NACA 0012 airfoil begin to diverge. The flat plate experiences deteriorating lift performance across all amplitudes studied. This is due to a novel mode of LEV behaviour characterized by pairing of the upper surface LEV with the lower surface LEV to create a vortex dipole that convects in an upwards / upstream direction away from the upper surface. The effect of this LEV dipole depends on the

strength of the LEVs, however it can generally be characterized as leading to increased time-averaged separation and therefore diminished lift performance.

5.3 FIGURES

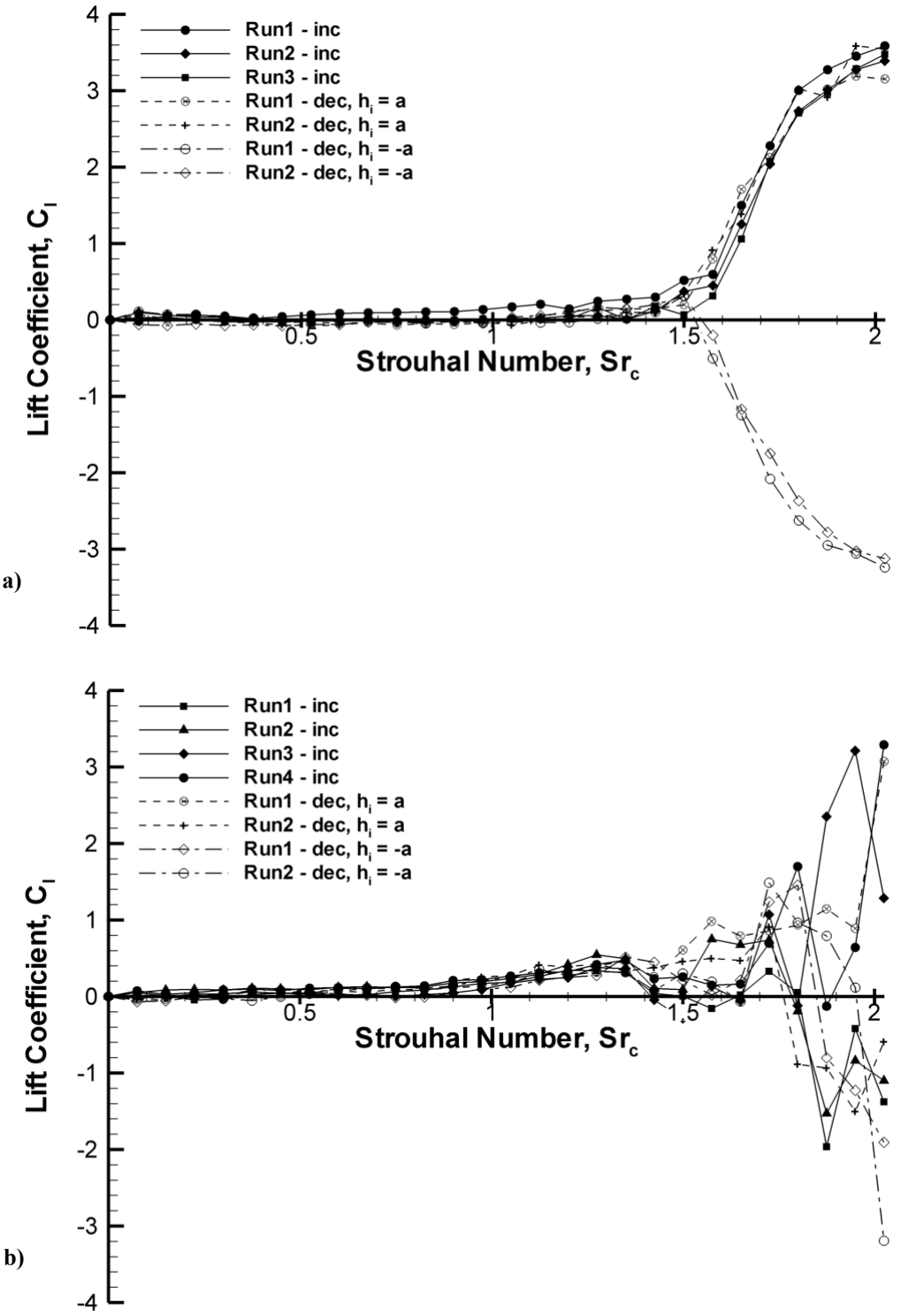

Fig. 5.1 Lift coefficient for a) NACA 0012 airfoil, and b) flat plate oscillating with a/c = 0.15 at α = 0°.

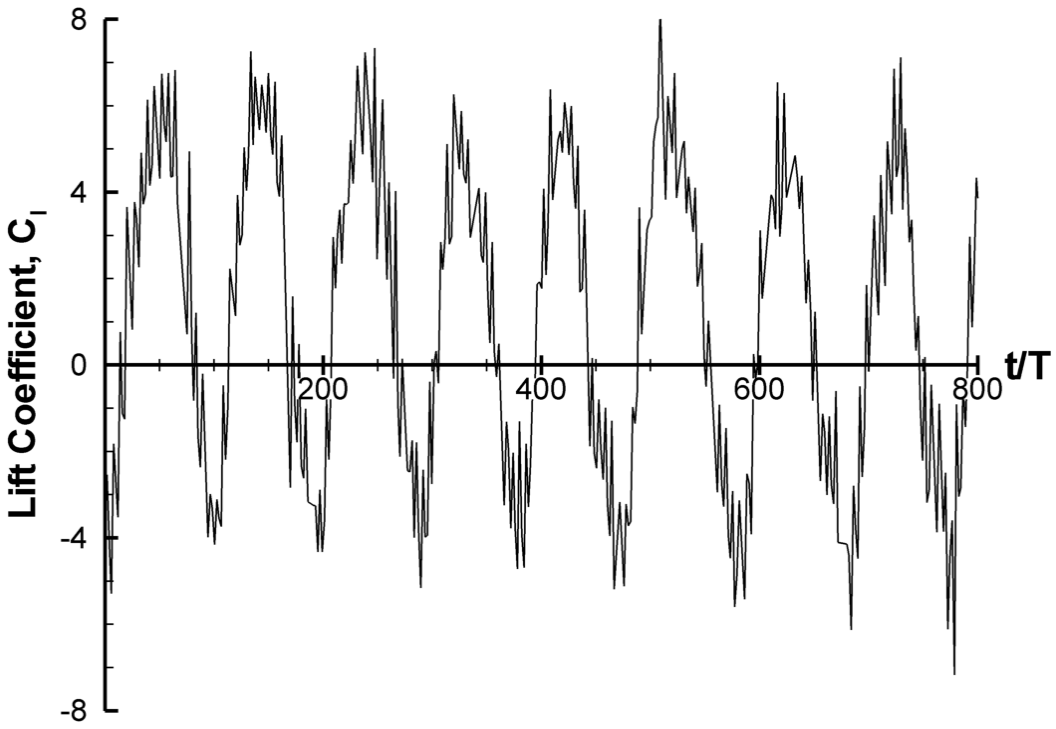

Fig. 5.2 Cycle-averaged lift coefficient for the rigid flat plate oscillating at a/c = 0.15, Sr_c = 2.025, and α = 0°.

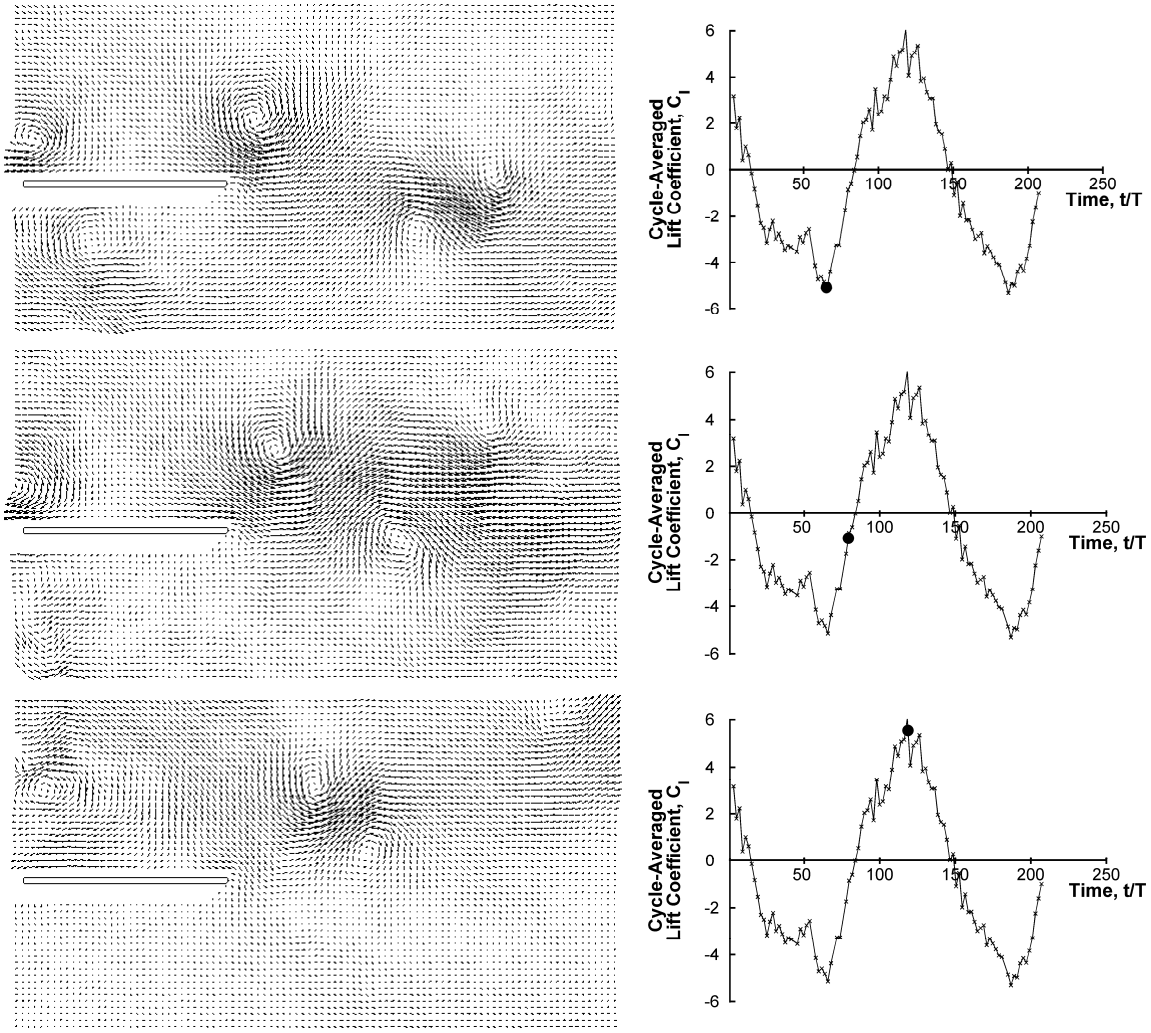

Fig. 5.3 Jet-switching phenomenon for the flat plate oscillating with α = 0°, Sr_c = 2.025 and a/c = 0.15. Shown on the left are instantaneous PIV results phase-locked to h = -a. Shown on the right are simultaneous cycle-averaged lift coefficient measurements with the time of the velocity vector plot denoted by a solid circular symbol.

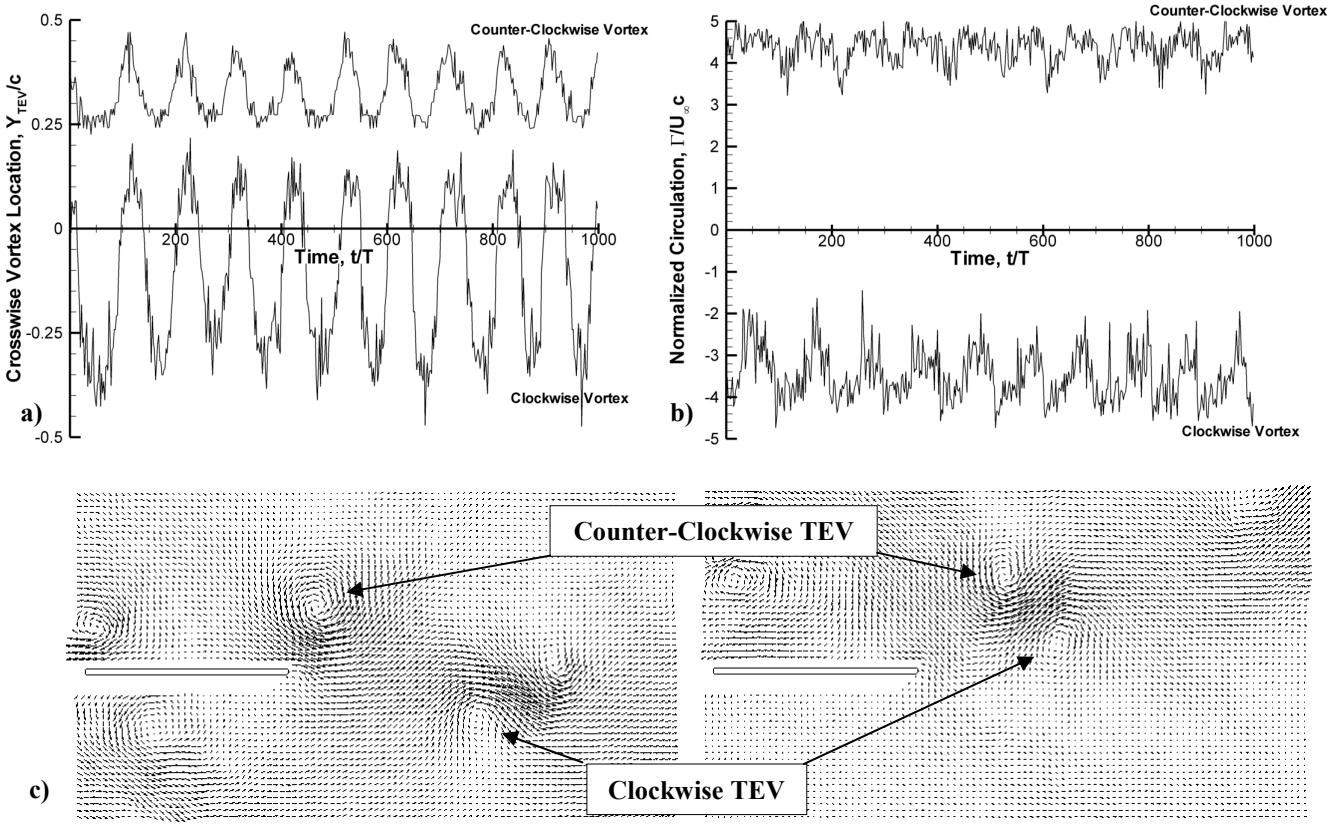

Fig. 5.4 a) Instantaneous trailing-edge vortex crossstream position as measured in phase-locked measurements at h = -a. b) Instantaneous normalized circulation as measured in phase-locked measurements at h = -a. c) Inset identifying clockwise and counter-clockwise vortex for two extreme cases.

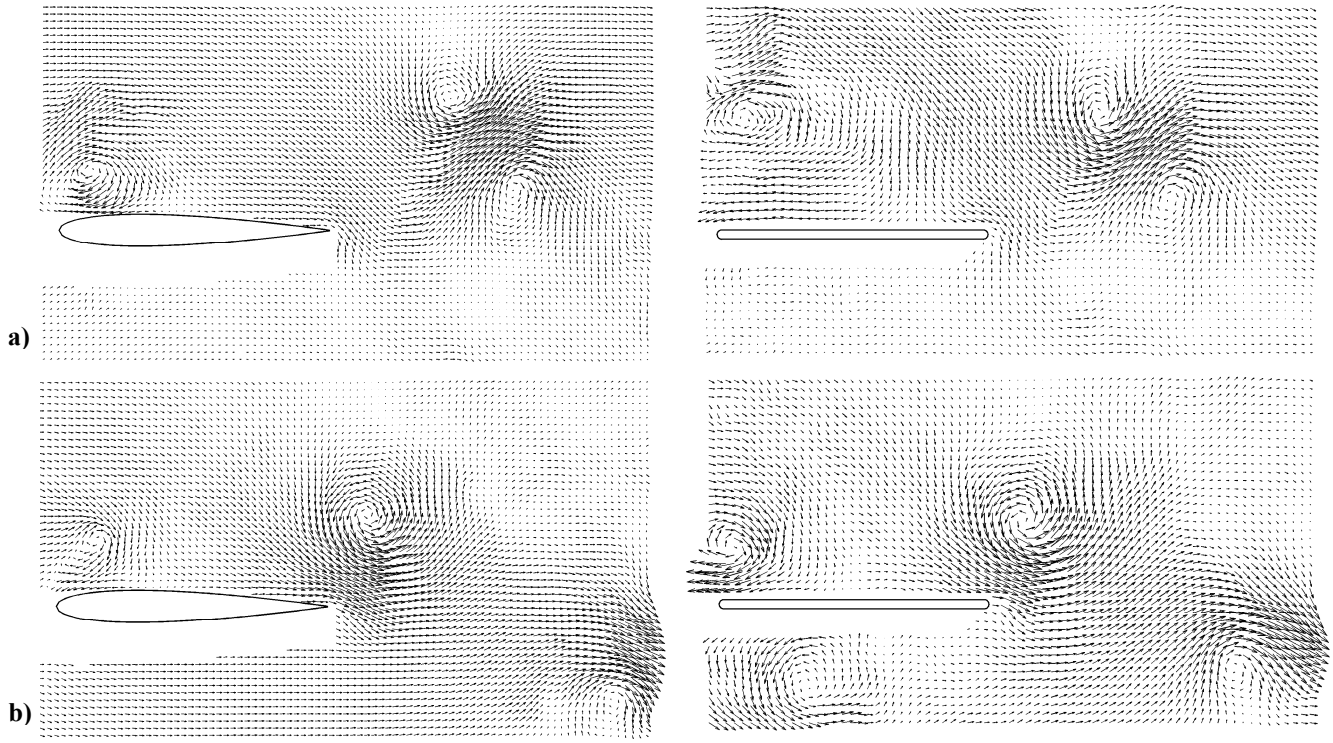

Fig. 5.5 Comparison of instantaneous NACA 0012 bifurcation flow fields with their flat plate equivalents: a) mode A, and b) mode B.

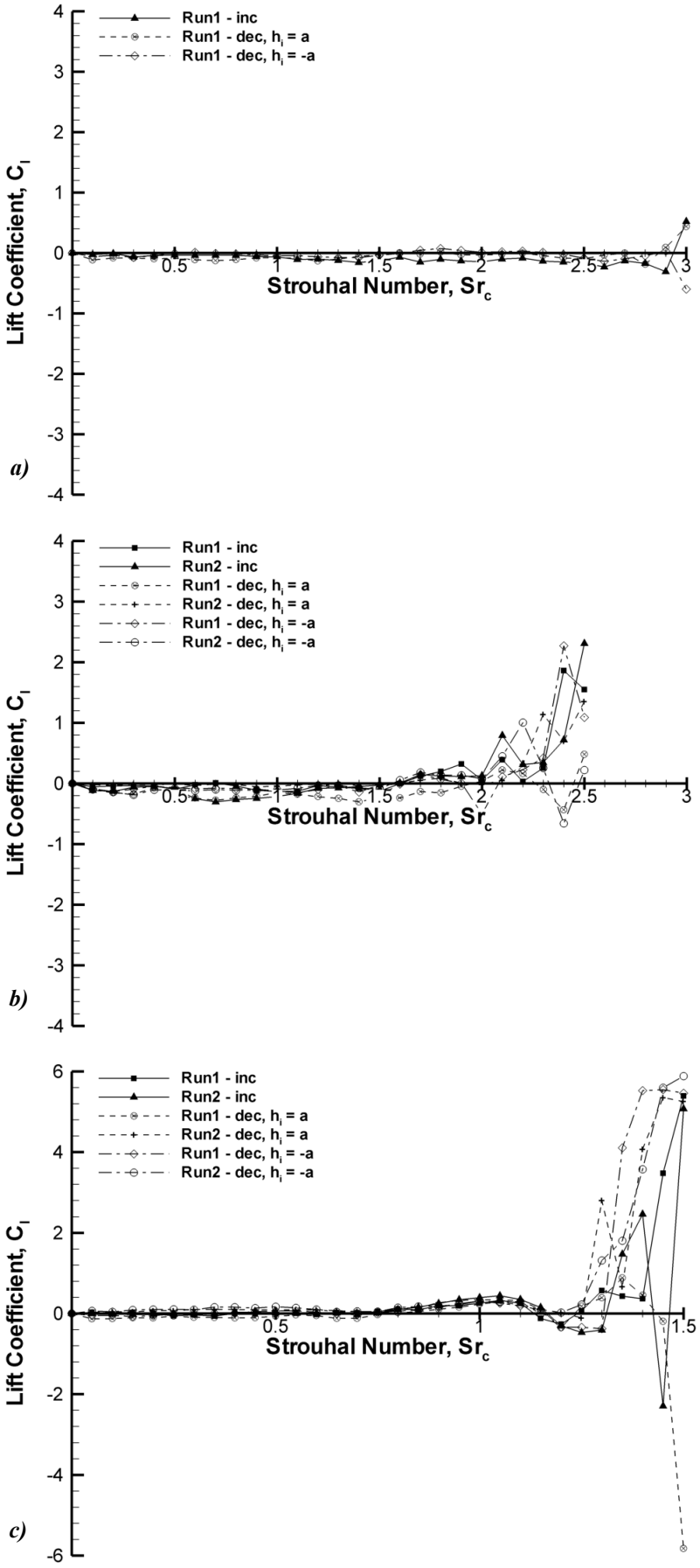

Fig. 5.6 Individual runs of time-averaged lift coefficient for the flat plate at α = 0°, and: a) a/c = 0.025, b) a/c = 0.100, and c) a/c = 0.200.

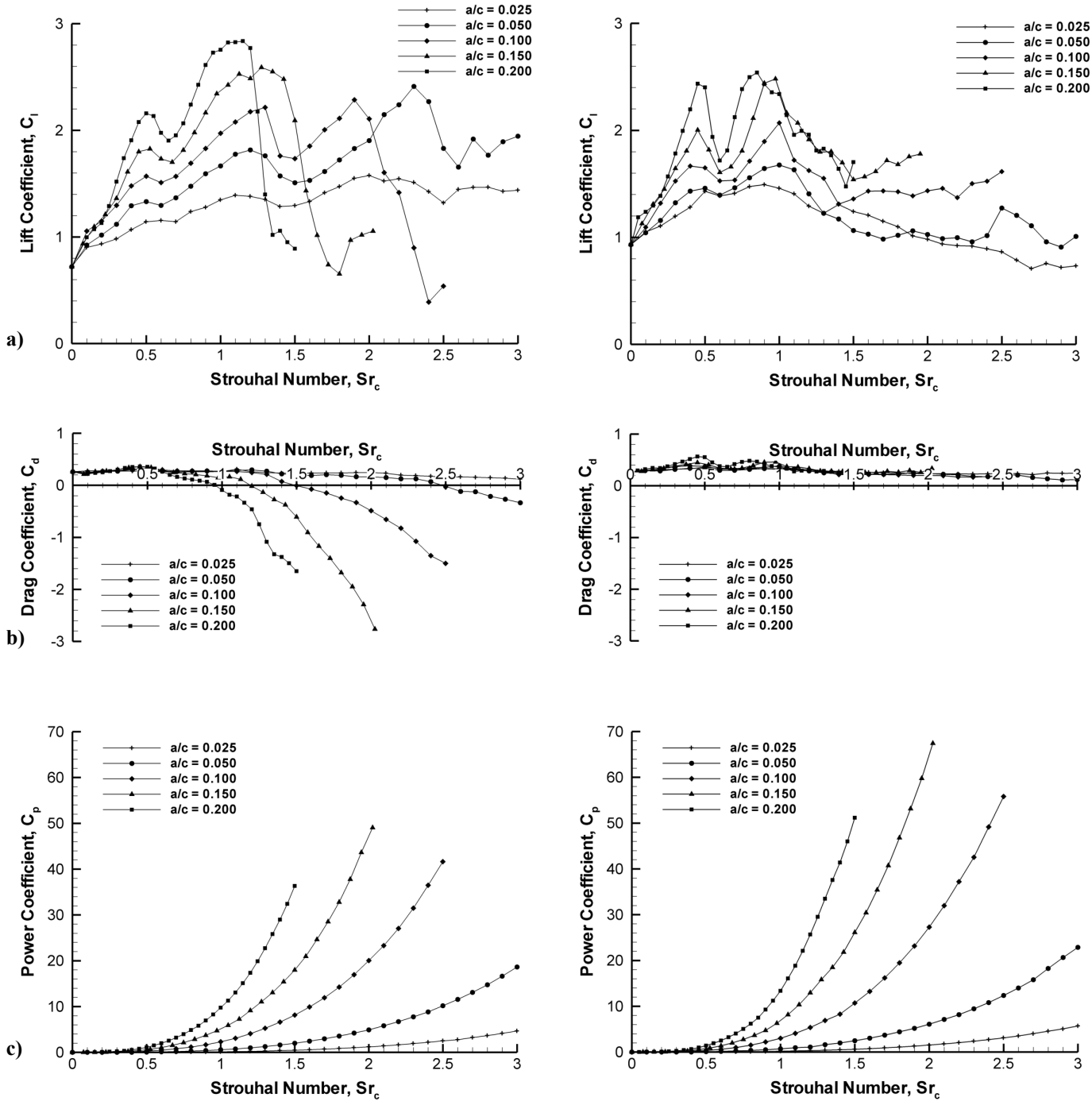

Fig. 5.7 a) lift coefficient, b) drag coefficient, and c) power coefficient plotted against Strouhal number based on chord for the NACA 0012 airfoil (left column) and the rigid flat plate (right column) at $\alpha = 15°$.

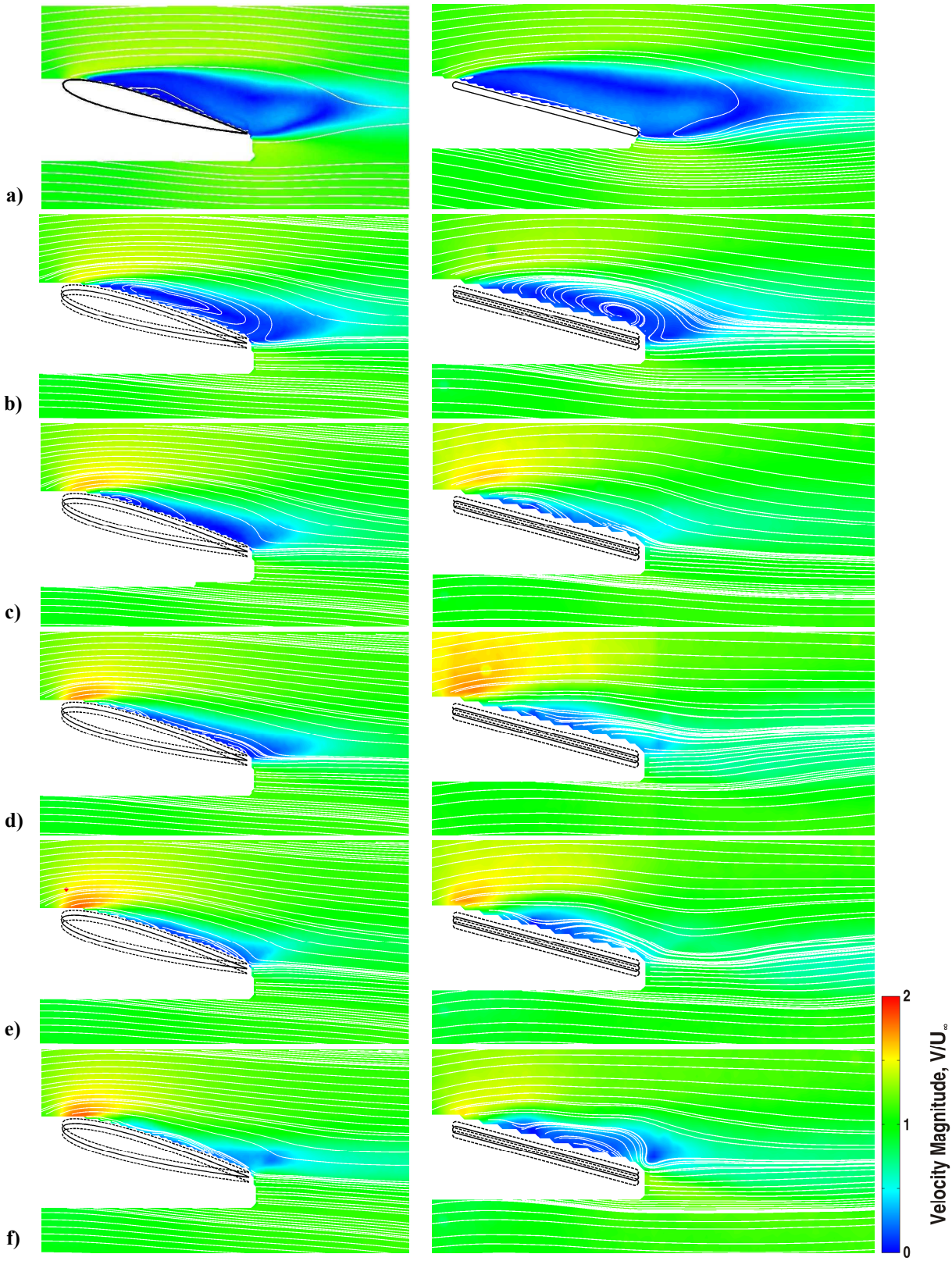

Fig. 5.8 Time-averaged velocity magnitude for the NACA 0012 airfoil (left column) and flat plate (Right column) for a/c = 0.025 and α = 15° at Strouhal numbers of: a) Sr_c = 0, b) Sr_c = 0.25, c) Sr_c = 0.50, d) Sr_c = 0.75, e) Sr_c = 1.00, f) Sr_c = 1.25, g) Sr_c = 1.50, h) Sr_c = 1.75, i) Sr_c = 2.00, j) Sr_c = 2.25, k) Sr_c = 2.50, l) Sr_c = 2.75, and m) Sr_c = 3.00 . **Continued next page**

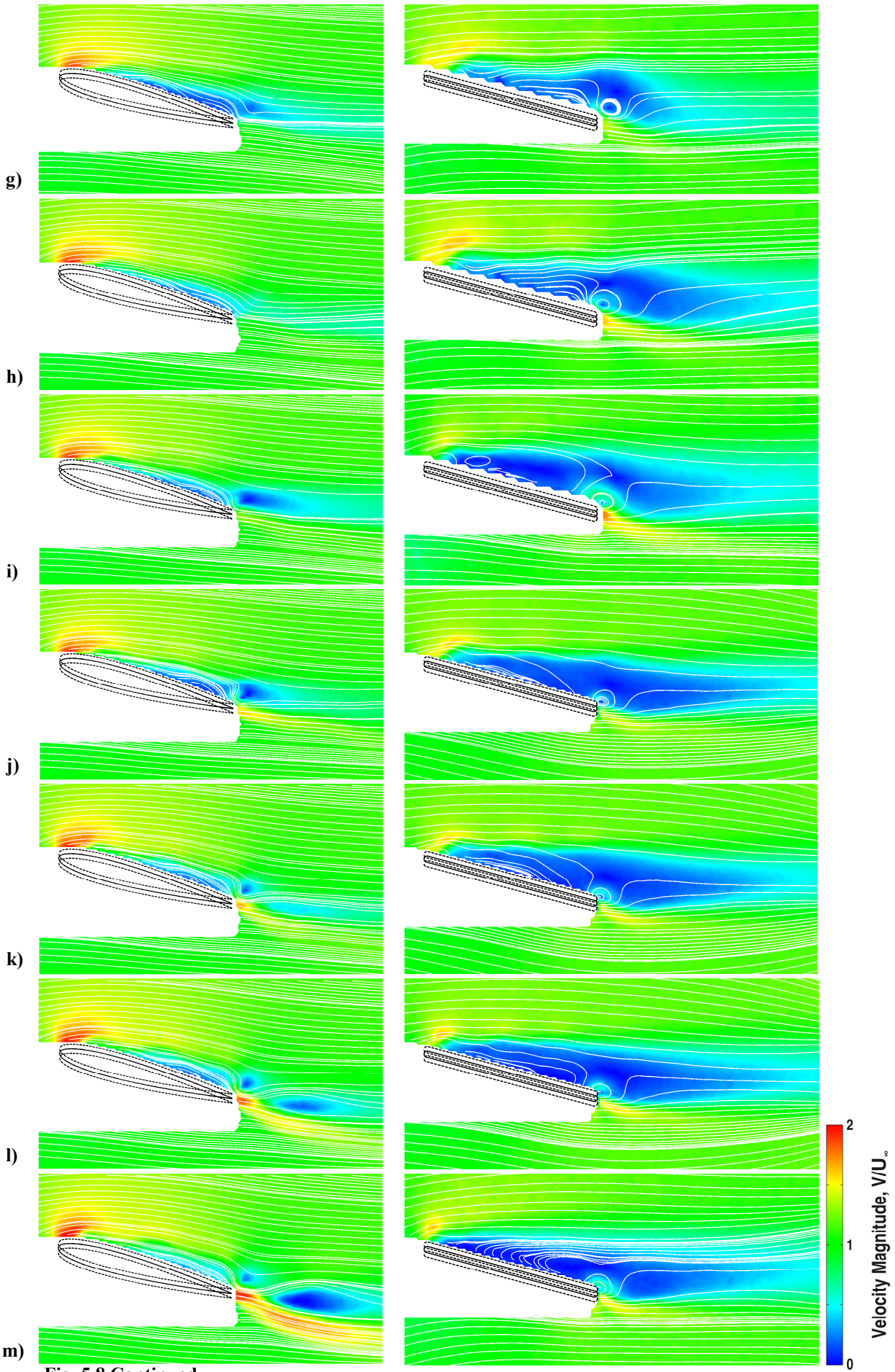

Fig. 5.8 Continued

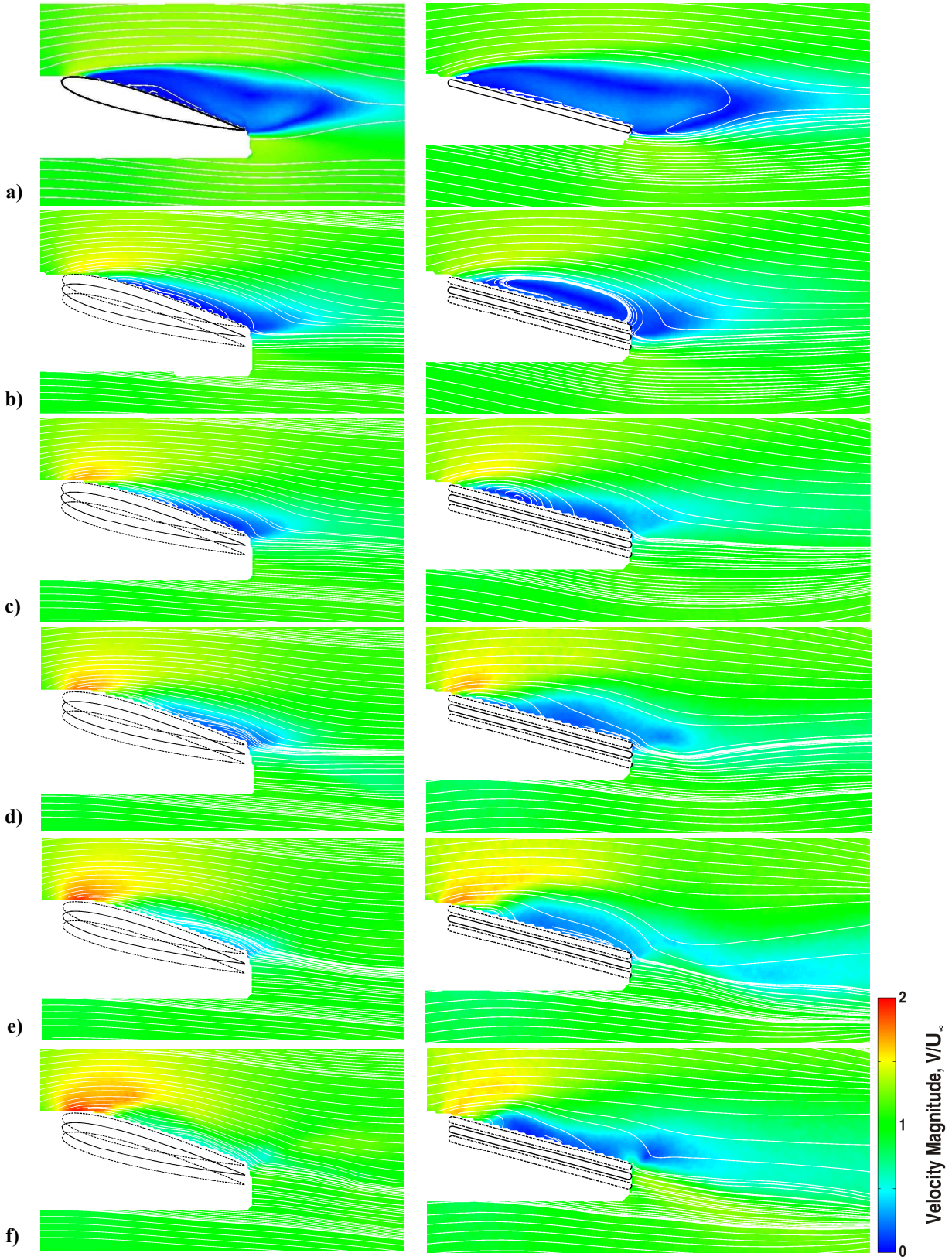

Fig. 5.9 Time-averaged velocity magnitude for the NACA 0012 airfoil (left column) and flat plate (Right column) for a/c = 0.050 and α = 15° at Strouhal numbers of: a) Sr_c = 0, b) Sr_c = 0.25, c) Sr_c = 0.50, d) Sr_c = 0.75, e) Sr_c = 1.00, f) Sr_c = 1.25, g) Sr_c = 1.50, h) Sr_c = 1.75, i) Sr_c = 2.00, j) Sr_c = 2.25, k) Sr_c = 2.50, l) Sr_c = 2.75, and m) Sr_c = 3.00 . Continued next page

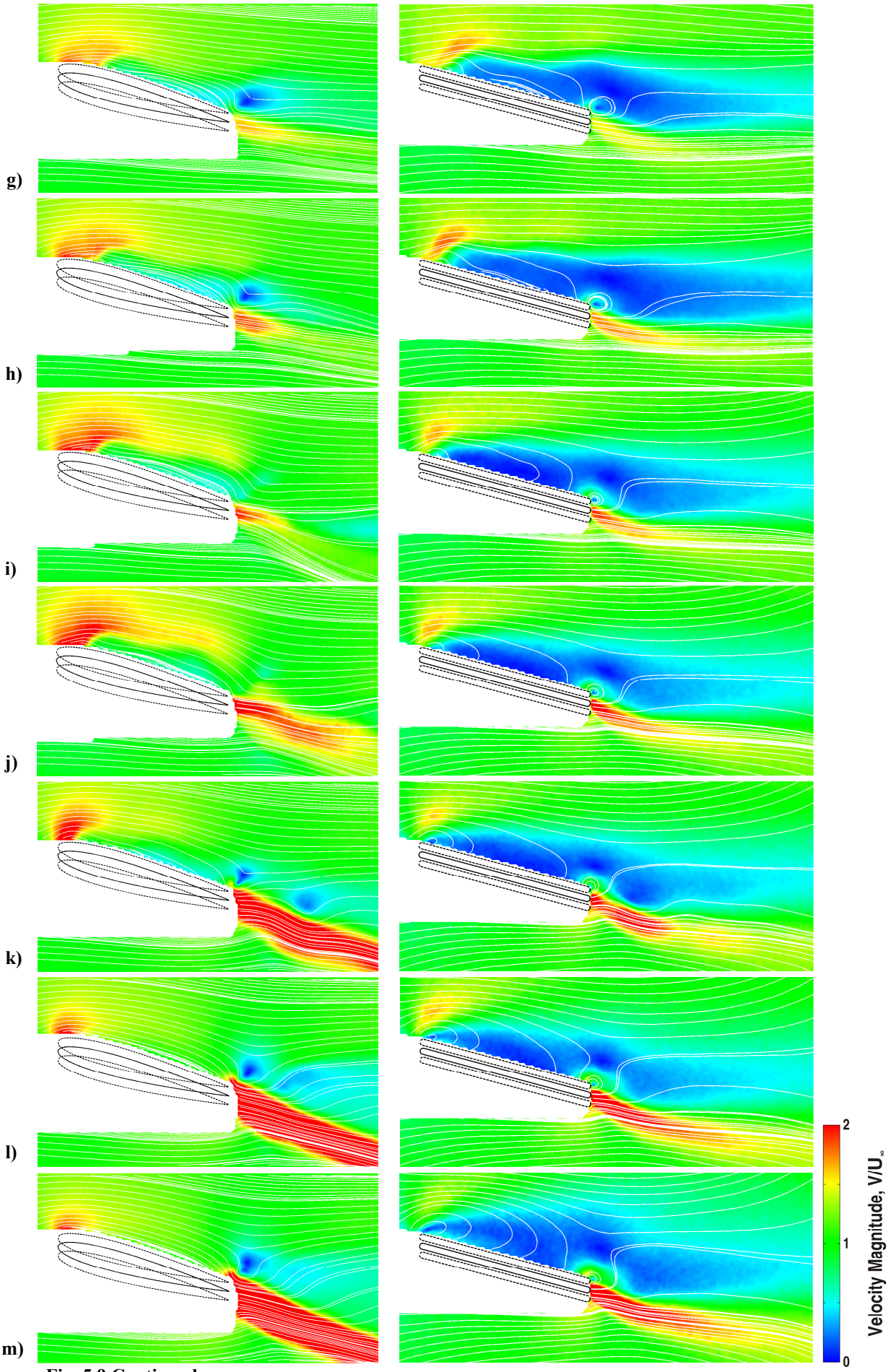

Fig. 5.9 Continued.

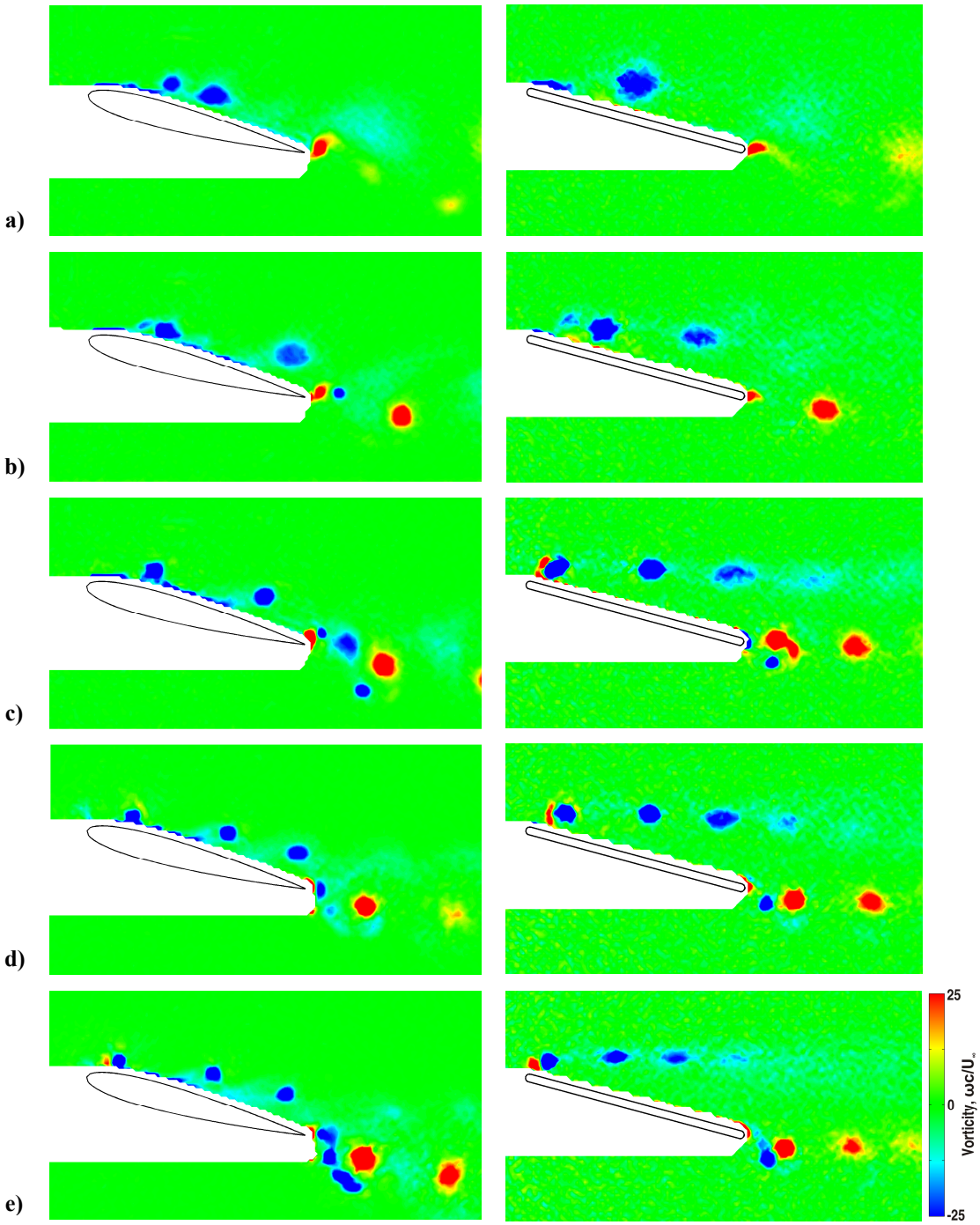

Fig. 5.10 Phase-averaged vorticity contour plots at the top of the motion for the NACA 0012 airfoil (left column) and flat plate (right column) for a/c = 0.025 and α = 15° at Strouhal numbers of: a) Sr_c = 1.00, b) Sr_c = 1.50, c) Sr_c = 2.00, d) Sr_c = 2.50, and e) Sr_c = 3.00.

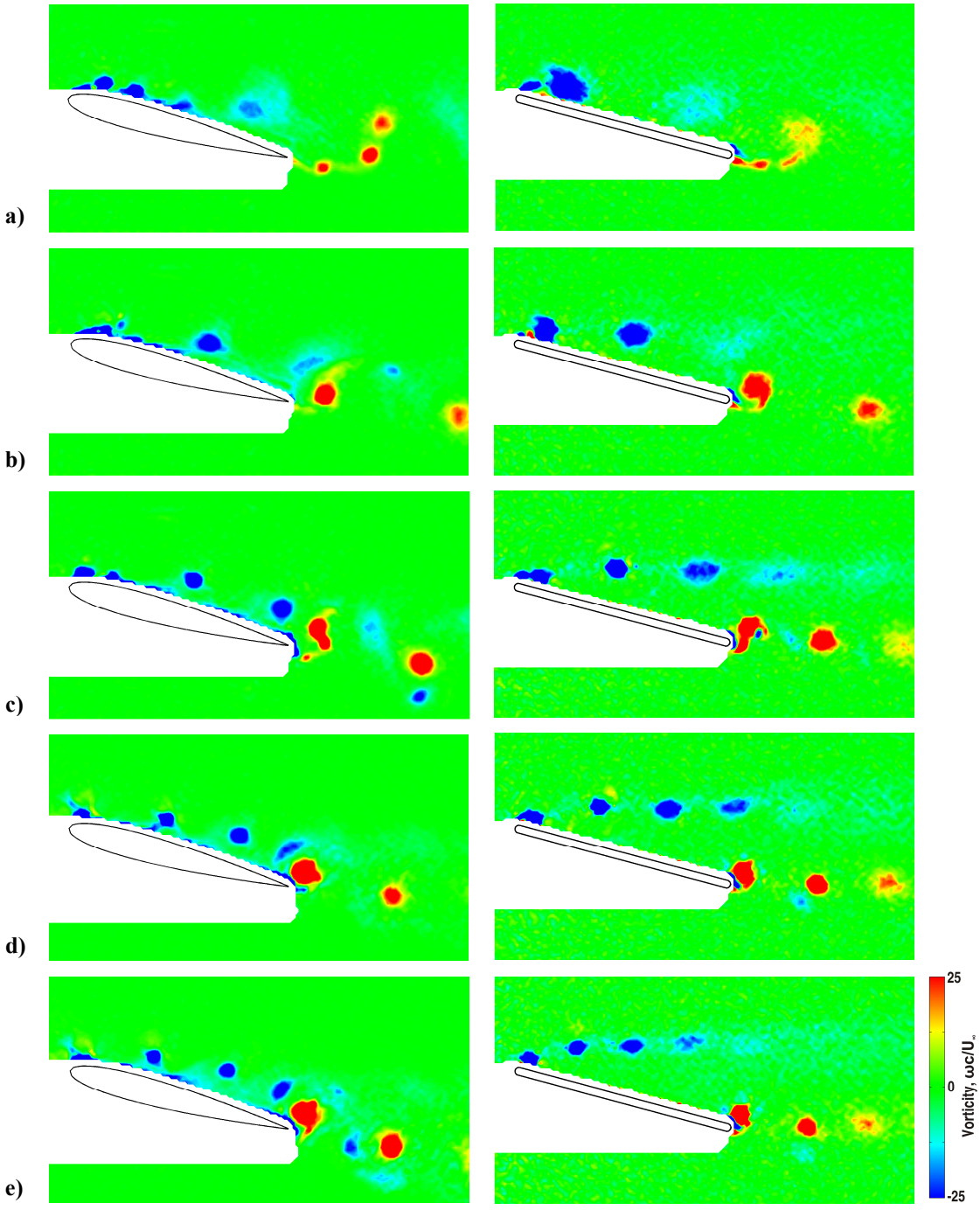

Fig. 5.11 Phase-averaged vorticity contour plots at the bottom of the motion for the NACA 0012 airfoil (left column) and flat plate (right column) for a/c = 0.025 and α = 15° at Strouhal numbers of: a) Sr_c = 1.00, b) Sr_c = 1.50, c) Sr_c = 2.00, d) Sr_c = 2.50, and e) Sr_c = 3.00.

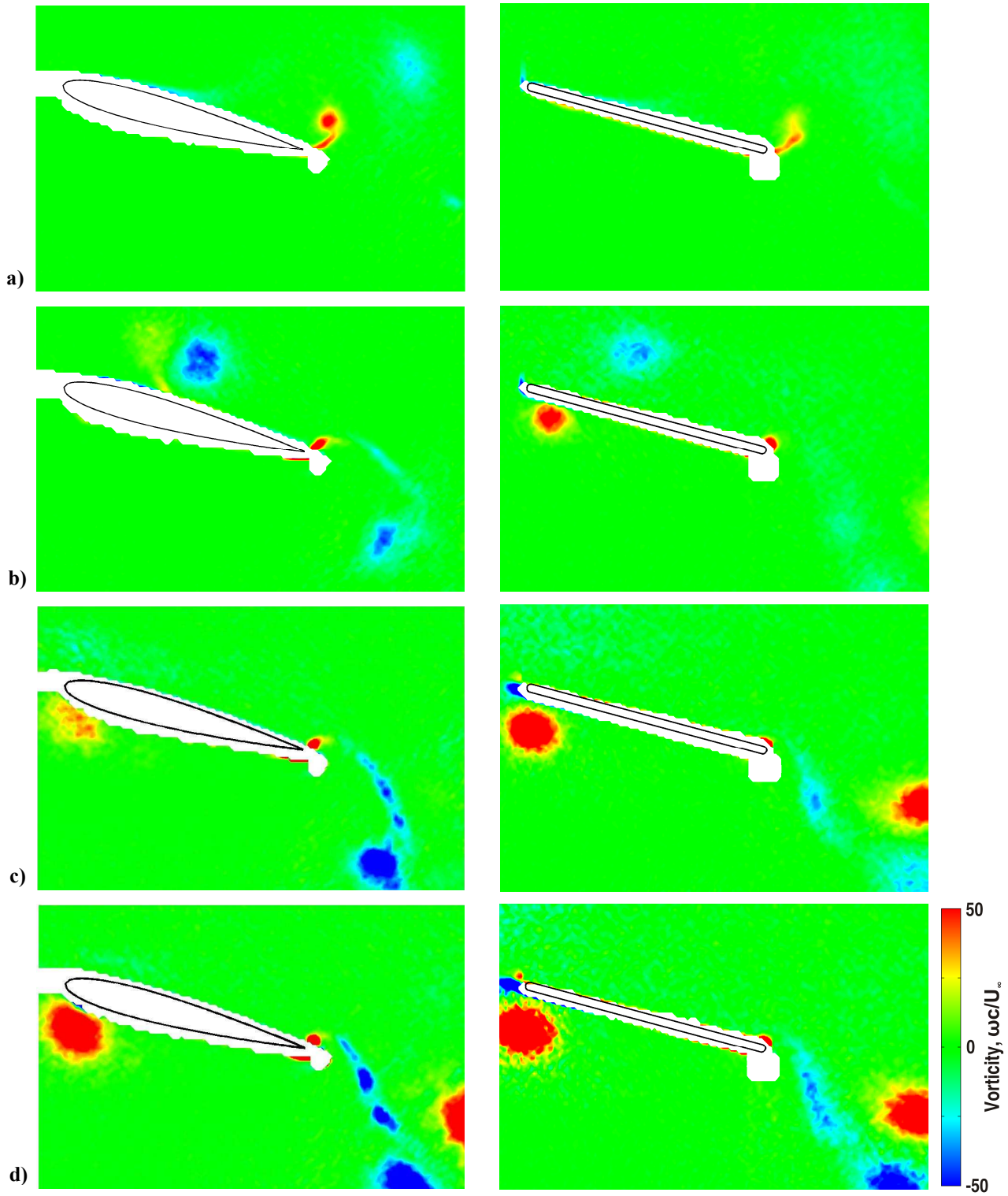

Fig. 5.12 Phase-averaged vorticity contour plots at the top of the motion for the NACA 0012 airfoil (left column) and flat plate (right column) for a/c = 0.150 and α = 15° at Strouhal numbers of: a) Sr_c = 0.50, b) Sr_c = 1.00, c) Sr_c = 1.50, and d) Sr_c = 2.00.

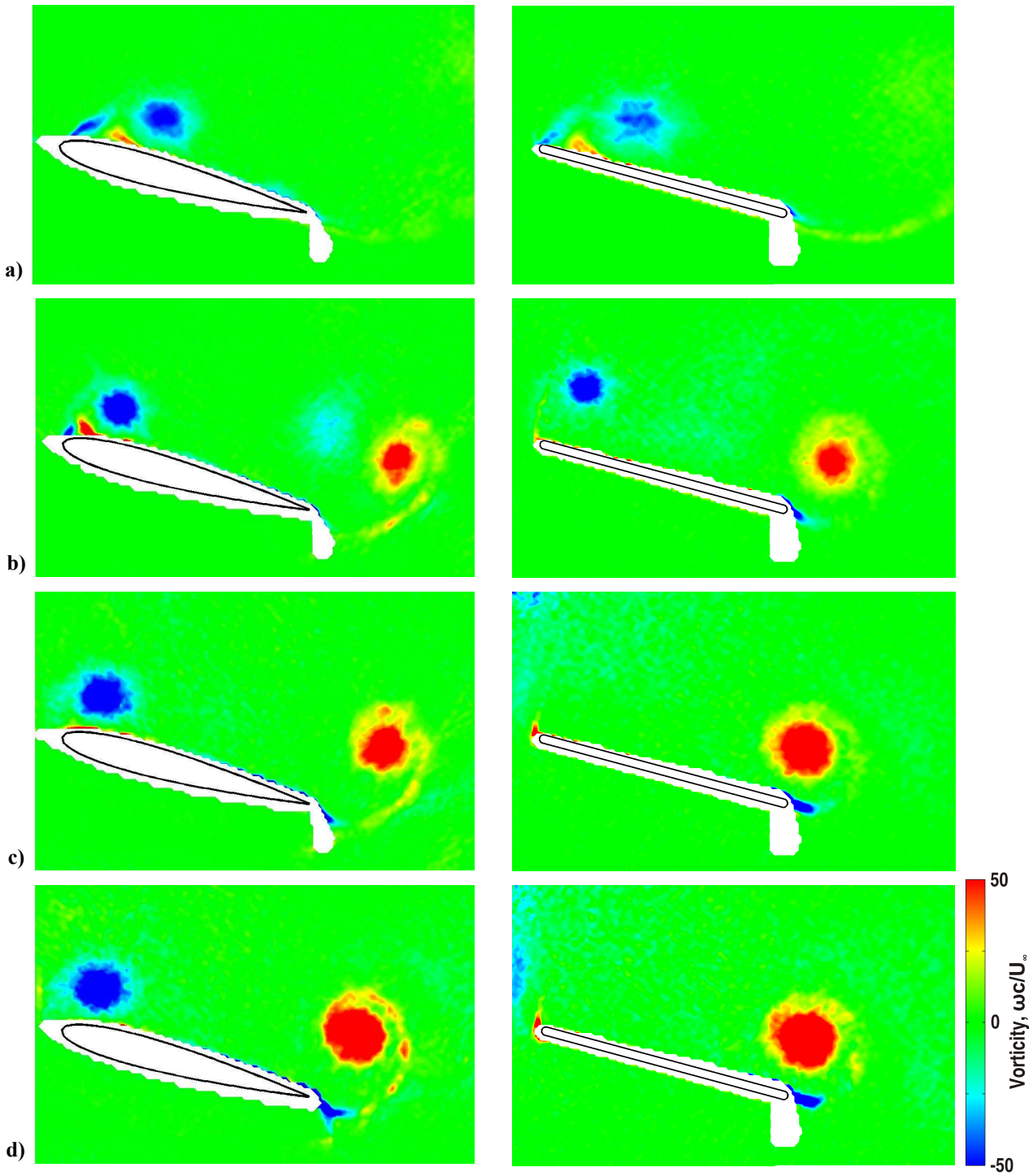

Fig. 5.13 Phase-averaged vorticity contour plots at the bottom of the motion for the NACA 0012 airfoil (left column) and flat plate (right column) for a/c = 0.150 and α = 15° at Strouhal numbers of: a) Sr_c = 0.50, b) Sr_c = 1.00, c) Sr_c = 1.50, and d) Sr_c = 2.00.

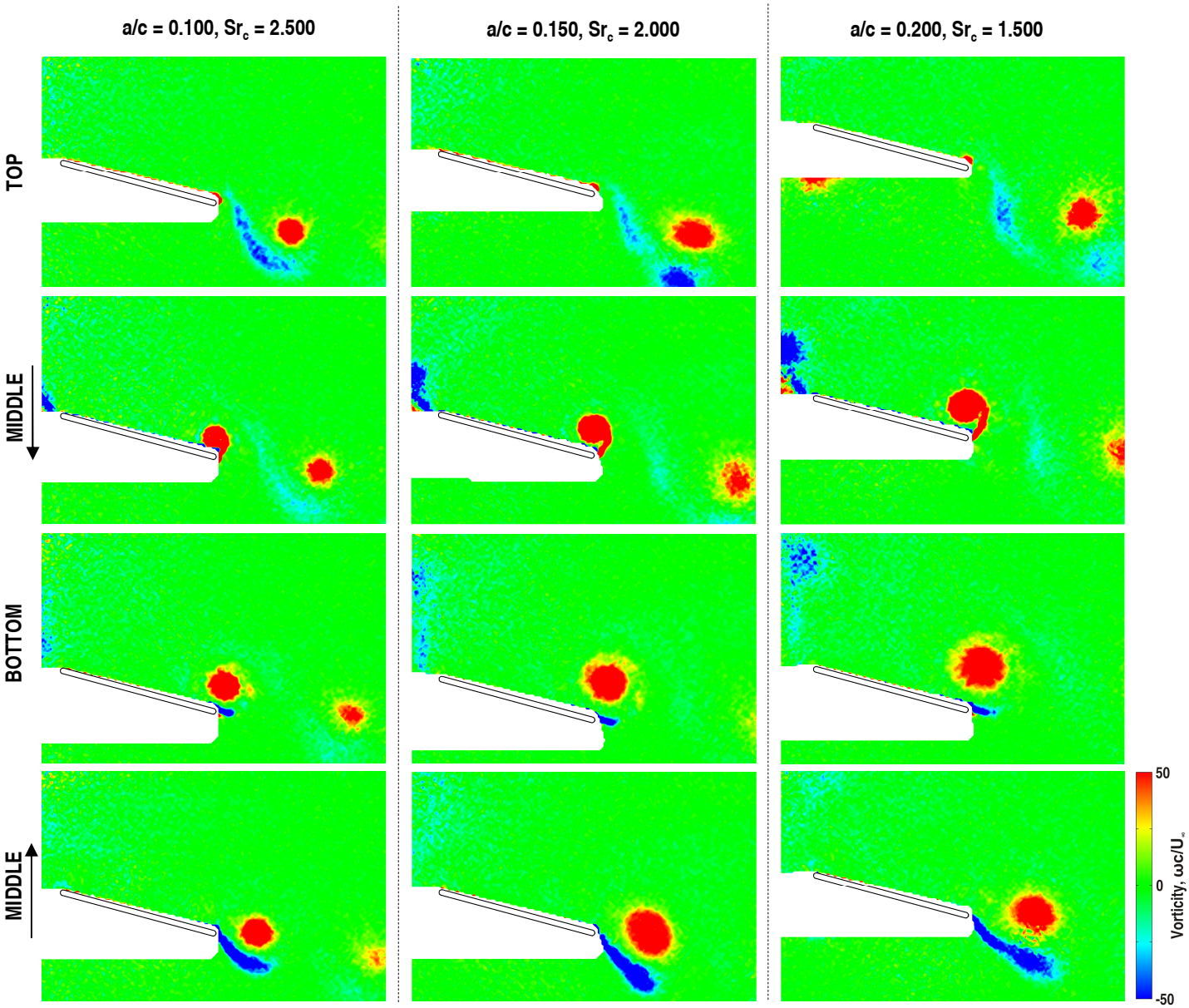

Fig. 5.14 Phase-averaged vorticity contour plots for the flat plate at four phases in the cycle for α = 15°, a/c = 0.10 (left column), a/c = 0.15 (central column), and a/c = 0.20 (right column) at the maximum Strouhal number studied for each case.

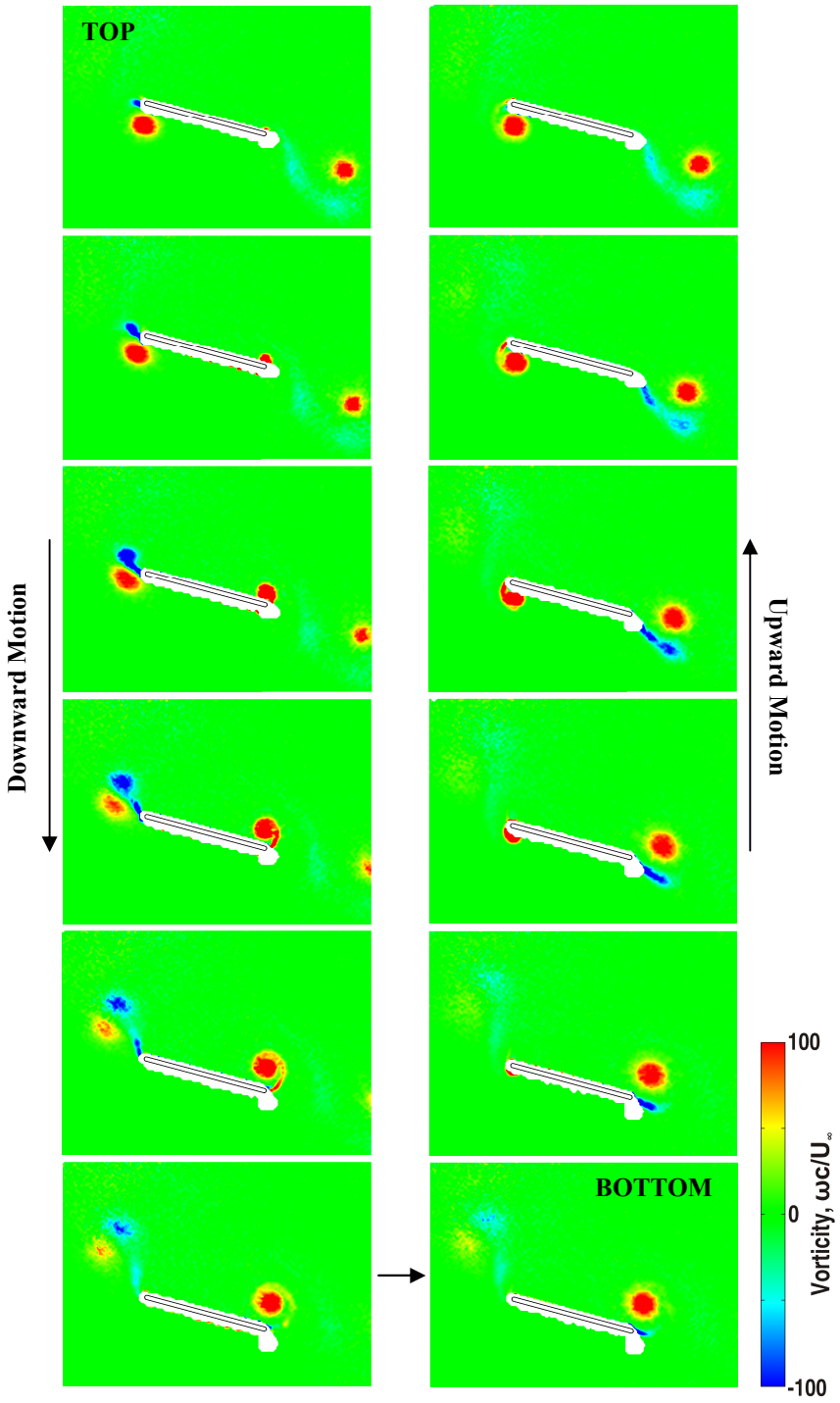

Fig. 5.15 Phase-averaged vorticity contour plots for the 2D rigid flat plate at twelve phases in the cycle for α = 15°, a/c = 0.15 and Sr_c = 2.00.

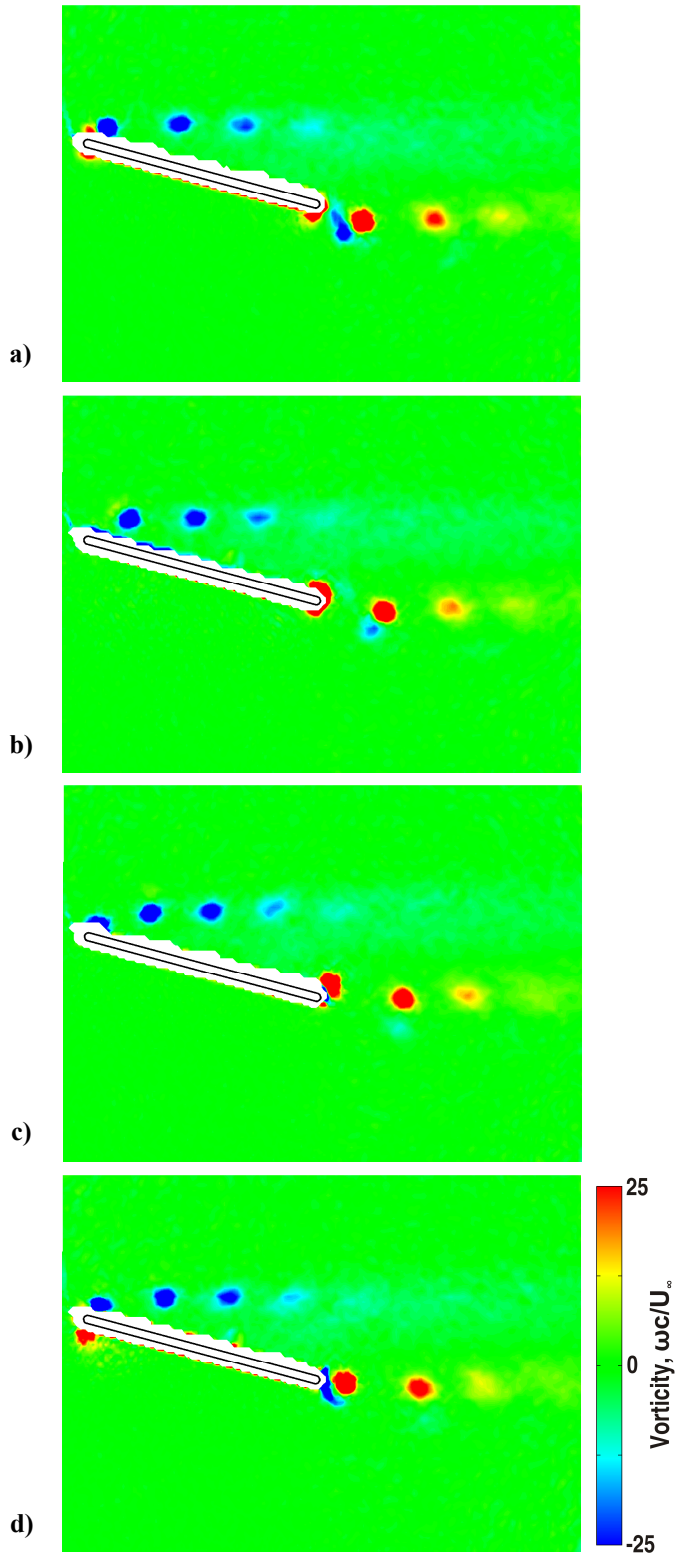

Fig. 5.16 Phase-averaged vorticity contour plots for the 2D rigid flat plate for α = 15°, a/c = 0.025 and Sr_c = 3.00 at : a) Top, b)middle (down), c) bottom, and d) middle (up), of the motion.

CHAPTER 6. SUMMARY

Small-amplitude high-frequency motion is an effective method of increasing lift and reducing drag. For small values of Sr_A, lift coefficient for a NACA 0012 airfoil at a post-stall angle of attack was shown to increase approximately proportionally to Sr_A. This increase was associated with growing strength of the convected upper surface leading-edge vortex. Superimposed onto this linear trend are several local peaks due to resonance with the natural shedding-frequency, its harmonics and sub-harmonics. At large values of Sr_A a sudden fall in lift coefficient is experienced due to the formation of a lower surface leading-edge vortex combined with the dissipation of the upper surface leading-edge vortex. This new mode of behaviour was shown to correlate very closely with the switch from drag to thrust production.

For angles of attack below ten degrees significant bifurcations were observed in the force coefficients due to the formation of deflected jets. The upwards deflected jet was associated with the clockwise trailing-edge vortex loitering over the airfoil to form a dipole with the forming counter-clockwise TEV, which convected in an upwards direction. Due to this asymmetry at the trailing-edge, fluid is drawn over the upper surface leading to a stronger upper surface leading-edge vortex and high positive lift. The downwards deflected jet is associated with the inverse, i.e, the counter-clockwise vortex loitering leading to negative lift. Which occurs depends on the initial conditions, but once the direction is determined all future cycles are 'locked-in' and the direction remains stable. Deflected jets did not occur at larger angles of attack due to asymmetry in the trailing-edge vortex strengths giving a natural inclination towards a downwards deflected jet, nor at smaller amplitudes due to insufficient trailing-edge vortex strength.

Geometry has a significant effect. At zero degrees angle of attack the flat plate geometry also created deflected jets however the direction switched approximately sinusoidally with a period on the order of 100 cycles. As a result the lift coefficient was also oscillatory. At fifteen degrees angle of attack the flat plate behaviour was qualitatively similar to the NACA 0012 airfoil below Strouhal numbers of one. Above a Strouhal number of one the behaviour diverged due to a novel mode of

leading-edge vortex behaviour. The upper surface and lower surface leading-edge vortices would pair to make a dipole that convects upwards away from the upper surface leading to greater time-averaged separation and reduced lift.

LIST OF PUBLICATIONS

Journal Articles

- Cleaver, D.J., Wang, Z., and Gursul, I., "Lift Enhancement by Means of Small Amplitude Airfoil Oscillations at Low Reynolds Numbers," *AIAA Journal*, Vol. 49, No. 9, 2011, pp. 2018 - 2033.
- Cleaver, D.J., Wang, Z., and Gursul, I., "Bifurcating Flows of Plunging Airfoils at High Strouhal Numbers," *submitted to Journal of Fluid Mechanics.*

Conference Papers

- Cleaver, D.J., Wang, Z.J., and Gursul, I. "Delay of Stall by Small Amplitude Airfoil Oscillation at Low Reynolds Numbers," 47th AIAA Aerospace Sciences Meeting, AIAA 2009-392, 2009.
- Cleaver, D.J., Wang, Z.J., and Gursul, I. "Lift Enhancement on Oscillating Airfoils," 39th AIAA Fluid Dynamics Conference, AIAA 2009-4028, 2009.
- Cleaver, D.J., Wang, Z., and Gursul, I. "Vortex Mode Bifurcation and Lift Force of a Plunging Airfoil at Low Reynolds Numbers," 48th AIAA Aerospace Sciences Meeting, AIAA 2010-390, 2010.
- Cleaver, D.J., Wang, Z., and Gursul, I. "Effect of Airfoil Shape on Flow Control by Small Amplitude Oscillations Control," 50th AIAA Aerospace Sciences Meeting, *accepted*.

REFERENCES

[1] Ho, S., Nassef, H., Pornsinsirirak, N., Tai, Y.C. and Ho, C.M., "Unsteady Aerodynamics and Flow Control for Flapping Wing Flyers". *Progress in Aerospace Sciences*,Vol. 39, No. 8, 2003, pp. 635-681.

[2] Michelson, R.C., "Novel Approaches to Miniature Flight Platforms". *Proceedings of the Institution of Mechanical Engineers - Part G: Journal of Aerospace Engineering*, Vol. 218, 2004, pp. 363-373.

[3] Jones, K.D., Bradshaw, C.J., Papadopoulos, J. and Platzer, M.F., "Bio-Inspired Design of Flapping-Wing Micro Air Vehicles". *Aeronautical Journal*,Vol. 109, No. 1098, 2005, pp. 385-393.

[4] Galinski, C. and Zabowski, R., "Some Problems of Micro Air Vehicles Development". *Bulletin of the Polich Academy of Sciences*,Vol. 55, 2007, pp. 91-98.

[5] Pines, D.J. and Bohorquez, F., "Challenges Facing Future Micro-Air-Vehicle Development". *Journal of Aircraft*,Vol. 43, No. 2, 2006, pp. 290-305.

[6] Shyy, W., Berg, M. and Ljungqvist, D., "Flapping and Flexible Wings for Biological and Micro Air Vehicles". *Progress in Aerospace Sciences*,Vol. 35, No. 5, 1999, pp. 455-505.

[7] Watkins, S., Milbank, J., Loxton, B.J. and Melbourne, W.H., "Atmospheric Winds and Their Implications for Microair Vehicles". *AIAA Journal*,Vol. 44, No. 11, 2006, pp. 2591-2600.

[8] Liu, H.T., "Unsteady Aerodynamics of a Wortmann Wing at Low Reynolds-Numbers". *Journal of Aircraft*,Vol. 29, No. 4, 1992, pp. 532-539.

[9] Stanford, B., Abdulrahim, M., Lind, R. and Ifju, P., "Investigation of Membrane Actuation for Roll Control of a Micro Air Vehicle". *Journal of Aircraft*,Vol. 44, No. 3, 2007, pp. 741-749.

[10] Woods, M.I., Henderson, J.F. and Lock, G.D., "Energy Requirements for the Flight of Micro Air Vehicles". *Aeronautical Journal*,Vol. 105, No. 1045, 2001, pp. 135-149.

[11] Amitay, M., Smith, D.R., Kibens, V., Parekh, D.E. and Glezer, A., "Aerodynamic Flow Control over an Unconventional Airfoil Using Synthetic Jet Actuators". *AIAA Journal*,Vol. 39, No. 3, 2001, pp. 361-370.

[12] Jones, K.D., Dohring, C.M. and Platzer, M.F., "Experimental and Computational Investigation of the Knoller-Betz Effect". *AIAA Journal*,Vol. 36, No. 7, 1998, pp. 1240-1246.

[13] Pornsin-sirirak, T.N., Tai, Y.C., Nassef, H. and Ho, C.M., "Titanium-Alloy MEMS Wing Technology for a Micro Aerial Vehicle Application". *Sensors and Actuators A: Physical*,Vol. 89, No. 1-2, 2001, pp. 95-103.

[14] Ramasamy, M., Lee, T.E. and Leishman, J.G., "Flowfield of a Rotating-Wing Micro Air Vehicle". *Journal of Aircraft*,Vol. 44, No. 4, 2007, pp. 1236-1244.

[15] Bohorquez, F., Samuel, P., Sirohi, J., Pines, D., Rudd, L. and Perel, R., "Design, Analysis and Hover Performance of a Rotary Wing Micro Air Vehicle". *Journal of the American Helicopter Society*,Vol. 48, No. 2, 2003, pp. 80-90.

[16] Gad-el-Hak, M., "Flow Control: The Future". *Journal of Aircraft*,Vol. 38, No. 3, 2001, pp. 402-418.

[17] Greenblatt, D. and Wygnanski, I.J., "The Control of Flow Separation by Periodic Excitation". *Progress in Aerospace Sciences*,Vol. 36, No. 7, 2000, pp. 487-545.

[18] Collis, S.S., Joslin, R.D., Seifert, A. and Theofilis, V., "Issues in Active Flow Control: Theory, Control, Simulation, and Experiment". *Progress in Aerospace Sciences*,Vol. 40, No. 4-5, 2004, pp. 237-289.

[19] Gad-el-Hak, M. and Bushnell, D.M., "Separation Control - Review". *Journal of Fluids Engineering - Transactions of the ASME*,Vol. 113, No. 1, 1991, pp. 5-30.

[20] Seifert, A., Bachar, T., Koss, D., Shepshelovich, M. and Wygnanski, I., "Oscillatory Blowing - a Tool to Delay Boundary-Layer Separation". *AIAA Journal*,Vol. 31, No. 11, 1993, pp. 2052-2060.

[21] Greenblatt, D. and Wygnanski, I., "Dynamic Stall Control by Periodic Excitation, Part 1: NACA 0015 Parametric Study". *Journal of Aircraft*,Vol. 38, No. 3, 2001, pp. 430-438.

[22] Seifert, A. and Pack, L.G., "Oscillatory Control of Separation at High Reynolds Numbers". *AIAA Journal*,Vol. 37, No. 9, 1999, pp. 1062-1071.

[23] Greenblatt, D. and Wygnanski, I., "Effect of Leading-Edge Curvature on Airfoil Separation Control". *Journal of Aircraft*,Vol. 40, No. 3, 2003, pp. 473-481.

[24] Greenblatt, D. and Wygnanski, I.J., "Use of Periodic Excitation to Enhance Airfoil Performance at Low Reynolds Numbers". *Journal of Aircraft*,Vol. 38, No. 1, 2001, pp. 190-192.

[25] Park, Y.W., Lee, S.G., Lee, D.H. and Hong, S., "Stall Control with Local Surface Buzzing on a NACA 0012 Airfoil". *AIAA Journal*,Vol. 39, No. 7, 2001, pp. 1400-1402.

[26] Munday, D. and Jacob, J., "Active Control of Separation on a Wing with Oscillating Camber". *Journal of Aircraft*,Vol. 39, No. 1, 2002, pp. 187-189.

[27] Chandrasekhara, M.S., Wilder, M.C. and Carr, L.W., "Unsteady Stall Control Using Dynamically Deforming Airfoils". *AIAA Journal*,Vol. 36, No. 10, 1998, pp. 1792-1800.

[28] Vardaki, E., Wang, Z. and Gursul, I., "Flow Reattachment and Vortex Re-Formation on Oscillating Low-Aspect-Ratio Wings". *AIAA Journal*,Vol. 46, No. 6, 2008, pp. 1453-1462.

[29] Moreau, E., "Airflow Control by Non-Thermal Plasma Actuators". *Journal of Physics D: Applied Physics*,Vol. 40, No. 3, 2007, pp. 605-636.

[30] Greenblatt, D., Goksel, B., Rechenberg, I., Schule, C.Y., Romann, D. and Paschereit, C.O., "Dielectric Barrier Discharge Flow Control at Very Low Flight Reynolds Numbers". *AIAA Journal*,Vol. 46, No. 6, 2008, pp. 1528-1541.

[31] Galinski, C., "Gust Resistant Fixed Wing Micro Air Vehicle". *Journal of Aircraft*,Vol. 43, No. 5, 2006, pp. 1586-1588.

[32] Rojratsirikul, P., Wang, Z. and Gursul, I., "Unsteady Fluid-Structure Interactions of Membrane Airfoils at Low Reynolds Numbers". *Experiments in Fluids*,Vol. 46, No. 5, 2009, pp. 859-872.

[33] Deluca, A.M., Reeder, M.F., Freeman, J. and Ol, M.V., "Flexible- and Rigid-Wing Micro Air Vehicle: Lift and Drag Comparison". *Journal of Aircraft*,Vol. 43, No. 2, 2006, pp. 572-575.

[34] Taylor, G., Wang, Z., Vardaki, E. and Gursul, I., "Lift Enhancement over Flexible Nonslender Delta Wings". *AIAA Journal*,Vol. 45, No. 12, 2007, pp. 2979-2993.

[35] Gursul, I., Gordnier, R. and Visbal, M., "Unsteady Aerodynamics of Nonslender Delta Wings". *Progress in Aerospace Sciences*,Vol. 41, No. 7, 2005, pp. 515-557.

[36] Gursul, I., Wang, Z. and Vardaki, E., "Review of Flow Control Mechanisms of Leading-Edge Vortices". *Progress in Aerospace Sciences*,Vol. 43, No. 7-8, 2007, pp. 246-270.

[37] Schmidtn, K., "Locomotion - Energy Cost of Swimming, Flying, and Running". *Science*,Vol. 177, No. 4045, 1972, pp. 222-228.

[38] Dickinson, M.H., "Unsteady Mechanisms of Force Generation in Aquatic and Aerial Locomotion". *American Zoologist*,Vol. 36, No. 6, 1996, pp. 537-554.

[39] Triantafyllou, M.S., Techet, A.H. and Hover, F.S., "Review of Experimental Work in Biomimetic Foils". *IEEE Journal of Oceanic Engineering*,Vol. 29, No. 3, 2004, pp. 585-594.

[40] Fish, F.E. and Lauder, G.V., "Passive and Active Flow Control by Swimming Fishes and Mammals". *Annual Review of Fluid Mechanics*,Vol. 38, 2006, pp. 193-224.

[41] Michelson, R.C. and Naqvi, M.A., "Beyond Biologically-Inspired Insect Flight". *Low Re Aerodynamics on Aircraft Including Applications Emerging in UAV Technology* von Karman Institute for Fluid Dynamics, Rhode-Saint-Genese, Belgium, 2008.

[42] Liu, H., Ellington, C.P., Kawachi, K., Van den Berg, C. and Willmott, A.P., "A Computational Fluid Dynamic Study of Hawkmoth Hovering". *Journal of Experimental Biology*,Vol. 201, No. 4, 1998, pp. 461-477.

[43] Yu, Y.L. and Tong, B.G., "A Flow Control Mechanism in Wing Flapping with Stroke Asymmetry During Insect Forward Flight". *ACTA Mechanica Sinica*,Vol. 21, No. 3, 2005, pp. 218-227.

[44] Sane, S.P., "The Aerodynamics of Insect Flight". *Journal of Experimental Biology*,Vol. 206, No. 23, 2003, pp. 4191-4208.

[45] Lehmann, F.O., "The Mechanisms of Lift Enhancement in Insect Flight". *Naturwissenschaften*,Vol. 91, No. 3, 2004, pp. 101-122.

[46] Dickinson, M.H. and Gotz, K.G., "Unsteady Aerodynamic Performance of Model Wings at Low Reynolds-Numbers". *Journal of Experimental Biology*,Vol. 174, 1993, pp. 45-64.

[47] Shyy, W. and Lin, H., "Flapping Wings and Aerodynamic Lift: The Role of Leading-Edge Vortices". *AIAA Journal*,Vol. 45, No. 12, 2007, pp. 2817-2819.

[48] Ellington, C.P., van den Berg, C., Willmott, A.P. and Thomas, A.L.R., "Leading-Edge Vortices in Insect Flight". *Nature*,Vol. 384, No. 6610, 1996, pp. 626-630.

[49] Lin, C.S., Hwu, C. and Young, W.B., "The Thrust and Lift of an Ornithopter's Membrane Wings with Simple Flapping Motion". *Aerospace Science and Technology*,Vol. 10, No. 2, 2006, pp. 111-119.

[50] van den Berg, C. and Ellington, C.P., "The Three-Dimensional Leading-Edge Vortex of a 'Hovering' Model Hawkmoth". *Philosophical Transactions of the Royal Society of London Series B: Biological Sciences*,Vol. 352, No. 1351, 1997, pp. 329-340.

[51] Lu, Y. and Shen, G.X., "Three-Dimensional Flow Structures and Evolution of the Leading-Edge Vortices on a Flapping Wing". *Journal of Experimental Biology*,Vol. 211, No. 8, 2008, pp. 1221-1230.

[52] Wang, Z.J., Birch, J.M. and Dickinson, M.H., "Unsteady Forces and Flows in Low Reynolds Number Hovering Flight: Two-Dimensional Computations vs Robotic Wing Experiments". *Journal of Experimental Biology*,Vol. 207, No. 3, 2004, pp. 449-460.

[53] Michelin, S. and Smith, S.G.L., "Resonance and Propulsion Performance of a Heaving Flexible Wing". *Physics of Fluids*,Vol. 21, No. 7, 2009, p. 15.

[54] Hall, K.C., Pigott, S.A. and Hall, S.R., "Power Requirements for Large-Amplitude Flapping Flight". *Journal of Aircraft*,Vol. 35, No. 3, 1998, pp. 352-361.

[55] Lai, J.C.S. and Platzer, M.F., "Jet Characteristics of a Plunging Airfoil". *AIAA Journal*,Vol. 37, No. 12, 1999, pp. 1529-1537.

[56] Triantafyllou, M.S., Triantafyllou, G.S. and Gopalkrishnan, R., "Wake Mechanics for Thrust Generation in Oscillating Foils". *Physics of Fluids A - Fluid Dynamics*,Vol. 3, No. 12, 1991, pp. 2835-2837.

[57] Heathcote, S. and Gursul, I., "Flexible Flapping Airfoil Propulsion at Low Reynolds Numbers". *AIAA Journal*,Vol. 45, No. 5, 2007, pp. 1066-1079.

[58] Taylor, G.K., Nudds, R.L. and Thomas, A.L.R., "Flying and Swimming Animals Cruise at a Strouhal Number Tuned for High Power Efficiency". *Nature*,Vol. 425, No. 6959, 2003, pp. 707-711.

[59] Lua, K.B., Lim, T.T., Yeo, K.S. and Oo, G.Y., "Wake-Structure Formation of a Heaving Two-Dimensional Elliptic Airfoil". *AIAA Journal*,Vol. 45, No. 7, 2007, pp. 1571-1583.

[60] Young, J. and Lai, J.C.S., "Mechanisms Influencing the Efficiency of Oscillating Airfoil Propulsion". *AIAA Journal*,Vol. 45, No. 7, 2007, pp. 1695-1702.

[61] Anderson, J.M., Streitlien, K., Barrett, D.S. and Triantafyllou, M.S., "Oscillating Foils of High Propulsive Efficiency". *Journal of Fluid Mechanics*,Vol. 360, 1998, pp. 41-72.

[62] Lewin, G.C. and Haj-Hariri, H., "Modelling Thrust Generation of a Two-Dimensional Heaving Airfoil in a Viscous Flow". *Journal of Fluid Mechanics*,Vol. 492, 2003, pp. 339-362.

[63] Tuncer, I.H. and Kaya, M., "Optimization of Flapping Airfoils for Maximum Thrust and Propulsive Efficiency". *AIAA Journal*,Vol. 43, No. 11, 2005, pp. 2329-2336.

[64] Young, J. and Lai, J.C.S., "Oscillation Frequency and Amplitude Effects on the Wake of a Plunging Airfoil". *AIAA Journal*,Vol. 42, No. 10, 2004, pp. 2042-2052.

[65] Koochesfahani, M.M., "Vortical Patterns in the Wake of an Oscillating Airfoil". *AIAA Journal*,Vol. 27, No. 9, 1989, pp. 1200-1205.

[66] Young, J. and Lai, J.C.S., "Vortex Lock-in Phenomenon in the Wake of a Plunging Airfoil". *AIAA Journal*,Vol. 45, No. 2, 2007, pp. 485-490.

[67] Heathcote, S. and Gursul, I., "Jet Switching Phenomenon for a Periodically Plunging Airfoil". *Physics of Fluids*,Vol. 19, No. 2, 2007.

[68] Godoy-Diana, R., Aider, J.L. and Wesfreid, J.E., "Transitions in the Wake of a Flapping Foil". *Physical Review E*,Vol. 77, No. 1, 2008.

[69] von Ellenrieder, K.D. and Pothos, S., "PIV Measurements of the Asymmetric Wake of a Two Dimensional Heaving Hydrofoil". *Experiments in Fluids*,Vol. 44, No. 5, 2008, pp. 733-745.

[70] Godoy-Diana, R., Marais, C., Aider, J.L. and Wesfreid, J.E., "A Model for the Symmetry Breaking of the Reverse Benard-Von Karman Vortex Street Produced by a Flapping Foil". *Journal of Fluid Mechanics*,Vol. 622, 2009, pp. 23-32.

[71] Wang, Z.J., "Two Dimensional Mechanism for Insect Hovering". *Physical Review Letters*,Vol. 85, No. 10, 2000, pp. 2216-2219.

[72] Wang, Z.J., "Vortex Shedding and Frequency Selection in Flapping Flight". *Journal of Fluid Mechanics*,Vol. 410, 2000, pp. 323-341.

[73] Bohl, D.G. and Koochesfahani, M.M., "MTV Measurements of the Vortical Field in the Wake of an Airfoil Oscillating at High Reduced Frequency". *Journal of Fluid Mechanics*,Vol. 620, 2009, pp. 63-88.

[74] Ashraf, M.H., Young, J. and Lai, J.C.S., "Effect of Airfoil Thickness, Camber and Reynolds Number on Plunging Airfoil Propulsion". *47th AIAA Aerospace Sciences Meeting*, Orlando, Florida, 2009.

[75] Ohmi, K., Coutanceau, M., Loc, T.P. and Dulieu, A., "Vortex Formation around an Oscillating and Translating Airfoil at Large Incidences". *Journal of Fluid Mechanics*,Vol. 211, 1990, pp. 37-60.

[76] Buchholz, J.H.J. and Smits, A.J., "The Wake Structure and Thrust Performance of a Rigid Low-Aspect-Ratio Pitching Panel". *Journal of Fluid Mechanics*,Vol. 603, 2008, pp. 331-365.

[77] Freymuth, P., "Propulsive Vortical Signature of Plunging and Pitching Airfoils". *AIAA Journal*,Vol. 26, No. 7, 1988, pp. 881-883.

[78] Rival, D., Prangemeier, T. and Tropea, C., "The Influence of Airfoil Kinematics on the Formation of Leading-Edge Vortices in Bio-Inspired Flight". *Experiments in Fluids*,Vol. 46, No. 5, 2009, pp. 823-833.

[79] Andro, J.Y. and Jacquin, L., "Frequency Effects on the Aerodynamic Mechanisms of a Heaving Airfoil in a Forward Flight Configuration". *Aerospace Science and Technology*,Vol. 13, No. 1, 2009, pp. 71-80.

[80] Parker, K., von Ellenrieder, K.D. and Soria, J., "Morphology of the Forced Oscillatory Flow Past a Finite-Span Wing at Low Reynolds Number". *Journal of Fluid Mechanics*,Vol. 571, 2007, pp. 327-357.

[81] Parker, K., Soria, J. and von Ellenrieder, K.D., "Thrust Measurements from a Finite-Span Flapping Wing". *AIAA Journal*,Vol. 45, No. 1, 2007, pp. 58-70.

[82] Parker, K., von Ellenrieder, K.D. and Soria, J., "Using Stereo Multigrid DPIV (SMDPIV) Measurements to Investigate the Vortical Skeleton Behind a Finite-Span Flapping Wing". *Experiments in Fluids*,Vol. 39, No. 2, 2005, pp. 281-298.

[83] Heathcote, S., "Flexible Flapping Airfoil Propulsion at Low Reynolds Numbers". Ph.D. Dissertation, Dept of Mechanical Engineering, University of Bath, Bath, 2006.

[84] Buchholz, J.H.J. and Smits, A.J., "On the Evolution of the Wake Structure Produced by a Low-Aspect-Ratio Pitching Panel". *Journal of Fluid Mechanics*,Vol. 546, 2006, pp. 433-443.

[85] Ringuette, M.J., Milano, M. and Gharib, M., "Role of the Tip Vortex in the Force Generation of Low-Aspect-Ratio Normal Flat Plates". *Journal of Fluid Mechanics*,Vol. 581, 2007, pp. 453-468.

[86] Rozhdestvensky, K.V. and Ryzhov, V.A., "Aerohydrodynamics of Flapping-Wing Propulsors". *Progress in Aerospace Sciences*,Vol. 39, No. 8, 2003, pp. 585-633.

[87] Garrick, I.E., "Propulsion of a Flapping and Oscillating Airfoil". NASA Technical Report, 567, 1936.

[88] Lee, T. and Gerontakos, P., "Investigation of Flow over an Oscillating Airfoil". *Journal of Fluid Mechanics*,Vol. 512, 2004, pp. 313-341.

[89] Joo, W., Lee, B.S., Yee, K. and Lee, D.H., "Combining Passive Control Method for Dynamic Stall Control". *Journal of Aircraft*,Vol. 43, No. 4, 2006, pp. 1120-1128.

[90] Carr, L.W., "Progress in Analysis and Prediction of Dynamic Stall". *Journal of Aircraft*,Vol. 25, No. 1, 1988, pp. 6-17.

[91] McCroskey, W.J., "The Phenomenon of Dynamic Stall". *NASA TM 81642*, 1981.

[92] Greenblatt, D., Nishri, B., Darabi, A. and Wygnanski, I., "Dynamic Stall Control by Periodic Excitation, Part 2: Mechanisms". *Journal of Aircraft*,Vol. 38, No. 3, 2001, pp. 439-447.

[93] Shih, C., Lourenco, L., Vandommelen, L. and Krothapalli, A., "Unsteady-Flow Past an Airfoil Pitching at a Constant Rate". *AIAA Journal*,Vol. 30, No. 5, 1992, pp. 1153-1161.

[94] McAlister, K.W., Carr, L.W. and McCroskey, W.J., "Dynamic Stall Experiments of the NACA 0012 Airfoil". *NASA Technical Paper 1100*, 1978.

[95] Panda, J. and Zaman, K.B.M.Q., "Experimental Investigation of the Flow-Field of an Oscillating Airfoil and Estimation of Lift from Wake Surveys". *Journal of Fluid Mechanics*,Vol. 265, 1994, pp. 65-95.

[96] Carr, L.W., McAlister, K.W. and McCroskey, W.J., "Analysis of the Development of Dynamic Stall Based on Airfoil Experiments". *NASA TN D-8382*, 1977.

[97] Oshima, H. and Ramaprian, B.R., "Velocity Measurements over a Pitching Airfoil". *AIAA Journal*,Vol. 35, No. 1, 1997, pp. 119-126.

[98] Lee, T., Petrakis, G., Mokhtarian, F. and Kafyeke, F., "Boundary-Layer Transition, Separation, and Reattachment on an Oscillating Airfoil". *Journal of Aircraft*,Vol. 37, No. 2, 2000, pp. 356-360.

[99] Walker, J.A. and Westneat, M.W., "Mechanical Performance of Aquatic Rowing and Flying". *Proceedings of the Royal Society of London Series B: Biological Sciences*,Vol. 267, No. 1455, 2000, pp. 1875-1881.

[100] Maresca, C., Favier, D. and Rebont, J., "Experiments on an Aerofoil at High Angle of Incidence in Longitudinal Oscillations". *Journal of Fluid Mechanics*,Vol. 92, No. Jun, 1979, pp. 671-690.

[101] Gursul, I. and Ho, C.M., "High Aerodynamic Loads on an Airfoil Submerged in an Unsteady Stream". *AIAA Journal*,Vol. 30, No. 4, 1992, pp. 1117-1119.

[102] Soueid, H., Guglielmini, L., Airiau, C. and Bottaro, A., "Optimization of the Motion of a Flapping Airfoil Using Sensitivity Functions". *Computers & Fluids*,Vol. 38, No. 4, 2009, pp. 861-874.

[103] Schouveiler, L., Hover, F.S. and Triantafyllou, M.S., "Performance of Flapping Foil Propulsion". *Journal of Fluids and Structures*,Vol. 20, No. 7, 2005, pp. 949-959.

[104] Read, D.A., Hover, F.S. and Triantafyllou, M.S., "Forces on Oscillating Foils for Propulsion and Maneuvering". *Journal of Fluids and Structures*,Vol. 17, No. 1, 2003, pp. 163-183.

[105] Oyama, A., Okabe, Y., Fujii, K. and Shimoyama, K., "A Study on Flapping Motion for MAV Design Using Design Exploration". *AIAA Infotech@Aerospace 2007 Conference and Exhibit*, Rohnert Park, California, 2007.

[106] Oyama, A., Okabe, Y., Shimoyama, K. and Fujii, K., "Aerodynamic Multiobjective Design Exploration of a Flapping Airfoil Using a Navier-Stokes Solver". *Journal of Aerospace Computing Information and Communication*,Vol. 6, No. 3, 2009, pp. 256-270.

[107] Hover, F.S., Haugsdal, O. and Triantafyllou, M.S., "Effect of Angle of Attack Profiles in Flapping Foil Propulsion". *Journal of Fluids and Structures*,Vol. 19, No. 1, 2004, pp. 37-47.

[108] Kaya, M. and Tuncer, I.H., "Nonsinusoidal Path Optimization of a Flapping Airfoil". *AIAA Journal*,Vol. 45, No. 8, 2007, pp. 2075-2082.

[109] Triantafyllou, M.S., Hover, F.S., Techet, A.H. and Yue, D.K.P., "Review of Hydrodynamic Scaling Laws in Aquatic Locomotion and Fishlike Swimming". *Applied Mechanics Reviews*,Vol. 58, No. 4, 2005, pp. 226-237.

[110] Tinar, E. and Cetiner, O., "Acceleration Data Correlated with PIV Images for Self-Induced Vibrations of an Airfoil". *Experiments in Fluids*,Vol. 41, No. 2, 2006, pp. 201-212.

[111] Murray, M.M. and Howle, L.E., "Spring Stiffness Influence on an Oscillating Propulsor". *Journal of Fluids and Structures*,Vol. 17, No. 7, 2003, pp. 915-926.

[112] Pankhurst, R.C. and Holder, D.W., *Wind-Tunnel Techniques*. Sir Isaac Pitman & Sons Ltd, London, 1965.

[113] von Ellenrieder, K.D., Parker, K. and Soria, J., "Flow Structures Behind a Heaving and Pitching Finite-Span Wing". *Journal of Fluid Mechanics*,Vol. 490, 2003, pp. 129-138.

[114] Moffat, R.J., "Contributions to the Theory of Single-Sample Uncertainty Analysis". *Journal of Fluids Engineering - Transactions of the ASME*,Vol. 104, No. 2, 1982, pp. 250-260.

[115] Mueller, T.J. and DeLaurier, J.D., "Aerodynamics of Small Vehicles". *Annual Review of Fluid Mechanics*,Vol. 35, 2003, pp. 89-111.

[116] Frampton, K.D., Goldfarb, M., Monopoli, D. and Cveticanin, D., "Passive Aeroelastic Tailoring for Optimal Flapping Wings". *Proceedings of Conference on Fixed, Flapping and Rotary Wing Vehicles at Very Low Reynolds Numbers*, Notre Dame, USA, 2000.

[117] Moffat, R.J., "Describing the Uncertainties in Experimental Results". *Experimental Thermal and Fluid Science*,Vol. 1, No. 1, 1988, pp. 3-17.

[118] Moffat, R.J., "Using Uncertainty Analysis in the Planning of an Experiment". *Journal of Fluids Engineering - Transactions of the ASME*,Vol. 107, No. 2, 1985, pp. 173-178.

[119] ESDU, "Response of Structures to Vortex Shedding". Engineering Science Data Unit, Item no. 96030, 1996.

[120] Graftieaux, L., Michard, M. and Grosjean, N., "Combining PIV, POD and Vortex Identification Algorithms for the Study of Unsteady Turbulent Swirling Flows". *Measurement Science & Technology*,Vol. 12, No. 9, 2001, pp. 1422-1429.

[121] Morgan, C.E., Babinsky, H. and Harvey, J.K., "Vortex Detection Methods for Use with PIV and CFD Data". *47th AIAA Aerospace Sciences Meeting*, Orlando, Florida, 2009.

[122] McCroskey, W.J., "A Critical Assessment of Wind Tunnel Results for the NACA 0012 Airfoil". *NASA TM 100019*, 1987.

[123] Huang, R.F. and Lin, C.L., "Vortex Shedding and Shear-Layer Instability of Wing at Low-Reynolds Numbers". *AIAA Journal*,Vol. 33, No. 8, 1995, pp. 1398-1403.

[124] Sunneechurra, K. and Crowther, W.J., "Problems with Leading-Edge Flow Control Experiments". *Journal of Aircraft*,Vol. 44, No. 3, 2007, pp. 1052-1055.

[125] Kim, D.H., Yuang, J.H., Chang, J.W. and Chung, J., "Boundary Layer and near-Wake Measurements of NACA 0012 Airfoil at Low Reynolds Numbers". *47th AIAA Aerospace Sciences Meeting*, Orlando, Florida, 2009.

[126] Visbal, M.R., Gordnier, R.E. and Galbraith, M.C., "High-Fidelity Simulations of Moving and Flexible Airfoils at Low Reynolds Numbers". *Experiments in Fluids*,Vol. 46, No. 5, 2009, pp. 903-922.

[127] Sunada, S., Yasuda, T., Yasuda, K. and Kawachi, K., "Comparison of Wing Characteristics at an Ultralow Reynolds Number". *Journal of Aircraft*,Vol. 39, No. 2, 2002, pp. 331-338.

[128] Sunada, S., Sakaguchi, A. and Kawachi, K., "Airfoil Section Characteristics at a Low Reynolds Number". *Journal of Fluids Engineering - Transactions of the ASME*,Vol. 119, No. 1, 1997, pp. 129-135.

[129] Tsang, K.K.Y., So, R.M.C., Leung, R.C.K. and Wang, X.Q., "Dynamic Stall Behavior from Unsteady Force Measurements". *Journal of Fluids and Structures*,Vol. 24, No. 1, 2008, pp. 129-150.

[130] Chen, J.M. and Choa, C.C., "Freestream Disturbance Effects on an Airfoil Pitching at Constant Rate". *Journal of Aircraft*,Vol. 36, No. 3, 1999, pp. 507-514.

[131] McKinney, W.D., J.;, "The Wingmill: An Oscillating-Wing Windmill". *Journal of Energy*,Vol. 5, No. 2, 1981, pp. 109-115.

[132] Abernathy, F.H., "Flow over an Inclined Plate". *Transactions of the ASME, Journal of Basic Engineering*,Vol. 84, 1962, pp. 380 - 388.

[133] Okamoto, M. and Azuma, A., "Aerodynamic Characteristics at Low Reynolds Numbers for Wings of Various Planforms". *AIAA Journal*,Vol. 49, No. 6, 2011, pp. 1135-1150.

[134] Mueller, T.J., "Aerodynamic Measurements at Low Reynolds Numbers for Fixed Wing Micro-Air Vehicles". *Development and Operation of UAVs for Military and Civil Applications*, von Karman Institute for Fluid Dynamics, Rhode-Saint-Genese, Belgium, 1999, p. 302.

[135] Fage, A. and Johansen, F.C., "On the Flow of Air Behind an Inclined Flat Plate of Infinite Span". *Proceedings of the Royal Society of London Series A*,Vol. 116, 1927, pp. 170-197.

[136] Schluter, J.U., "Lift Enhancement at Low Reynolds Numbers Using Pop-up Feathers". *39th AIAA Fluid Dynamics Conference*, San Antonio, Texas, 2009.

[137] Wu, J.Z., Lu, X.Y., Denny, A.G., Fan, M. and Wu, J.M., "Post-Stall Flow Control on an Airfoil by Local Unsteady Forcing". *Journal of Fluid Mechanics*,Vol. 371, 1998, pp. 21-58.

[138] Miranda, S., Vlachos, P.P., Telionis, D.P. and Zeiger, M.D., "Flow Control of a Sharp-Edged Airfoil". *AIAA Journal*,Vol. 43, No. 4, 2005, pp. 716-726.

[139] Bearman, P.W., "Vortex Shedding from Oscillating Bluff-Bodies". *Annual Review of Fluid Mechanics*,Vol. 16, 1984, pp. 195-222.

[140] Visbal, M.R., "High-Fidelity Simulation of Transitional Flows Past a Plunging Airfoil". *AIAA Journal*,Vol. 47, No. 11, 2009, pp. 2685-2697.

[141] Cleaver, D.J., Wang, Z.J. and Gursul, I., "Delay of Stall by Small Amplitude Airfoil Oscillation at Low Reynolds Numbers". *47th AIAA Aerospace Sciences Meeting*, Orlando, Florida, 2009.

[142] Emblemsvag, J.E., Suzuki, R. and Candler, G., "Numerical Simulation of Flapping Micro Air Vehicles". *32nd AIAA Fluid Dynamics Meeting*, St. Louis, MO; US, 2002.

[143] Liang, C.L., Ou, K., Premasuthan, S., Jameson, A. and Wang, Z.J., "High-Order Accurate Simulations of Unsteady Flow Past Plunging and Pitching Airfoils". *Computers & Fluids*,Vol. 40, No. 1, 2011, pp. 236-248.

[144] Tuncer, I.H. and Platzer, M.F., "Computational Study of Flapping Airfoil Aerodynamics". *Journal of Aircraft*,Vol. 37, No. 3, 2000, pp. 514-520.

[145] Jones, K.D. and Platzer, M.F., "Numerical Computation of Flapping-Wing Propulsion and Power Extraction". *35th Aerospace Sciences Meeting & Exhibit*, Reno, NV, 1997.

[146] Milne-Thomson, L.M., *Theoretical Hydrodynamics*. The Macmillan Press Ltd, London, 1968.

Appendices

Appendix 1 – Uncertainty Analysis

The force uncertainties were calculated based on the method of Moffat [114, 118]. In essence this method combines all possible sources of uncertainty in a systematic manner to obtain a 'true' value such that if the experiments were repeated at a different institution, by a different individual, using different equipment, the uncertainty bounds would cross in 95% of cases (or as the confidence intervals dictate). The core of the method is the equation:

$$\delta R = \left\{ \left(\frac{\partial R}{\partial x_1} \delta x_1 \right)^2 + \left(\frac{\partial R}{\partial x_2} \delta x_2 \right)^2 + ... \left(\frac{\partial R}{\partial x_i} \delta x_i \right)^2 \right\}^{\frac{1}{2}}$$

Where, R is the desired quantity (in this case C_l, C_d and C_P), and x represents the contributing variables.

Lift / Drag Coefficient

For C_l and C_d:

$$C_f = \frac{F}{\frac{1}{2}\rho b c U_\infty{}^2} = \frac{F}{Q}$$

then,

$$\delta C_f = \left\{ \left(\frac{\partial C_f}{\partial F} \delta F \right)^2 + \left(\frac{\partial C_f}{\partial Q} \delta Q \right)^2 \right\}^{\frac{1}{2}}$$

$$= \left\{ \left(\frac{1}{Q} \delta F \right)^2 + \left(\frac{F}{Q^2} \delta Q \right)^2 \right\}^{\frac{1}{2}}$$

where f / F is the force (lift or drag) under consideration and Q represents the aerodynamic constant. For convenience the two terms δF and δQ can therefore be further subdivided into their contributing variables and calculated separately.

Force Uncertainty - δF

The force F is derived from the average of ~20,000 voltages which is converted through a linear calibration. There are therefore four possible sources of uncertainty:

1. *Moment Uncertainty* – due to inadequacies in the force balance design it is possible that the same force at root and tip would be measured differently. This effect was measured and always found to be <1%, therefore:

$$\delta M = 0.01 * F$$

2. *Averaging Uncertainty* – any average is an estimate to the real value. The uncertainty of this estimate can be quantified through:

$$\delta N = \frac{\left(1.96 * \frac{\sigma(v)}{b}\right)}{N^{0.5}}$$

Where Volt is the raw voltage data, N is the number of data points, and a and b are the constants from the linear calibration. The 1.96 was selected for 95% confidence interval bounds.

3. *Calibration Uncertainty* – attached to each calibration will be an uncertainty. This is calculated separately by again quantifying all the contributing elements. The result is three calibration curves, a mean from which the average value is calculated, and an upper and lower which are used to determine the uncertainty.

$$\delta C = \frac{F_U - F_L}{2}$$

4. *Drift Uncertainty* – the calibration was performed before and after each run of tests. It therefore recorded any drift in the strain gauges and the difference between the two is therefore a good estimate of the uncertainty due to drift:

$$\delta D = \frac{F_B - F_A}{2}$$

These four uncertainties combine to give:

$$\delta F = \left\{ \left(\frac{\partial F}{\partial M}\delta M\right)^2 + \left(\frac{\partial F}{\partial N}\delta N\right)^2 + \left(\frac{\partial F}{\partial C}\delta C\right)^2 + \left(\frac{\partial F}{\partial D}\delta D\right)^2 \right\}^{\frac{1}{2}}$$

$$= \left\{ (0.01F)^2 + \left(\frac{\left(1.96 * \frac{\sigma(v)}{b} \right)}{N^{0.5}} \right)^2 + \left(\frac{F_U - F_L}{2} \right)^2 + \left(\frac{F_B - F_A}{2} \right)^2 \right\}^{\frac{1}{2}}$$

Aerodynamic Constant Uncertainty - δQ

The variables in the aerodynamic constant are either directly measured or calibrated. Each therefore has its own uncertainty:

1. *Density Uncertainty*– the water temperature was measured daily to within ±0.5 K and the density calculated through:

$$\rho = 0.0000492889 * T^3 - 0.0082567619 * T^2 + 0.635315873 * T + 999.8449523809$$

The uncertainty associated with this calculation is therefore:

$$\delta\rho = \frac{\partial \rho}{\partial T} \delta T = \left(3 * 0.0000492889 * T^2 - 2 * 0.0082567619 * T + 0.635315873 \right) * 0.5$$

2. *Velocity Uncertainty* – the velocity was calibrated relative to a water tunnel frequency setting. The uncertainty associated with this is estimated as 0.001 m/s.

$$\delta U_\infty = 0.001$$

3. *Span Uncertainty* – the span can realistically be measured to within 0.5 mm. The uncertainty is therefore:

$$\delta b = 0.0005$$

4. *Chord Uncertainty* – the chord can realistically be measured to within 0.5 mm. The uncertainty is therefore:

$$\delta c = 0.0005$$

These four uncertainties combine to give:

$$\delta Q = \left\{ \left(\frac{\partial Q}{\partial \rho} \delta\rho \right)^2 + \left(\frac{\partial F}{\partial U_\infty} \delta U_\infty \right)^2 + \left(\frac{\partial F}{\partial b} \delta b \right)^2 + \left(\frac{\partial F}{\partial c} \delta c \right)^2 \right\}^{\frac{1}{2}}$$

$$= \begin{Bmatrix} \left(\frac{1}{2} bcU_\infty{}^2 * 0.5\left(3 * 0.0000492889 * \mathrm{T}^2 - 2 * 0.0082567619 * \mathrm{T} + 0.635315873\right)\right)^2 + \ldots \\ \left(\rho bcU_\infty * 0.001\right)^2 + \left(\frac{1}{2}\rho cU_\infty{}^2 * 0.0005\right)^2 + \left(\frac{1}{2}\rho bU_\infty{}^2 * 0.0005\right)^2 \end{Bmatrix}^{\frac{1}{2}}$$

Power Coefficient

For C_p:

$$C_p = \frac{P}{\frac{1}{2}\rho bcU_\infty{}^3} = \frac{P}{Q_2}$$

then,

$$\delta C_p = \left\{ \left(\frac{\partial C_p}{\partial P}\delta P\right)^2 + \left(\frac{\partial C_p}{\partial Q_2}\delta Q_2\right)^2 \right\}^{\frac{1}{2}}$$

$$= \left\{ \left(\frac{1}{Q_2}\delta P\right)^2 + \left(\frac{P}{Q_2{}^2}\delta Q_2\right)^2 \right\}^{\frac{1}{2}}$$

Power Uncertainty - δP

The power $\overline{F_y V_y}$ is derived from the average of 20,000 voltages converted to a force through a through a linear calibration multiplied by the velocity which is estimated by recording the position in the cycle through a calibrated rotary encoder:

$$P = \overline{F_y V_y} = \overline{\left(\frac{V - L_{Const}}{L_{Grad}}\right)} - a2\pi f \sin(2\pi ft - b)$$

For every point there are therefore six possible sources of uncertainty:

1. *Calibration Uncertainty* – attached to each calibration will be an uncertainty. This is calculated separately by quantifying all the contributing elements. The result is three calibration curves, a mean from which the average value F_y is calculated, and an upper and lower that are used to determine the uncertainty:

$$\delta C = \frac{F_{y,U} - F_{y,L}}{2}$$

2. *Moment Uncertainty* – due to inadequacies in the force balance design it is possible that the same force at root and tip would be measured differently. This effect was measured for all force balances and always found to be <1%, therefore:

$$\delta M = 0.01 * F_y$$

3. *Drift Uncertainty* – the calibration was performed before and after each run of tests. It therefore recorded any drift in the strain gauges and the difference between the two is therefore a good estimate of the uncertainty due to drift:

$$\delta D = \frac{F_{y,B} - F_{y,A}}{2}$$

4. *Amplitude Uncertainty* – the amplitude is only certain to +/- 10%

$$\delta a = 0.1a$$

5. *Frequency Uncertainty* – the frequency is directly derived from the recorded data and is therefore relatively accurate, a suitable uncertainty is therefore:

$$\delta f = 0.01 f$$

6. *Cycle Uncertainty* – the accuracy of the position in the cycle ($2\pi ft$ - b) is:

$$\delta pos = 5°$$

A further seventh uncertainty arises through the averaging of all these points:

7. *Averaging Uncertainty* – any average is an estimate to the real value. The uncertainty of this estimate can be quantified through:

$$\delta N = \frac{\left(1.96 * \sigma(F_y V_y)\right)}{N^{0.5}}$$

These seven uncertainties combine to give:

$$\delta\overline{F_yV_y} = \left\{ \begin{array}{l} \overline{\left\{ \begin{array}{l} \left(\frac{\partial\overline{F_yV_y}}{\partial C}\delta C\right)^2 + \left(\frac{\partial\overline{F_yV_y}}{\partial M}\delta M\right)^2 + \left(\frac{\partial\overline{F_yV_y}}{\partial D}\delta D\right)^2 + \left(\frac{\partial\overline{F_yV_y}}{\partial a}\delta a\right)^2 \\ + \left(\frac{\partial\overline{F_yV_y}}{\partial f}\delta f\right)^2 + \left(\frac{\partial\overline{F_yV_y}}{\partial pos}\delta pos\right)^2 \end{array} \right\}^{\frac{1}{2}}} + \left(\frac{\partial\overline{F_yV_y}}{\partial N}\delta N\right)^2 \end{array} \right\}$$

$$= \left\{ \begin{array}{l} \overline{\left\{ \begin{array}{l} \left(\frac{F_{y,U}-F_{y,L}}{2} * a2\pi f\sin(2\pi ft-b)\right)^2 + \left(0.01F_y * a2\pi f\sin(2\pi ft-b)\right)^2 + \\ \left(\frac{F_{y,B}-F_{y,A}}{2} * -a2\pi f\sin(2\pi ft-b)\right)^2 + \left(F_y 2\pi f\sin(2\pi ft-b) * 0.1a\right)^2 + \\ \left(F_y a2\pi\sin(2\pi ft-b) * 0.01f\right)^2 + \left(F_y a2\pi f\frac{(\sin(2\pi ft-b+5°)-\sin(2\pi ft-b-5°))}{2}\right)^2 \end{array} \right\}^{\frac{1}{2}}} + \left(\frac{\left(1.96*\sigma(F_yV_y)\right)}{N^{0.5}}\right)^2 \end{array} \right\}^{\frac{1}{2}}$$

The aerodynamic constant will scale similarly to that for lift / drag coefficient except with a further freestream velocity term, thus giving:

$$\delta Q = \left\{ \begin{array}{l} \left(\frac{1}{2}bcU_\infty{}^3 * 0.5\left(3*0.0000492889*\mathrm{T}^2 - 2*0.0082567619*\mathrm{T} + 0.635315873\right)\right)^2 + \ldots \\ \left(\frac{3}{2}\rho bcU_\infty{}^2 * 0.001\right)^2 + \left(\frac{1}{2}\rho cU_\infty{}^3 * 0.0005\right)^2 + \left(\frac{1}{2}\rho bU_\infty{}^3 * 0.0005\right)^2 \end{array} \right\}^{\frac{1}{2}}$$

Finally, the two combine to give a power coefficient uncertainty:

$$\delta C_p = \left\{ \left(\frac{\partial C_P}{\partial P}\delta P\right)^2 + \left(\frac{\partial C_P}{\partial Q}\delta Q\right)^2 \right\}^{\frac{1}{2}}$$

$$= \left\{ \left(\frac{1}{Q}\delta P\right)^2 + \left(\frac{C_P}{Q^2}\delta Q\right)^2 \right\}^{\frac{1}{2}}$$

Combining Multiple Measurements

The value δC_f is for a single value of force / power coefficient. When combining multiple values across say different runs / sets, it is also necessary to combine their uncertainties. Given that the mean coefficient can be defined as:

$$\overline{C}_f = \frac{C_{f,1} + C_{f,2} + \cdots C_{f,n}}{n}$$

Then the uncertainty of this mean can be defined as:

$$\delta\overline{C}_f = \left\{ \left(\frac{\partial \overline{C}_f}{\partial C_{f,1}} \delta C_{f,1} \right)^2 + \left(\frac{\partial \overline{C}_f}{\partial C_{f,2}} \delta C_{f,2} \right)^2 + \cdots \left(\frac{\partial \overline{C}_f}{\partial C_{f,n}} \delta C_{f,n} \right)^2 + \left(\frac{1.96 * \sigma(C_{f,1\ldots N})}{N} \right)^2 \right\}^{0.5}$$

$$= \left\{ \left(\frac{1}{n} \delta C_{f,1} \right)^2 + \left(\frac{1}{n} \delta C_{f,2} \right)^2 + \cdots \left(\frac{1}{n} \delta C_{f,n} \right)^2 + \left(\frac{1.96 * \sigma(C_{f,1\ldots N})}{N} \right)^2 \right\}^{0.5}$$

$$= \left\{ \frac{\left\{ \delta C_{f,1}{}^2 + \delta C_{f,2}{}^2 + \cdots \delta C_{f,3}{}^2 \right\}^{0.5}}{n} + \left(\frac{1.96 * \sigma(C_{f,1\ldots N})}{N} \right)^2 \right\}^{\frac{1}{2}}$$

The first part takes account of the calibration uncertainty (bias error); the second part takes account of the precision error.

Appendix 2 – Mode-Switch Points

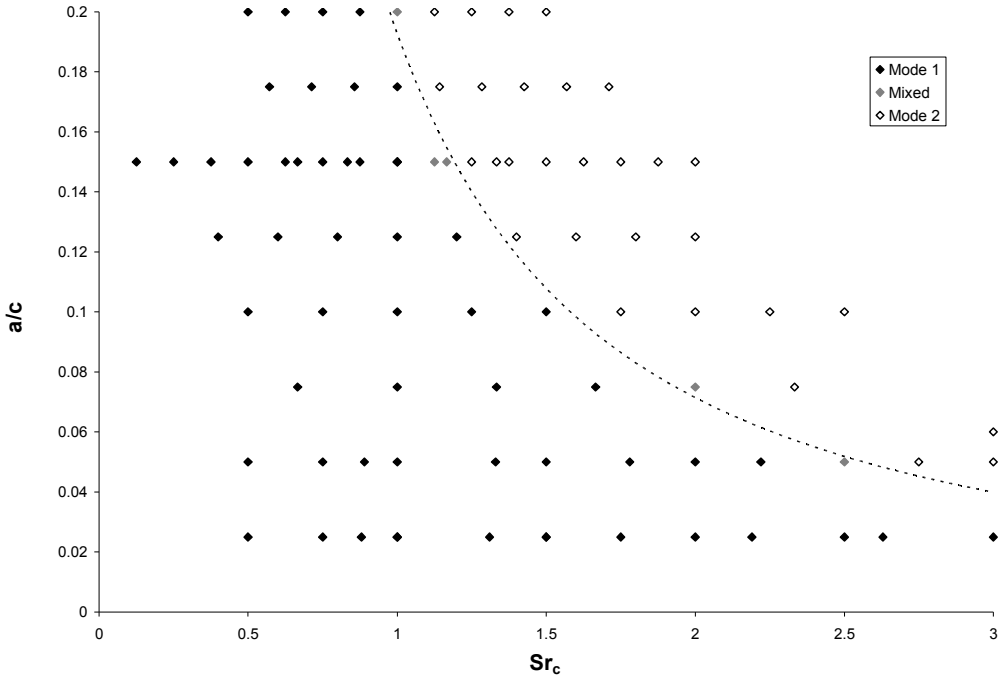

Fig. A.1 Phase-averaged PIV measurements used to determine the mode-switch boundary shown in Fig. 3.13.